EVOLUTION OF THE SUDBURY IGNEOUS COMPLEX SOUTHERN METAMORPHIC AUREOLE AND CONTROLS ON ANATEXIS

by

Taus Richardt Chræmmer Jørgensen

A thesis submitted in partial fulfillment of the requirements of the degree of Doctor of Philosophy (Ph.D.) in Mineral Deposits and Precambrian Geology

The Faculty of Graduate Studies

Laurentian University

Sudbury, Ontario, Canada

THESIS DEFENCE COMMITTEE/COMITÉ DE SOUTENANCE DE THÈSE
Laurentian Université/Université Laurentienne
Faculty of Graduate Studies/Faculté des études supérieures

Title of Thesis
Titre de la thèse: EVOLUTION OF THE SUDBURY IGNEOUS COMPLEX SOUTHERN METAMORPHIC AUREOLE AND CONTROL ON ANATEXIS

Name of Candidate
Nom du candidat: Jørgensen, Taus

Degree
Diplôme: Doctor of Philosophy

Department/Program
Département/Programme: PhD Mineral Deposits and Pre-Cambrian Geology

Date of Defence March 28, 2017

APPROVED/APPROUVÉ

Thesis Examiners/Examinateurs de thèse:

Dr. Douglas Tinkham
(Co-Supervisor/Co-directeur(trice) de thèse)

Dr. C. Michael Lesher
(Co-Supervisor/Co-directeur(trice) de thèse)

Dr. Pedro J. Jugo
(Committee member/Membre du comité)

Approved for the Faculty of Graduate Studies
Approuvé pour la Faculté des études supérieures
Dr. David Lesbarrères
Monsieur David Lesbarrères
Dean, Faculty of Graduate Studies
Doyen, Faculté des études supérieures

Dr. James S. Beard
(External Examiner/Examinateur externe)

Dr. Redhouane Henda
(Internal Examiner/Examinateur interne)

ACCESSIBILITY CLAUSE AND PERMISSION TO USE

Abstract

The South Range metamorphic aureole around the 1.85 Ga Sudbury Igneous Complex (SIC) is spatiotemporally connected to the world-class ore deposits of the Sudbury mining camp. Defining the physiochemical expression and understanding the evolution of the metamorphic aureole are therefore of economic interest to mineral exploration efforts. The importance of studying the SIC metamorphic aureole is highlighted by new insights into low-P/high-T (LP-HT) metamorphism of basalts including, LP-HT mineral assemblages, partial melting, melt mobilization, phase equilibria modelling of metabasalts at relatively LP-HT conditions, element mobility during metamorphic processes, and retrograde zircon formation with concurrent mobilization and fractionation of Zr-Hf.

The South Range metamorphic aureole is best preserved in Paleoproterozoic Elsie Mountain Formation (EMF) metabasalts that form a large proportion of the immediate footwall to the SIC along its southern margin, which also includes the Murray and Creighton granites. Mapping of the metamorphic aureole in the EMF metabasalts defines 3 metamorphic zones: 1) an up to *ca.* 500 m wide pyroxene-hornfels zone (PHZ) extending from the SIC contact and characterized by a peak metamorphic mineral assemblage of plagioclase-clinopyroxene-orthopyroxene-magnetite-ilmenite estimated to reflect peak temperatures of ≥925 °C; 2) a pyroxene-granofels zone (PGZ) extending from the PHZ and up to 750 m from the SIC contact characterized by a similar two-pyroxene assemblage, but typically with abundant retrograde high-Ti hornblende; 3) a hornblende-hornfels zone (HHZ) extending from the PGZ and to at least 1000 m from the SIC contact characterized by a hornblende-plagioclase-quartz-ilmenite ± biotite ±

magnetite assemblage indicating temperatures of up to 680 °C. Field evidence for partial melting and melt mobilization in the EMF metabasalts consist of mainly macroscopic leucocratic patches that locally coalesce. Microtextural evidence for partial melting includes optical continuous quartz domains containing plagioclase and pyroxenes locally with euhedral crystal faces, and relatively low-Ca plagioclase and quartz frameworks around mainly relatively high-Ca plagioclase representing nucleation from a melt onto existing crystals. Phase equilibria modelling using bulk rock compositions indicate that partial melting resulted in 10-20% melt generation in the PHZ, and probably even higher degrees of melting is recorded locally. Compared to the granites where partial melts have been traced as dikes for hundreds of meters injecting back into the SIC, no back-injections were documented to emanate from the EMF metabasalts. This indicates that while a high-T metamorphic aureole developed in the metabasalts, the granites were continuously experiencing high degrees of partial melting preventing the development of a metamorphic aureole even some time after solidification of the SIC. Thus, the width of the high-T contact aureole is wider in the EMF metabasalts than in the granites. This is also true in a comparison to the contact aureole documented in the North Range Archean gneisses. Furthermore, the estimated peak contact metamorphic temperatures in the EMF metabasalts are in better agreement with previous thermal models that required substantial thermomechanical erosion (800 m) of North Range footwall rocks to match the width of the observed contact aureole. Thus, the process of thermomechanical erosion might have been less significant in the EMF basalts and perhaps other mafic lithologies.

Trace element geochemistry of the EMF metabasalts successfully permits a subdivision of the PHZ into Hornfels A and B zones. The Hornfels A zone defines the

inner most *ca.* 250 m, and is characterized by metabasalts that generally show relative depletion in LILE, REE and HFSE. Thus, trace element systematics in the EMF metabasalts of the Hornfels A zone accentuates the potential for metamorphic processes including devolatilization reactions and partial melting to severely mobilizing not only relatively easy mobilized elements, e.g., LILE, but also the relatively immobile HFSE. Thus, the trace element systematics has the potential to identify high-T parts of the metamorphic aureole where the micro- and macroscopic petrographic evidence has subsequently experienced obliteration by tectonometamorphic events. The defining geochemical characteristic of Hornfels A samples is a pronounced negative Zr-Hf anomaly ($Zr/Zr^* < 0.67$) that is associated with sub-chondritic Zr/Hf values. Furthermore, zircon with uncharacteristic textures forming poikilitic, branching, and interstitial networks are observed exclusively in Hornfels A samples, and yield an U-Pb age of 1850 ± 24 Ma. The zircon textures, age, relation to high-T mineral assemblage, and chemistry suggests crystallization from trapped melt films during retrograde cooling. In combination with the whole rock trace element geochemistry these observations provides strong circumstantial evidence that Zr-Hf was mobilized in silicate melts, and that a 250 m zone from the SIC contact experienced melt segregation.

Important to mineral exploration efforts is the observation that the width of the contact aureole in the EMF basalts appear to correlate with the thickness of the SIC that is thought to have a primary control on the location of contact deposits. Also, the width of the high-T contact aureole might provide a limiting factor for the extent to which low-S Cu-PGE rich mineralization can penetrate into the footwall.

Keywords: contact metamorphism, LP-HT metamorphism, metabasalts, partial melting, anatexis, phase equilibria modelling, high-field-strength elements, Zr-Hf mobility, zircon, Sudbury Igneous Complex

Co-authorship statement

The research presented in this thesis is part of a larger project that focuses on the footwall environment of the Sudbury Igneous Complex. The main project proposal, general goals and focus was developed by Dr. D.K. Tinkham with input from Dr. C.M. Lesher. Chapters 2-4 that constitute 3 manuscripts intended for peer-review journal publication are co-authored with supervisor and co-supervisor Drs. D.K. Tinkham and C.M. Lesher, respectively. The candidate completed field work, sample collection, sample selection, sample preparation and petrological modelling under the supervision of the co-authors. The first drafts of all manuscripts and initial interpretations were completed by the candidate. Finalized manuscripts were edited and improved by scientific input and discussions with the co-authors.

Acknowledgements

This research project was part of a significant program on the footwall environment of the Sudbury Igneous Complex developed in collaboration with and approved by industry partners Vale, Glencore, Wallbridge, and KGHM. The project was funded through CEMI by Vale and Glencore with industry funds subsequently matched by NSERC Discovery grants to Drs. D. K. Tinkham and C. M. Lesher.

I am grateful to my main supervisor Dr. D. K. Tinkham, who initially encouraged me to pursue enrollment in the Ph.D. program at Laurentian University, and for constantly playing "devil's advocate" to help me become a better researcher. Also, thank you to Dr. Tinkham and my co-supervisor Dr. C.M. Lesher for allowing me the opportunity to do this project. Through my studies I have enjoyed and felt privileged to have your continued support, mentorship, and intellectual insights.

Vale is thanked for providing land access and diamond drill cores. Although numerous Vale personnel have contributed to the success of the project, I would like to extent a special thanks to Lisa Gibson and Peter Lightfoot for providing invaluable logistical assistance and for their constructive feedback on field trips and in meetings concerning the project.

Dr. P. Jugo, a member of the supervising committee, is thanked for discussions and suggestions to the manuscripts. Oral and poster presentations on the project and the thesis itself benefited from discussions with several current and former faculty members at the Harquail School of Earth Sciences at Laurentian University, in particular, Drs. D.J.

Kontak, B. Lafrance, A.M. McDonald, H.L. Gibson, and B. Kamber. Edda and Roxane are thanked for their kindness and help throughout my studies and to acclimatize when I first arrived.

Pierre Echaubard, James Rendle, Emilie Fournier, Dave Hawkins, Fabio Cafagna, Bob Corbeil, Eric Fournier, and Lindsay Richan are thanked for assisting me in the field. W. Desjardins is thanked for his help in preparing thin sections for the project. W. Zhe is thanked for his technical support on the SEM. Dave Crabtree and Sandra Clarke of the Ontario Geological Survey are thanked for helping with the microprobe analyses. Dr. J. Petrus is thanked for his LA-ICP-MS work.

Finally, I want to thank my family and friends for their endless encouragement, especially Pooks (and the Fam-Jam) and my parents - tak for den uundværlige støtte!

Contents

List of Figures

in hand sample showing its characteristic intermediate grey color and medium to coarse grain size (plagioclase-clinopyroxene-orthopyroxene-ilmenite-magnetite ± high-Ti hornblende ± quartz ± biotite assemblage). f) Relict pillow textures in basaltic hornfels unit rock in the PHZ. Triple junction highlighted by white stippled line. g) Potential in-situ Sudbury Breccia hosted in a metabasalt of the basaltic hornfels unit showing a sharp contact and slight difference in grain size between the matrix (center) and clast/host (margins). Also, note the black veins that are cross cutting the Sudbury Breccia and overprinting the peak mineral assemblage. h) Basaltic hornfels unit rock in hand sample showing its characteristic intermediate grey color and very fine to fine grain size (plagioclase-orthopyroxene-clinopyroxene-ilmenite-magnetite assemblage). Note the amphibole (brownish green high-Ti hornblende) porphyroblasts that are not part of the prograde assemblage, but formed on the retrograde path. i) Leucocratic and very coarse grained patch consisting of dominantly plagioclase, quartz, hornblende and pyroxene. These patches are most commonly observed in the PHZ and interpreted to represent partial melt. j) Leucocratic patches coalescing to form dike or network like features interpreted to represent segregation of partial melts. k) Contact between partially preserved basaltic hornfels unit rock and retrograde basaltic amphibolite unit rock in the PHZ. l) Black mm-scale wide veins overprinting basaltic hornfels and basaltic granofels unit rocks and replacing the peak assemblage by mainly low-Ti hornblende……97

Figure 2.5. a) High-Ti hornblende in a basaltic amphibolite unit rock from the HHZ. b) High-Ti hornblende replaced by both actinolite and sadanagaite. c, d) Plane polarized and cross polarized photomicrographs of plagioclase grains enclosed by optical continuous

List of Tables

List of Supporting Information

Figure S2.3. Plane- and cross polarized light photomicrographs, back-scatter electron and cathodoluminescence image, and laser spot location maps of zircons from leucocratic melt patches in the Elsie Mountain Formation metabasalts located in the pyroxene hornfels zone. The images document euhedral to subhedral zircon grains with oscillatory zoning consistent with having grown from a melt. All grains have fine irregular fractures that locally appear to contain other material. Minor incipient alteration is observed in the BSE image of Zircon-2. The concordia diagrams are showing zircon ages for all data and a concordia age calculated for a tight cluster of concordant ages yielding an age of 1839 ± 10 Ma. Zircon-1 and Zircon-3 that contributes the analyses for this age estimate are also

White *et al*. (2007) garnet, biotite, and melt models; White *et al*. (2005) ilmenite model; Holland and Powell (2003) plagioclase model; White *et al*. (2002) orthopyroxene and magnetite models; Coggon and Holland (2002) white mica; and the Holland and Powell (1998) chlorite, talc, epidote, staurolite and cordierite models. Currently, no amphibole a-x model in the chemical system of interest exists that is consistent with the v. 6.2 Holland and Powell (2011, 2012) thermodynamic database, and therefore only activity models valid with the v. 5.5 Holland and Powell (1998, 2003) database were used in the generation of phase diagram sections to maintain consistency……...113

Appendix S2.2. Estimates of water contents in oceanic crust range from ca. 1-6 wt. %, and the higher estimates represent fully hydrated basalts (Anderson *et al*., 1976; Peacock, 1990; Schmidt and Poli, 1998). Although amphibolite facies peak metamorphism and deformation of the Huronian strata are generally attributed to the Blezardian Orogeny (Riller and Schwerdtner, 1997), hydrous metamorphic mineral assemblages at amphibolite facies conditions are also attributed to the Penokean Orogeny (e.g., Mukwakwami *et al*., 2012). Because of the general lack of overprinting relationships between the two events the hydrous nature of the EMF basalts at the onset of SIC contact metamorphism is unknown. However, EMF basalts generally display typical greenschist to amphibolite facies metamorphic mineral assemblages consisting mainly of amphiboles (hornblende, actinolite-tremolite), plagioclase (An_{20}-An_{60}), quartz, and chlorite with minor mica, epidote, and clinozoisite (Innes, 1977; Card, 1978b), suggesting that it is reasonable to assume that the EMF basalts were largely hydrated compared to unaltered mid-ocean ridge basalts (< 0.5 wt. % H_2O; Stern, 2002). The H_2O content of amphibole

metaborate:lithium iodide flux (Geo Labs) and 49.75:49.75:0.5 lithium tetraborate:lithium metaborate:lithium bromine (UWO) to produce glass discs that were analyzed for major elements by wavelength-dispersive X-ray fluorescence spectrometry (XRFS). Replicate samples analyzed at both laboratories indicate that analytical precision (relative standard deviation) is better than 1% for high-moderate abundance elements, but as high as to 3% for low-abundance elements. Interlaboratory precision (percent difference) is better than better than 4% for SiO_2, TiO_2, Al_2O_3, Fe_2O_3, MgO, Na_2O, K_2O, and P_2O_5, 7% for CaO, and 15% for MnO. Rock standard BHVO-2 (Hawaiian Volcano Observatory basalt) was analyzed with the samples at Geo Labs, and the measured results are within analytical errors (relative) for all oxides except CaO (0.2%), Fe_2O_3 (0.6%), and Al_2O_3 (0.8%) of recommended values. Rock standard JB-1a was analyzed with the samples at UWO and the results are within 4% (relative) of the recommended values (no uncertainties). Ferrous iron was measured on 14 samples by titration with ca. 0.02 M $KMnO_4$ (exact concentrations were calibrated before use). $Fe^{2+}/\sum Fe$ ranged from 0.72 to 0.93 (mean = 0.82, $2\sigma = 0.1$). This ratio is slightly lower than the ratios of 0.86 determined by Presnall *et al*. (1979) and 0.84 ± 0.01 determined by Cottrell and Kelley (2011) for least-altered mid-ocean ridge tholeiites. $Fe^{2+}/\sum Fe$ of continental flood basalts are less well constrained, but Hoover and Murphy (1989) report values of 0.82-0.63 for Columbia River basalts, the higher of which presumably reflect least-altered samples. Thus, for the purpose of this study Fe is allocated as 0.82 Fe^{2+} and 0.18 Fe^{3+}. However, post-solidus oxidation could have affected the bulk rock iron oxidation state, but these values are considered reasonable approximations……...116

CHAPTER 1: INTRODUCTION TO THESIS

INTRODUCTION

The 1850 ± 1 Ma Sudbury Impact Structure (Krogh, 1984) is the second largest known impact structure on Earth, and includes the Sudbury Igneous Complex (SIC) that represents the solidified remains of an impact melt sheet. The SIC hosts one of the world's largest accumulations of magmatic Ni-Cu-PGE mineralization (Naldrett, 2004). More than half of the known mineralization occurs along the base of the SIC or in nearby footwall rocks and appears to have formed early during the cooling history of the SIC (e.g., Coleman, 1913; Hawley, 1965; Lightfoot et al., 1997; Keays and Lightfoot, 2004, Farrow et al., 2005; Ames and Farrow 2007). A melt sheet cooling from estimated initial temperatures between 1700-2200 °C (Grieve et al., 1977; Ivanov and Deutsch, 1999) would have continuously modified the contact mineralization, footwall rocks, and potentially also footwall ores by several processes, including: 1) thermomechanical erosion (Prevec and Cawthorn, 2002); 2) footwall anatexis and contact metamorphism (e.g., Thomson 1935; Coast and Snajdr, 1984; Dressler 1984; Boast and Spray, 2006; Péntek et al., 2011 and 2013), and 3) high temperature hydrothermal fluids (deuteric, metamorphic, and magmatic fluids as the base of the SIC advanced and during subsequent contact heating as the SIC crystallized (e.g., Farrow and Watkinson, 1992; Li and Naldrett, 1993; Jago et al., 1994; Marshall et al., 1999; Molnar et al., 2001; Hanley et al., 2005 and 2011). Thus, understanding the nature and geometry of the high-T metamorphic aureole in the footwall of the SIC provides important constraints on the

evolution of the SIC and its associated mineralization, as significant amounts of Cu-Pt-Pd-rich mineralization occurs within the contact metamorphic aureole (e.g., Naldrett, 1984; Coast and Snajdr, 1984; Morrison, 1994; Naldrett et al., 1994; Farrow and Lightfoot, 2002; Ames and Farrow, 2007).

RESEARCH PROBLEMS

The main research problem focuses on identifying, characterizing, and understanding the evolution of the metamorphic aureole in the South Range of the SIC. Although numerous studies have focused on the metamorphic aureole or aspects thereof (e.g., Dressler 1984; Boast and Spray, 2006; Péntek et al., 2011 and 2013), only a few discuss it in the context of the South Range of the SIC (e.g., Thomson 1935; Riller et al., 1996). This is primarily due to the preconceived notion that the metamorphic aureole in the South Range footwall has been completely obliterated by post-SIC tectonometamorphic events (e.g., Dressler 1984; Boast and Spray, 2006; White, 2012). In the North Range the metamorphic aureole is documented to a distance of ca. 2 km and comprises four distinct metamorphic zones: 1) an outermost 1 km wide albite-epidote hornfels facies; 2) a 900 m wide hornblende hornfels facies; 3) a 200 m wide pyroxene hornfels facies; and 4) an innermost 25 m wide zone of assimilation and anatexis (Boast and Spray, 2006). Péntek et al. (2011) described the presence partial melts in footwall rocks to a distance of approximately 500 m from the base of the SIC, and using amphibole-plagioclase geothermometry on mafic rocks in the East and North Ranges, estimated that temperatures reached about 850-900 °C at least 200 m from the SIC contact. Thermal modelling by Prevec and Cawthorn (2002) predicted maximum temperatures to 820 °C at 500 m and 650 °C at 1 km below the SIC,

which led to the suggestion that 800 m of immediate footwall rock adjacent to the SIC contact was removed by thermally induced erosion, in order for the predictions to match the observed width of the metamorphic aureole in the North Range. Pressure estimates from Al-in-hornblende barometry indicate pressures to be 1.5 ± 0.5 kbar (Molnár et al., 2001; Péntek et al., 2011), which is in good agreement with the estimated 5 km depth of erosion in the Sudbury structure (Dence, 1972).

Significant contributions to the understanding of the metamorphic aureole from studies on the South Range are few in comparison. Although contact metamorphic minerals and textures in metabasalts along the South Range have been previously described (e.g., Thomson, 1935), their distribution, detailed petrographic description and characterization were not reported. Riller et al. (1996) and Rosenberg and Riller (2000) divided the Murray granite of the South Range footwall into a NW and SE domain based on microscopic incipient melt textures. All attempts at geothermometry on South Range footwall rocks have provided results interpreted to reflect post-SIC regional metamorphism (e.g., White, 2012; Mukwakwami et al., 2014). With the lack of studies focused on the South Range metamorphic aureole it is worth noting the contrasts that exist between the South and North Range footwalls, which include differences in lithologies (Archean gneisses in the North Range versus Paleoproterozoic granites and volcanic rocks in the South Range), original position with respect to the SIC (North Range footwall presumably closer to the crater wall as opposed to the South Range footwall being located below the crater floor), primary SIC thickness (the entire SIC in the South Range had a larger initial thickness than in the North Range), and deformation history (most deformation in the North Range is pre-SIC, whereas the South Range is

also locally strongly deformed by post-SIC deformation events), all of which would have implications for the nature and evolution of the metamorphic aureole. Consequently, the South Range metamorphic aureole still has a lot of research potential and impending contributions to our overall understanding of the Sudbury Impact Structure.

THESIS OBJECTIVES

The objectives of the thesis are to:

- Demonstrate the presence of a metamorphic contact aureole in the South Range of the SIC.
- Characterize high-T mineral assemblages and partial melt textures, and map their distribution.
- Characterize the metamorphic aureole by geochemical signatures.
- Determine the controls on anatexis, and the magnitude of partial melting and melt segregation in the metamorphic aureole.
- Constrain peak metamorphic P-T condition in the metamorphic aureole and absolute timing of contact metamorphism.
- Discuss the implications for mineralization.

METHODOLOGY

The objectives of this study required detailed field mapping and petrography, geochemical studies, phase equilibria modelling and geochronology.

SURFACE MAPPING

Surface mapping at several locations in the SIC South Range at a scale of 1:2000 (traverse mapping) was completed between July 2010 and November 2014 for a total of ca. 160 days. The surface mapping was complemented by diamond drill core inspection. Mapping and core logging were done to: 1) demonstrate the presence of a metamorphic aureole; 2) define metamorphic zones and determine the distribution of high-T mineral assemblages, including anatexis; and 3) collect samples for petrographic analyses, whole rock chemistry, and mineral chemistry, and geochronology.

GEOCHEMICAL STUDIES

Fifty-eight representative samples of Elsie Mountain Formation metabasalts were collected for whole-rock major and trace element geochemical analysis. The analyses were performed at the Ontario Geoscience Laboratories (Geo Labs) in Sudbury, Ontario, and at the Department of Earth Sciences at the University of Western Ontario (Dr. C. Wu, analyst) in London, Ontario. Analytical methods are described in Chapter 2 (see Supporting Information Appendix S2.6) and 3 (see Sampling and Analytical Methods). Major element oxide and trace element ranges and averages for individual units and complete geochemical data with precision and accuracy values for individual elements are given in Table 3.1 and Supplementary Table S3.1. Mineral chemistry was obtained by wavelength-dispersive X-ray emission spectrometry using an electron probe microanalyzer at Geo Labs and method details presented in Chapter 2 (see Supporting Information Appendix S2.5). Representative mineral chemistry is presented in Tables 2.2, 2.3, and 2.4. A complete suite of analyses are provided in Supplementary Tables S2.2a-c.

PHASE EQUILIBRIA MODELLING

Phase equilibria modelling was performed to determine the peak SIC contact metamorphic conditions experienced by metabasalts of the EMF, and constraining solidus temperatures and melt modes. Furthermore, the modelling was performed to investigate the usefulness for this approach to metabasalts at LP-HT conditions. Phase diagram sections were calculated using a modified version of THERIAK-DOMINO v.01.08.09 (De Capitani, 1987). Details on the thermodynamic dataset and activity models utilized are presented in Chapter 2 (see Supporting Information Appendix S2.1).

GEOCHRONOLOGY

U-Pb dating and trace element geochemistry on zircon separates and in-situ zircon was carried out at the Laurentian University Geochemical Fingerprinting Laboratory in Sudbury, ON, by laser ablation inductively-coupled plasma mass spectrometry (LA-ICP-MS). Details on the analytical technique are presented in the Chapter 2 (Supporting Information Appendix S2.4) and 4.

STRUCTURE OF THE THESIS

The thesis includes an introductory chapter (Chapter 1), three self-contained manuscripts (Chapters 2, 3, and 4) ready for submittal to peer-reviewed scientific journals, and a concluding chapter (Chapter 5). Chapters 2-4 are repetitive to a certain extent because they are intended for publication as stand-alone individual manuscripts. Chapter 1

introduces the research problems, the objectives, and the methods applied to meet the objectives.

Chapter 2, entitled "LOW-PRESSURE AND HIGH-TEMPERATURE (LP-HT) METAMORPHISM OF BASALTS: INSIGHTS FROM THE SUDBURY IMPACT MELT SHEET AUREOLE AND THERMODYNAMIC MODELLING" provides the first comprehensive description of the metamorphic aureole that developed in the Elsie Mountain Formation metabasalts that constitute the dominant lithology in the SIC South Range footwall. It is demonstrated that a physical expression of the metamorphic aureole is still preserved and exposed, highlighted by the characterization and distribution of high-T/low-P mineral assemblages in the Elsie Mountain Formation metabasalts. It is shown that the South Range metamorphic aureole evolved differently depending on the footwall lithology and a wider high-T aureole is preserved in the Elsie Mountain Formation metabasalts compared to the Murray granite. Furthermore, constraints on peak metamorphic temperatures and pressures in the South Range metamorphic aureole are presented for the first time.

Chapter 3, entitled "HIGH FIELD-STRENGTH ELEMENT MOBILITY AND FORMATION OF METAMORPHIC CHEMOSTRATIGRAPHY: AN EXAMPLE FROM IMPACT MELT SHEET INDUCED CONTACT METAMORPHISM AND ANATEXIS OF BASALTS, SUDBURY, CANADA", presents a geochemical investigation of the Elsie Mountain Formation metabasalts in the vicinity of the Frood-Stobie Mine. The geochemical signatures resulting from high-T metamorphic processes are identified and shown to have a spatial distribution in the metamorphic aureole that

allows for a sub-division of previously established metamorphic zones. The melt mode in Elsie Mountain Formation metabasalts is constrained by trace element modelling.

Chapter 4, entitled "FORMATION OF POIKILITIC ZIRCON AND Zr-Hf MOBILIZATION DURING PARTIAL MELTING OF METABASALTS IN AN IMPACT MELT SHEET INDUCED CONTACT AUREOLE, SUDBURY, CANADA", presents a study on zircon petrography, zircon geochemistry, zircon geochronology, and whole-rock Zr-Hf systematics that combined provide strong evidence for melt segregation in the Elsie Mountain Formation metabasalts in the high-T part of the SIC South Range metamorphic aureole. The study includes SIC U-Pb zircon ages from trapped melt films, and also describes zircon morphologies previously only observed in lunar meteorites.

Chapter 5 presents the overall conclusions of the project and possible future work.

STATEMENT OF RESPONSIBILITIES

The candidate performed all surface mapping and core logging, collection of rock samples, sample preparation, petrographic analyses, scanning electron microscopy and electron microprobe analysis, selection and submittal of samples for whole rock and trace element geochemistry, zircon separation and mounting, selection and preparation of thick section samples suitable for in-situ zircon U-Pb dating, interpretation of all data, trace element modelling, phase equilibria modelling, and wrote the three manuscripts and thesis version. Drs. D. K. Tinkham and C. M. Lesher supervised all aspects of the project and they edited the manuscripts and the thesis. Dr. D. K. Tinkham significantly facilitated

the phase equilibria modelling by allowing the candidate to use his modified version of Theriak-Domino v.01.08.09, and an updated version of the THERMOCALC thermodynamic database (tcdb55.txt) that included appropriate solution data for modelling mafic rocks with an approximately mid-ocean ridge basalt compositions. Dave Crabtree assisted with electron probe microanalyses. Dr. J. Petrus performed the LA-ICP-MS U-Pb dating of zircon separates and in-situ zircons in thin sections.

STATEMENT OF ORIGINAL CONTRIBUTIONS

The following is a summary of the original contributions made by this study:

1) Documents the presence of a partially preserved South Range SIC contact aureole in the Elsie Mountain Formation metabasalts. No detailed metamorphic study has previously been published.
2) Documents the metamorphic zones, metamorphic mineral assemblages and partial melting textures associated with SIC contact metamorphism in the Elsie Mountain Formation metabasalts.
3) Provides the first bulk rock geochemical data set (major, minor, and trace elements) of Elsie Mountain Formation metabasalts in the proximal SIC contact aureole.
4) Provides the first estimates of peak SIC contact metamorphic temperatures in Elsie Mountain Formation metabasalts.
5) Provides the first estimates of partial melt mode in the Elsie Mountain Formation metabasalts during SIC contact metamorphism based on petrological modelling

6) Provides the first comprehensive test of phase equilibria modelling and the generation of phase diagram sections for MORB-like compositions at LP-HT conditions.
7) Documents the first example of a reverse AFC-like trend on a Th/Yb vs. Nb/Yb diagram that reflects the effects of partial melting and melt segregation in a suite of basaltic volcanics.
8) Documents the first terrestrial example of poikilitic zircon formed from crystallization of trapped melt films in Elsie Mountain Formation metabasalts and the first in-situ U-Pb dates of SIC contact metamorphism from these rocks.
9) Provides the first evidence for significant mobilization of LREE and HFSEs in the Elsie Mountain Formation metabasalts by partial melting processes during SIC contact metamorphism.
10) Provides the first empirical evidence from the SIC South Range footwall that the SIC contact aureole might be thicker below thicker parts of the SIC.
11) Provides the first empirical evidence of a thicker high-temperature SIC South Range aureole compared to that in the SIC North Range.
12) Provides the first direct evidence from Elsie Mountain Formation metabasalts that partial melts from these rocks contributed to the formation of the SIC Sublayer.

REFERENCES

Ames D.E. and Farrow, C.E.G., 2007. Metallogeny of the Sudbury mining camp, Ontario, GAC-MDD Spec Publ 5: p. 329–350.

Boast, M. and Spray, J. G., 2006. Superimposition of a thrust-transfer fault system on a large impact structure: Implications for Ni-Cu-PGE exploration at Sudbury; Economic Geology 101, p. 1583-1594.

Coats, C.J.A. and Snajdr, P., 1984. Ore deposits of the North Range, Onaping-Levack Area, Sudbury. In: Pye, E.G., Naldtrett A.J. and Giblin, P.E. (Eds.), The Geology and Ore Deposits of the Sudbury Structure. Ontario Geological Survey Special Volume 1, pp. 327-346.

Coleman, A. P., 1913. The nickel industry, with special reference to the Sudbury Region, Ontario; Canada Department of Mines, Mines Branch, no. 170, 206p.

de Capitani, C., and Brown, T. H., 1987. The computation of chemical equilibrium in complex systems containing non-ideal solutions. Geochimica et Cosmochimica Acta, v. 51, p. 2639–2652.

Dence, M. R., 1972. Meteorite impact craters and the structure of the Sudbury basin. The Geological Association of Canada, Special Paper no. 10, p. 7-18.

Dressler, B. O., 1984. The effects of the Sudbury event and the intrusion of the Sudbury Igneous Complex on the Footwall Rocks of the Sudbury structure. In: Pye, E. G., Naldrett, A. J., Giblin, P. E. (Eds.), The geology and ore deposits of the Sudbury structure: Ontario Geological Survey Special Volume 1, p. 97–136.

Farrow, C.E.G., Everest, J.O., King, D.M. and Jolette, C., 2005. Sudbury Cu-(Ni)-PGE systems: Refining the classification using McCreedy West mine and Podolsky project

case studies, in Mungall, J.E., ed., Exploration for Deposits of Platinum-Group Elements, Short Course Series 35 ed., Mineralogical Association of Canada, p. 163.

Farrow, C.E.G., and Lightfoot, P.C., 2002. Sudbury PGE revisited: Toward an Integrated model, in Cabri, L.J., ed., The Geology, Geochemistry, Mineralogy and Mineral Beneficiation of Platinum Group Element: Canadian Institute of Mining, Metallurgy and Petroleum, Special Volume 54, p. 13-130.

Farrow, C.E.G., Watkinson, D.H., 1992. Alteration and the role of fluids in Ni, Cu and platinum-group element deposition, Sudbury Igneous Complex contact, Onaping–Levack Area, Ontario. Mineral. Petrol. 46, p. 67–83.

Grieve, R.A.F., Dence, M.R. and Robertson, P.B., 1977. Cratering processes: As interpreted from the occurrence of impact melts, in Impact and Explosion Cratering, edited by D. J. Roddy, R. O. Pepin, and R. B. Merrill, p. 791–814, Pergamon, New York.

Hanley, J., Ames, D., Barnes, J, Sharp, Z., Guillong, M., 2011. Interaction of magmatic fluids and silicate melt residues with saline groundwater in the footwall of the Sudbury Igneous Complex, Ontario, Canada: New evidence from bulk rock geochemistry, fluid inclusions and stable isotopes. Chemical Geology, 281, p. 1-25.

Hanley, J.J., Mungall, J.E., Pettke, T., Spooner, E.T.C., Bray, C.J., 2005. Ore metal redistribution by hydrocarbon–brine and hydrocarbon–halide melt phases, North Range footwall of the Sudbury Igneous Complex, Mineralium Deposita v. 40, p. 237–256.

Hawley, J.E., 1965. Upside-Down Zoning at Frood, Sudbury, Ontario. Economic Geology v. 60, p. 529–575.

Ivanov, B.A. and Deutsch, A., 1999. Sudbury impact event: Cratering mechanics and thermal history. In: Dressler, B.O., Sharpton, V.L. (Eds.), Large Meteorite Impacts and Planetary Evolution II. Geological Society of America Special Paper 339, pp.389–397.

Jago, B.C., Morrison, G.G., and Little, T.L., 1994. Metal zonation patterns and microtextural and micromineralogical evidence for alkali- and halogen-rich fluids in the genesis of the Victor Deep and McCreedy East footwall copper orebodies, Sudbury Igneous Complex, in Lightfoot, P. C., and Naldrett, A. J., eds., Proceedings of the Sudbury-Noril'sk Symposium, Special Volume 5, Ontario Geological Survey, p. 65-75.

Keays, R.R., Lightfoot P.C., 2004. Formation of Ni–Cu–PGE sulfide mineralization in the Sudbury Impact Melt, Min Pet 82: p. 217–258.

Krogh, T. E., Davis, D. W., Corfu, F., 1984. Precise U-Pb zircon and baddeleyite ages for the Sudbury area. In: The Geology and Ore Deposits of the Sudbury Structure, Ontario Geological Survey, Special Volume 1, p. 431-446.

Li, C., Naldrett, A.J., Rucklidge, J.C. and Kilius, L.R., 1993. Concentration of platinumgroup elements and gold in sulfides from the Strathcona deposit, Sudbury, Ontario. The Canadian Mineralogist v. 31, p. 523–531.

Lightfoot, P.C., Keays, R.R., Morrison, G.G., Bite, A., and Farrell, K.P., 1997. Geologic and geochemical relationships between the contact sublayer, inclusions, and the main mass of the Sudbury Igneous Complex: a case study of the Whistle mine embayment. Economic Geology, v. 92, p. 647-673.

Marshall, D., Watkinson, D., Farrow, C., Molnár, F. and Fouillac, A-M., 1999. Multiple fluid generations in the Sudbury Igneous Complex: fluid inclusion, Ar, O, H, Rb and Sr evidence. Chemical Geology 154, 1-19.

Molnar, F., Watkinson, D. H., and Jones, P. C., 2001. Multiple hydrothermal processes in footwall units of the North Range, Sudbury Igneous Complex, Canada, and implications for the genesis of vein-type Cu-Ni-PGE deposits: Economic Geology, v. 96, p. 1645-1670.

Morrison, G.G., Jago, B.C., and White, T.L., 1994. Footwall mineralization of the Sudbury Igneous Complex, in Lightfoot, P.C., and Naldrett, A.J., eds., Proceedings of the Sudbury-Noril'sk Symposium: Ontario Geological Survey, Special Volume 5, p. 119-132.

Naldrett, A.J., 1984. Mineralogy and composition of the Sudbury ores, in Pye, E.G., Naldrett, A.J., and Giblin, P.E., eds., The Geology and Ore Deposits of the Sudbury Structure: Ontario Geological Survey, Special Volume 1, p. 309-326.

Naldrett, A.J., 2004. Magmatic Sulfide Deposits: Geology, Geochemistry, and Exploration; Springer, 727p.

Naldrett, A.J., Pessaran, R., Asif, M., and Li, C., 1994. Compositional variation in the Sudbury ores and prediction of the proximity of Footwall Copper-PGE orebodies, in Lightfoot, P.C., and Naldrett, A.J., eds., Proceedings of the Sudbury-Noril'sk Symposium: Ontario Geological Survey, Special Volume 5, p. 133-143.

Péntek, A., Molnár, F., Tuba, G., Watkinson, D.H., and Jones, P.C., 2013. The Significance of Partial Melting Processes in Hydrothermal Low Sulfide Cu-Ni-PGE Mineralization Within the Footwall of the Sudbury Igneous Complex, Ontario, Canada. Economic Geology, 108, p. 59-78.

Péntek, A., Molnár, F., Watkinson, D. H., Jones, P. C., Mogessie, A., 2011. Partial melting and melt segregation in footwall units within the contact aureole of the Sudbury Igneous Complex (North and East Ranges, Sudbury structure), with implications for their relationship to footwall Cu–Ni–PGE mineralization. International Geology Review, v. 51, no. 2, p. 291-235.

Prevec, S.A. and Cawthorn, R.G. 2002. Thermal evolution and interaction between impact melt sheet and footwall: A genetic model for the contact sublayer of the Sudbury Igneous Complex, Canada; Journal of Geophysical Research, v. 107(B8), p. 2176.

Riller, U., Cruden, A. R., and Schwerdtner, W. M., 1996. Magnetic fabric, microstructure and high temperature metamorphic overprint of the Murray granite pluton, central Ontario: Journal of Structural Geology, v. 18, p. 1005–1016.

Rosenberg, C. L., and Riller, U., 2000. Partial-melt topology in statically and dynamically recrystallized granite: Geology, v. 28, p. 7–10.

Thomson, R., 1935. Sudburite, a metamorphic rock near Sudbury, Ontario. Journal of Geology, 43, 427-435.

White, C. J., 2012. Low-Sulfide PGE-Cu-Ni Mineralization From Five Prospects Within The Footwall Of The Sudbury Igneous Complex, Ontario, Canada. Unpublished PhD thesis, University of Toronto, Ontario, 337p.

CHAPTER 2: LOW-PRESSURE AND HIGH-TEMPERATURE (LP-HT) METAMORPHISM OF BASALTS: INSIGHTS FROM THE SUDBURY IMPACT MELT SHEET AUREOLE AND THERMODYNAMIC MODELLING

T.R.C. JØRGENSEN[1*], D.K. TINKHAM[1], and C.M. LESHER[1]

[1]*Harquail School of Earth Sciences, Mineral Exploration Research Centre, Laurentian University, 935 Ramsey Lake Rd., Sudbury, ON, P3E 2C6, Canada*

(trc.joergensen@gmail.com; dtinkham@laurentian.ca; mlesher@laurentian.ca)

**corresponding author*

ABSTRACT

Metabasalts along the southern margin of the Sudbury Igneous Complex (SIC), Canada, record evidence of high-grade contact metamorphism. Peak metamorphism involved partial melting and melt segregation, and culminated in conditions of at least 925 °C and ~1-3 kbar near the SIC contact. Preservation of the peak mineral assemblage indicates that most of the generated melt was lost from these rocks resulting in a residuum characterized by a plagioclase-orthopyroxene-clinopyroxene-ilmenite-magnetite ± melt assemblage. Peak temperatures reached ~875 °C up to 500 m from the SIC lower contact, which marks the transition to metabasalts that only experienced incipient partial melting without melt loss. From 500 m to ca. 750 m from the SIC contact the metabasalts are characterized by a similar two-pyroxene mineral assemblage, but typically contain abundant hornblende that overgrew clino- and orthopyroxene along an isobaric cooling path. Between ~750 and 1000 m from the SIC contact the metabasalts are characterized by a hornblende-plagioclase-quartz-ilmenite mineral assemblage, indicating temperatures up to ~680 °C. Mass balance and phase equilibria calculations indicate that anatexis resulted in 10-20% melt generation in the inner ~500 m of the aureole, with even higher degrees of melting towards the contact. Forward modelling of mineral and melt equilibria for given rock compositions is shown to be a useful tool in the investigation of basaltic rock compositions at low-pressure and high-temperature metamorphic conditions, which otherwise rely on conventional thermometry that commonly underestimates peak-metamorphic temperatures. Compared to observed rock data and experimental results such as mineral assemblages, mineral abundances, and mineral compositions, forward

calculations provide valuable supplementary thermometric information and constraints on anatexis. Discrepancies between models, experiments, and natural samples indicate that the most reliable calculations are obtained by modelling in the Na_2O-CaO-FeO-MgO-Al_2O_3-SiO_2-H_2O-TiO_2-O_2 (NCFMASHTO) system, and that the incorporation of K_2O requires an expansion of the current amphibole solution model to include a K_2O end-member. Other possible improvements include a reassessment of the current melt solution model to provide better predictions for more mafic and CaO-rich melts.

INTRODUCTION

Basaltic composition rocks develop high variance mineral assemblages during high-temperature (~650-1000 °C) metamorphism at low pressure (~1-3 kbar) due to significant solid solution in the dominant phases plagioclase, amphibole, and pyroxene. An unfortunate consequence is the lack of significant diagnostic assemblage changes allowing identification of isograds in metamorphic aureoles compared to other rock types (e.g., pelites). However, their high solidus temperatures make them useful as indicators of the upper limits of high-temperature contact metamorphism (e.g., Tracy and Frost, 1991). Evidence that rocks of basaltic composition experienced high-temperature metamorphism at low pressures include granoblastic pyroxene hornfels facies assemblages (e.g., Marks *et al*. 2011) and initiation of hydrous and anhydrous melting (Gillis and Coogan, 2002). However, quantitative estimates of peak metamorphic conditions commonly rely on two-pyroxene Fe-Mg exchange and Ca-partitioning thermometry (e.g., Lindsley, 1983; Lindsley and Andersen, 1983; Brey and Köhler, 1990; Andersen *et al*., 1993; Putirka, 2008), methods criticized for commonly underestimating peak temperatures due to

compositional re-equilibration of minerals during cooling (e.g., Frost and Chacko, 1989). Only at higher pressures is it possible to circumvent the issue of re-equilibration by using a geothermobarometer based on aluminum solubility in orthopyroxene in equilibrium with garnet (e.g., Pattison *et al*., 2003). An underutilized method for extracting P-T information from metabasaltic rocks at LP-HT conditions is forward modelling using bulk rock compositions and the construction of phase diagram sections. This approach helps in estimating peak metamorphic temperatures and investigating dehydration and partial melting processes.

This study is one of the first to document the ability to perform phase diagram section modelling of metabasalts at LP-HT conditions. Modelling of compositions used in experimental studies were performed to compare with experimental result and to test their ability to adequately predict mineral assemblages and phase abundances. The White *et al.* (2007) melt activity model, although developed for more felsic systems, was also employed to test the capability of predicting solidus temperatures, melt abundance, and melt composition. The importance of this method to accurately model metabasalts at LP-HT, in general, is illustrated by the application to the contact metamorphic aureole preserved along the southern margin of the 1.85 Ga Sudbury Igneous Complex (SIC; Fig. 2.1), which appears to include one the widest known and most readily accessible sequences of high-grade contact-metamorphosed metabasalts. Detailed mapping, petrography, mineral chemistry, and whole-rock chemistry of metabasalts in the SIC aureole provide a basis for the calculation of P-T conditions and comparison with phase diagram sections to provide important constraints on the evolution and controls on

anatexis in the aureole. The study also outlines areas where improvement to mineral solution models could significantly improve the reliability of modelling predictions.

GEOLOGICAL BACKGROUND

The 1850 Ma (Krogh *et al*., 1984) Sudbury impact structure is one of the largest impact structures known on Earth (Dietz, 1964; see review by Grieve and Therriault, 2000). The original 150-250 km in diameter crater outline was subsequently deformed by Paleo- and Neo-Proterozoic orogenic activity, and eventually eroded to its current elliptical circumferential plan-view shape (e.g., Grieve *et al.*, 1991; Shanks and Schwerdtner, 1991; Spray *et al*., 2004; Riller, 2005; Fig. 2.1). The Sudbury impact structure is the only one of its size with a preserved and exposed differentiated impact melt sheet, which is referred to as the Sudbury Igneous Complex Main Mass (e.g., Naldrett *et al.*, 1970; Lightfoot *et al.*, 1997; Lightfoot, 2017). The melt sheet is believed to have been initially been superheated to ~2000 °C (Grieve *et al.*, 1977) and had the dimensions of a sill-like body less than 5 km thick but exceeding 100 km in diameter (e.g., Golightly, 1994; Keays and Lightfoot, 2004; Lightfoot, 2017). The sill-like geometry and superheated temperatures caused extensive contact metamorphism in the underlying footwall rocks, although it is not clear whether continued incorporation of impact debris drove it rapidly to the liquidus (see discussion by Golightly, 1994).

The SIC overlies the boundary between Archean Superior Province gneissic basement rocks, exposed to the west, north, and northeast (North Range) of the SIC, and polydeformed Paleoproterozoic granitoids, metavolcanic, and metasedimentary rocks of the Huronian Supergroup, exposed to the south and southeast of the SIC (South Range;

Fig. 2.1). The SIC Main Mass consists of a lower noritic zone, middle quartz gabbroic zone, and an upper granophyric zone. The South Range is interpreted to represent a deeper and thicker part of the complex (Naldrett and Hewins, 1984; Golightly, 1994). A discontinuous layer below the SIC Main Mass, the Sublayer norite, is present within footwall embayment structures at the base of the SIC Main Mass and within the throats of Main Mass-related radial and concentric quartz diorite dikes emplaced into the underlying footwall rocks (e.g., Pattison, 1979; Naldrett, 1984; Lightfoot *et al*., 2001; Lightfoot and Farrow, 2002; Lightfoot, 2017). The Sudbury impact structure also includes brecciated and shock-metamorphosed footwall rocks (Sudbury Breccia: SUBX: Rousell *et al*., 2003) and base surge, suevitic, and phreatic breccias of the Onaping Formation (e.g., Ames, 1999; Ames *et al*., 2002), which are overlain by sedimentary rocks of the Paleoproterozoic Whitewater Group (e.g., Cantin and Walker 1972; Rousell 1972). The SIC is also renowned for the world-class Ni-Cu-PGE ores that formed at a relatively early stage in its cooling and crystallization history (Lightfoot *et al*., 2001; Keays and Lightfoot, 2004; Naldrett, 2004; Lightfoot, 2017).

The proximal South Range footwall is dominated by the Huronian Elsie Mountain Formation (EMF) metabasalts and the Murray and Creighton granites (e.g., Bennett *et al*., 1991; Fig. 2.1). Constraints on the age of the EMF metabasalts is provided by their intrusive equivalents, the 2480 +10/-5 Ma East Bull Lake intrusive suite (Krogh *et al*., 1984) and the intruding 2477 ± 9 Ma Murray (Krogh *et al*., 1996) and 2415 ± 5 Creighton (Smith, 2002) granites. The Huronian rocks were deformed during multiple orogenic tectonic events with the oldest known deformation event corresponding to the pre-impact ca. 2330 Ma Blezardian Orogeny (Riller and Schwerdtner, 1997), the

minimum age of which is bracketed by 2343 ± 17 Ma granitic dikes overprinting a strong gneissic fabric in the Creighton pluton (Raharimahefa *et al*., 2014). The pre- to post-impact 1.89-1.83 Ga Penokean Orogeny deformation observed along strike from the Sudbury area in the southern Lake Superior region of Wisconsin, Minnesota, and Michigan (e.g., Sims *et al*., 1989; Van Schmus *et al*. 1996) has long been connected to ductile fabrics in the SIC and its overlying cover rocks (e.g., Card, 1978a, b; Card *et al*., 1984; Riller and Schwerdtner, 1997). The SIC was folded into a large synclinorium and transected by prominent reverse faults in the South Range Shear Zone (SRSZ) that formed due to localization of fold-induced strain near the hinge zone during the folding event (Riller *et al*., 2010). The first well-constrained evidence that the SIC impact structure was deformed during the Penokean Orogeny comes from 1849 ± 6 Ma metamorphic titanite that overgrows an earlier Penokean D1 deformation fabric developed in the Main Mass norite and Huronian metavolcanic rocks from the Garson Mine area (Mukwakwami *et al*., 2014). Younger events that subsequently affected the Southern Province include the ca. 1773-1691 Ma Yavapai and ca. 1.6-1.4 Ga Mazatzal Orogenies (e.g., Davidson *et al*., 1992; Bailey *et al*., 2006; Raharimahefa *et al*., 2014), the 1.45 Ga Chieflakien event (e.g., Fueten and Redmond, 1997; Szentpéteri, 2009), and the ca. 1235-945 Ma Grenville Orogeny (e.g., Bethune, 1997; Rivers, 1997; Raharimahefa *et al*., 2014). However, their effects on the SIC and proximal footwall are not clearly understood, partly because all Paleoproterozoic deformation events contributed to the formation of the prominent NE-SW trending structural grain in the southern part of the Sudbury area (e.g., Lenauer, 2012; Mukwakwami *et al*., 2014; Raharimahefa *et al*., 2014).

Coleman (1913) noted the presence of certain rocks described under various names, including “micronorite”, “older norite”, and “sudburite” that occurred in the vicinity of the SIC, and at the time thought to be part of the SIC. Thomson (1935) described “sudburite” as a hornfels rock, composed essentially of plagioclase and pyroxene, and concluded that “sudburite” was metamorphic in origin and formed through high-grade metamorphism caused by cooling of the SIC. Photomicrographs showed a characteristic granoblastic polygonal texture, and a sketch map of the Sudbury area showed that the hornfels rock occurrences were restricted to the vicinity of the outer margin of the southern SIC. Thomson (1935) noted that alteration of the hornfels rocks by mainly amphibole, locally to great extent, impeded detailed mapping of the hornfels rocks. Since then, there has been a common perception that the contact aureole along the southern margin was completely obliterated (e.g., Dressler, 1984a; Prevec and Cawthorn, 2002; Rousell *et al*., 2003; Boast and Spray, 2006). However, Thomson *et al*. (1985) showed that the Ti content of green-brown hornblende cores increased with proximity to the SIC contact, and speculated that this represented evidence for the existence of a poorly defined contact aureole. Riller *et al*. (1996) and Rosenberg and Riller (2000) observed microscopic melt textures that characterized the ~800 m wide NW domain of the Murray granite that runs parallel to the strike length of the SIC contact (Fig. 2.1), and explained it by thermal perturbation induced by a cooling SIC. Riller *et al*. (1999) also suggested that the boundary between the two Murray granite domains roughly correlates with the lower limit of hornblende-hornfels contact metamorphism in the Huronian metavolcanic rocks, but as we shall see below this is incorrect. Dikes of remelted Murray and Creighton granites back-injecting the SIC norite are shown in Figures S2.1 and S2.2 (see Supporting

Information) and have previously been described along with meter- to hundreds of meter-scale granitic bodies scattered throughout the South Range SIC norite (e.g., Peredery and Morrison, 1984).

GEOLOGY OF THE SOUTHERN SIC METAMORPHIC AUREOLE

MAP AREA FIELD RELATIONSHIPS

This study is based on detailed mapping in two areas shown in Figures 2.2 and 2.3, respectively, which are separated from each other by the prominent Murray granite. The dominant map units in the field areas include metabasalts of the EMF and Stobie Formation (SF), Murray granite, SIC, and SUBX. The EMF and SF are subdivided into metasedimentary, basaltic granofels, basaltic hornfels, basaltic amphibolite, and gray gabbro map units. A summary of the characteristics of the main metabasalt map unit is presented in Table 2.1, and the geology of the Murray granite – SIC contact relationships between the two map areas is presented under Supporting Information Figures S2.1 and S2.2. Map Area 1 is located north of the Ni-Cu-PGE Frood-Stobie deposit, east of the Little Stobie deposit, and ~1 km southeast of the Murray granite (Fig. 2.2). The contact between the SIC and country rocks is consistently NE-SW trending, steeply dipping to the NW. In surface plan view the base of the SIC appears planar without any major embayment structures. The majority of the SIC footwall rocks in Map Area 1 belong to the EMF, which generally dips vertically, youngs uniformly southward, and includes mainly massive basaltic flows containing minor intervals of pillows or columnar joints (Innes, 1977). Minor intercalated quartzites (<10%) occur locally. EMF metabasalts also

locally contain xenoliths of gabbroic rocks that likely belong to the contemporaneous East Bull Lake intrusive suite (James *et al*., 2002). SUBX is locally developed in the footwall rocks as mainly: 1) straight-walled dike-like polymictic clastic breccia zones that are up to several tens of meters wide and composed of rounded to subrounded clasts enclosed in a clastic matrix locally showing flow banding, and 2) mm-m wide monomictic pseudotachylitic and clastic breccias with dike, network, or jigsaw geometry composed of clasts of nearby rock set in a black to dark grey aphanitic matrix. The most prominent manifestation of SUBX in Map Area 1 makes up part of the South Range Breccia Belt (Spray, 1997) that hosts the Frood-Stobie deposit and possibly continues for as much as 45 km sub-concentric to the SIC to the Victoria Offset in the SW corner of the Sudbury Structure (J.P, Golightly and E.F. Pattison, pers. comm. 2016). Map Area 2 is located near Murray mine, 4.5 km SW of Map Area 1 (Fig. 2.3). The trend of the SIC contact is similar to that in Map Area 1. The footwall in Map Area 2 includes metabasalts of the EMF, metasedimentary and bimodal metavolcanic rocks of the Stobie Formation (SF) that conformably overlie the EMF, the SW portion of the Murray granite, and cross-cutting dikes of the 1238 ± 4 Ma Sudbury swarm (Krogh *et al*., 1987).

METAMORPHIC ZONES

The contact metamorphic aureole is defined by mineralogy and textures developed in metabasalts of the EMF and SF and locally by mineralogy of thermally recrystallized SUBX, and is divided into an up to ~250-500m wide pyroxene hornfels zone (PHZ) adjacent to the SIC, a ~200-350 m wide pyroxene granofels zone (PGZ), and a hornblende hornfels zone (HHZ) at the outer limit of the aureole (Table 2.1). The zones

represent a continuous LP-HT metamorphic sequence (Figs. 2.2 and 2.3). In both map areas the metamorphic grade increases from the SE toward the NW as the SIC contact is approached, and the zonation is broadly concordant with the base of the SIC. The outer margin of the aureole at the low-grade limit of the hornblende hornfels zone is poorly delineated, but is defined by the appearance of noticeable high-Ti hornblende in amphibolites and represents the high-Ti hornblende-in isograd. The pyroxene-in isograd defines the HHZ-PGZ contact and represents the first appearance of contact metamorphic clinopyroxene and orthopyroxene in metabasalts. The PGZ-PHZ contact is gradational and is not defined in the traditional sense of a mineral- or melt-in isograd, but is defined by both an overall grain size decrease in metabasalts and a significant decrease in high-Ti hornblende across the transition from the PGZ to the PHZ.

The peak contact metamorphic mineral assemblage of metabasalts in the HHZ is characterized by high-Ti hornblende-plagioclase-quartz-ilmenite ± biotite ± magnetite. Regional metamorphism during the Penokean or Mazatzal orogeny reached lower-middle amphibolite facies conditions, and appears to have overprinted the outer limit of the contact metamorphic HHZ. Thus, the original width of the HHZ might have been greater than presently observed. The peak contact metamorphic mineral assemblage of metabasalts in the PGZ is characterized by plagioclase-clinopyroxene-orthopyroxene-ilmenite-magnetite ± high-Ti hornblende ± quartz ± biotite. Much of the quartz, biotite, and coarse high-Ti hornblende are commonly associated with leucosomes or partial melt zones and are interpreted to be retrograde in origin, associated with melt crystallization. The peak contact metamorphic mineral assemblage for metabasalts in the PHZ is similar to that of the PGZ, but lacks prograde high-Ti hornblende, the abundance of retrograde

high-Ti hornblende is generally minor, and quartz and biotite are interpreted to have coexisted with a partial melt. The presence of remnant prograde and greater abundance of retrograde high-Ti hornblende high-Ti hornblende in the PGZ, and higher modal abundance of pyroxene in the PHZ metabasalts provide the basis for treating the PGZ and PHZ as distinct zones even though their peak mineral assemblages are similar.

The contact between the PGZ and the PHZ is transitional. Locally, metabasalts in the PHZ are associated with cm-scale leucocratic and very coarse-grained patches of quartz, plagioclase, hornblende, and pyroxene that are interpreted as partial melt that locally amalgamate to form dike or network like features (Fig. 2.4i, j). In the field the partial melt patches appear to be restricted to the basaltic hornfels unit, but in drill core they are also less commonly observed in the PGZ.

METABASALT PETROLOGY

Primary and secondary volcanic features and SUBX in metabasalts become more difficult to identify as metamorphic grade increases. Metabasalts in the HHZ contain well-preserved primary and secondary volcanic features (e.g., pillows, columnar joints, amygdules, silica evacuation tubes; Fig. 2.4a). Columnar jointing is absent or not preserved in the PGZ and PHZ. Volcanic pillow textures are only locally well preserved in the PGZ, and only occur as relict (but definitive) features in the PHZ. Amygdules are only locally preserved in the PGZ and are absent or not preserved in the PHZ. SUBX is relatively easy to identify and well preserved in the HHZ (Fig. 2.4b), locally easy to identify in the PGZ, but extremely difficult to identify in the field and diamond drill core in the PHZ (Fig. 2.4f, g).

BASALTIC AMPHIBOLITE

The basaltic amphibolite unit is typically dark greenish grey to nearly black, medium- to coarse-grained, massive, non- to weakly magnetic, and locally contains well-preserved pillow textures and amygdules, when encountered in the field (Fig. 2.4a, c). Green-brown pleochroic high-Ti hornblende (~50 modal%) is fine to coarse grained, granoblastic polygonal (Fig. 2.5a), and locally replaced by pale green actinolite and later by blue-green sadanagaite (Fig. 2.5b). Plagioclase (~30-40 modal%) is very fine to medium grained, granoblastic polygonal or decussate, equant, and commonly arranged in clusters suspended in optically continuous quartz patches (Fig. 2.5c, d). Locally, plagioclase is zoned with relatively Ca-rich cores and Ca-poor rims (Fig. 2.5e), which are interconnected and form a network around the Ca-rich plagioclase. The Ca-rich cores often have subrounded margins when a relatively Ca-poor rim is present. Quartz (trace to 50 modal%, but commonly 5-15 modal%) is ubiquitous in the amphibolites. Fine- to medium-sized grains often occur as granoblastic polygonal clusters with a subrounded outline, possibly representing amygdules, or as anhedral inclusions within amphibole, whereas coarser grains typically form anhedral optically continuous patches (Fig. 2.5c, d). Locally, coarse quartz patches shows undulose extinction and/or incipient recrystallization. Ilmenite (4-5 modal%) is very fine to medium grained, and often occurs as anhedral and subrounded grains with occasional titanite overgrowths (Fig. 2.5f). Ilmenite also occur as eu- to anhedral elongated prismatic grains, and very fine grains decorating the margins of sadanagaite or as fine needles along cleavages in the high-Ti hornblende. Magnetite (commonly absent and rarely more than 1 modal%) forms fine exsolution lamellae in ilmenite or rare isolated grains. Biotite (2 modal%, rarely up to 15

modal%) is very fine to coarse grained, occurring as overgrowths or intergrowths with sadanagaite and ilmenite, or less frequently as subhedral grains within quartz patches (Fig. 2.5g). Sulfides are usually present in trace amounts, and typically represented by very fine- to medium-grained pyrite and chalcopyrite with lesser extent pyrrhotite. Pyrite is commonly associated with sadanagaite and is also observed as elongated stringers controlled by biotite cleavage (Fig. 2.5h). Chalcopyrite is mainly hosted by or anchored at the margins of biotite (Fig. 2.5h) and is occasionally associated with actinolite.

BASALTIC GRANOFELS

In the field, the basaltic granofels unit is characterized by its intermediate grey to brownish-grey color on fresh surfaces (brownish Opx), medium- to coarse-grained granoblastic polygonal texture, moderate magnetism, and locally, the presence of pillow textures and amygdules (Fig. 2.4d, e). Plagioclase (35-40 modal%) is commonly zoned and with cores locally showing euhedral crystal faces (Fig. 2.5e, i, j). This is consistent with plagioclase rims crystallizing from an incipient partial melt, nucleating on pre-existing peak metamorphic plagioclase (e.g., Sawyer, 2014). Clino- and orthopyroxene (combined 25 modal%) are texturally similar, preventing individual modal estimates by transmitted light microscopy. The pyroxenes are fine to coarse grained and occur as anhedral, highly poikiloblastic grains with inclusions of plagioclase and oxides, and as subhedral, porphyroblastic grains with fewer inclusions. The porphyroblastic grains typically occur in optically continuous quartz patches, and commonly show subrounded edges (Fig. 2.5i, j). Clinopyroxene exhibits 1 μm wide Ca-poor exsolution lamellae parallel to (001) and simple twinning. Orthopyroxene rarely shows closely spaced sub-

μm twin lamellae approximately parallel to (100). Ilmenite and magnetite (combined 5-10 modal%) are very fine to medium grained, and occur as an- to subhedral grains. Exsolution lamellae or domains of magnetite in ilmenite and vice versa are commonly present. The oxides are often overgrown by biotite, high-Ti hornblende, or rarely titanite (Fig. 2.5i, j). High-Ti hornblende (2-25 modal%, but commonly > 10 modal%) is fine to coarse grained and occur as an- to subhedral, poikiloblastic or polygonal granoblastic grains (Fig. 2.5i, j) overgrowing pyroxene, plagioclase, oxides, grunerite, and locally also biotite. These relationships suggest that the majority of the high-Ti hornblende in the basaltic granofels unit rocks formed on the retrograde path. Locally, relict prograde fine- to medium-grained high-Ti hornblende occurs in patches and is clearly overgrown by pyroxene (Fig. 2.6c-e). The high-Ti hornblende is locally replaced by sadanagaite or very fine-grained, pale green, fibrous, low-Ti hornblende within mm-scale veins that also crosscut and replaces pyroxene and magnetite (Fig. 2.4l). Grunerite occurs locally as ~2-3 μm haloes defining the contact between orthopyroxene and overgrowing high-Ti hornblende, and rarely as fine- to medium-grained, subhedral, nearly colorless grains. Quartz (5-10 modal%) is medium to coarse grained and occurs as anhedral, optically continuous grains hosting variable amounts of plagioclase (Fig. 2.5i, j and 2.6a-b), and locally as granoblastic polygonal grains. The quartz-rich domains are interpreted as in situ unsegregated partial melts (e.g., Sawyer, 2014). In general, the higher modal abundance of quartz in basaltic granofels unit rocks is a distinct difference between it and basaltic hornfels unit rocks. Biotite (1-10 modal%) is very fine to medium grained and occurs as anhedral overgrowths on oxides; as highly poikiloblastic grains around

plagioclase, oxides, and pyroxene; locally, as sub- to euhedral grains in coarse anhedral quartz grains; and rarely, as granoblastic polygonal clusters.

BASALTIC HORNFELS

Field characteristics of the basaltic hornfels unit include an intermediate grey to brownish-grey color, very fine- to medium granoblastic polygonal texture, moderate magnetism, and rare poorly preserved pillow textures (Fig. 2.4f, h). Because the peak mineral assemblage of the basaltic hornfels unit rocks closely resembles that of the basaltic granofels unit rocks, the finer grained nature and the generally lower modal% of retrograde high-Ti hornblende and quartz in basaltic hornfels are good discriminators (Fig. 2.5k, l, m). Plagioclase (40-45 modal%) contains cores of relatively high-Ca plagioclase overgrown by relatively low-Ca plagioclase, forming continuous networks with low dihedral angles along three-grain junctions of high-Ca plagioclase (e.g., Fig. 2.5n). Pyroxenes (40 modal%) are generally finer grained and more abundant than in the basaltic granofels unit, dominantly occurring as polygonal granoblastic grains. Magnetite and ilmenite (5-10 modal% combined in equal proportions) are generally similar to those in the basaltic granofels unit, although locally, ilmenite occurs as very fine-grained, sub- to euhedral, slender prisms. High-Ti hornblende (0-20 modal%) is fine to coarse grained and occurs as porphyroblastic, poikiloblastic, and granoblastic polygonal grains overgrowing and replacing mainly pyroxene (Fig. 2.5m). Locally, grunerite and sadanagaite are present as overgrowths on orthopyroxene and high-Ti hornblende, respectively. Vein-related low-Ti hornblende is similar to that in the basaltic granofels unit. Quartz (≤ 5 modal%) forms anhedral and optically continuous grains or forms part

of the relative low-Ca plagioclase framework as cuspate projections between adjacent crystals of relatively high-Ca plagioclase, both microtextures indicating partial melting (e.g., Sawyer, 2014; Fig. 2.5n). The abundance of quartz generally decreases proximal to the SIC, to the point where it is rarely detected petrographically. Biotite (trace to 5 modal%) is fine to medium-grained, dominantly occurring as narrow overgrowths on oxides and pyroxene (Fig. 2.5m), and rarely as subhedral, poikiloblastic grains. K-feldspar is locally present in trace amounts where it occurs as very fine-grained anhedral inclusions in plagioclase, probably representing incipient alteration of the plagioclase.

MINERAL CHEMISTRY

Mineral chemistry was obtained from eleven samples collected along two traverses perpendicular to the strike of the SIC contact. Representative analyses are given in Tables 2.2-2.4, compositions used for two-pyroxene thermometric calculations are given in Table 2.5, and all analyses with analytical details are given under Supporting Information in Appendices S2.3 and S2.5, and Tables S2.2a-c. Element maps for pyroxene and plagioclase were produced to investigate the presence of mineral chemical zonation (Fig. 2.5n, o).

CLINOPYROXENE

Fe# (molar FeO/(MgO+FeO)) in clinopyroxene ranges 0.31-0.56 and mimics fluctuations in bulk rock composition (Fig. 2.7; Tables 2.2 and S2.2a). Ca ranges 0.69-0.88 atoms per formula unit (apfu; ave. 0.82 +/- 0.03, 1σ) and Al ranges 0.02-0.06 apfu (ave. 0.043 ± 0.008). Al shows a fairly strong positive correlation with bulk rock Al, whereas there is

no such correlation observed for Ca. The clinopyroxene data tends to form a compositional trend toward the interior of the Di-Hd-En-Fs quadrilateral and higher Fe# as the contribution of exsolved orthopyroxene lamellae to the analysis increases. The linear trends of the clinopyroxene data points are subparallel to the tie-lines between clinopyroxene and orthopyroxene, suggesting that an integrated clinopyroxene composition would plot along the tie-line. When possible, an average of two or more clinopyroxene analyses was used from one or more grains all in textural equilibrium with orthopyroxene for use in geothermometry. Analyses attempting to analyze clinopyroxene zones between orthopyroxene exsolution lamellae and only orthopyroxene exsolutions were also acquired for some grains to evaluate the influence on temperature estimates. These commonly resulted in compositional outliers and consequently had dramatic effects on peak temperature estimates (up to ± 80 °C).

ORTHOPYROXENE

Point analyses, X-ray maps, and BSE imaging show no evidence for any systematic zonation or core-to-rim variations in orthopyroxene (Fig. 2.5o; Tables 2.2 and S2.2a). However, point analyses in sample FSTJ294_site_1_opx_12 to 19 from within a single grain include 4 spots at the center (FSTJ294_site_1_opx_12 to 15) and 4 spots at the margin (FSTJ294_site_1_opx_16 to 19) and show a relatively wide range in Fe# (0.64-0.71), but no systematic core-rim variation. Overall, orthopyroxene Fe# ranges 0.43-0.71, and as for clinopyroxene there is a strong correlation with bulk rock Fe# (Fig. 2.7). Al ranges 0.014-0.074 apfu, and Ca ranges 0.038-0.068 apfu.

AMPHIBOLE

The amphibole population is diverse, including four Ca-amphiboles according to the recalculation and classification scheme of Hawthorne *et al*. (2012; Fig. 2.8a) and a fifth amphibole species that falls within the group of monoclinic Mg-Fe-Mn amphiboles (Hawthorne *et al*. 2012; Fig. 2.8b; Tables 2.3 and S2.2b). Actinolite to ferro-actinolite (plots in tremolite field of Fig. 2.8a) is present in samples FSTJ098 and FSTJ326. Relative to the other Ca-amphiboles in the metabasalts actinolite is characterized by relatively low Al. Actinolite is best distinguished from sadanagaite by higher Si and Mg, and lower Na and K. Compared to high-Ti hornblende actinolite is best discriminated by lower Ti and Al content. Although some actinolite contains Cl above the lower limit of detection (~0.02 wt. %), it is still much lower than the Cl content of vein-related low-Ti hornblende (0.2-0.7 wt. %). Intersample differences between actinolite are significant, especially with regards to Ti, Fe#, and K. Sample FSTJ098, ca. 10 m from the SIC contact, has consistently higher Ti and K, and lower Fe# compared to sample FSTJ326, located ca. 708 m from the SIC contact. Ferro-sadanagaite was analyzed in sample FSTJ326 and is characterized by high Al and low Si content relative to all the other amphibole species that were analyzed in this study. Compared to high-Ti hornblende, the Fe-sadanagaite has lower Ti, and higher Na and K. The classification diagram in Figure 2.8a shows Fe-sadanagaite plotting near ferrotschermakite that formed during the Penokean orogeny (Mukwakwami *et al*., 2014). High-Ti hornblende was analyzed in all but two samples, i.e., FSTJ098 and FSTJ326, although sample FSTJ098 might have contained trace amounts. High-Ti hornblende clusters within the same broad compositional boundaries as the magnesio-hornblende end-member (Fig. 2.8a), but most

are characterized as ferro-ferri-hornblende or magnesio-ferri-hornblende (Hawthorne *et al*. 2012). There is minor overlap with the vein-related low-Ti hornblende that plot within the same compositional boundaries, but have lower Ti contents and Cl significantly above the lower limit of detection. High-Ti hornblende has been previously described by Thomson *et al*. (1985) and Mukwakwami *et al*. (2014) in EMF metavolcanic rocks and in Main Mass norite. They interpreted those in the metabasalt as either magmatic or potentially related to contact metamorphism, and those in the norite as a late stage magmatic phase. Low-Ti hornblende (Fig. 2.8a) is distinguished from high-Ti hornblende by lower Ti and Cl above the lower limit of detection. Low-Ti hornblende shows major element variability between samples and within the same sample. The most significant change between samples is a higher Fe# in the sample with higher whole rock Fe. Fe-Mg clinoamphiboles were analyzed in samples FSTJ118, FSTJ069, and FSTJ307 and plot within the grunerite field (Fig. 2.8b).

Figures 2.8c, d shows the Ca-amphiboles plotted on Ti - ^{IV}Al and ^{IV}Al - ^{VI}Al diagrams. Because Al in tetrahedral coordination sites (^{IV}Al) and Ti contents of Ca-amphiboles increase with temperature and Al in octahedral coordination sites (^{VI}Al) increases with pressure, high temperature magmatic and low- to medium grade metamorphic amphiboles can be distinguished (Leake, 1971; Fleet and Barnett, 1978; Zenk and Schulz, 2004). The high Ti content and high ^{IV}Al - ^{VI}Al ratios in high-Ti hornblende are consistent with formation during low pressure and high temperature conditions, e.g., magmatic or hornblende hornfels conditions (Raase, 1974; Hammarstrom and Zen, 1986). The Ti - ^{IV}Al trends are defined by Ca-amphiboles in metabasites from the Dalradian (Zenk, 2001) and experiments. Ca-amphiboles in mafic rocks (Colombi, 1989)

are also plotted in Figure 2.8c, and indicate pressures between 1-3 kbar. Sadanagaite from this study plots similar to the Ca-amphiboles in metabasites from the Dalradian Kyanite zone (Zenk and Schulz, 2004), and Ca-amphiboles in metabasalts from the EMF near the Garson Mine area where they are interpreted to have formed in response to the Penokean Orogeny (Mukwakwami et al., 2012). The plotting position of both actinolite and low-Ti hornblende suggest a low-pressure, and low-moderate temperature formation (Fig. 2.8c, d).

FELDSPAR

The majority of samples show two groups of plagioclase compositions, and one sample (FSTJ294) contained K-feldspar. The relatively high-Ca plagioclase cores vary from ca. An_{30} to An_{95}, and show a strong correlation with the whole rock Na content (Fig. 2.9, Table 2.4 and S2.2c). Plagioclase rims are always more albitic than their respective cores and range from ca. An_{10} to An_{80}.

WHOLE ROCK COMPOSITIONS

For the purposes of petrological modelling an average major element bulk composition was obtained from 7 EMF metabasalts belonging to the basaltic amphibolite unit (see Tables 2.6 and S2.3 for compositions and sample details). Six samples are located in the HHZ zone and 1 sample in the PGZ. Although some of these samples potentially experienced incipient melting, they are from below the PHZ and of the samples available are therefore considered to represent the most likely starting composition as the thermal perturbation from the SIC commenced. Table 2.6 also includes the composition of sample

478 from experiments by Beard and Lofgren (1991), used to explore our current capability to model MORB-like (mid-ocean ridge basalt) compositions at low-P and high-T conditions. Two basaltic hornfels unit samples believed to have experienced significant melt segregation and an average composition (n = 16) for basaltic hornfels unit rocks located proximal to the SIC contact is presented in Table 2.6 (see Table S2.3 for individual analyses), for the purpose of comparison with calculated results. EMF metabasalts are relatively high in Fe and quite variable with respect to Fe#. The 7 samples selected for use in this paper are lower in #Fe than five other samples of basaltic amphibolite (see Table S2.3), but were selected to better match the experimental composition of Beard and Lofgren (1991) and because the phase diagram section modelling showed that #Fe exerts a strong control on clinopyroxene stability with the result that clinopyroxene becomes stable at anomalously low temperatures (<600 °C; discussed below). Major element oxides of interest for samples collected for mineral chemistry are shown in Figures 2.7 and 2.9, illustrating correlations between bulk rock composition and mineral chemistry. For the purpose of this study, Fe is allocated as 0.82 Fe^{2+} and 0.18 Fe^{3+} (see Supporting Information Appendix S2.6 and Table S2.3 for details).

The compositions of average basaltic amphibolite and basaltic hornfels unit EMF rocks show noticeable differences for several major elements (Table 2.6). Potassium shows the greatest change from > 0.70 wt. % K_2O in the basaltic amphibolite unit samples to <0.18 wt. % K_2O in the average basaltic hornfels unit. Other significant changes include lower Si and Na, and higher Ca and Mg in the average basaltic hornfels unit composition. The average basaltic hornfels unit composition also contains lower Ti and Al, and higher

Fe_{total} and Mn. Two basaltic hornfels samples FSTJ092C and FSTJ091 contain lower amounts of Si Na, and K together with higher Ca. The trends for the other major element oxides show a similar variation from the average basaltic amphibolite unit sample composition with the exception of Ti in basaltic hornfels unit sample FSTJ092C, which is higher than that in average basaltic amphibolite unit.

PHASE EQUILIBRIA

Phase relations were modelled in the Na_2O-CaO-K_2O-FeO-MgO-Al_2O_3-SiO_2-H_2O-TiO_2-Fe_2O_3 (NCKFMASHTO) system using a modified version of THERIAK-DOMINO v. 01.08.09 (De Capitani, 1987) and the v. 5.5 data set of Holland and Powell (1998, 2003). Activity models for solid solution minerals used in the calculations are listed in Appendix S2.1. Cations normalized to a 100% oxide sum used as input data in the calculations are provided in Table 2.6. Fluid-saturated conditions were assumed for EMF metabasalt at the onset of contact metamorphism because of their submarine setting that would have substantially increased the amount of chemically bound water (further discussion of this assumption is provided in Supporting Information Appendix S2.2). Calculations using the Beard and Lofgren (1991) sample 478 tholeiitic basaltic composition provide a basis for comparison with experimental results. These comparisons focus on mineral assemblages, mineral modes, solidus temperatures, and melt compositions. The principal modelling calculations for an average basaltic amphibolite unit rock are presented as phase diagram sections, and additional T-M_{H_2O} diagrams were calculated to illustrate the fluid control on the solidus and pyroxene stability.

The lack of garnet in EMF metabasalts precludes the use of garnet-orthopyroxene thermobarometry, but the widespread occurrence of coexisting pyroxenes allows two-pyroxene thermometry calculations for HHZ and PGZ. The calibrations of Brey and Köhler (1990), Andersen *et al*. (1993), and Putirka (2008) were tested (see discussion in Appendix S2.3). Independent pressure estimates from the literature (Dence, 1972; Molnar *et al*., 2001; Péntek *et al*. 2011) and in this study (Fig 2.8c, d), indicates pressures of 1-3 kbar in the SIC footwall during contact metamorphism. A pressure of 1.5 kbar was chosen for the calculations, but changing the pressure from 1 to 3 kbar has an insignificant effect on the temperature estimates (less than ~10 °C).

TWO-PYROXENE THERMOMETRY

The temperatures recorded by clino- and orthopyroxene pairs were calculated by 3 different thermometers using what is considered to represent the best analyses from 10 samples based on indications of textural equilibrium, and the lack of chemical zoning, inclusions, and retrogression. The results are presented in Table 2.5 and include the approximate distance from each sample location to the SIC contact. Table 2.5 also contains results from calculations performed using analyses where clinopyroxene exsolutions were preferentially included or excluded to evaluate the effect on temperature estimates. The QUILF thermometer of Andersen *et al*. (1993) and the thermometer of Putirka (2008) shows the best overlap in the range of temperature estimates of 784-851 °C and 809-887 °C, respectively, whereas the Brey and Köhler (1990) thermometer yields lower temperatures of 700-795 °C. However, the Brey and Köhler (1990) and Putirka (2008) thermometers are essentially calibrated using the same experimental data

and show a similar inter-sample variation with increased distance to the SIC contact, whereas the QUILF thermometer yields greater fluctuations in temperature. All thermometers yield the highest T for the most proximal sample and the lowest T for the most distal sample, indicating a temperature difference of 70-100 °C, but the maximum and minimum temperatures overlap within analytical/calibration uncertainties. Clinopyroxene analyses that deliberately forced the inclusion or exclusion of exsolution lamellae significantly influence the temperature estimates (up to 50 °C) toward higher or lower temperatures, respectively. The Brey and Köhler (1990) and Putirka (2008) thermometers perform best for mafic systems where $Mg\#_{Cpx} > 0.75$, somewhat higher than the range in $Mg\#_{Cpx}$ for clinopyroxene in this study (ca. 0.45-0.70). Thus, the QUILF thermometer might be most appropriate with respect to the pyroxene pairs presented here, because the amount of non-quadrilateral component are relatively low.

PHASE DIAGRAM SECTIONS

COMPARISON TO MORB MELTING EXPERIMENTS

SIC contact metamorphism occurred at relatively low pressures of 0.5 – 3.5 kbar (Molnár *et al*. (2001); Péntek *et al*. (2011), and this study (See section on amphibole chemistry). To test the modelling capability in this pressure range it is beneficial to model a mid-ocean ridge basalt (MORB) composition previously used in melting experiment conducted a similar pressures as SIC contact metamorphism. Figure 2.10 shows the experimental results of Beard and Lofgren (1991) at 1 kbar at 900-1000 °C and at 3 kbar from 850-1000 °C (Fig. 2.10a, b) compared to modelling results at similar pressures and

temperatures at 700-1000 °C in the NCFMASHTO and NCKFMASHTO systems (Fig. 2.10c-f). Modelling of the Beard and Lofgren (1991) MORB composition also provides an opportunity to evaluate the usefulness of the White et al. (2007) melt model to predict melting relations in mafic rocks.

At 1 kbar, the K-absent model adequately predicts the observed experimental assemblages, the temperature of initial melting, and amount of melt produced. The model also correctly predicts that amphibole is reacted out subsolidus. However, Opx-in is predicted at 725 °C compared to 900 °C in the experiments, the modal abundance of clino- and orthopyroxene is generally under- and overpredicted by 7-20% and 5-15%, respectively, and a steady increase in the An component with temperature predicted for plagioclase contrast with a positive, but irregular correlation in the experiments. In the 1 kbar K-bearing model system, biotite becomes part of the subsolidus mineral assemblage and the solidus is lowered from 905 °C to 770 °C. However, the abundance of melt remains below ~10% up to ~905 °C, from which point the melt abundance increases similar to the K-absent model and the experimental results.

At 3 kbar, the K-absent model effectively predicts the experimental assemblage above ~900 °C. However, the predicted Cpx-in (~740 °C) and Opx-in (~790 °C) isograds are lower than their experimental introductions at ~850 °C, the experimental solidus (850 ^{o}C) is ~45 °C higher than the model prediction (~805 °C), the abundance of melt is higher in the model at any given temperature and increasingly overpredicted towards higher temperatures (~20% at 1000 °C), a steady increase in the An component of plagioclase with temperature is predicted compared to a slight drop in the experiments, and amphibole is incorrectly predicted to have reacted out prior to melting at this pressure.

Furthermore, the model predicts a two-amphibole (low- and high-Ca) assemblage at subsolidus conditions, compared to only one amphibole (high-Ca) reported in the experimental runs. Introducing K to the model system at 3 kbar has a similar effect as at 1 kbar with the addition of amphiboles being stable with the melt phase.

Figure 2.11 shows the melt composition evolution in NC±KFMASHTO observed in the Beard and Lofgren (1991) experiments (Fig. 2.11a, b, e, f) compared to calculated melt compositions at 1 and 3 kbar (Fig. 2.11c, d, g, h). The experimental melt compositions are recast to a 100 wt. % oxide basis to allow comparison to the melt model (NCKFMASH). The model best predicts the experimental results at 1kbar in a system excluding K. The evolution of the experimental melt composition is characterized by a decrease in Si, and modest to minor increases in Al, Fe, Mg, and Ca. Na and H_2O remains fairly constant. These trends are similar to those predicted by the K-absent 1 kbar melt model. However, the main discrepancies occur in the model predictions of lower Al-Ca and higher Fe-Mg. As noted above, the addition of K initiates melting at significantly lower temperatures in the model predictions. The melt composition evolution at temperatures above 900 °C is near identical to the 1 kbar model. At temperatures below 900 °C the predicted melt composition is characterized by an early enrichment in K, corresponding to the consumption of all biotite with an increase in temperature of less than ca. 5 °C. This early stage of melting observed in the model system is not captured in the experimental results. At 3 kbar, the melt composition trends in the model systems are similar to those observed at 1 kbar. However, no melt composition analysis is available from the experiments at low melt abundances near the solidus.

AVERAGE BASALTIC AMPHIBOLITE UNIT MODEL P-T SECTION

A P-T phase diagram section calculated in the NCFMASHTO system for an average basaltic amphibolite unit composition, contoured for anorthite component in plagioclase and % melt volume, is presented in Figure 2.12. As is typical of metabasaltic equilibria at relatively low pressures, large high-variance mineral assemblage fields dominate P-T space, and the appearance and disappearance of phases are represented by steeply sloping curves. Along a 1.5 kbar isobaric heating path appropriate for SIC contact metamorphism, the stable mineral assemblage starting at 550 °C is high-Ca Amph-Low-Ca Amph-Pl-Qtz-Ilm. With increasing temperature magnetite enters the assemblage at ca. 560 °C. The predicted Cpx-in isograd is encountered at ca. 680 °C, closely followed by the high-Ca Amph-out isograd at ca. 700 °C. Orthopyroxene becomes part of the assemblage at ca. 740 °C, accompanied by the disappearance of low-Ca Amph within a couple of degrees. The solidus is intersected at ca. 875 °C and is sharply followed by the Qtz-out isograd at ca. 885 °C.

The inclusion of K in the calculations has a profound effect on the solidus temperature, which drops to ca. 760 °C at 1.5 kbar (Fig. 2.13), a behavior also predicted in the calculations of the Beard and Lofgren (1991) MORB composition above. Along the 1.5 kbar isobar, clinopyroxene enters the assemblage at a slightly lower temperature of ca. 660 °C, whereas Opx-in is essentially unaffected by the addition of K. Addition of K also stabilizes biotite that remains part of the assemblage past the solidus to a temperature of ca. 795 °C. In contrast to the K-absent system, high-Ca Amph is the only amphibole present until ca. 675 °C at which point low-Ca Amph enters the assemblage. The final

consumption of the two amphiboles follows shortly after the Cpx-in isograd for high-Ca Amph, and Opx-in isograd for low-Ca Amph, similar to the K-absent system.

In both compositional systems the onset of melting correlates with a sudden increase in the An component in plagioclase, and subsequently the An component shows a strong positive correlation with the amount of melt. At the solidus the plagioclase is ca. An_{66} and increases to ca. An_{86} at ca. 40 vol.% melt. There is also a minor increase in the An component toward lower temperatures. The initial increase in the amount of melt corresponds to the complete consumption of Qtz in both compositional systems, and subsequently biotite in the system including K. Primarily plagioclase and orthopyroxene is consumed from this point on.

RESTITE EVOLUTION MODEL FOR AVERAGE BASALTIC AMPHIBOLITE UNIT

The liquid percolation or permeability threshold describes the point at which melt can move out of, into, or through, the solid framework of a rock (Maaløe, 1982; Vigneresse *et al*., 1996; Sawyer, 2008). The permeability threshold is reached at less than 2 vol.% melt (e.g., Lupulescu and Watson, 1999) and a complete melt-saturated grain boundary state is approached at a melt fraction of ca. 7 vol.% (Rosenberg and Handy, 2005). These low melt fractions then represent the lower limit for melt segregation that also requires a driving force and a dilatant site to proceed (Sawyer, 1994, 2008). A melt fraction of ca. 26 vol.% marks the transition to a magma-like rheology (MacGregor and Wilson, 1939; Arzi, 1978), but in the absence of deviatoric stresses, crossing this threshold is not necessarily enough to separate the melt and solid fractions (Holness, 1999). Figure 2.14 shows the evolution of the bulk rock composition for the average basaltic amphibolite

unit composition for 100% melt segregation in steps of 7 vol.% melt; after 7 vol.% melt is generated with increasing temperature, the melt is removed from the bulk composition. The 7 vol.% melt step is an appropriate lower limit as discussed above, and even though it is physically impossible to remove all the melt from the restite (Sawyer, 2001), complete removal does not obscure the trend observed in the bulk rock composition of the model restite. Similarly, greater step values yield a similar evolution of the restite material. With increasing melt segregation the bulk rock composition of the model restite is decreases in Si, Na, and - when included - K. In contrast, the model restite increases in Ti, Al, Fe, Mg, and Ca. The trends are similar for models at 1 and 3 kbar in both the K-bearing and K-absent systems. For comparison, Figure 2.14 also shows the average proximal basaltic hornfels unit composition along with two individual basaltic hornfels unit samples showing the greatest relative depletions in Si, Na, and K. With the exception of Ti and Al, the model trends mimic the observed change in composition from average basaltic amphibolite to average basaltic hornfels. The oxides that best reflect the observed changes from average basaltic amphibolite to average basaltic hornfels suggest that 15-20% melting is a good approximation to the amount of melt extracted from basaltic hornfels, and that individual basaltic hornfels unit samples probably experienced even greater modes of melting.

T-M_{H_2O} MODEL FOR AVERAGE BASALTIC AMPHIBOLITE UNIT

Locally, the limit of the PGZ is up to ca. 750 m from the base of the SIC, and a clinopyroxene zone without the presence of orthopyroxene is apparently absent. This is difficult to reconcile with the phase diagram section of the average basaltic amphibolite

unit (Fig. 2.12), which predicts a one-pyroxene (Cpx) assemblage over a significant temperature interval of ca. 60 °C along a 1.5 kbar isobaric heating path. Increasing the stability range of orthopyroxene towards lower temperatures is another way of explaining the dominance of the two-pyroxene assemblages. An influx of low-$a$$H_2O$ fluids would allow anhydrous minerals such as clino- and orthopyroxene to form at temperatures well below those required under experimental fluid-absent conditions (Pattison, 2003). In the case of the SIC contact aureole, there is no obvious available source of low-$a$$H_2O$ fluid, and the influence a CO_2 dilutent would impose on mineral assemblages in mafic rocks is not observed in the field. The T-M_{H_2O} diagram for the average basaltic amphibolite unit composition (Fig. 2.15) shows that the bulk rock H_2O mode can have a similar effect on the orthopyroxene stability as a low-$a$$H_2O$ fluid. In a closed system equivalent to a dehydration experiment, it would be appropriate to start just below the H_2O saturation curve before following an H_2O isoplethic heating path. After a few degrees heating along this path, the system would include a free H_2O phase. Even in an open system where all the excess fluid was allowed to escape, the orthopyroxene-in curve would not intersect the H_2O saturation curve until temperatures where orthopyroxene, in the H_2O saturated system, is stable. Thus, it would require a H_2O undersaturated bulk rock composition at the onset of contact metamorphism in order to force orthopyroxene stability to lower temperatures. This is difficult to envision, considering the pre-contact metamorphic history of the EMF metabasalts.

The T-M_{H_2O} diagram (Fig.2.15) also indicates that the solidus is unaffected by the bulk rock H_2O content and intersected at virtually the same temperature across the entire diagram. However, the melt vol.% isopleths indicate that the H_2O content does have a

significant effect on melt abundance. The H_2O saturation and solidus curves merge where bulk rock H_2O content approaches zero, at the left side of the diagram. With increasing bulk rock H_2O content the H_2O saturation curve diverges toward higher temperatures. The slope of the H_2O saturation curve is only slightly positive as the bulk rock H_2O content increases, until around a third of the way across the diagram, where the gradient approximately doubles. All melt abundance isopleths on the H_2O saturated side of the H_2O saturation curve are horizontal and independent of H_2O content. Above the H_2O saturation curve, melt abundance isopleths are near vertical in the left quarter of the diagram, and an increase in melt abundance is strongly controlled by an increase in bulk rock H_2O content. With an increase in bulk rock H_2O content, melt abundance isopleths also gradually rotate counter-clockwise towards the horizontal. A similar trend is observed in the An isopleths for plagioclase, where the increase of An component correlates with an increase in melt abundance.

DISCUSSION

THE PHASE DIAGRAM SECTION APPROACH APPLIED TO LP-HT METABASALTS

There are essentially no applications of phase diagram sections to constrain temperature in mafic contact aureoles at relatively low pressures (< 3kbar) and high temperatures (>500 °C) (e.g., Ferry *et al*., 1987; Manning and Bird, 1991; Gillis and Roberts, 1999; Gillis and Coogan, 2002; Koepke *et al*., 2008; Marks *et al*., 2011). Instead, most previous studies rely on experimentally- and/or theoretically-constrained petrogenetic grids for basaltic bulk compositions (e.g., Spear, 1981) and two-pyroxene thermometers (e.g.,

Brey and Köhler, 1990; Andersen *et al*., 1993; Putirka, 2008) to establish peak metamorphic temperatures. Although earlier studies on mafic contact aureoles were conducted before the proliferation of the phase diagram section approach, later studies may have opted for conventional thermobarometry because the fields of interest on a phase diagram section are large, and the mineral proportions and compositions exhibit slow gradual changes in P-T space when modelling MORB-like bulk rock compositions at low-P/high-T. However, by not utilizing the information contained in the bulk rock composition, valuable additional thermobarometric information and other constraints are potentially lost (e.g., Powell and Holland, 2008).

The above modelling results of a MORB composition in the NCFMASHTO system at 1 kbar compared to the experimental results of Beard and Lofgren (1991) are encouraging. In particular, the predicted solidus temperature, mineral assemblages, melt volumes, and several mineral abundances are in good agreement with the Beard and Lofgren (1991) experiments (Fig. 2.10). Also, the modelled evolution of the melt composition predicts trends that are comparable to the Beard and Lofgren (1991) experiments (Fig. 2.11). This allows for some confidence in the construction of phase diagram sections of EMF metabasalt compositions, and their use in determining peak metamorphic temperatures, investigating mineral assemblages, and partial melting. However, there are some serious discrepancies between the models and the Beard and Lofgren (1991) experiments. First, there is an inherent difference between the compositional space of the model system and the compositional space considered in the Beard and Lofgren (1991) experiments. A primary example is whether K is considered a model system component, which has significant implications for the predicted solidus temperature. In this situation, ignoring K

as a model system component appears to yield the best results. However, the absence of K as a model system component prevents the prediction of biotite, which is only a minor issue for the Beard and Lofgren (1991) experimental results because they do not report biotite as part of the starting material nor do they report biotite in any of the experimental run products. In contrast, biotite is often present in the natural EMF metabasalt samples, albeit interpreted as a retrograde phase. Part of the problem when expanding the compositional space to include K may rest with the melting model, because it was not intended for mafic rocks. Compared to the Holland and Powell (2001) melt model that allowed for calculation of mineral-melt equilibria in the NCKASH system, the later models were extended by the addition of FeO (to include fayalite end-member) and MgO (to include fosterite end-member). Thus, the later melt models have been utilized extensively to explore mineral-melt equilibria in metamorphosed sedimentary rocks (e.g., White *et al*., 2007). An important requirement following the expansion to the NCKFMASH is the calibration of the thermodynamic properties for the new end-members and their interaction energies when mixing with the other end-members. Consequently, as stated by White *et al*. (2001), certain assumptions such as the provisionally zero interaction energy involving the new liquid end-members mixing with the anorthite liquid end-member, might be inadequate for systems involving more calcic and mafic melts. Nevertheless, the model results in this study where the melt model is applied to mineral-melt equilibria for metamorphosed mafic rocks closely resembles that of the Beard and Lofgren (1991) experiments at 1 kbar in the NCFMASHTO system. Similarly, the predicted model melt composition and composition trends fairly closely match those of the Beard and Lofgren (1991) experiments. However, the warning offered

by White *et al*. (2001) might exactly be expressed by the overestimation of FeO and MgO combined with an underestimation of CaO in the calculated melt composition (Fig. 2.11). These discrepancies do not discourage the use of the melt model because it still appears to offer reliable and valuable predictions for mafic rocks. Furthermore, as the only solid-solution models used in this study that include K are biotite and melt, it is not difficult to see why the melting temperature is suppressed towards lower temperatures when K is considered.

A more likely reason for the seemingly underestimation of the solidus temperatures in the NCKFMASHTO system is the amphibole a-x model, which ignores K. Amphibole analysed in this study and amphibole compositions reported in the Beard and Lofgren (1991) experiments contain significant K. Beard and Lofgren (1991) also report that the K content of the amphibole varies with the K content of the melt and, therefore, is a function of both starting composition and temperature. Thus, the development of a new a-x model for amphibole that includes K might increase the reliability of predictions in the larger NCKFMASHTO system for mafic rocks at low-P/high-T conditions.

Another notable discrepancy concerning amphibole is the model prediction of two amphiboles, a low-Ca and high-Ca species. Although the prediction does not match the observations in the Beard and Lofgren (1991) experimental runs that only report a high-Ca amphibole, a low-Ca amphibole (grunerite) occurs in the natural rocks of this study. However, the grunerite in the natural EMF metabasalts dominantly occur as overgrowths on orthopyroxene, and rarely exceeds a modal abundance of ca. 2%. This is much lower than observed in the model prediction where clinopyroxene and low-Ca amphibole increase in modal abundance at the expense of high-Ca amphibole, and low-Ca

amphibole reaches a maximum modal abundance of ca. 20%. Thus, it is encouraging that the model actually predicts a two-amphibole assemblage that is observed in the natural rocks, but the predicted modal abundances for the low-Ca amphibole is questionable. Furthermore, it is easy to envision that a low modal abundance of grunerite could be difficult to identify in experimental runs. A better understanding of this two-amphibole stability field could have important implications for temperature estimates, especially if the model increase in modal abundance of the low-Ca species, which occur over a relatively narrow temperature interval (~40 °C), holds true. An additional concern potentially related to the amphibole a-x model are the first appearances of clinopyroxene and orthopyroxene. Although peak metamorphic temperatures are often a primary objective, a good temperature prediction for the clinopyroxene- and orthopyroxene-in isograds for mafic compositions at low-P/high-T conditions would be tremendously valuable to help investigate thermal gradients in contact aureoles. The model at 1kbar agrees with the Beard and Lofgren (1991) experimental results with respect to amphibole reacting out prior to reaching the solidus. This also appears to be in agreement with the observations from the natural rocks, where hornblende is a retrograde phase in the basaltic granofels unit rocks that experienced incipient partial melting. However, the Opx-in isograd is located at ca. 900 °C and between 850-900 °C in the 1 and 3 kbar Beard and Lofgren (1991) experiments, respectively, significantly higher than the model predictions of 725 °C (1kbar) and 790 °C (3 kbar). Other experimental work on similar rock compositions at low pressures by Spear (1981) indicates that orthopyroxene enters the assemblage at ca. 790 °C at 1 kbar and at ca. 820 °C at 3 kbar. Similar lower temperature predictions compared to the experimental results for clinopyroxene isograds

are observed in the models. However, the margin of discrepancy in the pyroxene isograd predictions appears to diminish toward higher pressures. Furthermore, similar to the Spear (1981) experiments, the model predicts pyroxene stable toward lower temperatures as pressure decreases, whereas this is not as obvious in the Beard and Lofgren (1991) experiments. The experimental results also point to a fairly narrow temperature interval (25-50 °C) between the first appearances of clino- and orthopyroxene. If this is closer to 25 °C in reality, it might help explain the consistent presence of a two-pyroxene assemblage in the natural pyroxene bearing samples. Overall, the models appear to underestimate the temperature for the first appearance of clino- and orthopyroxene. These pyroxene prediction problems at LP-HT conditions might result from the pyroxene activity models used. For example, the clinopyroxene activity model does not allow an orthopyroxene component and vice versa. Thus, at high temperatures these pyroxene models are less than ideal. Testing the Jennings and Holland (2015) activity model for pyroxenes with the latest version of the Holland and Powell (2011) thermodynamic database could not be done due to lack of an appropriate amphibole activity model compatible with the same database.

The phase equilibria modelling of an average basaltic amphibolite unit composition shows a positive correlation between the X_{An} content of plagioclase and the melt abundance (Fig. 2.12). From analyzed plagioclase core compositions in metabasalts from the metamorphic aureole it appears there is a general trend from relatively high X_{An} plagioclase towards lower X_{An} plagioclase with increasing distance to the SIC within at least the first ca. 300 m (Fig. 2.9). This would suggest the X_{An} plagioclase isopleths on the phase diagram section in Figure 2.12 could be utilized to not only provide better

constraints for peak metamorphic temperatures, but also to give an approximation for the melt abundance. However, it is clear from the feldspar ternary that the X_{An} plagioclase is strongly controlled by the bulk rock Na content (Fig. 2.9). Because Na is relatively mobile during seafloor alteration and post-depositional metamorphism, secondary variation in the Na content of the EMF metabasalts prior to SIC contact metamorphism is expected and probably played a role. Therefore, while partial melting probably played an important role in the high X_{An} plagioclase observed in, e.g., samples FSTJ098, FSTJ301 and FSTJ069, it is difficult to determine exactly how much of an effect is owed to post-depositional, but pre-SIC changes to the Na content. The combination of textural evidence provided by the relatively low-Ca plagioclase frameworks resembling trapped melt and high-Ca plagioclase cores with calculated isopleths are strong indications that partial melting and melt segregation was an important process in the mafic aureole. Furthermore, plagioclase compositions from the EMF metabasalts have previously been estimated to range from An_{20}-An_{60} (Innes, 1977; Card, 1978b).

METAMORPHIC EVOLUTION OF THE EMF METABASALTS IN THE SIC AUREOLE

Two-pyroxene thermometry for the peak metamorphic assemblage in the basaltic hornfels unit yields temperatures up to 887 °C (Table 2.5), but results from phase equilibria modelling indicate peak temperatures of at least 925 °C. The predicted peak mineral assemblage of Pl-Cpx-Opx-Ilm-Mt-Liq is in agreement with the observed peak mineral assemblage of the basaltic hornfels unit rocks and although this might provide a minimum peak temperature of ca. 885 °C at 1.5 kbar it is clear that this is a high variance assemblage stable at a wide P-T range. Indications that peak metamorphic temperatures

were even higher are supported by isopleths of X_{An} and melt volumes. Furthermore, the melt extraction model shows that modification to the bulk rock composition by melt segregation is similar to the compositional changes observed between the average natural protolith and residuum compositions (Fig. 2.14). Thus, if significant melt was lost, at least some of the basaltic hornfels unit rocks, like sample FSTJ098, experienced metamorphic conditions of at least 925 °C. The basaltic granofels unit rocks also contain both clino- and orthopyroxene as part of the mineral assemblage, and although hornblende is commonly a major phase, it is regarded as a retrograde phase. Quartz is ubiquitous in the basaltic granofels unit resulting in a peak assemblage of Pl-Cpx-Opx-Ilm-Mt ± Qtz ± Liq that corresponds to peak temperatures of ca. 745-885 °C when following the isobaric 1.5 kbar path in Figure 2.12. Because the quartz exhibits microtextures interpreted to represent former melt, peak temperatures for the basaltic granofels unit rocks might be closer to the upper limit of this range. However, there are no indications from field observations, petrographic analyses, or bulk rock compositions that suggests melt extraction from the basaltic granofels unit. No natural samples were collected that match the predicted clinopyroxene-only (orthopyroxene absent) mineral assemblage. An increase in the stability field of coexisting clino- and orthopyroxene towards lower temperatures could result from low bulk rock H_2O content (Fig. 2.15). Regardless, it is not currently clear whether the missing one-pyroxene zone is a result of bulk rock H_2O content, reaction overstepping, or retrogression of this entire zone. Also, a steep geothermal gradient induced by the SIC could have resulted in a narrow one-pyroxene zone that could have been missed altogether, but this is unlikely given the estimate of temperature decrease with distance from the SIC contact. A two-amphibole

assemblage characterizes the predicted mineral assemblage before pyroxene formation (Fig. 2.12). The dominant contact metamorphic related amphibole species in the natural samples are typically high-Ti hornblende with only small amounts of grunerite present. Furthermore, the grunerite is most commonly observed in the pyroxene-bearing rocks as a retrograde phase overgrowing mainly orthopyroxene. Similarly, high-Ca amphibole is the dominant amphibole species in the model Beard and Lofgren (1991) composition, and the predicted modal abundance of low-Ca amphibole is less than 10 wt. % before the appearance of clinopyroxene (Fig. 2.10). The basaltic amphibolite unit samples most likely to represent a prograde contact metamorphic assemblage are then fairly consistent with the predicted assemblage below the clinopyroxene-in line, although the modal abundance of grunerite might be an overestimation. This suggests that temperatures reached up to ca. 680 °C at a distance of at least 1000 m from the SIC contact.

The basaltic hornfels unit rocks on average are significantly more dehydrated than the basaltic granofels unit rock as indicated by the general higher modal abundance of high-Ti hornblende in the basaltic granofels unit. However, the fact that the majority of the high-Ti hornblende is overgrowing pyroxene combined with the presence of trapped melt in the basaltic granofels unit rocks suggest that the mineral assemblage was anhydrous at one point in time. Because the majority of basaltic granofels unit rocks avoided complete retrogression it seems reasonable to propose that H_2O contained in incipient partial melts was released upon crystallization to form only local retrogression during cooling during which peak-metamorphic pyroxene was only partially replaced by high-Ti hornblende at high temperature. The H_2O contained by the basaltic granofels unit rocks were lost from the basaltic hornfels unit rocks during partial melt segregation. Another consideration is

that maximum temperatures in the contact aureole would have been reached later in time at increasing distance from the SIC. Thus, another potential H_2O source for later rehydration of the basaltic granofels and basaltic hornfels unit rocks during the retrograde path could have been H_2O released from metabasalts further below the SIC contact. Nevertheless, the later retrograde history was dominated by near-isobaric cooling as indicated by the plotting position of high-Ti hornblende overgrowing pyroxene on Ti - ^{IV}Al and ^{IV}Al - ^{VI}Al diagrams yielding a pressure range from ca. 1-3 kbar (Fig. 2.8c, d).

LITHOLOGICAL CONTROLS ON ANATEXIS

Field evidence for significant melt mobilization in the EMF metabasalts is restricted to the PHZ where partial melt patches locally coalesce, and indirectly from the destruction of pillow textures in the basaltic hornfels unit rocks compared to intact and well-preserved pillow textures in rocks from the PGZ and HHZ. Whereas partial melts from the Murray and Creighton granites are known to form dikes back-injecting SIC norite (e.g., Peredery and Morrison, 1984), similar back-injections have not been observed originating from EMF metabasalts. This suggests that melt segregation from the metabasalts was largely constrained to a period prior to the complete solidification of the SIC, and segregated melts were incorporated into a still convecting melt sheet or possibly directly contributing to the formation of the Sublayer norite (e.g., Prevec and Cawthorn, 2002). Alternatively, mobile phases from the proximal contact aureole were driven outwards but field evidence is yet to be found in support of this. Nonetheless, the high-temperature metamorphic aureole developed earlier in EMF metabasalts than in Murray granites, which evidently continued to experience high degrees of melting even after

solidification of the Main Mass. Features interpreted as microscopic melt textures in the Murray granites NW domain occurring up to ~500 m from the base of the SIC (Riller *et al*., 1996 and Rosenberg and Riller, 2000) show a much better correlation with the lower limit of pyroxene-hornfels metamorphism and not the lower limit of hornblende-hornfels metamorphism as previously stated by Riller *et al.* (1999).

Péntek *et al*. (2011) describes an association between the degree of partial melting and the presence of SUBX zones in felsic rocks in the North Range, and the localization of partial melts in the breccia zones rather than a gradational decrease in the intensity of partial melting with increasing distance to the SIC. The finer grained breccia matrix and increased fluid availability in the SUBX may explain the enhanced degree of partial melting (Péntek *et al*., 2011). Well-developed in-situ SUBX zones within the studied parts of the PHZ with matrix and clast compositions matching EMF metabasalts are extremely difficult to identify. Potential zones of in-situ SUBX developed in basaltic hornfels unit rocks were observed in drill core, and are characterized by a sharp contact defined only by a slight change in grain size (Fig. 2.4g). The paucity of observed in-situ SUBX development in the EMF metabasalts within the high-T part of the aureole probably reflects a combination of complete recrystallization, the meso- to melanocratic nature of the rocks, and black silica coatings frequently covering outcrops in the field areas. Thus, the potential control of SUBX on anatexis of EMF is difficult to evaluate at present. However, if the first melting reaction encountered at these relatively low pressures, even in water undersaturated metabasalts, is not a dehydration reaction, the availability of an H_2O fluid phase is not expected to be the controlling factor for melting

to commence, but if SUBX zones acted as fluid channels they could potentially be important for the volume of melt generated.

A COMPARISON OF THERMAL MODELLING AND THE SIC NORTH RANGE AUREOLE

The mapping presented here divides EMF metabasalts into three metamorphic zones extending from the base of the SIC: 1) an inner PHZ that is up to ca. 500 m wide, 2) an intermediate PGZ extending up to ca. 750 m from the base of the SIC, and 3) an outer HHZ that is observed at least 1000 m normal to the SIC. From the phase diagram section in Figure 2.12 this would indicate that the inner 500 m experienced temperatures of at least 875 °C, and possibly upward of 1000 °C near the contact. Similarly, the footwall would have reached at least 740 °C at a distance of 750 m. As illustrated by the T-M_{H_2O} phase diagram section (Fig. 2.15) the estimate of the solidus temperature is unaffected by the H_2O content, but lower H_2O content could stabilize a two-pyroxene assemblage at lower temperatures. Finally, temperatures reached up to 680 °C at 1000 m from the SIC contact.

In a model that took into account both conductive heat loss to the floor rocks and convective heat loss within the Main Mass, Prevec and Cawthorn (2002) predicted that the footwall below the SIC melt sheet reached a maximum temperature of ~820 °C at 500 m, ~750 °C at 750 m, and 620 °C at ~1000 m. They compared their results to the North Range aureole that includes a 100 m wide pyroxene hornfels inner zone reflecting temperatures of at least 600 °C, a 300 m wide hornblende hornfels zone corresponding to temperatures around 540 °C, and a 1200 m zone of recrystallized plagioclase feldspar

reflecting temperatures around 400 °C (Dressler, 1984b). Hence, for the model to fit the observations in the North Range it required thermal erosion of approximately 800 m of country rock immediately adjacent to the contact (Prevec and Cawthorn, 2002). However, the lithological units and modelling parameters used by Prevec and Cawthorn (2002) were selected to match the South Range, which includes a 1000 m upper footwall layer of Huronian basalt. Compared to the width of the aureole in the EMF metabasalts presented in this study, the Prevec and Cawthorn (2002) model of the aureole width is nearly identical, invalidating the requirement for removal of ~800 m of country rock. This comparison also indicates that the high-T metamorphic aureole is much wider in the South Range than the North Range, even if compared to the North Range metamorphic zones documented by Boast and Spray (2006) that include a ≤25 m anatectic zone, a wider pyroxene hornfels zone (≤180 m), and a wider hornblende hornfels zone (≤900 m) compared to that of Dressler (1984b).

Another important factor, which is difficult to quantify and not included in previous models, was the physical nature of the footwall rocks (massive, fractured, brecciated), which would have affected their susceptibility to mechanical erosion and therefore on the rate of cooling of the melt sheet. Ultimately, integrated models involving thermomechanical erosion (see e.g., Williams et al. 1998 *JGR*) and contact metamorphism will be required to better constrain the thermal history of the crystallizing SIC.

CONCLUSIONS

This study provides the first detailed documentation of the SIC South Range contact aureole developed in metabasalts based on mapping, petrography, mineral and bulk rock chemistry, and phase equilibria modelling. Our observations and results lead to the following conclusions:

1) Starting from the SIC contact, the metamorphic aureole can be subdivided into three zones: 1) an inner pyroxene hornfels zone (PHZ) extending up to 500 m from the SIC contact; 2) an intermediate pyroxene granofels zone (PGZ) extending up to 750 m from the SIC contact; and 3) an outer hornblende hornfels zone (HHZ) extending upwards of 1000 m. Conservative estimates of peak contact metamorphic temperature are 925 °C in the PHZ and up to 680 °C in the HHZ at 1000 m from the SIC contact.
2) The high-temperature contact aureole recorded in EMF metabasalts of the SIC South Range is wider than the aureole documented in the North Range (Dressler, 1984; Boast and Spray, 2006) and in considerably better agreement with the width predicted from thermal models assuming a superheated melt sheet (Prevec and Cawthorn, 2002). A corollary of this is that the additional 800 m of thermomechanical erosion of the footwall in the North Range proposed by Cawthorn and Spray (2002) is not required to explain the narrower width of the observed aureole in the SIC North Range footwall (Dressler, 1984b; Boast and Spray, 2006).
3) Macroscopic leucocratic melt patches and networks associated with metabasalts in the PHZ, and microscopic optically continuous quartz grains and networks of quartz and relatively low-Ca plagioclase in PHZ and PGZ metabasalts provides evidence

for partial melting. Phase equilibria modelling suggest that melting of metabasalts in the PHZ reached about 10-20% and probably even higher degrees of melting near the SIC contact.

4) Brownish green high-Ti hornblende in pyroxene-bearing metabasalts dominantly grew during the retrograde path and misinterpretation leading to the incorporation of this phase as part of the peak assemblage would lead to an erroneous view on the prograde history and a gross underestimation of peak temperatures. Furthermore, the commonly high modal abundance of high-Ti hornblende in the PGZ indicates that dehydration of these rocks was not complete, potentially through the retainment and crystallization of incipient partial melting resulting in the release of H_2O and consequently retrogression of clino- and orthopyroxenes. The lower modal abundance of high-Ti hornblende in the PHZ is therefore another good indication that melt segregation occurred, resulting in almost complete dehydration of the metabasalts in the most proximal parts of the aureole.
5) Phase equilibria modelling indicates that the first melting reaction encountered is not a dehydration reaction, and that the bulk rock $a H_2O$ has no or insignificant effect on the solidus. Thus, the availability of an H_2O fluid might be more important for the melt abundance. This would support the interpretation that SUBX zones acting as fluid conduits might enhance the melt abundance (Péntek *et al*., 2011).
6) The White *et al*. (2007) melt model yielded convincing results in modelling partial melting of metabasalts in the NCFMASHTO system at pressures near 1 kbar with respect to solidus, melt abundances, and evolution of melt compositions. Problems in NCFKMASHTO underestimating the solidus temperature might be directly targeted

by the development of an amphibole solution model that includes a potassium end-member. It would also be helpful to know if such a model would have any implications for the current prediction of no dehydration melting (around 1 kbar).

7) The approach followed in this study demonstrated the potential for using the bulk rock compositions of basaltic rocks in phase equilibria modelling at low pressure and high temperature conditions, which has previously been neglected primarily due to high variance mineral assemblage fields in P-T space. Currently, the model is able to adequately predict the observed mineral assemblages, but continuous improvement of *a-x* relationships is obviously critical to improve realistic predictions, e.g., underestimation of temperatures for orthopyroxene stability, clino- and orthopyroxene modal abundances, overestimation of the modal abundance of low-Ca amphiboles. The investigation of shallow crustal contact aureoles where mafic rocks form the majority of the country rocks, and the secular high-temperature contact metamorphism near the sheeted dike – plutonic transition at mid-ocean ridges would greatly benefit from improvements in the modelling capability.

ACKNOWLEDGEMENTS

Financial support was provided by grants from the Centre for Excellence in Mining Innovation (project sponsors Vale Ltd. and Glencore Ltd.) and the Natural Sciences and Engineering Council of Canada (CRD to DKT and CML, Discovery Grant to DKT, and Discovery Grants #203171-2007 and #203171-2012 to CML). Field and logistical support was provided by Vale Ltd. and we are particularly grateful to Peter Lightfoot and Lisa Gibson for their assistance.

REFERENCES

Ames, D. E., 1999. Geology and regional hydrothermal alteration of the crater-fill Onaping Formation: Association with Zn-Pb-Cu mineralization, Sudbury Structure Canada. Unpublished Ph.D. thesis, Carleton University, Ottawa, Canada 460 pp.

Ames, D. E., Golightly, J. P., Lightfoot, P. C., and Gibson, H. L., 2002. Vitric compositions in the Onaping Formation and their relationship to the Sudbury Igneous Complex, Sudbury structure: Economic Geology, v. 97, p. 1541-1562.

Andersen, D., Lindsley, D., and Davidson, P., 1993. QUILF: A Pascal program to assess equilibria among Fe-Mg-Mn-Ti oxides, pyroxenes, olivine, and quartz, Computers & Geosciences, v. 19(9), p. 1333–1350.

Anderson, R. N., Uyeda, S., and Miyashiro, A., 1976. Geophysical and Geochemical Constraints at Converging Plate Boundaries – Part I: Dehydration in the Downgoing Slab. Geophysical Journal of the Royal Astronomical Society, v. 44, p. 333-357.

Arzi, A., 1978. Critical phenomena in the rheology of partially melted rocks. Tectonophysics, v. 44, p. 173–184.

Bailey, J., McDonald, A. M., Lafrance, B., and Fedorowich, J. S., 2006. Variations in Ni content in sheared magmatic sulfide ore at the Thayer Lindsley mine, Sudbury, Ontario. The Canadian Mineralogist 44, 1063–1077.

Beard, J. S., and Lofgren, G. E., 1991. Dehydration Melting and Water-Saturated Melting of Basaltic and Andesitic Greenstones and Amphibolites at 1, 3, and 6·9 kb. Journal of Petrology, v. 32, p. 2, pp. 365-401.

Bennett, G., Dressler, B. O., and Robertson, J. A., 1991. The Huronian Supergroup and associated intrusive rocks, Chapter 14 in Geology of Ontario: Ontario Geological Survey, Special Volume 4, Part 1, p. 549-591.

Bethune, K. M., 1997. The Sudbury dyke swarm and its bearing on the tectonic development of the Grenville Front, Ontario, Canada. Precambrian Research 85, p. 117–146.

Boast, M. and Spray, J. G., 2006. Superimposition of a thrust-transfer fault system on a large impact structure: Implications for Ni-Cu-PGE exploration at Sudbury; Economic Geology 101, p. 1583-1594.

Brey, G. P., and Köhler, T., 1990. Geothermobarometry in four-phase lherzolites II. New thermobarometers, and practical assessment of existing thermobarometers, Journal of Petrology, v. 31(6), p. 1353–1378.

Cantin, R., and Walker, W.G. 1972. Was the Sudbury Basin circular during deposition of the Chelmsford Formation? In: New Developments in Sudbury Geology, Geological Association of Canada, Special Paper Number 10, p. 93-101.

Card, K. D., 1978a. Geology of the Sudbury-Manitoulin Area, Districts of Sudbury and Manitoulin; Ontario Geological Survey, Report 166, 238p.

Card, K. D., 1978b. Metamorphism of the middle Precambrian (Aphebian) rocks of the eastern Southern Province; in Metamorphism in the Canadian Shield, Geological Survey of Canada, Paper 78-10, p. 269-282.

Card, K. D., Gupta, V. K., McGrath, P. H. and Grant, F. S., 1984. The Sudbury structure: Its regional geological and geophysical setting. In: Pye, E. G., Naldrett, A. J., Giblin, P. E. (Eds.), The Geology and Ore Deposits of the Sudbury Structure. Ontario Geological Survey Special Volume 1, pp. 25–44.

Coggon, R., and Holland, T. J. B., 2002. Mixing properties of phengitic micas and revised garnet-phengite thermobarometers. Journal of Metamorphic Geology, v. 20, p. 683–696.

Coleman, A. P., 1913. The nickel industry, with special reference to the Sudbury Region, Ontario; Canada Department of Mines, Mines Branch, no. 170, 206p.

Colombi, A., 1989. Métamorphisme et géochimie des roches mafiques des Alpes ouest-centrales (géoprofil Viège-Domodossola-Locarno). Mémoires de Géologie, 4, 1-216, Lausanne.

Cottrell, E., and Kelley, K. A., 2011. The oxidation state of Fe in MORB glasses and the oxygen fugacity of the upper mantle. Earth and Planetary Science Letters, v. 305, p. 270-282.

Davidson, A., van Breemen, O. and Sullivan, R. W., 1992. Circa 1.75 Ga ages for plutonic rocks from the Southern Province and adjacent Grenville Province: what is the

expression of the Penokean Orogeny? In: Radiogenic age and isotopic studies, Report 6. Geological Survey of Canada Paper 92–2, p. 107–118.

de Capitani, C., and Brown, T. H., 1987. The computation of chemical equilibrium in complex systems containing non-ideal solutions. Geochimica et Cosmochimica Acta, v. 51, p. 2639–2652.

Deer, W. A., Howie, R. A., and Zussman, J., 1992. An Introduction to the Rock-forming Minerals, 2nd ed. Longman Group, Essex, U.K.

Dence, M. R. 1972. Meteorite impact craters and the origin of the Sudbury Basin; in New Developments in Sudbury Geology, Geological Association of Canada, Special Paper Number 10, p. 7-18.

Diener, J. F. A., and Powell, R., 2012. Revised activity–composition models for clinopyroxene and amphibole. Journal of Metamorphic Geology, v. 30, p. 131–142.

Dietz, R.S., 1964. Sudbury structure as an astrobleme: Journal of Geology, v. 72, p. 412-434.

Dressler, B. O., 1984a. General geology of the Sudbury area. In: Pye, E. G., Naldrett, A. J., Giblin, P. E. (Eds.), The geology and ore deposits of the Sudbury structure: Ontario Geological Survey Special Volume 1, p. 57–82.

Dressler, B. O., 1984b. The effects of the Sudbury event and the intrusion of the Sudbury Igneous Complex on the Footwall Rocks of the Sudbury structure. In: Pye, E. G.,

Naldrett, A. J., Giblin, P. E. (Eds.), The geology and ore deposits of the Sudbury structure: Ontario Geological Survey Special Volume 1, p. 97–136.

Droop, G. T. R., 1987. A general equation for estimating Fe3+ concentrations in ferromagnesian silicates and oxides from microprobe analyses, using stoichiometric criteria. Mineralogical Magazine, v. 51, p. 431-435.

Farrow, C. E. G., Watkinson, D. H., and Jones, P. C., 1994. Fluid inclusions in sulfides from North and South range Cu-Ni-PGE deposits, Sudbury Structure, Ontario: Economic Geology, v. 89, p. 647-655.

Ferry, J. M., L. J. Mutti, and G. J. Zuccala, 1987. Contact metamorphism/hydrothermal alteration of Tertiary basalts from the Isle of Skye, northwest Scotland, Contributions to Mineralogy and Petrology, v. 95(2), p. 166–181.

Fleet, M. E., Barnett, R. L., 1978. AlIV/AIVI partitioning in calciferous amphiboles from the Frood mine, Sudbury, Ontario. Canadian Mineralogist v. 16, p. 527–532.

Frost, B. R. and Chacko, T., 1989. The granulite uncertainty principle: limitations on thermobarometry in granulites, Journal of Geology, v. 97, p. 435–450.

Fueten, F. and Redmond, D. J., 1997. Documentation of a 1450 Ma contractional orogeny preserved between the 1850 Ma Sudbury impact structure and the 1 Ga Grenville orogenic front, Ontario. Geological Society of America Bulletin 109, 268–279.

Gillis, K. M., and Coogan, L. A., 2002. Anatectic Migmatites from the Roof of an Ocean Ridge Magma Chamber, Journal of Petrology, v. 43, n. 11, p. 2075-2095.

Gillis, K. M., and Roberts, M. D., 1999. Cracking at the magma-hydrothermal transition: Evidence from the Troodos Ophiolite, Cyprus, Earth and Planetary Science Letters, v. 169(3–4), p. 227–244.

Golightly, J.P., 1994. The Sudbury Igneous Complex as an Impact Melt: Evolution and Ore Genesis. In: Lightfoot, P.C., Naldrett, A.J. (Eds.), Proceedings of the Sudbury-Noril'sk Symposium. OGS Special Volume 5, 105-118.

Green, E. C. R., Holland, T. J. B., Powell, R. and White, R.W., 2012. Garnet and spinel lherzolite assemblages in MgO–Al2O3–SiO2 and CaO–MgO–Al2O3–SiO2: thermodynamic models and an experimental conflict. Journal of Metamorphic Geology, v. 30, p. 561–577.

Grieve, R.A.F., M.R. Dence, and P.B. Robertson, 1977. Cratering processes: As interpreted from the occurrence of impact melts, in Impact and Explosion Cratering, edited by D. J. Roddy, R. O. Pepin, and R. B. Merrill, Pergamon, New York, p.791–814.

Grieve, R. A. F., Stöffler, D., and Deutsch, A., 1991. The Sudbury structure-controversial or misunderstood: Journal of Geophysical Research, v. 96, p. 22753–22764.

Grieve, R. A. F., and Therriault, A. M. 2000. Vredefort, Sudbury, Chicxulub: Three of a kind? Annual Review of Earth and Planetary Sciences v. 28, p. 305–338.

Hammarstrom, J. M., Zen, E., 1986. Aluminum in hornblende: An empirical igneous geobarometer. American Mineralogist v. 71, p. 1297–1313.

Hawthorne, F. C., Oberti, R., Harlow, G. E., Maresch, W. V., Marin, R. F., Schumacher, J. C., and Welch, M. D., 2012. Nomenclature of the amphibole supergroup. American Mineralogist, v. 97, p. 2031-2048.

Holland, T. J. B., and Powell, R., 1998. An internally-consistent thermodynamic dataset for phases of petrological interest. Journal of Metamorphic Geology, v. 16, p. 309–344.

Holland, T. J. B., and Powell, R., 2001. Calculation of phase relations involving haplogranitic melts using an internally-consistent thermodynamic data set. Journal of Petrology, v. 42, p. 673-683.

Holland, T. J. B., and Powell, R., 2003. Activity–composition relations for phases in petrological calculations: an asymmetric multicomponent formulation. Contributions to Mineralogy and Petrology, v. 145, p. 492–501.

Holland, T. J. B., and Powell, R., 2011. An improved and extended internally-consistent thermodynamic dataset for phases of petrological interest, involving a new equation of state for solids. Journal of Metamorphic Geology, v. 29, p. 333–383.

Holness, M. B., 1999. Contact metamorphism and anatexis of Torridonian arkose by minor intrusions of the Rum Igneous Complex, Inner Hebrides, Scotland. Geological Magazine, v. 136, p. 527–542.

Hoover, J. D., and Murphy, W. M., 1989. Quench fractionation in Columbia River basalt and implications for basalt-ground water interaction, in Reidel, S. P., and Hooper, P. R. (eds.), Volcanism and tectonism in the Columbia River flood-basalt province: Boulder, Colorado, Geological Society of America, Special Paper 239.

Innes, D. G., 1977. Proterozoic volcanism in the Southern Province of the Canadian Shield. M.Sc. Thesis, Laurentian University.

James, R. S., Easton, R. M., Peck, D. C., Hrominchuk, J. L., 2002. The East Bull Lake intrusive suite; remnants of an approximately 2.48 Ga large igneous and metallogenic province in the Sudbury area of the Canadian Shield. Economic Geology, v. 97, p. 1677-1606.

Jennings, E. S., and Holland, T. J. B., 2015. A Simple Thermodynamic Model for Melting of Peridotite in the System NCFMASOCr. Journal of Petrology, v. 56, p. 869-892.

Keays, R. R., Lightfoot P. C., 2004. Formation of Ni–Cu–PGE sulfide mineralization in the Sudbury Impact Melt, Min Pet 82: p. 217–258.

Koepke, J., Christie, D. M., Dziony, W., Holtz, F., Lattard, D., Maclennan, J., Park, S., Scheibner, B., Yamasaki, T., and Yamazaki S., 2008. Petrography of the dike-gabbro transition at IODP Site 1256 (equatorial Pacific): The evolution of the granoblastic dikes, Geochemistry, Geophysics, Geosystems, 9.

Krogh, T. E., Corfu, F., Davis, D. W., Dunning, G.R., Heaman, L .M., Kamo, S. L., Machado, N., Greenhough, J. D., and Nakamura, E., 1987. Precise U-Pb isotopic ages of diabase dykes and mafic to ultramafic rocks using trace amounts of baddeleyite and zircon, in Halls, H.C. and Fahrig, W.F. (eds.), Mafic dyke swarms: Geological Association of Canada Special Paper 34, p. 147–152.

Krogh, T. E., Davis, D. W., Corfu, F., 1984. Precise U-Pb zircon and baddeleyite ages for the Sudbury area. In: The Geology and Ore Deposits of the Sudbury Structure, Ontario Geological Survey, Special Volume 1, p. 431-446.

Krogh T. E., Kamo S. L., and Bohor B. F. 1996. Shock metamorphosed zircons with correlated U-Pb discordance and melt rocks with concordant protolith ages indicate an impact origin for the Sudbury structure. Geophysical Monograph 85, p. 343–353.

Leake, B. E., 1971. On aluminous and edenitic hornblendes. Mineralogical Magazine v. 38, p. 389–406.

Lenauer, I., 2012. Structural analysis and 3D kinematic restoration of the Southern Sudbury Basin, Ontario. Unpublished Ph.D. thesis, Hamilton, Ontario, McMaster University, 131 p.

Lightfoot, P.C., 2017. Nickel Sulfide Ores and Impact Melts: Origin of the Sudbury Igneous Complex. Elsevier, 680 p.

Lightfoot, P.C., Doherty, W., Farrell, K., Keays, R.R., Moore, M., and Pekeski, D., 1997. Geochemistry of the Main Mass, Sublayer, Offsets, and Inclusions from the Sudbury Igneous Complex, Ontario: Ontario Geological Survey, Open File Report 5959, 231 p.

Lightfoot, P. C., and Farrow, C. E., 2002. Geology, geochemistry and mineralogy of the Worthington Offset Dike: A genetic model for offset dike mineralization in the Sudbury Igneous Complex: Economic Geology, v. 97, p. 1419-1446.

Lightfoot, P. C., Keays, R. R., and Doherty, W., 2001. Chemical evolution and origin of nickel sulfide mineralization in the Sudbury Igneous Complex, Ontario, Canada: Economic Geology, v. 96, p. 1855-1875.

Lindsley, D. H., 1983. Pyroxene thermometry. American Mineralogist, v. 68, p. 477-493.

Lindsley, D. H., and Andersen, D. J., 1983. A two-pyroxene thermometer. Journal of Geophysical Research Supplement, v. 88, p. A887-A906.

Ludwig, K.R., 2003. Isoplot/Ex Version 3.00: a Geochronological Toolkit for Microsoft Excel. Berkeley Geochronology Center, Berkeley, CA.

Lupulescu, A., and Watson, E. B., 1999. Low melt fraction connectivity of granitic and tonalitic melts in a mafic crustal rock at 800°C and 1 GPa. Contributions to Mineralogy and Petrology, v. 134, p. 202–216.

Maaløe, S., 1982. Geochemical aspects of permeability controlled partial melting and fractional crystallization. Geochimica et Cosmochimica Acta, v. 46, p. 43-57.

MacGregor, M., and Wilson, G., 1939. On granitization and associated processes, Geological Magazine, v. 76, p. 210-212.

Manning, C. E., and D. K. Bird, 1991. Porosity evolution and fluid flow in the basalts of the Skaergaard magma-hydrothermal system, East Greenland, American Journal of Science, v. 291(3), p. 201–257.

Marks, N., Schiffman, P., Zierenberg, R. A., 2011. High-grade contact metamorphism in the Reykjanes geothermal system: Implications for fluid-rock interactions at mid-oceanic ridge spreading centers, Geochemistry, Geophysics, and Geosystems, v. 12, n. 8.

Molnar, F., Watkinson, D. H., and Jones, P. C., 2001. Multiple hydrothermal processes in footwall units of the North Range, Sudbury Igneous Complex, Canada, and implications for the genesis of vein-type Cu-Ni-PGE deposits: Economic Geology, v. 96, p. 1645-1670.

Mukwakwami, J., Lafrance, B., and Lesher, C. M., 2012. Back-thrusting and overturning of the southern margin of the 1.85 Ga Sudbury Igneous Complex at the Garson mine, Sudbury, Ontario. Precambrian Research, v. 196–197, p. 81–105.

Mukwakwami J., Lafrance B., Lesher C. M., Tinkham D., Rayner N., and Ames D. E., 2014. Fabrics and textures of deformed and metamorphosed Ni-Cu-PGE sulfide ores at Garson Mine and their implications for sulfide mobilization processes, Mineralium Deposita, v. 49(2), p. 175-198.

Naldrett, A. J., 1984. Mineralogy and composition of the Sudbury ores, in Pye, E.G., Naldrett, A.J., and Giblin, P.E., eds., The Geology and Ore Deposits of the Sudbury Structure: Ontario Geological Survey, Special Volume 1, p. 309-326.

Naldrett, A.J., 2004. Magmatic Sulfide Deposits, Geology, Geochemistry, and Exploration; Springer, 727p.

Naldrett, A.J., Bray, J.G., Gasparinni, E.L., Podolsky, T., and Rucklidge, J.C., 1970. Cryptic variation and the petrology of the Sudbury Nickel Irruptive, Economic Geology, v. 65, p. 122-155.

Paton, C., Hellstrom, J., Paul, B.,Woodhead, J. and Hergt, J. 2011. Iolite: Freeware for the visualisation and processing of mass spectrometric data. Journal of Analytical Atomic Spectrometry, 26, 2508-2518.

Paton C., Woodhead J.D., Hellstrom J.C., Hergt J.M., Greig A., and Maas R., 2010. Improved laser ablation U-Pb zircon geochronology through robust downhole fractionation correction. Geochemistry Geophysics Geosystems, 11, p. 1–36.

Pattison, D. R. M., 2003. Petrogenetic significance of orthopyroxene-free garnet + clinopyroxene + plagioclase-bearing metabasites with respect to the amphibolite and granulite facies. Journal of Metamorphic Geology, v.21, p. 21-34.

Pattison, D. R. M., Chacko, T., Farquhar, J., McFarlane, C. R. M., 2003. Temperatures of Granulite-facies Metamorphism: Constraints from Experimental Phase Equilibria and Thermobarometry Corrected for Retrograde Exchange. Journal of Petrology, v. 44, n. 5, p. 867-900.

Pattison, E. F., 1979. The Sudbury sublayer: Canadian Mineralogist, v. 17, p. 257-274.

Peacock, S. M., 1990. Fluid processes in subduction zones, Science, 248, p. 329-337.

Péntek, A., Molnár, F., Watkinson, D. H., Jones, P. C., Mogessie, A., 2011. Partial melting and melt segregation in footwall units within the contact aureole of the Sudbury

Igneous Complex (North and East Ranges, Sudbury structure), with implications for their relationship to footwall Cu–Ni–PGE mineralization. International Geology Review, v. 51, no. 2, p. 291-235.

Peredery, W. V. 1972. Chemistry of fluidal glasses and melt bodies in the Onaping Formation; in New Development in Sudbury Geology, Geological Association of Canada, Special Paper Number 10, p. 49-59.

Peredery, W.V., and Morrison, G.G., 1984. Discussion of the origin of the Sudbury structure, in

Petrus, J.A., and Kamber, B.S., 2012. VizualAge: A Novel Approach to Laser Ablation ICP-MS U-Pb Geochronology Data Reduction. Geostandards and Geoanalytical Research, 36, 247-270.

Pye, E.G., Naldrett, A.J., and Giblin, P.E., eds., The Geology and Ore Deposits of the Sudbury Structure: Ontario Geological Survey, Special Volume 1, p. 491-511.

Powell R., and Holland T. J. B., 1994. Optimal geothermometry and geobarometry. American Mineralogist, v. 79, p. 120-133.

Powell, R., and Holland, T. J. B., 2008. On thermobarometry. Journal of Metamorphic Geology, v. 26, p. 155–180.

Prevec, S. A. and Cawthorn, R.G. 2002. Thermal evolution and interaction between impact melt sheet and footwall: A genetic model for the contact sublayer of the Sudbury Igneous Complex, Canada; Journal of Geophysical Research 107(B8), 2176.

Presnall, D. C., Dixon, J. R., O'Donnell, T. H., and Dixon, S. A., 1979. Generation of mid-ocean ridge tholeiites. Journal of Petrology v. 20, p. 3–35.

Putirka, K., 2008. Thermometers and barometers for volcanic systems. Reviews in Mineralogy and Geochemistry, v. 69(1), p. 61–120.

Raase, P., 1974. Al and Ti contents of hornblende, indicators of pressure and temperature of regional metamorphism. Contributions to Mineralogy and Petrology, v. 45, p. 231-236.

Raharimahefa T., Lafrance, B., Tinkham, D. K., 2014. Structural, metamorphic, and U-Pb Geochronological evolution of the Southern Province, Sudbury, Canada. Precambrian Research, v. 51, p. 750-774.

Riller, U., 2005. Structural characteristics of the Sudbury Impact Structure, Canada: impact-induced and orogenic deformation — a review. Meteoritics & Planetary Science, v. 40, n. 11, p. 1723–1740.

Riller, U., Boutelier, D., Schrank, C., Cruden, A. R., 2010. Role of kilometer-scale weak circular heterogeneities on upper crustal deformation patterns: evidence from scaled analogue modeling and the Sudbury Basin, Canada. Earth and Planetary Earth Science Letters 297, p. 587–597.

Riller, U., Cruden, A. R., and Schwerdtner, W. M., 1996. Magnetic fabric, microstructure and high temperature metamorphic overprint of the Murray granite pluton, central Ontario: Journal of Structural Geology, v. 18, p. 1005–1016.

Riller, U. and Schwerdtner, W. M., 1997. Mid-crustal deformation at the southern flank of the Sudbury Basin, central Ontario, Canada. Geological Society of America Bulletin 109, p. 841–854.

Riller, U., Schwerdtner, W. M., Halls, H. C. and Card, K. D., 1999. Transpressive tectonism in the eastern Penokean orogen, Canada: Consequences for Proterozoic crustal kinematics and continental fragmentation. Precambrian Research, v. 93, p. 51–70.

Rivers, T., 1997. Lithotectonic elements of the Grenville Province: review and tectonic implications. Precambrian Research, v. 86, p. 117–154.

Robinson, P., 1980. The composition space of terrestrial pyroxenes - internal and external limits. In: Pyroxenes (ed. Perwitt, C. T.), Reviews in Mineralogy, v. 7, p. 419-494.

Rosenberg, C. L., and Handy, M.R., 2005. Experimental deformation of partially melted granite revisited: implications for the continental crust. Journal of Metamorphic Geology, v. 23, p. 19–28.

Rosenberg, C. L., and Riller, U., 2000. Partial-melt topology in statically and dynamically recrystallized granite: Geology, v. 28, p. 7–10.

Rousell, D.H. 1972. The Chelmsford Formation of the Sudbury Basin - a Precambrian turbidite. In: New Developments in Sudbury Geology, Geological Association of Canada, Special Paper Number 10, p.79-91.

Rousell, D. H., Fedorowich, J. S., and Dressler, B. O., 2003. Sudbury Breccia (Canada): A product of the 1850 Ma Sudbury event and host to footwall Cu-Ni-PGE deposits: Earth-Science Reviews, v. 60, p. 147–174.

Sawyer, E. W., 1994. Melt segregation in the continental crust. Geology 22, p. 1019-1022.

Sawyer, E. W., 2001. Melt segregation in the continental crust: distribution and movement of melt in anatectic rocks. Journal of Metamorphic Geology, v. 19, p. 291–309.

Sawyer, E. W., 2008. Atlas of Migmatites. The Canadian Mineralogist, Special Publication 9, NRC Research Press, Ottawa, ON, 371 pp.

Sawyer, E. W., 2014. The inception and growth of leucosomes: microstructure at the start of melt segregation in migmatites. Journal of Metamorphic Geology, v. 32, p. 695–712.

Schmidt, M. W., and Poli, S., 1998. Experimentally based water budgets for dehydrating slabs and consequences for arc magma generation, Earth and Planetary Science Letters, v. 163, p. 361-379.

Shanks, W.S., and Schwerdtner, W.M., 1991. Structural analysis of the central and southwestern Sudbury Structure, Southern Province, Canadian Shield, Canadian Journal of Earth Sciences, v. 28, p. 411-430.

Sims, P. K., Van Schmus, W. R., Schulz, K. J., and Peterman, Z. E., 1989. Tectonostratigraphic evolution of the Early Proterozoic Wisconsin magmatic terranes of the Penokean Orogen. Canadian Journal of Earth Sciences 26, p. 2145–2158.

Smith, M. D., 2002. The timing and petrogenesis of the Creighton pluton, Ontario: An example of felsic magmatism associated with Matachewan igneous events: Unpublished M.Sc. thesis, Edmonton, Alberta, University of Alberta, 123 p.

Spear, F., 1981. An experimental study of hornblende stability and compositional variability in amphibolite. American Journal of Science, v. 281(6), p. 697–734.

Spray, J.G., 1997. Superfaults: Geology, v. 25, p. 275-287.

Spray, J. G., Butler, H. R., Thompson, L. M., 2004. Tectonic influence on the morphometry of the Sudbury impact structure: Implications for terrestrial cratering and modeling. Meteoritics and Planetary Science 39 (2), p. 287-301.

Stern, R. J., 2002. Subduction Zones. Reviews of Geophysics, v. 40, p. (3)1-(3)38.

Szentpéteri, K., 2009. Geology and mineralization of the proximal Worthington offset area in the Sudbury Igneous Complex, Canada. Unpublished PhD thesis. Eötvös Loránd University, Hungary, 145 p.

Thomson, M. L., Bernett, R.L., Fleet, M.E. and Kerrich, R., 1985. Metamorphic assemblages in the South Range norite and footwall mafic rocks near the Kirkwood mine, Sudbury, Ontario. Canadian Mineralogist 23, 173–186.

Thomson, R., 1935. Sudburite, a metamorphic rock near Sudbury, Ontario. Journal of Geology, 43, 427-435.

Tracy, R. J., and Frost, B. R. 1991. Phase equilibria and thermobarometry of calcareous, ultramafic and mafic rocks, and iron formations. In Kerrick, D. (ed.), Contact Metamorphism. Review in Mineralogy 26, 43-104, Mineralogical Society of America, Washington, DC.

Van Schmus, W. R., Bickford, M. E. and Turek, A., 1996. Proterozoic geology of the eastcentral Midcontinent basement. In: van der Pluijm, B.E. and Catacosinos, P. A. (Eds.), Basement and Basins of Eastern North America. Boulder, Colorado, Geological Society of America Special Paper 308, pp. 7–32.

Vigneresse, J.-L., Barbey, P., and Cuney, M., 1996. Rheological transitions during partial melting and crystallization with application to felsic magma segregation and transfer. Journal of Petrology, v. 37, p. 1597–1600.

White, R. W., Powell, R., and Clarke, G. L., 2002. The interpretation of reaction textures in Fe-rich metapelitic granulites of the Musgrave Block, central Australia: Constraints from mineral equilibria calculations in the system K2O–FeO–MgO–Al2O3–SiO2–H2O–TiO2–Fe2O3. Journal of Metamorphic Geology, v. 20, p. 41–55.

White, R. W., Powell, R., and Holland, T. J. B., 2001. Calculation of partial melting equilibria in the system Na2O-CaO-K2O-FeO-MgO-Al2O3-SiO2-H2O (NCKFMASH). Journal of Metamorphic Geology, v. 19, p. 139-153.

White, R. W., Powell, R., and Holland, T. J. B., 2007. Progress relating to calculation of partial melting equilibria for metapelites. Journal of Metamorphic Geology, v. 25, p. 511–527.

White, R. W., Pomroy, N. E., and Powell, R., 2005. An in situ metatexite–diatexite transition in upper amphibolite facies rocks from Broken Hill, Australia. Journal of Metamorphic Geology, v. 23, p. 579 – 602.

Zenk, M., 2001. Mikrostrukturen, Mineralchemie und Geothermobarometrie der Metabasite in den Mineralzonen nach Barrow im schottischen Dalradian (Microstructures, mineral chemistry and geothermobarometry of metabasites from Barrow's mineral zones in the Dalradian of Scotland). Erlanger geologische Abhandlungen, 133, 1-199 (publication of thesis).

Zenk, M., Schulz, B., 2004. Zoned Ca-amphiboles and related P–T evolution in metabasites from the classical Barrovian metamorphic zones in Scotland. Mineralogical Magazine v. 68, p. 769–786.

FIGURES AND TABLES

Table 2.1. Overview of map units and metamorphic zones.

Map Units	Basaltic amphibolite	Basaltic granofels	Basaltic hornfels
Peak metamorphic mineral assemblage	High-Ti Hbl - Pl - Qtz - Ilm ± Bi ± Mt	Pl - Cpx - Opx - Ilm - Mt ± High-Ti Hbl ± Qtz ± Bi	Pl - Opx - Cpx - Ilm - Mt ± Melt
Map unit field characteristics	Dark grey to black colour; medium to coarse-grained; preservation of pillow textures and amygdules; rarely magnetic	Intermediate grey; medium to coarse-grained; preservation of pillow textures but not amygdules; magnetic	Intermediate grey; very fine to fine-grained; local leucocratic melt patches and networks; rare remnant pillow textures; magnetic
Map unit petrographic characteristics			
High-Ti hornblende	50 modal%; fine to coarse-grained, granoblastic polygonal (Fig. 2.5a)	2-25 modal%, but commonly > 10 modal%; medium to coarse-grained; an-subhedral, poikiloblastic grains (Fig. 2.5i, j); locally fine grained granoblastic polygonal; overgrows plagioclase, pyroxene, oxides, grunerite, and locally also biotite, majority interpreted to have formed on retrograde path; locally where these relationships are absent it potentially forms part of the peak assemblage (Fig. 2.6c-e); locally replaced by sadanagaite or very fine grained, pale green, fibrous, low-Ti hornblende related to mm-scale veins, which also replaces pyroxene and magnetite that are crosscut by these veins (Fig. 2.4g, i and 2.5b)	0-20 modal%; very fine to coarse-grained; commonly porphyroblastic, poikiloblastic, or granoblastic polygonal; overgrowing and replacing pyroxene (Fig. 2.5m)
Plagioclase	30-40 modal%; fine to medium-grained, granoblastic polygonal, decussate or equant; locally zoned with relatively Ca-rich cores and Ca-poor rims (Fig. 2.5e); rims interconnect to form a network around the cores; cores often have sub-rounded margins when a rim is present	35-40 modal%; very fine to medium-grained, granoblastic polygonal, decussate or equant; commonly arranged in clusters suspended in optically continuous quartz patches (Fig. 2.5c, d and 2.6 a, b); commonly zoned with relatively Ca-rich cores and Ca-poor rims (Fig. 2.5e); rims interconnect to form a network around the cores; cores often have sub-rounded margins when a rim is present	40-45 modal%; texturally similar to plagioclase in the Granofels unit (Fig. 2.5e, n)
Quartz	Trace to 50 modal%, but commonly 5-15%; very fine to coarse-grained; commonly occur as granoblastic polygonal clusters with a subrounded outline resembling amygdules or as anhedral inclusions within amphibole; locally form anhedral optically continuous patches with abundant plagioclase inclusions (Fig. 2.5c, d); locally, coarse quartz patches shows undulose extinction and/or incipient recrystallization	5-10 modal%; commonly coarse grained, anhedral, optically continuous grains with variable amounts of plagioclase inclusions (Fig. 2.5i, j and 2.6a, b); the higher modal abundance of quartz in this unit is a distinct from the Hornfels units; locally, quartz occurs as medium grained granoblastic polygonal grains	Rarely approaches 5 modal%; generally, the modal% becomes very low proximal to the SIC, to the point where it is rarely detected petrographically (Fig. 2.5n); very fine to medium-grained; occur as anhedral and optically continuous grains that commonly host a very high proportion of plagioclase or form part of the relative low-Ca plagioclase framework; both microtextures indicating partial melting (Fig. 2.5n)
Ilmenite	4-5 modal%; very fine to medium-grained; often occur as anhedral and subrounded grains (Fig. 2.5f); locally occur as eu- to anhedral elongated prismatic grains, very fine equant grains decorating margins of sadanagaite or as fine needles along cleavages in the high-Ti hornblende	Ilmenite and magnetite combined form around 5-10 modal%; often occur as very fine to medium, an-subhedral grains with a fairly homogenously distribution; exsolution of magnetite in an ilmenite host or vice versa are both common internal textures; grains with domains of ilmenite and magnetite, respectively, are also common; they are often overgrown by biotite, high-Ti hornblende, or more rarely titanite (Fig. 2.5i, j)	Ilmenite and magnetite are present in approximately equal proportions and combine for 5-10 modal%; very fine to medium-grained; commonly occur as equant, an- to subhedral grains; exsolution textures are common in both ilmenite and magnetite hosts; locally, ilmenite occurs as very fine grained, sub- to euhedral, slender prisms

Table 2.1. Overview of map units and metamorphic zones *(cont.)*.

Magnetite	0-1 modal%; occur as fine exsolution in the ilmenite; very rarely as isolated grains	See ilmenite	See ilmenite
Biotite	2 modal%, rarely up to 15 modal%; very fine to coarse-grained; typically occur as overgrowths or intergrowths with sadanagaite and ilmenite; less commonly occur as subhedral grains within quartz domains (Fig. 2.5g)	1-10 modal%; very fine to medium-grained; commonly occur as anhedral overgrowths on oxides or as highly poikiloblastic grains around plagioclase, oxides, and pyroxene; locally occur as sub- to euhedral grains in coarse anhedral quartz grains; rarely occur as very fine to fine grained granoblastic polygonal clusters in quartz	Commonly trace and rarely up to 5 modal%; fine grained; commonly occur as overgrowths on oxides and pyroxene (Fig. 2.5m); rarely, medium grained, subhedral and poikiloblastic, overgrowing oxides and pyroxene
Clino- and orthopyroxene	Not present	Combined 25 modal%; the pyroxenes are texturally very similar and individual modal estimates are very difficult to determine by transmitted light microscopy; fine to coarse grained; occur as anhedral and highly poikiloblastic grains with inclusions of mainly plagioclase and oxides; also occur as subhedral porphyroblastic grains with fewer inclusions; latter texture is typical for pyroxene hosted in optically continuous quartz patches, and they commonly show sub-rounded edges (Fig. 2.5i, j); clinopyroxene commonly exhibit Ca-poor exsolution lamellae of around 1 µm width parallel to the (001) and display simple twinning; orthopyroxene rarely exhibit extremely fine and closely spaced sub-µm twin lamellae approximately parallel to (100)	Combined 40 modal%; dominantly very fine to fine grained; occur as granoblastic polygonal (Fig. 2.5k); locally, similar textures as observed in the Granofels unit; clinopyroxene commonly exhibit Ca-poor exsolution lamellae of around 1 µm width parallel to the (001) and display simple twinning
Downgrade or retrograde phases			
Sadanagaite (related to Penokean regional metamorphism)	Commonly minor to complete downgrade of high-Ti hornblende (Fig. 2.5b)	Commonly minor to partial downgrade of high-Ti hornblende and pyroxene; locally complete downgrade	Commonly minor to partial downgrade of high-Ti hornblende and pyroxene; locally complete downgrade
Grunerite (retrograde SIC contact metamorphism)	Not observed	Locally occur as micron scale haloes defining the contact between orthopyroxene and overgrowing high-Ti hornblende; rarely occur as fine to medium, subhedral, near colourless grains	Rarely occur as micron scale haloes around orthopyroxene
Vein related low-Ti hornblende (retrograde SIC contact metamorphism)		Very fine grained; fibrous; locally replaces both pyroxenes and high-Ti hornblende (Fig. 2.4g, l)	Very fine grained; fibrous; locally replaces both pyroxenes and high-Ti hornblende

Metamorphic zone	Hornblende-hornfels (HHZ)	Pyroxene-granofels (PGZ)	Pyroxene-hornfels (PHZ)
Zone width	The HHZ extends to a distance of at least ca. 1 km (Map Area 2; station FSTJ545; Fig. 2.3); the original width of the HHZ might be greater than observed due to downgrading during Penokean regional metamorphism	In Map Area 1 the PGZ is up to 350 m wide and occurs at distances up to 750 m from the SIC contact; in Map Area 2 the PGZ is observed to a distance of up to 650 m and has a width of up to 200 m	The PHZ forms the inner contact metamorphic zone and extends from the base of the SIC to a maximum width of 500 m
Zone boundaries	The PGZ-HHZ boundary is defined by the pyroxene isograd and the low-T boundary is defined by the appearrance of high-Ti hornblende	The inner contact of the PGZ is transitional toward the PHZ and best described by an increase in grain size, high-Ti hornblende, quartz and biotite in the PGZ; the outer contact is defined by the first appearence of pyroxenes	The inner contact of the PHZ is toward the SIC; the outer contact is transitional and best described by a decrease in grain size, high-Ti hornblende, quartz and biotite in the PHZ

Table 2.2. Representative compositions of pyroxene in wt.% and atoms per formula unit.

Sample #		**FSTJ098**	**FSTJ098**	**FSTJ301**	**FSTJ301**	**FSTJ299**	**FSTJ299**	**FSTJ298**	**FSTJ298**	**FSTJ294**	**FSTJ294**	**FSTJ118**	**FSTJ118**	**FSTJ292**	**FSTJ292**
Rock Type		BH	BH	BH	BH	BH	BH	BH	BH	BH	BH	BH	BH	BH	BH
Pyroxene Species	L.O.D.*	Opx	Cpx	Opx	Cpx	Opx	Cpx	Opx	Cpx	Opx	Cpx	Opx	Cpx	Opx	Cpx
SiO_2	0.036	51.70	52.41	50.36	51.61	49.61	50.91	49.82	50.93	50.13	50.94	49.96	51.19	50.72	51.55
TiO_2	0.031	0.21	0.26	0.18	0.23	0.17	0.21	0.15	0.19	0.17	0.20	0.14	0.23	0.12	0.14
Al_2O_3	0.029	0.67	1.09	0.55	1.10	0.50	1.01	0.40	0.94	0.46	0.87	0.49	1.06	0.35	0.68
Cr_2O_3	0.029	0.03	0.05	L.O.D.	L.O.D.	L.O.D.	L.O.D.	L.O.D.	L.O.D.	L.O.D.	L.O.D.	L.O.D.	L.O.D.	L.O.D.	L.O.D.
FeOt	0.026	26.48	11.30	32.46	14.92	36.44	18.90	36.25	19.46	36.31	18.57	34.08	15.24	34.70	16.68
MnO	0.022	0.52	0.27	0.66	0.35	1.01	0.52	0.93	0.52	0.83	0.44	0.89	0.41	1.01	0.54
MgO	0.031	19.29	13.61	14.76	11.54	11.66	9.72	11.61	9.64	11.70	9.69	13.57	10.93	12.71	9.92
CaO	0.024	1.12	21.25	1.23	20.41	1.44	19.18	1.17	18.73	1.29	18.87	1.03	20.74	1.42	20.07
Na_2O	0.024	L.O.D.	0.17	L.O.D.	0.17	L.O.D.	0.15	L.O.D.	0.15	L.O.D.	0.16	L.O.D.	0.19	L.O.D.	0.26
K_2O	0.017	L.O.D.	L.O.D.	L.O.D.	L.O.D.	L.O.D.	L.O.D.	L.O.D.	L.O.D.	L.O.D.	L.O.D.	L.O.D.	L.O.D.	L.O.D.	L.O.D.
TOTAL		100.03	100.41	100.20	100.33	100.83	100.59	100.33	100.57	100.89	99.74	100.16	99.99	101.02	99.85
T (Ideally 2 a.p.f.u.)															
Si		1.97	1.96	1.97	1.96	1.97	1.96	1.99	1.97	1.99	1.98	1.97	1.96	2.00	1.99
Al		0.03	0.04	0.03	0.04	0.02	0.04	0.01	0.03	0.01	0.02	0.02	0.04	0.00	0.01
Fe^{3+}		0.00	0.00	0.00	0.00	0.00	0.00	0.00	0.00	0.00	0.00	0.00	0.00	0.00	0.00
T subtotal		2.00	2.00	2.00	2.00	2.00	2.00	2.00	2.00	2.00	2.00	2.00	2.00	2.00	2.00
M1+M2 (Ideally 2 a.p.f.u.)															
$Ti^{(M1)}$		0.01	0.01	0.01	0.01	0.00	0.01	0.00	0.01	0.01	0.01	0.00	0.01	0.00	0.00
$Al^{(M1)}$		0.00	0.01	0.00	0.01	0.00	0.01	0.01	0.01	0.01	0.02	0.00	0.00	0.01	0.02
$Cr^{(M1)}$		0.00	0.00												
$Fe^{3+\ (M1)}$		0.02	0.03	0.02	0.03	0.02	0.03	0.00	0.03	0.00	0.00	0.02	0.04	0.00	0.00
$Mg^{(M1+M2)}$		1.09	0.76	0.86	0.65	0.69	0.56	0.69	0.55	0.69	0.56	0.80	0.62	0.75	0.57
$Fe^{2+\ (M1+M2)}$		0.82	0.32	1.04	0.45	1.19	0.58	1.21	0.60	1.21	0.60	1.10	0.45	1.14	0.54
$Mn^{(M2)}$		0.02	0.01	0.02	0.01	0.03	0.02	0.03	0.02	0.03	0.01	0.03	0.01	0.03	0.02
$Ca^{(M2)}$		0.05	0.85	0.05	0.83	0.06	0.79	0.05	0.77	0.06	0.79	0.04	0.85	0.06	0.83
$Na^{(M2)}$			0.01		0.01		0.01		0.01		0.01		0.01		0.02
$K^{(M2)}$															
M1+M2 subtotal		2.00	2.00	2.00	2.00	2.00	2.00	2.00	2.00	2.00	2.00	2.00	2.00	2.00	2.00
SUM T,M1,M2		4.00	4.00	4.00	4.00	4.00	4.00	4.00	4.00	4.00	4.00	4.00	4.00	4.00	4.00
End-members															
Wo%		2.3	43.4	2.6	42.4	3.1	40.4	2.6	39.6	2.8	40.3	2.2	43.4	3.1	42.8
En%		55.3	38.6	43.7	33.4	35.3	28.5	35.4	28.3	35.4	28.8	40.7	31.8	38.3	29.4
Fs%		42.4	18.0	53.7	24.2	61.6	31.1	62.0	32.1	61.7	30.9	57.1	24.9	58.6	27.8

*L.O.D. = Limit of detection is defined as 3 x standard deviation of the total accumulated background counts; BG = basaltic granofels; BH = basaltic hornfels

Table 2.2. Representative compositions of pyroxene *(cont.)* .

Sample #	FSTJ069	FSTJ069	FSTJ308	FSTJ308	FSTJ307	FSTJ307
Rock Type	BG	BG	BH	BH	BH	BH
Pyroxene Species	Opx	Cpx	Opx	Cpx	Opx	Cpx
SiO_2	50.09	51.30	49.57	50.83	49.07	50.22
TiO_2	0.06	0.14	0.12	0.20	0.11	0.19
Al_2O_3	0.50	0.78	0.40	0.98	0.39	0.90
Cr_2O_3	L.O.D.	L.O.D.	L.O.D.	L.O.D.	L.O.D.	L.O.D.
FeOt	34.35	15.60	36.59	18.60	38.04	17.97
MnO	0.77	0.36	0.94	0.48	1.05	0.45
MgO	13.48	10.78	11.25	9.12	10.07	9.06
CaO	1.30	20.89	1.34	19.41	1.31	19.70
Na_2O	L.O.D.	0.06	L.O.D.	0.15	L.O.D.	0.18
K_2O	L.O.D.	L.O.D.	L.O.D.	L.O.D.	L.O.D.	L.O.D.
TOTAL	100.55	99.88	100.19	99.76	100.03	98.67
T (Ideally 2 a.p.f.u.)						
Si	1.97	1.97	1.99	1.98	1.99	1.97
Al	0.02	0.03	0.01	0.02	0.01	0.03
Fe^{3+}	0.00	0.00	0.00	0.00	0.00	0.00
T subtotal	2.00	2.00	2.00	2.00	2.00	2.00
M1+M2 (Ideally 2 a.p.f.u.)						
$Ti^{(M1)}$	0.00	0.00	0.00	0.01	0.00	0.01
$Al^{(M1)}$	0.00	0.00	0.01	0.02	0.01	0.01
$Cr^{(M1)}$						
$Fe^{3+\,(M1)}$	0.02	0.02	0.00	0.00	0.00	0.01
$Mg^{(M1+M2)}$	0.79	0.62	0.67	0.53	0.61	0.53
$Fe^{2+\,(M1+M2)}$	1.10	0.48	1.23	0.61	1.29	0.58
$Mn^{(M2)}$	0.03	0.01	0.03	0.02	0.04	0.01
$Ca^{(M2)}$	0.05	0.86	0.06	0.81	0.06	0.83
$Na^{(M2)}$		0.00		0.01		0.01
$K^{(M2)}$						
M1+M2 subtotal	2.00	2.00	2.00	2.00	2.00	2.00
SUM T,M1,M2	4.00	4.00	4.00	4.00	4.00	4.00
End-members						
Wo%	2.8	43.5	2.9	41.6	2.9	42.5
En%	40.1	31.2	34.4	27.2	31.1	27.2
Fs%	57.1	25.3	62.7	31.1	66.0	30.3

*L.O.D. = Limit of detection is defined as 3 x standard deviation of the total accumulated background counts; BG = basaltic granofels; BH = basaltic hornfels

Table 2.3. Representative compositions of amphiboles in wt.% and atoms per formula unit.

Sample #		**FSTJ098**	**FSTJ299**	**FSTJ299**	**FSTJ294**	**FSTJ118**	**FSTJ118**	**FSTJ118**	**FSTJ292**
Rock Type		BH	BH	BH	BH	BH	BH	BH	BH
Amphibole Species	L.O.D.*	Act	FF-Hbl	FF-Hbl	FF-Hbl	MF-Hbl	MF-Hbl	Gru	FF-Hbl
SiO_2	0.036	52.15	46.04	47.21	45.87	46.04	49.30	51.92	46.67
TiO_2	0.031	0.47	0.92	0.19	1.39	1.01	0.13	0.07	1.41
Al_2O_3	0.029	4.23	7.35	5.67	7.31	7.82	5.00	1.29	6.82
Cr_2O_3	0.029	L.O.D.	L.O.D.	L.O.D.	L.O.D.	L.O.D.	L.O.D.	L.O.D.	L.O.D.
FeO_{total}	0.026	12.41	23.32	28.03	23.30	20.38	25.22	28.32	22.28
MnO	0.022	0.17	0.31	0.38	0.34	0.24	0.55	0.77	0.35
MgO	0.031	16.25	8.29	5.68	8.03	10.03	10.70	12.24	9.23
CaO	0.024	11.44	10.60	10.17	10.23	10.92	6.96	3.42	10.38
Na_2O	0.024	0.39	1.06	0.63	0.98	0.87	0.32	L.O.D.	1.20
K_2O	0.017	0.26	0.51	0.14	0.58	0.65	0.22	0.06	0.42
F	0.112	L.O.D.	L.O.D.	L.O.D.	L.O.D.	L.O.D.	L.O.D.	L.O.D.	L.O.D.
Cl	0.014	L.O.D.	L.O.D.	0.43	L.O.D.	L.O.D.	0.28	0.09	0.02
O=F,Cl (calc.)		0.00	0.00	-0.10	0.00	0.00	-0.06	-0.02	0.00
INITIAL TOTAL		97.80	98.39	98.44	98.01	97.97	98.62	98.16	98.77
Final wt% values									
FeO		10.56	18.84	24.81	20.04	15.84	22.47	27.30	18.16
Fe_2O_3		2.06	4.98	3.58	3.63	5.05	3.06	1.13	4.58
H_2O+		2.09	1.98	1.83	1.98	2.00	1.92	1.97	1.98
TOTAL		100.09	100.87	100.63	100.36	100.48	100.85	100.25	101.21
T (ideally 8 a.p.f.u.)									
Si		7.46	6.91	7.24	6.94	6.85	7.35	7.81	6.95
Al		0.54	1.09	0.76	1.07	1.15	0.65	0.19	1.05
Ti		0.00	0.00	0.00	0.00	0.00	0.00	0.00	0.00
Fe^{3+}		0.00	0.00	0.00	0.00	0.00	0.00	0.00	0.00
T subtotal		8.00	8.00	8.00	8.00	8.00	8.00	8.00	8.00
C (ideally 5 a.p.f.u.)									
Ti		0.05	0.10	0.02	0.16	0.11	0.01	0.01	0.16
Al		0.17	0.22	0.27	0.24	0.23	0.23	0.04	0.15
Cr									
Fe^{3+}		0.22	0.56	0.42	0.41	0.57	0.34	0.13	0.51
Mn^{2+}		0.00	0.00	0.00	0.00	0.00	0.00	0.00	0.00
Fe^{2+}		1.09	2.26	2.99	2.38	1.87	2.03	2.08	2.13
Mg		3.46	1.86	1.30	1.81	2.23	2.38	2.74	2.05
C subtotal		5.00	5.00	5.00	5.00	5.00	5.00	5.00	5.00
B (ideally 2 a.p.f.u.)									
Mn^{2+}		0.02	0.04	0.05	0.04	0.03	0.07	0.10	0.04
Fe^{2+}		0.17	0.10	0.19	0.15	0.10	0.77	1.35	0.13
Mg		0.00	0.00	0.00	0.00	0.00	0.00	0.00	0.00
Ca		1.75	1.71	1.67	1.66	1.74	1.11	0.55	1.66
Na		0.05	0.15	0.09	0.15	0.13	0.05		0.17
B subtotal		2.00	2.00	2.00	2.00	2.00	2.00	2.00	2.00
A (from 0 to 1 a.p.f.u.)									
Ca		0.00	0.00	0.00	0.00	0.00	0.00	0.00	0.00
Na		0.05	0.16	0.09	0.14	0.13	0.05		0.17
K		0.05	0.10	0.03	0.11	0.12	0.04	0.01	0.08
A subtotal		0.10	0.25	0.12	0.25	0.25	0.09	0.01	0.25
O (non-W)		22.00	22.00	22.00	22.00	22.00	22.00	22.00	22.00
W (ideally 2 a.p.f.u.)									
OH		2.00	2.00	1.89	2.00	2.00	1.93	1.98	2.00
F									
Cl				0.11			0.07	0.02	0.01
O									
W subtotal		2.00	2.00	2.00	2.00	2.00	2.00	2.00	2.00
SUM T,C,B,A		15.10	15.25	15.12	15.25	15.25	15.09	15.01	15.25
^{C}(Al+Fe^{3+}+2Ti) (a.p.f.u.)		0.49	0.99	0.73	0.97	1.02	0.60	0.18	0.98
^{A}(Na+K+2Ca) (a.p.f.u.)		0.10	0.25	0.12	0.25	0.25	0.09	0.01	0.25
^{A}Si		7.46	6.91	7.24	6.94	6.85	7.35	7.81	6.95
^{C}Mg/(Mg+Fe^{2+})		0.76	0.45	0.30	0.43	0.54	0.54	0.57	0.49

Amphibole analyses recalculated and classified following the scheme of Hawthorne *et al.* (2012).

Act (actinolite); Hbl (hornblende); Gru (grunerite); F-Sad (Ferro-sadanagaite); FF (Ferro-ferri), MF (Magnisio-ferri).

*L.O.D. = Limit of detection is defined as 3 x standard deviation of the total accumulated bacground counts.

Table 2.3. Representative compositions of amphiboles in wt.% and atoms per formula unit *(cont.)* .

Sample #	**FSTJ069**	**FSTJ069**	**FSTJ308**	**FSTJ307**	**FSTJ307**	**FSTJ326**	**FSTJ326**
Rock Type	BG	BG	BH	BH	BH	BA	BA
Amphibole Species	FF-Hbl	Gru	FF-Hbl	FF-Hbl	Gru	F-Sad	Act
SiO_2	45.65	53.04	45.00	46.03	52.32	38.34	52.15
TiO_2	1.23	0.03	1.48	0.82	0.07	0.38	0.09
Al_2O_3	7.76	0.05	7.98	8.20	0.25	17.88	2.34
Cr_2O_3	L.O.D.	L.O.D.	L.O.D.	L.O.D.	L.O.D.	L.O.D.	L.O.D.
FeO_{total}	21.09	28.84	23.56	23.23	32.98	23.90	20.28
MnO	0.23	0.62	0.29	0.28	0.85	0.25	0.36
MgO	9.21	13.89	7.76	7.63	10.83	3.66	11.18
CaO	10.83	0.88	10.43	10.75	0.84	11.24	11.36
Na_2O	0.73	L.O.D.	1.11	0.97	L.O.D.	1.63	0.35
K_2O	0.67	L.O.D.	0.66	0.55	L.O.D.	0.80	0.02
F	L.O.D.	L.O.D.	L.O.D.	L.O.D.	L.O.D.	L.O.D.	L.O.D.
Cl	0.02	L.O.D.	L.O.D.	L.O.D.	L.O.D.	0.11	0.02
O=F,Cl (calc.)	-0.01	0.00	0.00	0.00	0.00	-0.03	0.00
INITIAL TOTAL	97.42	97.36	98.26	98.45	98.14	98.14	98.14
Final wt% values							
FeO	17.42	28.84	19.51	19.86	32.98	20.27	19.09
Fe_2O_3	4.08	0.00	4.50	3.74	0.00	4.04	1.33
H_2O+	1.99	2.00	1.97	1.98	1.96	1.92	2.02
TOTAL	99.82	99.36	100.68	100.81	100.10	100.47	100.29
T (ideally 8 a.p.f.u.)							
Si	6.88	8.00	6.80	6.92	7.99	5.87	7.71
Al	1.13	0.00	1.20	1.08	0.01	2.13	0.29
Ti	0.00	0.00	0.00	0.00	0.00	0.00	0.00
Fe^{3+}	0.00	0.00	0.00	0.00	0.00	0.00	0.00
T subtotal	8.00	8.00	8.00	8.00	8.00	8.00	8.00
C (ideally 5 a.p.f.u.)							
Ti	0.14	0.00	0.17	0.09	0.01	0.04	0.01
Al	0.25	0.01	0.22	0.37	0.04	1.10	0.12
Cr							
Fe^{3+}	0.46	0.00	0.51	0.42	0.00	0.47	0.15
Mn^{2+}	0.00	0.00	0.00	0.00	0.00	0.00	0.00
Fe^{2+}	2.08	1.87	2.35	2.41	2.49	2.56	2.26
Mg	2.07	3.12	1.75	1.71	2.47	0.84	2.47
C subtotal	5.00	5.00	5.00	5.00	5.00	5.00	5.00
B (ideally 2 a.p.f.u.)							
Mn^{2+}	0.03	0.08	0.04	0.04	0.11	0.03	0.05
Fe^{2+}	0.12	1.77	0.11	0.09	1.73	0.04	0.10
Mg	0.00	0.00	0.00	0.00	0.00	0.00	0.00
Ca	1.75	0.14	1.69	1.73	0.14	1.84	1.80
Na	0.11		0.16	0.14		0.08	0.05
B subtotal	2.00	1.99	2.00	2.00	1.98	2.00	2.00
A (from 0 to 1 a.p.f.u.)							
Ca	0.00	0.00	0.00	0.00	0.00	0.00	0.00
Na	0.11		0.17	0.14		0.40	0.05
K	0.13		0.13	0.11		0.16	0.00
A subtotal	0.24	0.00	0.29	0.25	0.00	0.56	0.05
O (non-W)	22.00	22.00	22.00	22.00	22.00	22.00	22.00
W (ideally 2 a.p.f.u.)							
OH	1.99	2.00	2.00	2.00	2.00	1.97	2.00
F							
Cl	0.01					0.03	0.00
O							
W subtotal	2.00	2.00	2.00	2.00	2.00	2.00	2.00
SUM T,C,B,A	15.24	15.00	15.29	15.25	14.98	15.56	15.05
^{C}(Al+Fe^{3+}+2Ti) (a.p.f.u.)	0.99	0.02	1.07	0.98	0.06	1.65	0.29
^{A}(Na+K+2Ca) (a.p.f.u.)	0.24	0.00	0.29	0.25	0.00	0.56	0.05
^{A}Si	6.88	8.00	6.80	6.92	7.99	5.87	7.71
^{C}Mg/(Mg+Fe^{2+})	0.50	0.63	0.43	0.42	0.50	0.25	0.52

Amphibole analyses recalculated and classified following the scheme of Hawthorne *et al.* (2012).

Act (actinolite); Hbl (hornblende); Gru (grunerite); F-Sad (Ferro-sadanagaite); FF (Ferro-ferri), MF (Magnisio-ferri).

*L.O.D. = Limit of detection is defined as 3 x standard deviation of the total accumulated bacground counts.

Table 2.4. Representative feldspar analyses in wt.% and atoms per formula unit.

Sample #		**FSTJ098**	**FSTJ098**	**FSTJ301**	**FSTJ301**	**FSTJ299**	**FSTJ299**	**FSTJ298**	**FSTJ294**	**FSTJ294**	**FSTJ294**
Rock Type		BH	BH	BH	BH	BH	BH	BH	BH	BH	BH
Feldspar species	L.O.D.*	anorthite	bytownite	bytownite	andesine	labradorite	andesine	andesine	andesine	andesine	K-felspar
SiO_2	0.036	45.54	48.64	49.84	55.26	53.41	57.86	56.90	56.94	59.06	64.71
TiO_2	0.022	L.O.D.	0.04	L.O.D.	L.O.D.	L.O.D.	L.O.D.	L.O.D.	L.O.D.	L.O.D.	L.O.D.
Al_2O_3	0.030	34.77	32.76	31.87	27.90	29.59	26.67	27.20	27.29	25.51	18.59
MgO	0.021	L.O.D.	L.O.D.	L.O.D.	L.O.D.	L.O.D.	L.O.D.	L.O.D.	L.O.D.	L.O.D.	L.O.D.
CaO	0.025	18.34	15.84	14.76	10.46	12.31	8.59	9.21	9.25	7.21	0.28
MnO	0.019	L.O.D.	L.O.D.	L.O.D.	L.O.D.	L.O.D.	L.O.D.	L.O.D.	L.O.D.	L.O.D.	L.O.D.
FeO_{total}	0.024	0.39	0.41	0.17	0.34	0.42	0.21	0.20	0.18	0.10	0.17
SrO	0.100	L.O.D.	L.O.D.	L.O.D.	0.10	L.O.D.	L.O.D.	L.O.D.	L.O.D.	L.O.D.	L.O.D.
BaO	0.054	L.O.D.	L.O.D.	L.O.D.	L.O.D.	L.O.D.	L.O.D.	L.O.D.	L.O.D.	L.O.D.	0.67
Na_2O	0.013	1.06	2.49	3.11	5.82	4.71	6.86	6.44	6.39	7.54	1.19
K_2O	0.020	L.O.D.	0.02	0.04	0.10	0.06	0.14	0.07	0.10	0.16	14.58
TOTAL		100.09	100.21	99.80	99.98	100.50	100.34	100.03	100.16	99.58	100.18
Structural formula on the basis of 8 oxygens											
Si		2.10	2.23	2.28	2.50	2.41	2.59	2.55	2.55	2.65	2.99
Ti			0.00								
Al		1.89	1.77	1.72	1.49	1.58	1.41	1.44	1.44	1.35	1.01
Ca		0.91	0.78	0.72	0.51	0.60	0.41	0.44	0.44	0.35	0.01
Fe		0.01	0.01	0.00	0.01	0.01	0.00	0.00	0.00	0.00	0.00
Sr					0.00						
Ba											0.01
Na		0.09	0.22	0.28	0.51	0.41	0.59	0.56	0.56	0.66	0.11
K			0.00	0.00	0.01	0.00	0.01	0.00	0.01	0.01	0.86
SUM		5.00	5.00	5.00	5.02	5.00	5.01	5.00	5.00	5.01	4.99
End-members											
Or		0.0	0.1	0.2	0.6	0.4	0.8	0.4	0.6	0.9	87.7
Ab		9.4	22.1	27.6	49.9	40.8	58.6	55.6	55.2	64.9	10.9
An		90.6	77.7	72.2	49.5	58.9	40.6	44.0	44.2	34.3	1.4

*L.O.D. = Limit of detection is defined as 3 x standard deviation of the total accumulated background counts; BA = basaltic amphibolite; BG = basaltic granofels; BH = basaltic hornfels.

Table 2.4. Representative feldspar analyses in wt.% and atoms per formula unit *(cont.)*.

Sample #	**FSTJ118**	**FSTJ118**	**FSTJ292**	**FSTJ069**	**FSTJ308**	**FSTJ307**	**FSTJ307**	**FSTJ326**	**FSTJ326**
Rock Type	BH	BH	BH	BG	BH	BH	BH	BA	BA
Feldspar species	labradorite	labradorite	andesine	anorthite	labradorite	labradorite	andesine	labradorite	oligoclase
SiO_2	51.99	54.33	60.58	44.53	54.30	55.19	54.80	54.21	63.65
TiO_2	L.O.D.	L.O.D.	L.O.D.	L.O.D.	L.O.D.	L.O.D.	L.O.D.	L.O.D.	0.03
Al_2O_3	30.25	28.83	25.29	35.50	28.73	27.97	28.17	28.94	22.70
MgO	L.O.D.	L.O.D.	L.O.D.	L.O.D.	L.O.D.	L.O.D.	L.O.D.	L.O.D.	L.O.D.
CaO	13.19	11.61	6.62	19.09	11.56	10.42	11.07	11.21	3.87
MnO	L.O.D.	L.O.D.	L.O.D.	L.O.D.	L.O.D.	L.O.D.	L.O.D.	L.O.D.	L.O.D.
FeO_{total}	0.23	0.44	0.24	0.16	0.20	0.17	0.41	0.10	0.22
SrO	L.O.D.	L.O.D.	L.O.D.	L.O.D.	L.O.D.	0.12	0.12	L.O.D.	L.O.D.
BaO	L.O.D.	L.O.D.	L.O.D.	L.O.D.	L.O.D.	L.O.D.	L.O.D.	0.05	0.08
Na_2O	4.14	5.03	8.01	0.60	5.11	5.70	5.36	5.23	9.90
K_2O	0.11	0.15	0.10	0.02	0.12	0.06	0.13	L.O.D.	L.O.D.
TOTAL	99.92	100.38	100.83	99.91	100.01	99.62	100.07	99.74	100.45
Structural formula on the basis of 8 oxygens									
Si	2.37	2.45	2.68	2.06	2.49	2.50	2.59	2.45	2.81
Ti									0.00
Al	1.62	1.53	1.32	1.94	1.50	1.49	1.40	1.54	1.18
Ca	0.64	0.56	0.31	0.95	0.53	0.51	0.41	0.54	0.18
Fe	0.00	0.01	0.00	0.00	0.00	0.00	0.00	0.00	0.00
Sr						0.00	0.00		
Ba								0.00	0.00
Na	0.37	0.44	0.69	0.05	0.48	0.50	0.59	0.46	0.85
K	0.01	0.01	0.01	0.00	0.01	0.00	0.00		
SUM	5.01	5.00	5.01	5.00	5.00	5.01	5.00	5.00	5.02
End-members									
Or	0.6	0.8	0.5	0.1	0.8	0.3	0.2	0.0	0.0
Ab	36.0	43.6	68.3	5.4	47.2	49.5	58.9	45.7	82.2
An	63.4	55.6	31.2	94.5	52.0	50.1	40.9	54.3	17.8

*L.O.D. = Limit of detection is defined as 3 x standard deviation of the total accumulated background counts; BA = basaltic amphibolite; BG = basaltic granofels; BH = basaltic hornfels.

Table 2.5. Pyroxene compositions (wt.%) used in two-pyroxene thermometry and calculated temperatures.

Sample	FSTJ098		FSTJ301		FSTJ299		FSTJ298		FSTJ294	
Analysis	EMP098Q 1S3, -1, -2 (avg.; n=3)	EMP098Q 1S11, -1, -2 (avg.; n=3)	FSTJ301_site_1_opx_4 - 6 (avg.; n=3)	FSTJ301_site_1_cpx_1 - 2 (avg.; n=2)	FSTJ299_site_2_opx_4 - 6 (avg.; n=3)	FSTJ299_site_2_cpx_8 - 9 (avg.; n=2)	FSTJ298_site_1_opx_9 (n=1)	FSTJ298_site_1_cpx_3 - 4 (avg.; n=2)	FSTJ294_site_1_opx_20 - 21 (avg.; n=2)	FSTJ294_site_1_cpx_3 - 4 (avg.; n=2)
Pyroxene species	Opx	Cpx	Opx	Cpx	Opx	Cpx	Opx	Cpx	Opx	Cpx
SiO2	51.59	52.12	50.22	51.43	49.50	50.72	49.55	50.77	50.02	50.77
TiO2	0.20	0.30	0.14	0.24	0.15	0.21	0.16	0.20	0.17	0.19
Al2O3	0.69	1.26	0.54	1.06	0.48	1.05	0.48	0.90	0.44	0.92
Cr2O3	0.03	0.06	0.00	0.02	0.01	0.00	0.00	0.01	0.00	0.01
FeOt	26.52	11.42	32.51	14.77	36.44	19.14	36.43	18.83	36.30	18.73
MnO	0.51	0.26	0.67	0.35	1.02	0.52	0.91	0.52	0.82	0.45
MgO	19.31	13.49	14.78	11.57	11.68	9.59	11.70	9.60	11.63	9.67
CaO	1.03	21.23	1.07	20.43	1.43	18.91	1.19	19.08	1.31	18.74
Na2O	0.00	0.16	0.00	0.17	0.00	0.15	0.00	0.16	0.00	0.15
K2O	0.00	0.00	0.00	0.00	0.00	0.00	0.00	0.00	0.00	0.00
TOTAL	99.87	100.30	99.93	100.03	100.72	100.30	100.42	100.07	100.68	99.63
Distance (m) from SIC	98		112		155		193		257	
Traverse	1		1		1		1		1	
Notes	-		-		-		-		-	
Two-pyroxene-thermometry (T, °C)										
Brey and Köhler (1990)	795		754		759		751		760	
Putirka (2008)	887		862		848		850		864	
Andersen et al. (1993)	851 ±28		808 ±38		849 ±42		799 ±38		819 ±42	

Table 2.5. Pyroxene compositions (wt.%) used in two-pyroxene thermometry and calculated temperatures *(cont.)* .

Sample	FSTJ292		FSTJ308		FSTJ307		FSTJ118		FSTJ069		FSTJ294		FSTJ307	
Analysis	FSTJ292_site_1_opx_4 - 5 (avg.; n=2)	FSTJ292_site_1_cpx_10 - 11 (avg.; n=2)	FSTJ308_site_1_opx_2 (n=1)	FSTJ308_site_1_cpx_4 (n=1)	FSTJ307_site_1_opx_6 (n=1)	FSTJ307_site_1_cpx_2 (n=1)	EMP118 Q3S1 (n=1)	EMP118 Q3S11 (n=1)	069Q1_6 S11 (n=1)	069Q1_6 S1 (n=1)	FSTJ294_site_1_opx_24 - 25 (avg.; n=2)	FSTJ294_site_1_cpx_5 - 6 (avg.; n=2)	FSTJ307_site_1_opx_7 (n=1)	FSTJ307_site_1_cpx_3 (n=1)
Pyroxene species	Opx	Cpx	Opx	Cpx	Opx	Cpx	Opx	Cpx	Opx	Cpx	Opx	Cpx	Opx	Cpx
SiO2	50.66	51.42	49.57	50.83	49.07	50.22	49.91	51.27	50.09	51.30	49.75	51.51	49.61	51.17
TiO2	0.12	0.14	0.12	0.20	0.11	0.19	0.15	0.24	0.06	0.14	0.17	0.18	0.15	0.17
Al2O3	0.37	0.68	0.40	0.98	0.39	0.90	0.44	1.01	0.50	0.78	0.38	0.84	0.41	0.88
Cr2O3	0.00	0.00	0.00	0.01	0.00	0.01	0.00	0.00	0.01	0.00	0.00	0.00	0.01	0.01
FeOt	34.73	17.65	36.59	18.60	38.04	17.97	34.26	15.18	34.35	15.60	36.25	17.01	37.32	20.98
MnO	1.02	0.55	0.94	0.48	1.05	0.45	0.92	0.38	0.77	0.36	0.83	0.42	0.96	0.49
MgO	12.64	10.07	11.25	9.12	10.07	9.06	13.59	11.18	13.48	10.78	11.63	9.54	10.56	9.31
CaO	1.41	19.11	1.34	19.41	1.31	19.70	1.14	20.81	1.30	20.89	1.44	20.56	1.36	17.37
Na2O	0.00	0.23	0.00	0.15	0.00	0.18	0.00	0.21	0.00	0.06	0.00	0.17	0.00	0.13
K2O	0.00	0.00	0.00	0.00	0.00	0.00	0.00	0.00	0.00	0.00	0.00	0.00	0.00	0.00
TOTAL	100.94	99.86	100.19	99.77	100.03	98.69	100.40	100.27	100.56	99.89	100.43	100.25	100.38	100.49
Distance (m) from SIC	302		403		447		262		390		257		447	
Traverse	1		1		1						1		1	
Notes	-		-		-		-		-		Exsolution avoided		Exsolution favored	
Two-pyroxene-thermometry (T, °C)														
Brey and Köhler (1990)	766		736		700		717		718		703		779	
Putirka (2008)	842		834		809		829		837		833		867	
Andersen et al. (1993)	849 ±28		818 ±27		784 ±61		799 ±57		827 ±36		823 ±34		822 ±58	

Table 2.6. Whole-rock compositions used for phase diagram modelling and comparison.

Figure	Sample	mol. %	SiO_2	TiO_2	Al_2O_3	Fe_2O_3	FeO	MnO	MgO	CaO	Na_2O	K_2O	P_2O_5	H_2O
Fig. 9 & 10	478 (Beard and Lofgren, 1991)		56.79	1.42	9.75	0.96	8.75	0.20	8.53	10.68	2.68	0.11	0.13	+
Fig. 11, 12, 13 & 14	Avg. Amphibolite unit in HHZ and PGZ (n = 7)		53.80	1.43	9.04	1.29	11.72	0.22	8.53	11.48	1.90	0.50	0.10	+
Fig. 13	Avg. Hornfels unit in PHZ (n=16)		50.30	1.34	8.62	1.38	12.56	0.24	10.57	13.18	1.59	0.12	0.09	+
Fig. 13	FSTJ092C		47.72	1.93	8.18	1.56	14.25	0.26	9.51	15.32	1.10	0.07	0.09	+
Fig. 13	FSTJ091		48.4	1.29	8.99	1.45	13.3	0.26	10.6	14.6	1.02	0.07	0.09	+

Notes: NCFMASHTO - omits MnO, K_2O, and P_2O_5 ; NCKFMASHTO - omits MnO and P_2O_5. Input for Theriak Domino in cations on 100% oxide sum.

FIGURES AND TABLES

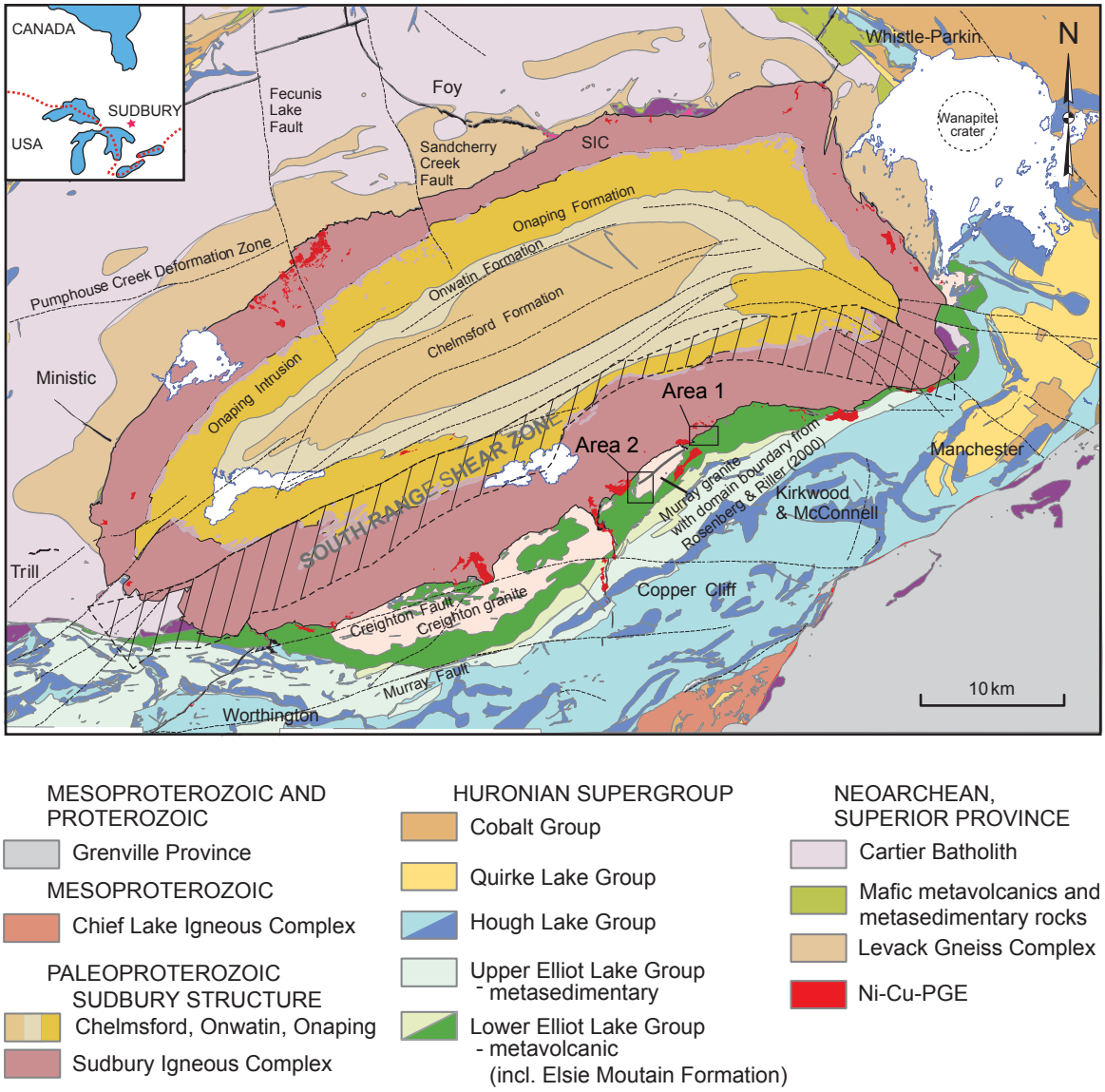

Fig. 2.1. Geology of the Sudbury area (after Ames et al., 2005).

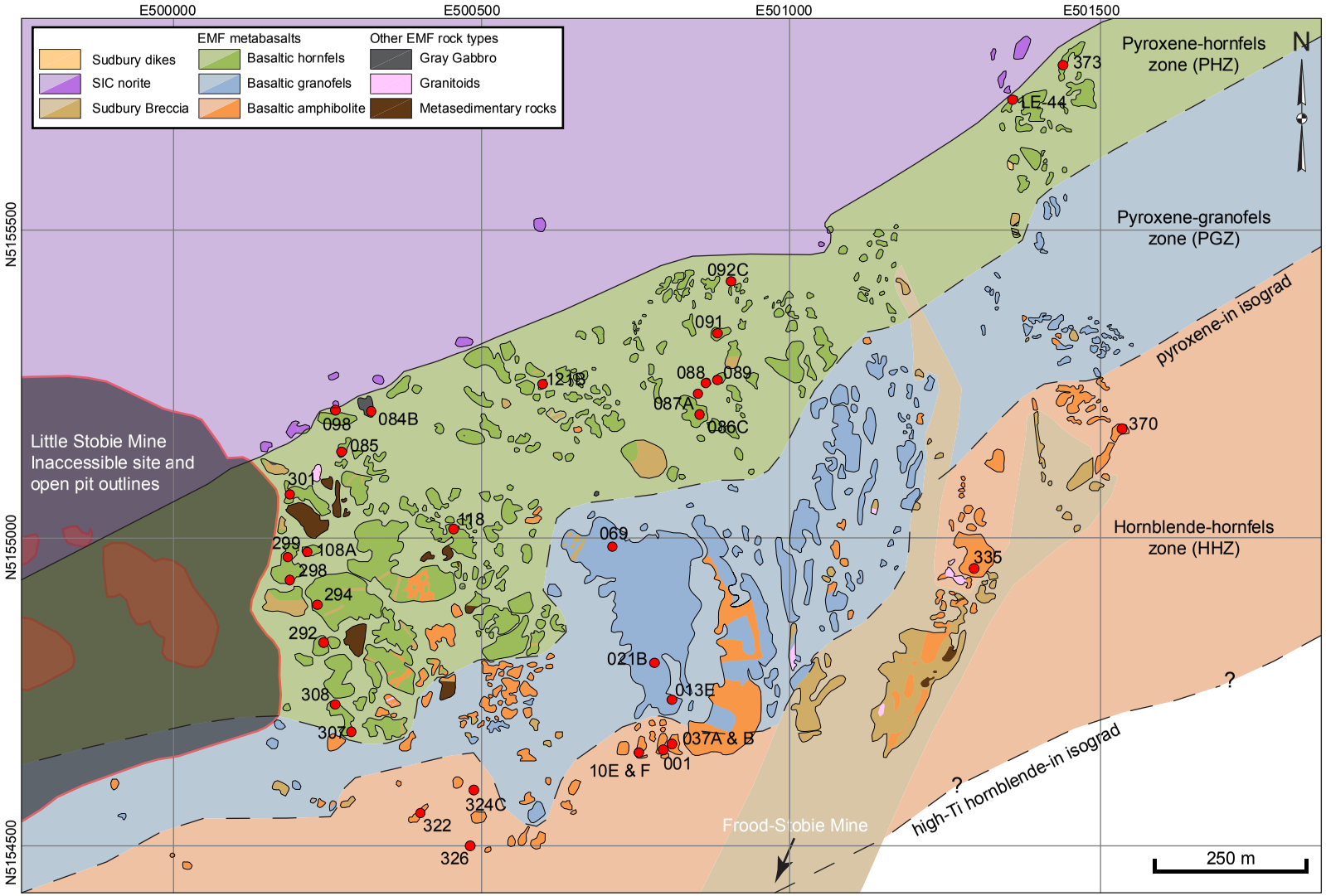

Fig. 2.2. Map area 1 showing the distribution of Elsie Mountain Formation metabasalt units and metamorphic zones. Locations for samples collected for mineral chemistry and whole rock geochemistry are indicated by a red circle.

Fig. 2.3. Map area 2 showing the distribution of Elsie Mountain Formation metabasalt units and metamorphic zones.

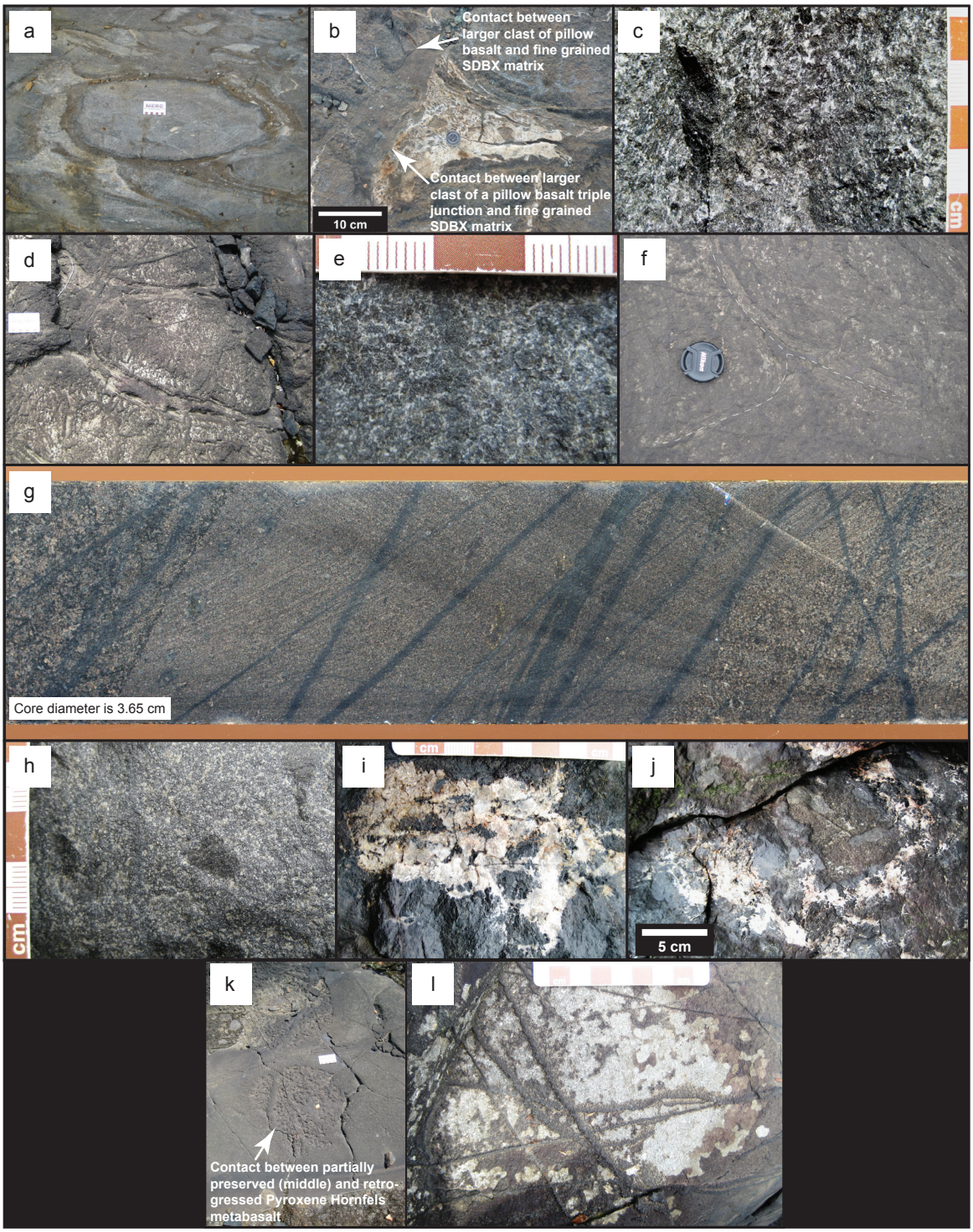

Fig. 2.4. a) Well-preserved pillow textures in EMF metabasalts belonging to the basaltic amphibolite unit in the HHZ. b) Pillow basalt triple junction as a clast in Sudbury Breccia hosted by EMF metabasalt belonging to the basaltic amphibolite unit in the HHZ. c) Basaltic amphibolite unit rock (from the HHZ) in hand sample showing its characteristic dark grey to black color and medium to coarse grain size (hornblende-plagioclase-quartz-ilmenite ± biotite ± magnetite assemblage). d) Fairly well-preserved pillow textures in a basaltic granofels unit rock in the PGZ. e) Basaltic granofels unit rock in hand sample showing its characteristic intermediate grey color and medium to coarse grain size (plagioclase-clinopyroxene-orthopyroxene-ilmenite-magnetite ± high-Ti

Fig. 2.4. (*cont.*) hornblende ± quartz ± biotite assemblage). f) Relict pillow textures in basaltic hornfels unit rock in the PHZ. Triple junction highlighted by white stippled line. g) Potential in-situ Sudbury Breccia hosted in a metabasalt of the basaltic hornfels unit showing a sharp contact and slight difference in grain size between the matrix (center) and clast/host (margins). Also, note the black veins that are cross cutting the Sudbury Breccia and overprinting the peak mineral assemblage. h) Basaltic hornfels unit rock in hand sample showing its characteristic intermediate grey color and very fine to fine grain size (plagioclase-orthopyroxene-clinopyroxene-ilmenite-magnetite assemblage). Note the amphibole (brownish green high-Ti hornblende) porphyroblasts that are not part of the prograde assemblage, but formed on the retrograde path. i) Leucocratic and very coarse grained patch consisting of dominantly plagioclase, quartz, hornblende and pyroxene. These patches are most commonly observed in the PHZ and interpreted to represent partial melt. j) Leucocratic patches coalescing to form dike or network like features interpreted to represent segregation of partial melts. k) Contact between partially preserved basaltic hornfels unit rock and retrograde basaltic amphibolite unit rock in the PHZ. l) Black mm-scale wide veins overprinting basaltic hornfels and basaltic granofels unit rocks and replacing the peak assemblage by mainly low-Ti hornblende.

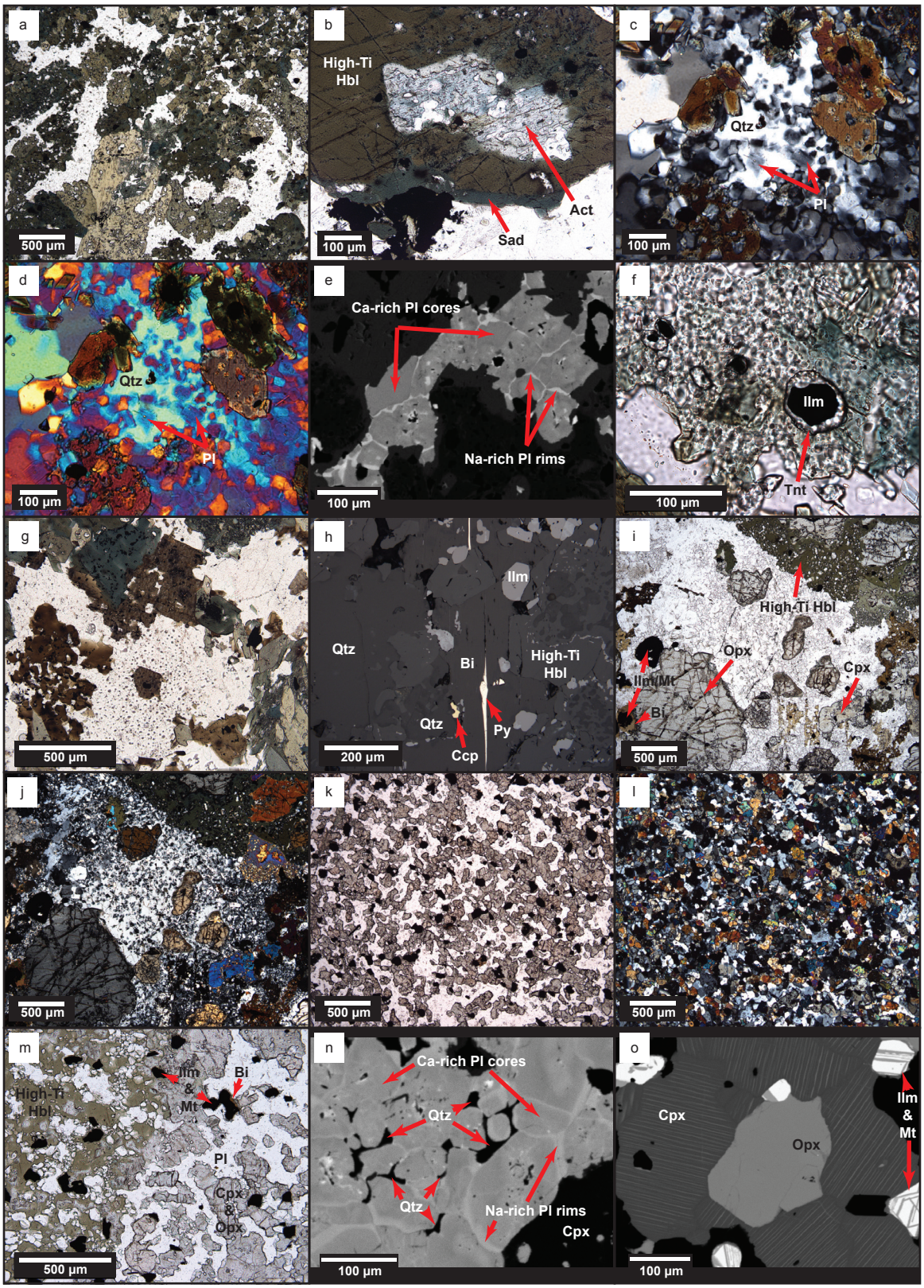

Fig. 2.5. a) High-Ti hornblende in a basaltic amphibolite unit rock from the HHZ. b) High-Ti hornblende replaced by both actinolite and sadanagaite. c, d) Plane polarized and cross polarized photomicrographs of plagioclase grains enclosed by optical continuous quartz. e) Element map of

Fig. 2.5. *(cont.)* Na revealing relatively Ca-rich plagioclase cores and interconnected relatively Ca-poor plagioclase rims. f) Subrounded ilmenite grain overgrown by titanite. g) Photomicrograph of biotite overgrowing sadanagaite and ilmenite, and locally hosted in quartz. h) Reflected light photomicrograph showing sulfide grains associated with biotite. i, j) Plane and cross polarized photomicrographs of a basaltic granofels unit rock showing co-existing clino- and orthopyroxene hosted in optical continuous quartz and locally overgrown by high-Ti hornblende. Plagioclase, ilmenite, magnetite, and biotite are also present. k, l) Plane and cross polarized photomicrographs of a basaltic hornfels unit rock illustrating the very fine to fine-grained granoblastic polygonal texture characteristic of the clinopyroxene, orthopyroxene, and plagioclase. m) Pyroxene overgrown by high-Ti hornblende and oxides overgrown by narrow rims of biotite in a basaltic hornfels unit rock. n) Element map of Na revealing relatively Ca-rich plagioclase cores and relatively interconnected Ca-poor plagioclase rims with quartz forming part of the network. o) Element map of Fe showing exsolution lamellae in clinopyroxene and absence of chemical zonation in clino- and orthopyroxene. The image also shows ilmenite exsolutions in magnetite.

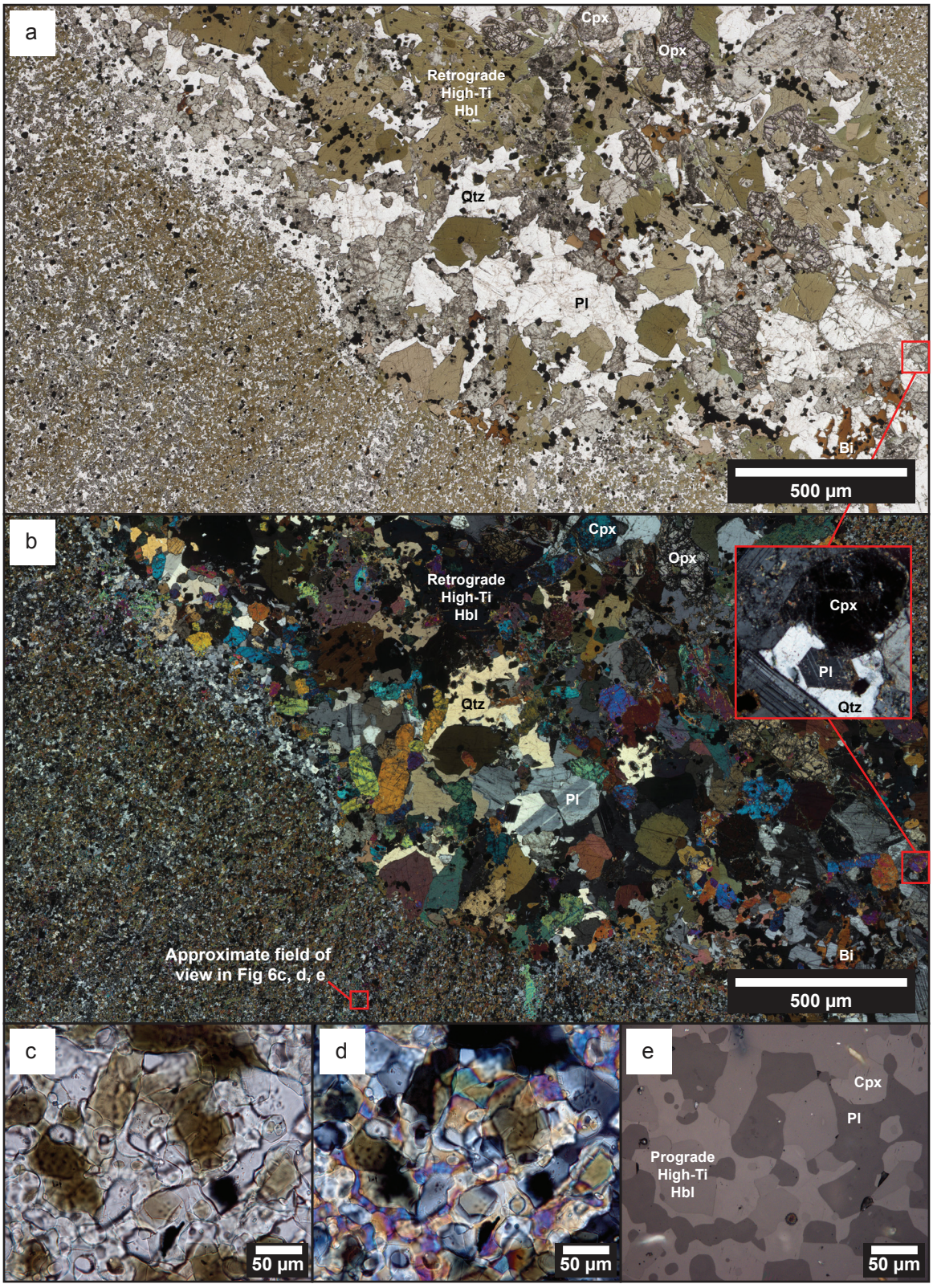

Fig. 2.6. a, b) Plane and cross polarized photomicrographs showing a coarse grained melt patch with high-Ti hornblende replacing pyroxene and also euhedral plagioclase growing in optical continous quartz. c-e) Plane and cross polarized and reflected light photomicrographs showing fine grained host rock with prograde high-Ti hornblende being replaced by pyroxene.

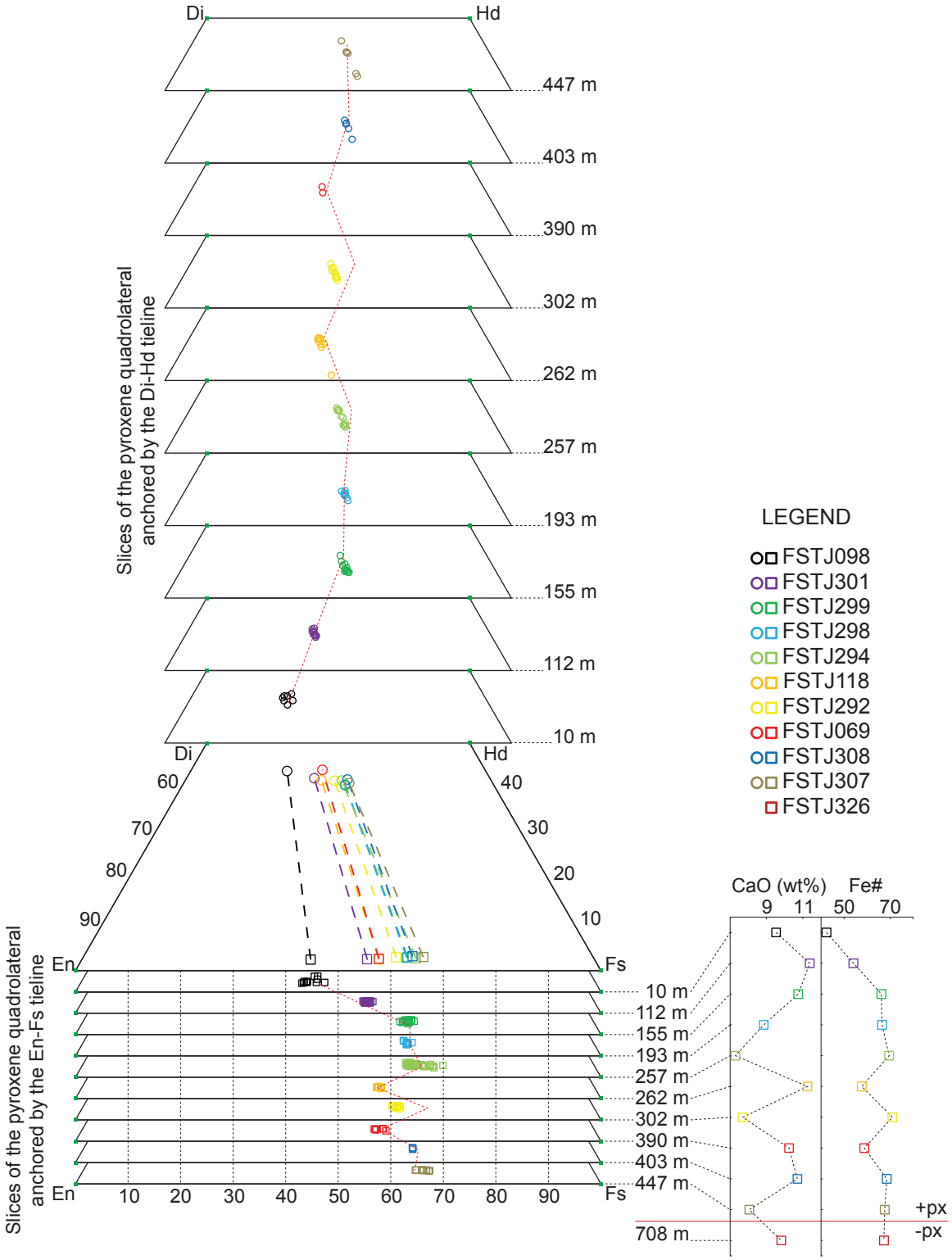

Fig. 2.7. Pyroxene analyses plotted in the diopside-hedenbergite-enstatite-ferrosilite (Di-Hd-En-Fs) quadrilateral. Average compositions are plotted in the main part and all analyses are plotted in individual dissections for each sample indicating the distance from the SIC contact (m). Bulk rock CaO (wt.%) and Fe# is shown on the lower right of the figure to illustrate the correlation between mineral chemistry and bulk rock composition.

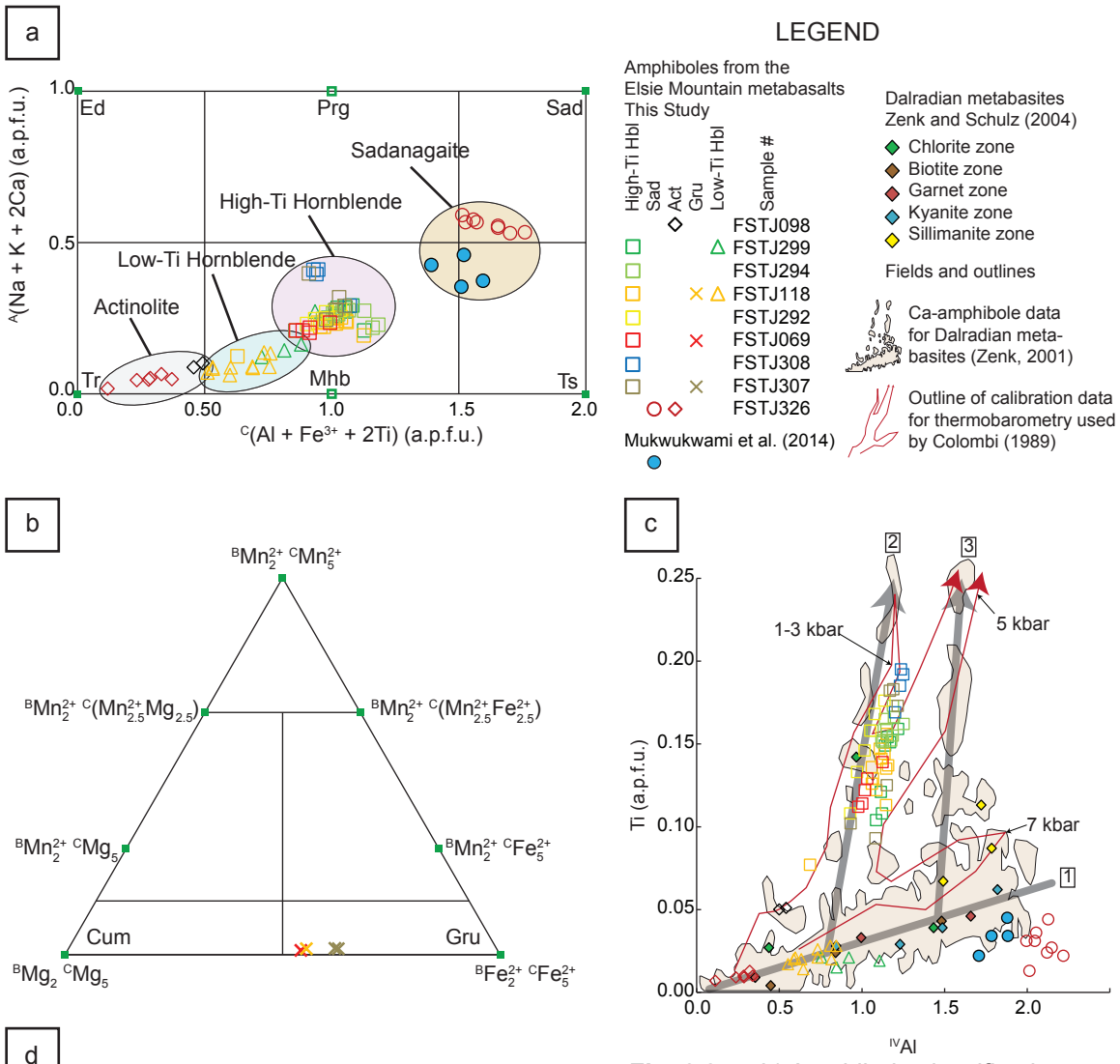

Fig. 2.8. a, b) Amphibole classification diagrams following the scheme of Hawthorne et al. (2012). c) Ti versus IVAl plot discriminating between low-pressure and high-pressure amphiboles indicating a pressure between 1-3 kbar for the high-Ti hornblende in the EMF metabasalts (Colombi, 1989; Zenk, 2001). d) IVAl versus VIAl plot showing the high-Ti hornblende mainly plotting as a tight cluster within the unaltered/magmatic field, whereas the sadanagaite in the high-pressure field similar to amphiboles interpreted to form in response to the Penokean Orogeny (Mukwakwami et al., 2012).

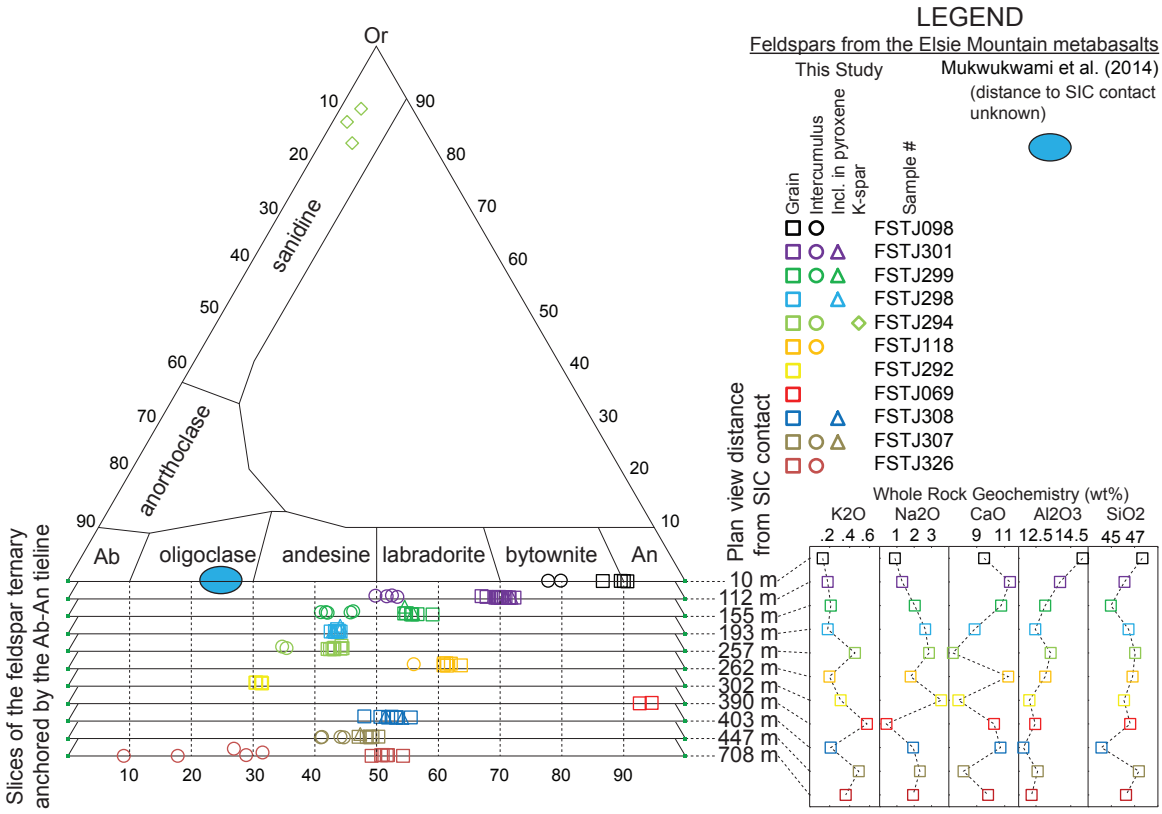

Fig. 2.9. Feldspar ternary showing plotting positions for plagioclase and k-feldspar grains from EMF metabasalts. Sample distance from the SIC are indicated to the right of the albite-anorthite binary dissections together with the bulk rock compositions.

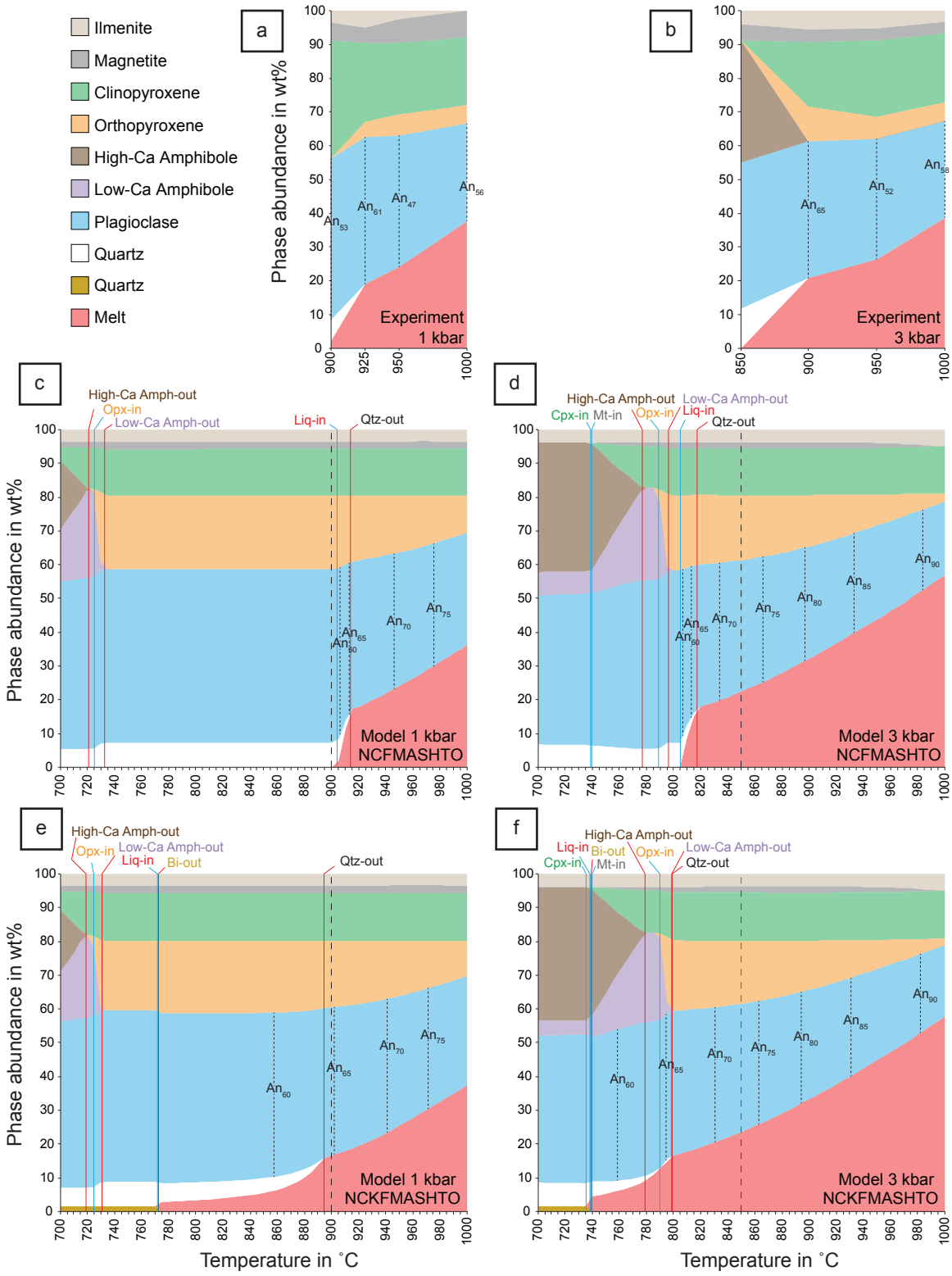

Fig. 2.10. a, b) Phase abundances in wt.% for the Beard and Lofgren (1991) experiments at 1 and 3 kbar with increasing temperature. c-f) Phase abundances in wt.% for models calculated in NCFMASHTO and NCKFMASHTO at 1 and 3 kbar with increasing temperature and using the starting composition from the Beard and Lofgren (1991) experiment. An = anorthite isopleths.

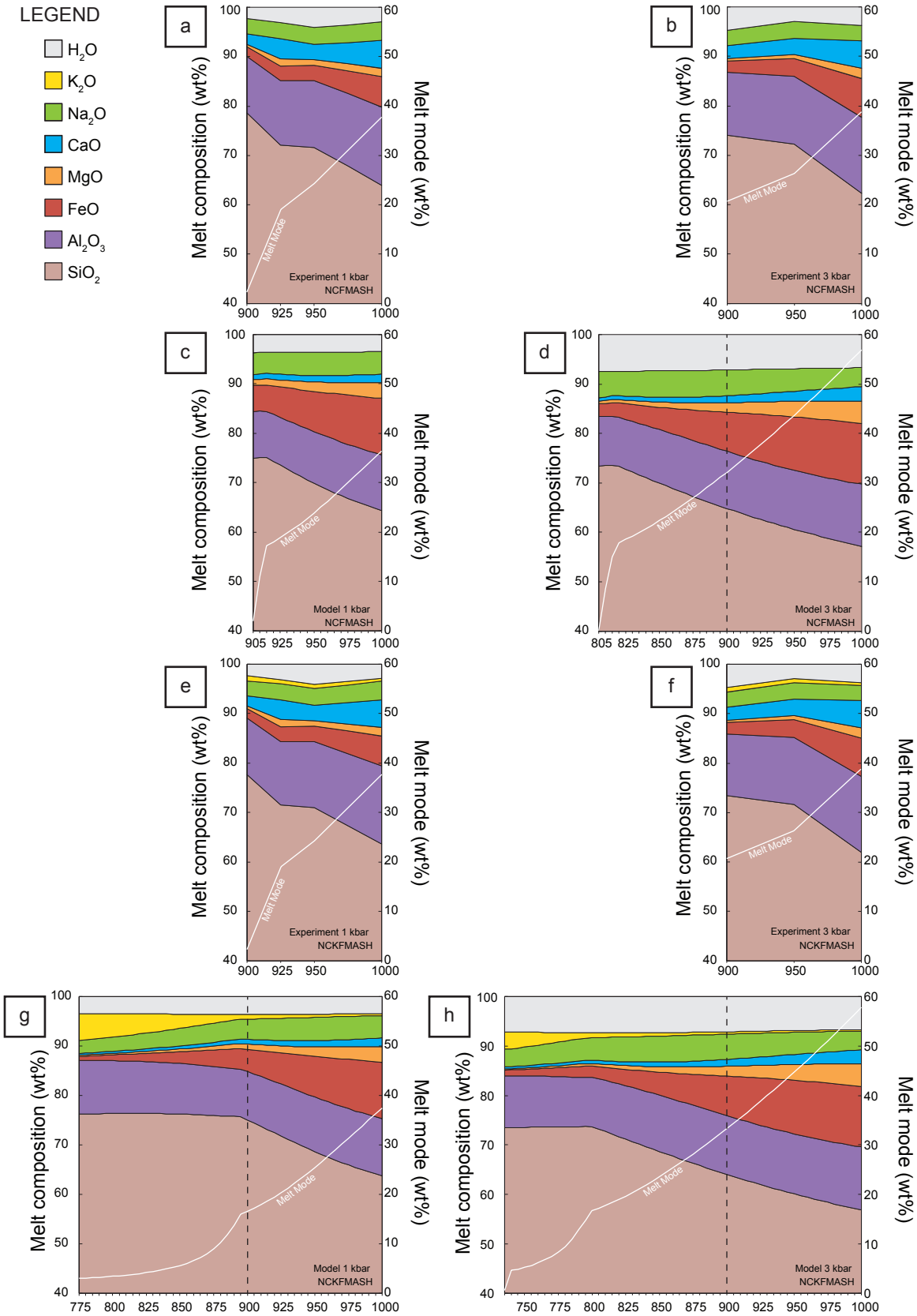

Fig. 2.11. a, b) Melt composition in wt.% for the Beard and Lofgren (1991) experiments in NCFMASHTO at 1 and 3 kbar with increasing temperature. c, d) Melt composition in wt.% for

Fig. 2.11. *(cont.)* models calculated in NCFMASHTO at 1 and 3 kbar with increasing temperature. e, f) Melt composition in wt.% for the Beard and Lofgren (1991) experiments in NCKFMASHTO at 1 and 3 kbar with increasing temperature. g, h) Melt composition in wt.% for models calculated in NCKFMASHTO at 1 and 3 kbar with increasing temperature.

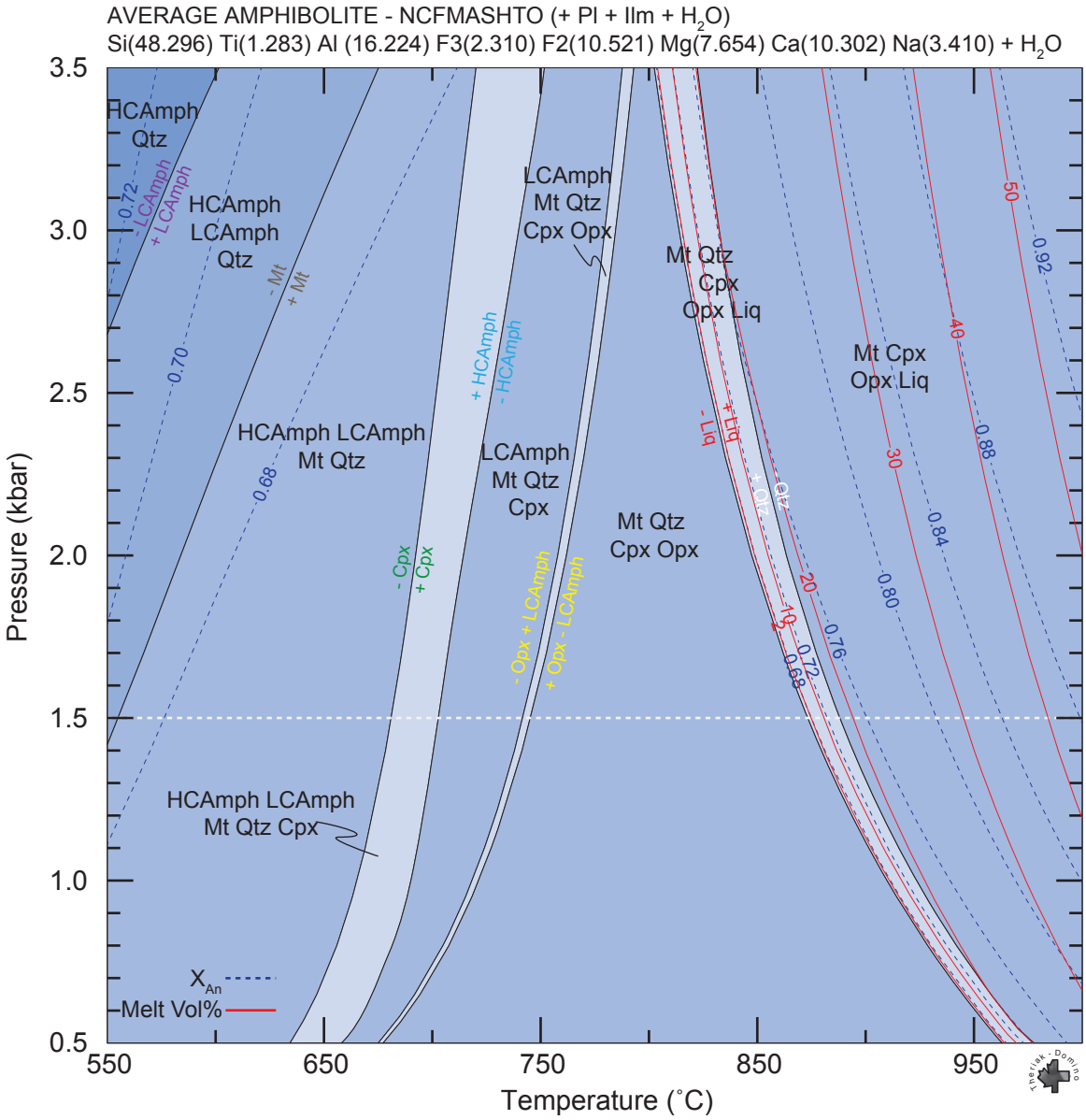

Fig. 2.12. Pressure-temperature phase diagram section for an average amphibolite unit composition calculated for the NCFMASHTO chemical system, using a modified version of THERIAK-DOMINO v. 01.08.09 (De Capitani, 1987) and the data set of Holland and Powell (1998, v. 5.5, 2003). Melt abundance (vol.%) isopleths are solid red lines and X_{An} isopleths are stippled blue lines. The stippled white line at 1.5 kbar indicate a reasonable pressure estimate during SIC contact metamorphism.

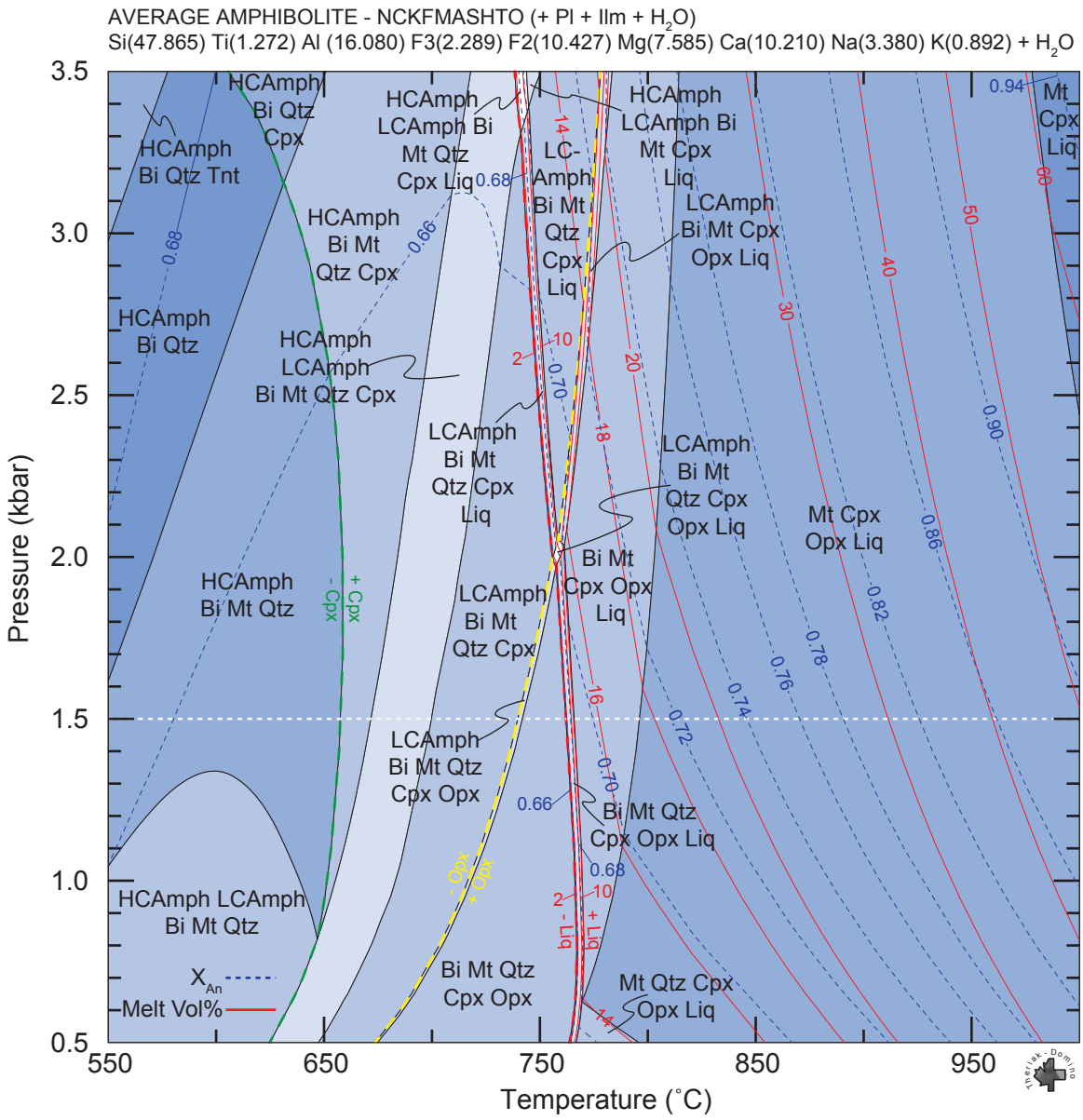

Fig. 2.13. Pressure-temperature phase diagram section for an average amphibolite unit composition calculated for the NCKFMASHTO chemical system, using a modified version of THERIAK-DOMINO v. 01.08.09 (De Capitani, 1987) and the data set of Holland and Powell (1998, v. 5.5, 2003). Melt abundance (vol.%) isopleths are solid red lines and X_{An} isopleths are stippled blue lines. The stippled white line at 1.5 kbar indicate a reasonable pressure estimate during SIC contact metamorphism. Adding K as a system component has a significant effect on the solidus that is lowered by more than 100 °C.

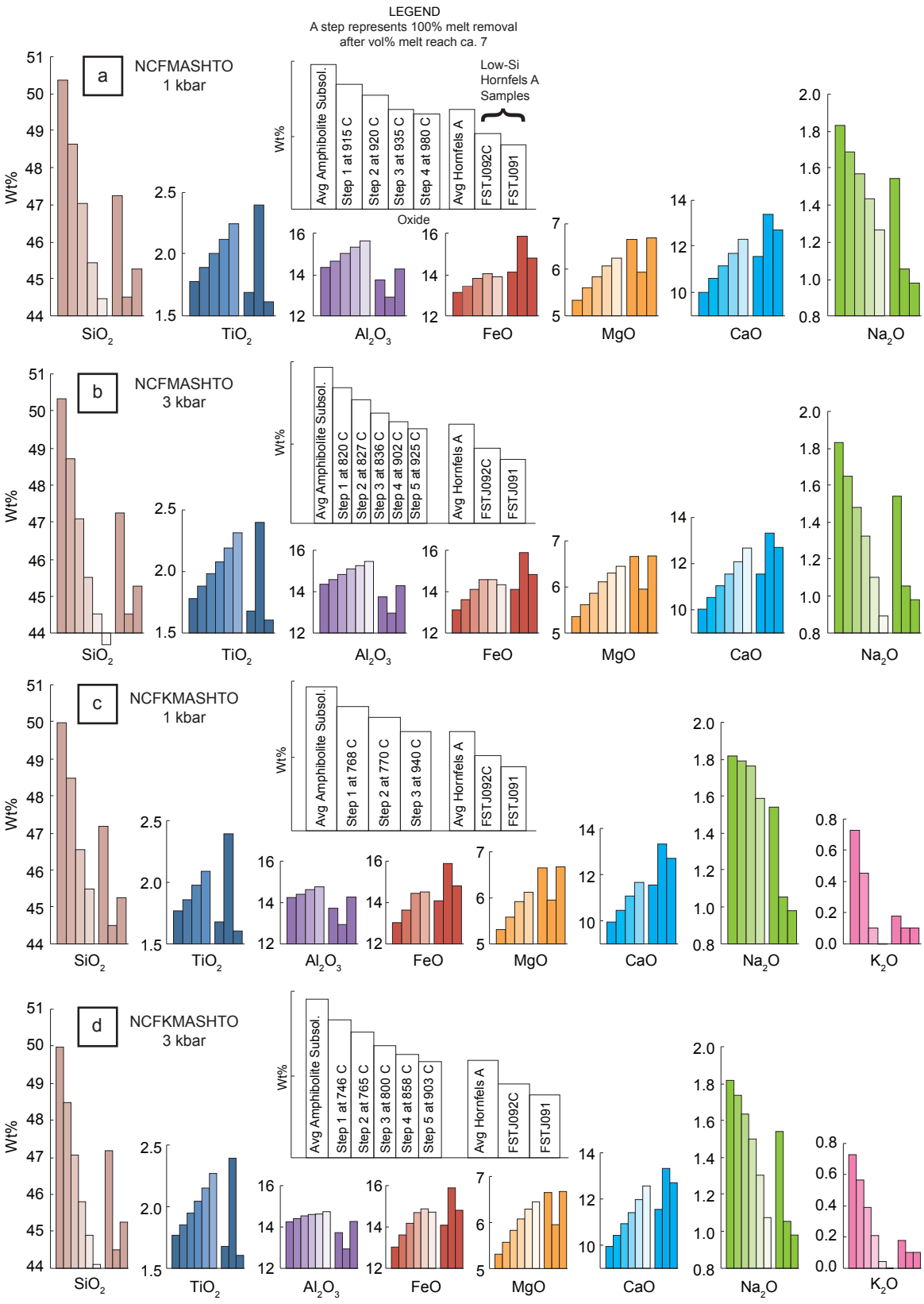

Fig. 2.14. Model showing the compositional evolution for an average basaltic amphibolite unit rock undergoing partial melting and melt segregation. The first bar for each major oxide indicates the starting composition for an average basaltic amphibolite unit rock. The subsequent 3-5 bars

Fig. 2.14. *(cont.)* indicate a 100% removal of 7 vol.% melt. The last 3 bars represent an average proximal basaltic hornfels unit rock composition followed by 2 individual basaltic hornfels unit rock samples that are good candidates for having experienced high degrees of partial melting and melt segregation. a, b) Model calculated in NCFMASHTO at 1 and 3 kbar. c, d) Model calculated in NCKFMASHTO at 1 and 3 kbar. The models suggest that melt segregation depletes the restite in, e.g., SiO_2 and K_2O, which is also the evolution observed for these oxides when comparing an average basaltic amphibolite unit rock composition to basaltic hornfels unit rock compositions.

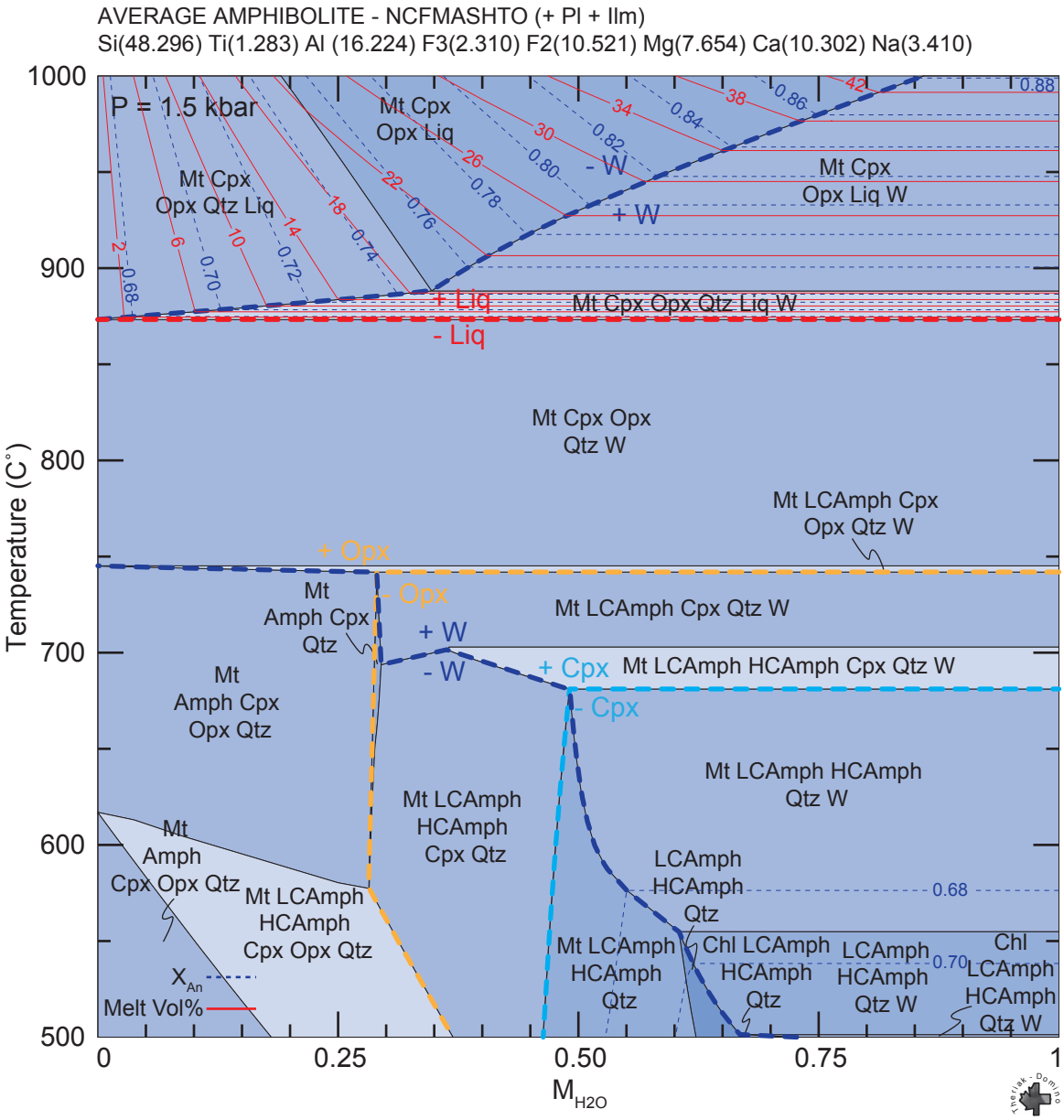

Fig. 2.15. Temperature-M-H_2O phase diagram section for an average amphibolite unit composition calculated for the NCFMASHTO chemical system, using a modified version of THERIAK-DOMINO v. 01.08.09 (De Capitani, 1987) and the data set of Holland and Powell (1998, v. 5.5, 2003). At lower bulk rock H_2O, clino- and orthopyroxene are stabilized towards lower temperatures. The model also predicts that the solidus is essentially unaffected by a decrease in bulk rock H_2O. However, the abundance of melt is highly dependent on the bulk rock H_2O.

SUPPORTING INFORMATION

LOW-PRESSURE AND HIGH-TEMPERATURE (LP-HT) METAMORPHISM OF BASALTS: INSIGHTS FROM THE SUDBURY IMPACT MELT SHEET AUREOLE AND THERMODYNAMIC MODELLING

T.R.C. Jørgensen, D.K. Tinkham, and C.M. Lesher

Appendix S2.1. Phase equilibria calculations involved the following solid solution minerals and *a-x* relationships: Diener *et al*. (2012) clinopyroxene and amphibole models; White *et al*. (2007) garnet, biotite, and melt models; White *et al*. (2005) ilmenite model; Holland and Powell (2003) plagioclase model; White *et al*. (2002) orthopyroxene and magnetite models; Coggon and Holland (2002) white mica; and the Holland and Powell (1998) chlorite, talc, epidote, staurolite and cordierite models. Currently, no amphibole a-x model in the chemical system of interest exists that is consistent with the v. 6.2 Holland and Powell (2011, 2012) thermodynamic database, and therefore only activity models valid with the v. 5.5 Holland and Powell (1998, 2003) database were used in the generation of phase diagram sections to maintain consistency.

Appendix S2.2. Estimates of water contents in oceanic crust range from ca. 1-6 wt. %, and the higher estimates represent fully hydrated basalts (Anderson *et al*., 1976; Peacock, 1990; Schmidt and Poli, 1998). Although amphibolite facies peak metamorphism and deformation of the Huronian strata are generally attributed to the Blezardian Orogeny (Riller and Schwerdtner, 1997), hydrous metamorphic mineral assemblages at amphibolite facies conditions are also attributed to the Penokean Orogeny (e.g., Mukwakwami *et al*., 2012). Because of the general lack of overprinting relationships

between the two events the hydrous nature of the EMF basalts at the onset of SIC contact metamorphism is unknown. However, EMF basalts generally display typical greenschist to amphibolite facies metamorphic mineral assemblages consisting mainly of amphiboles (hornblende, actinolite-tremolite), plagioclase (An_{20}-An_{60}), quartz, and chlorite with minor mica, epidote, and clinozoisite (Innes, 1977; Card, 1978b), suggesting that it is reasonable to assume that the EMF basalts were largely hydrated compared to unaltered mid-ocean ridge basalts (< 0.5 wt. % H_2O; Stern, 2002). The H_2O content of amphibole generally ranges from 1.5-4 wt. %, and a reasonable estimate for the modal abundance of amphibole in the metabasalts post-SIC is approximately 55% (Card, 1978b). Thus, a conservative estimate of the H_2O content of the EMF metabasalts prior to contact metamorphism would be ca. 1%. This is also close to the H_2O^+ estimate of 1.04 wt. % by Card (1978b) of an EMF metabasalt outside the high-T contact aureole. A pure H_2O fluid phase is assumed mainly on the basis of field and petrographic observations that show no indication of significant carbonate veining or calc-silicates in the aureole.

Appendix S2.3. The QUILF program of Andersen *et al*. (1993) incorporates the graphical version of the two-pyroxene thermometer of Lindsley (1983) and Lindsley and Andersen (1983) and combines thermodynamic solution models for clino- and orthopyroxene in the CFMS system (CaO-FeO-MgO-SiO_2) with the four end-members $Mg_2Si_2O_6$ (enstatite, En), $Fe_2Si_2O_6$ (ferrosilite), $CaMgSi_2O_6$ (diopside), and $CaFeSi_2O_6$ (hedenbergite). Projecting mineral compositions into the CFMS (CaO-FeO-MgO-SiO_2) system, following the method of Lindsley and Andersen (1983), is the only procedure employed by the method to diminish the effects of non-quadrilateral components on the partitioning of Ca, Mg, and Fe between coexisting pyroxenes. However, the reduction includes

corrections for Al, Fe^{3+}, Cr, and Na, but none for Ti because of inadequate data (Andersen *et al*., 1993). Consequently, the QUILF two-pyroxene thermometer is best suited for pyroxene pairs whose compositions plot near the Di-En-Hd-Fs quadrilateral (Wo + En + Fs ≥ 90%). The Brey and Köhler (1990) thermometer is an empirical model fitted to experimental data in systems CMS, CMAS, CMASCr (CaO-MgO-Al_2O_3-SiO_2-Cr_2O_3) and natural data. Corrections for Fe and Na probably make it applicable to compositions down to Mg# = 80, with minimal error (Brey and Köhler, 1990). Putirka (2008) performed a global regression based on the partitioning of enstatite + ferrosilite between clino- and orthopyroxene to increase the precision for the available experimental data of Brey and Köhler (1990). The Putrika (2008) thermometer performs best for mafic systems where $Mg\#^{Cpx} > 75$. The standard error estimate (SEE) is ±70 °C in the Brey and Köhler (1990) model and ±56 °C in the Putirka (2008) model (and ±50 °C and ±45 °C, respectively, if only clinopyroxene with Mg# > 75 were used).

Appendix S2.4. U-Pb data for zircon in partial melt patches in Elsie Mountain Formation metabasalts. The data were acquired at the Laurentian University Geochemical Fingerprinting Laboratory, Canada by in-situ laser ablation (Resonetic RESOlution M-50 193 nm ArF excimer laser) inductively coupled plasma mass spectrometry (Thermo X-Series II). Data were processed with Iolite (e.g., Paton et al., 2010, 2011) and VizualAge (Petrus and Kamber, 2012), and concordia ages were calculated using Isoplot (e.g., Ludwig, 2003).

Appendix S2.5. Pyroxene (a), amphibole (b), and feldspar (c) analyses for Elsie Mountain Formation metabasalts. Mafic silicates were analyzed for Si, Ti, Al, Cr, Fe_{total}, Mn, Mg, Ca, Na, K, F, and Cl. The mineral formulae recalculation for pyroxenes was

performed using a 6-oxygen and 4-cation per formula unit following Deer *et al*. (1992), and provide identical results for Fe^{3+} as the scheme of Droop (1987). The recalculation and classification scheme for amphiboles follow that of Hawthorne *et al*. (2012). Feldspars were analyzed for Si, Ti, Al, Mg, Ca, Mn, Fe_{total}, Sr, Ba, Na, and K, and reduced using an 8-oxygen and 5-cation per formula unit following Deer *et al*. (1992). Compositional data were obtained by wavelength-dispersive X-ray emission spectrometry (WD-XRES) using a Cameca SX-100 electron probe microanalyzer (EPMA) at the Geo Labs. Operating conditions were 20 kV acceleration voltage, 20 nA beam current, and a 10 μm beam size that were slightly defocused (15 μm) during some clinopyroxene analyses due to fine scale exsolution lamellae (1-3 μm). Also, an attempt was made to only target clinopyroxene cut at high angles to the exsolution lamellae. Counting times for each element were the same for peak and background measurements, and ranged from 10-30 s. Natural materials were used as standards.

Appendix S2.6. Whole-rock geochemistry for samples making up the average composition used in phase equilibria modelling, disregarded for phase equilibria modelling because of high Fe#, and those that provided mineral chemistry. Whole-rock geochemical analyses were performed at the Ontario Geoscience Laboratories (Geo Labs) in Sudbury, Ontario and the Department of Earth Sciences at the University of Western Ontario, London, Ontario (UWO). Weathered surfaces were removed in the field wherever possible and any remaining weathering was removed with a water-cooled rock saw with a diamond-embedded brass blade. Any visible burns from the rock saw were removed by grinding on a diamond-embedded steel lapping disc. The samples were cleaned carefully to remove sawing/grinding slimes, dried in air, crushed in a jaw crusher

with low-Cr steel case-hardened plates, and pulverized in an agate ball mill. All samples were analyzed for loss on ignition (LOI) by heating at 1000 °C under an oxidizing atmosphere until a constant weight was determined. 1.0 g aliquots of the anhydrous rock powders were fused with a 49.75:49.75:0.5 dilithium tetraborate:lithium metaborate:lithium iodide flux (Geo Labs) and 49.75:49.75:0.5 lithium tetraborate:lithium metaborate:lithium bromine (UWO) to produce glass discs that were analyzed for major elements by wavelength-dispersive X-ray fluorescence spectrometry (XRFS). Replicate samples analyzed at both laboratories indicate that analytical precision (relative standard deviation) is better than 1% for high-moderate abundance elements, but as high as to 3% for low-abundance elements. Interlaboratory precision (percent difference) is better than better than 4% for SiO_2, TiO_2, Al_2O_3, Fe_2O_3, MgO, Na_2O, K_2O, and P_2O_5, 7% for CaO, and 15% for MnO. Rock standard BHVO-2 (Hawaiian Volcano Observatory basalt) was analyzed with the samples at Geo Labs, and the measured results are within analytical errors (relative) for all oxides except CaO (0.2%), Fe_2O_3 (0.6%), and Al_2O_3 (0.8%) of recommended values. Rock standard JB-1a was analyzed with the samples at UWO and the results are within 4% (relative) of the recommended values (no uncertainties). Ferrous iron was measured on 14 samples by titration with ca. 0.02 M $KMnO_4$ (exact concentrations were calibrated before use). $Fe^{2+}/\sum Fe$ ranged from 0.72 to 0.93 (mean = 0.82, $2\sigma = 0.1$). This ratio is slightly lower than the ratios of 0.86 determined by Presnall *et al*. (1979) and 0.84 ± 0.01 determined by Cottrell and Kelley (2011) for least-altered mid-ocean ridge tholeiites. $Fe^{2+}/\sum Fe$ of continental flood basalts are less well constrained, but Hoover and Murphy (1989) report values of 0.82-0.63 for Columbia River basalts, the higher of which presumably reflect least-altered samples.

Thus, for the purpose of this study Fe is allocated as 0.82 Fe^{2+} and 0.18 Fe^{3+}. However, post-solidus oxidation could have affected the bulk rock iron oxidation state, but these values are considered reasonable approximations.

Table S2.1. U-Pb data for zircon in partial melt patches in Elsie Mountain Formation metabasalts.

	Zircon	Zircon 1							Zircon 2		Zircon 3				Zircon 4	
	Spot	1a	1b	1c	1d	1e	1f	1g	2a	2b	3a	3b	3c	3d	4a	4b
Isotopic ratios	$^{207}Pb/^{235}U$	4.78	5	5.14	5.13	5.1	5.13	5.31	4.87	6.06	5.08	5.54	4.81	5.3	6.23	5.07
	2σ	0.16	0.17	0.18	0.18	0.18	0.11	0.2	0.24	0.24	0.12	0.17	0.25	0.18	0.27	0.24
	$^{206}Pb/^{238}U$	0.31	0.326	0.33	0.321	0.331	0.33	0.309	0.3052	0.3137	0.33	0.333	0.302	0.336	0.304	0.295
	2σ	0.008	0.005	0.007	0.008	0.004	0.006	0.008	0.008	0.0049	0.005	0.006	0.01	0.007	0.006	0.008
	ρ	0.48	0.16	0.37	0.24	0.13	0.66	0.25	0.36	0.08	0.35	0.21	0.44	0.14	0.22	0.22
	$^{207}Pb/^{206}Pb$	0.11	0.111	0.112	0.118	0.111	0.111	0.123	0.1166	0.1434	0.114	0.121	0.115	0.115	0.15	0.126
	2σ	0.005	0.004	0.004	0.005	0.004	0.002	0.005	0.005	0.006	0.003	0.004	0.006	0.004	0.006	0.006
Age estimates [Ma]	$^{207}Pb/^{235}U$	1778	1814	1841	1844	1830	1838	1873	1788	1983	1838	1910	1790	1863	1993	1826
	2σ	29	29	29	31	29	18	32	42	36	21	26	42	29	34	40
	$^{206}Pb/^{238}U$	1739	1818	1838	1794	1848	1836	1731	1716	1758	1835	1852	1698	1866	1711	1665
	2σ	40	24	31	39	21	31	39	40	24	22	27	47	33	30	38
	$^{207}Pb/^{206}Pb$	1782	1804	1814	1931	1791	1824	1984	1902	2254	1864	1955	1892	1866	2323	2024
	2σ	82	63	60	69	59	32	75	87	70	44	53	96	62	65	86
% Discordance		2	-1	-1	7	-3	-1	13	10	22	2	5	10	0	26	18
Compositional data	Pb [ppm]	19.7	18.59	15.97	17.69	38.1	86.3	28.1	20.8	39	39.1	39.6	29.7	26.7	57.5	42.2
	2σ	1.7	0.93	0.79	0.98	1.2	3.9	2.9	2.5	3.3	1.3	1.9	2.3	1.5	4.1	2.2
	U [ppm]	44.03	44.87	43.9	41.22	77	168.8	62.3	54.8	69.6	74.8	65.61	70.8	52.19	85.4	77.9
	2σ	0.77	0.69	1.2	0.75	1.9	9.7	2	1.3	0.75	2	0.82	1.3	0.98	3.8	1.6
	Th [ppm]	23.08	22.72	21.32	21.11	48.4	101.8	28.8	27.08	31.05	44.2	35.71	45.5	28.48	46	46.8
	2σ	0.61	0.58	0.47	0.49	2	7.3	1.6	0.69	0.5	1.3	0.95	1.2	0.84	1.6	1.4
	U/Th	1.9	2.0	2.1	2.0	1.6	1.7	2.2	2.0	2.2	1.7	1.8	1.6	1.8	1.9	1.7

Table S2.2a. Pyroxene analyses in wt.% and atoms per formula unit for Elsie Mountain Formation metabasalts.

Sample #		**FSTJ098**	**FSTJ098**	**FSTJ098**	**FSTJ098**	**FSTJ098**	**FSTJ098**	**FSTJ098**	**FSTJ098**	**FSTJ098**	**FSTJ098**	**FSTJ098**	**FSTJ098**
		EMP098Q1	EMP098Q	EMP098Q1	EMP098Q1	EMP098Q	EMP098Q1	EMP098Q1	EMP098Q2	EMP098Q2_	EMP098Q2	EMP098Q2	EMP098Q
Analysis		S4	1S4-1	S3	S3-1	1S3-2	S1	_1S1	_1S1	1S2	_1S2-1	_1S3	3_1S4
Rock Type		BH	BH	BH	BH	BH	BH	BH	BH	BH	BH	BH	BH
Pyroxene Species	L.O.D.*	Opx	Opx	Opx	Opx	Opx	Opx	Opx	Opx	Opx	Opx	Opx	Opx
SiO_2	0.036	51.41	51.72	51.38	51.70	51.68	52.01	51.71	50.52	51.15	50.91	51.59	51.24
TiO_2	0.031	0.18	0.17	0.17	0.21	0.20	0.21	0.19	0.26	0.25	0.23	0.22	0.21
Al_2O_3	0.029	0.68	0.72	0.66	0.67	0.72	0.68	0.63	1.65	1.45	1.25	0.66	0.73
Cr_2O_3	0.029	0.04	0.04	0.04	0.03	L.O.D.	L.O.D.	L.O.D.	0.27	0.24	0.21	0.05	0.07
FeO_{total}	0.026	26.82	26.78	26.40	26.48	26.69	26.52	26.63	27.29	27.57	27.77	27.30	28.58
MnO	0.022	0.52	0.51	0.49	0.52	0.52	0.51	0.52	0.50	0.48	0.51	0.47	0.67
MgO	0.031	19.06	19.11	19.44	19.29	19.18	19.47	19.05	17.98	18.22	18.41	18.38	17.76
CaO	0.024	1.01	1.05	0.93	1.12	1.05	0.98	1.11	1.67	1.34	1.01	1.66	1.00
Na_2O	0.024	L.O.D.	L.O.D.	L.O.D.	L.O.D.	L.O.D.	L.O.D.	L.O.D.	L.O.D.	L.O.D.	L.O.D.	L.O.D.	L.O.D.
K_2O	0.017	L.O.D.	L.O.D.	L.O.D.	L.O.D.	L.O.D.	L.O.D.	L.O.D.	L.O.D.	L.O.D.	L.O.D.	L.O.D.	L.O.D.
TOTAL		99.72	100.12	99.51	100.03	100.05	100.39	99.84	100.14	100.70	100.31	100.33	100.26
T (Ideally 2 a.p.f.u.)													
Si		1.96	1.97	1.96	1.97	1.97	1.97	1.97	1.93	1.94	1.94	1.97	1.96
Al		0.03	0.03	0.03	0.03	0.03	0.03	0.03	0.07	0.06	0.06	0.03	0.03
Fe^{3+}		0.01	0.00	0.01	0.00	0.00	0.00	0.00	0.00	0.00	0.00	0.00	0.00
T subtotal		2.00	2.00	2.00	2.00	2.00	2.00	2.00	2.00	2.00	2.00	2.00	2.00
M1+M2 (Ideally 2 a.p.f.u.)													
$Ti^{(M1)}$		0.01	0.00	0.00	0.01	0.01	0.01	0.01	0.01	0.01	0.01	0.01	0.01
$Al^{(M1)}$		0.00	0.00	0.00	0.00	0.00	0.00	0.00	0.00	0.01	0.00	0.00	0.00
$Cr^{(M1)}$		0.00	0.00	0.00	0.00				0.01	0.01	0.01	0.00	0.00
$Fe^{3+\,(M1)}$		0.03	0.02	0.03	0.02	0.02	0.02	0.02	0.04	0.03	0.04	0.02	0.02
$Mg^{(M1+M2)}$		1.08	1.08	1.11	1.09	1.09	1.10	1.08	1.02	1.03	1.05	1.04	1.02
$Fe^{2+\,(M1+M2)}$		0.83	0.83	0.81	0.82	0.82	0.82	0.83	0.83	0.85	0.84	0.84	0.89
$Mn^{(M2)}$		0.02	0.02	0.02	0.02	0.02	0.02	0.02	0.02	0.02	0.02	0.02	0.02
$Ca^{(M2)}$		0.04	0.04	0.04	0.05	0.04	0.04	0.05	0.07	0.05	0.04	0.07	0.04
$Na^{(M2)}$													
$K^{(M2)}$													
M1+M2 subtotal		2.00	2.00	2.00	2.00	2.00	2.00	2.00	2.00	2.00	2.00	2.00	2.00
SUM T,M1,M2		4.00	4.00	4.00	4.00	4.00	4.00	4.00	4.00	4.00	4.00	4.00	4.00
End-members													
Wo%		2.1	2.2	1.9	2.3	2.2	2.0	2.3	3.5	2.8	2.1	3.4	2.1
En%		54.9	54.8	55.9	55.3	55.0	55.6	54.8	52.1	52.6	53.1	52.8	51.5
Fs%		43.0	43.0	42.2	42.4	42.8	42.4	42.9	44.4	44.6	44.8	43.8	46.4

*L.O.D. = Limit of detection is defined as 3 x standard deviation of the total accumulated background counts.
BG = basaltic granofels; BH = basaltic hornfels

Table S2.2a. Pyroxene analyses in wt.% and atoms per formula unit for Elsie Mountain Formation metabasalts *(cont.)*.

FSTJ098	**FSTJ098**	**FSTJ098**	**FSTJ098**	**FSTJ098**	**FSTJ098**	**FSTJ098**	**FSTJ301**	**FSTJ301**	**FSTJ301**	**FSTJ301**	**FSTJ301**	**FSTJ301**	**FSTJ301**	**FSTJ301**
EMP098Q1S11	EMP098Q1S11-1	EMP098Q1S11-2	EMP098Q1S8	EMP098Q1_1S4	EMP098Q2_1S7	EMP098Q2_1S8	FSTJ301_site_1_opx_1	FSTJ301_site_1_opx_2	FSTJ301_site_1_opx_3	FSTJ301_site_1_opx_4	FSTJ301_site_1_opx_5	FSTJ301_site_1_opx_6	FSTJ301_site_1_opx_7	FSTJ301_site_1_opx_8
BH Cpx	BH Cpx	BH Cpx	BH Cpx	BH Cpx	BH Cpx	BH Cpx	BH Opx	BH Opx	BH Opx	BH Opx	BH Opx	BH Opx	BH Opx	BH Opx
52.07	51.87	52.41	51.93	52.28	51.44	51.77	50.30	50.03	50.39	50.44	50.36	50.00	50.25	50.27
0.29	0.34	0.26	0.39	0.32	0.37	0.40	0.14	0.15	0.13	0.14	0.18	0.14	0.15	0.15
1.26	1.41	1.09	1.43	1.28	1.23	1.42	0.48	0.54	0.48	0.50	0.55	0.58	0.56	0.53
0.06	0.06	0.05	0.07	0.04	0.10	0.06	L.O.D.	L.O.D.	L.O.D.	L.O.D.	L.O.D.	L.O.D.	L.O.D.	L.O.D.
10.98	11.99	11.30	11.23	11.03	12.15	11.58	32.66	32.66	32.40	32.40	32.46	32.62	32.53	32.97
0.26	0.27	0.27	0.28	0.25	0.26	0.26	0.69	0.67	0.67	0.67	0.66	0.67	0.67	0.69
13.37	13.49	13.61	13.04	13.69	12.77	12.65	14.61	14.43	14.74	14.83	14.76	14.72	14.59	14.32
21.71	20.74	21.25	21.50	21.73	20.87	21.71	1.07	1.06	1.08	1.12	1.23	1.03	1.13	1.12
0.16	0.14	0.17	0.15	0.17	0.16	0.17	L.O.D.	L.O.D.	L.O.D.	L.O.D.	L.O.D.	L.O.D.	L.O.D.	L.O.D.
L.O.D.	L.O.D.	L.O.D.	L.O.D.	L.O.D.	L.O.D.	L.O.D.	L.O.D.	L.O.D.	L.O.D.	L.O.D.	L.O.D.	L.O.D.	L.O.D.	L.O.D.
100.17	100.30	100.41	100.02	100.80	99.33	100.03	99.96	99.53	99.90	100.10	100.20	99.77	99.88	100.05
1.95	1.94	1.96	1.95	1.94	1.95	1.95	1.98	1.98	1.98	1.98	1.97	1.97	1.98	1.98
0.05	0.06	0.04	0.05	0.06	0.05	0.05	0.02	0.02	0.02	0.02	0.03	0.03	0.02	0.02
0.00	0.00	0.00	0.00	0.00	0.00	0.00	0.00	0.00	0.00	0.00	0.00	0.01	0.00	0.00
2.00	2.00	2.00	2.00	2.00	2.00	2.00	2.00	2.00	2.00	2.00	2.00	2.00	2.00	2.00
0.01	0.01	0.01	0.01	0.01	0.01	0.01	0.00	0.00	0.00	0.00	0.01	0.00	0.00	0.00
0.01	0.01	0.01	0.02	0.00	0.01	0.01	0.00	0.00	0.00	0.00	0.00	0.00	0.00	0.00
0.00	0.00	0.00	0.00	0.00	0.00	0.00								
0.03	0.04	0.03	0.02	0.05	0.03	0.02	0.02	0.02	0.01	0.02	0.02	0.02	0.01	0.01
0.75	0.75	0.76	0.73	0.76	0.72	0.71	0.86	0.85	0.86	0.87	0.86	0.86	0.85	0.84
0.31	0.34	0.32	0.34	0.29	0.36	0.34	1.06	1.06	1.05	1.05	1.04	1.04	1.05	1.07
0.01	0.01	0.01	0.01	0.01	0.01	0.01	0.02	0.02	0.02	0.02	0.02	0.02	0.02	0.02
0.87	0.83	0.85	0.87	0.87	0.85	0.88	0.05	0.04	0.05	0.05	0.05	0.04	0.05	0.05
0.01	0.01	0.01	0.01	0.01	0.01	0.01								
2.00	2.00	2.00	2.00	2.00	2.00	2.00	2.00	2.00	2.00	2.00	2.00	2.00	2.00	2.00
4.00	4.00	4.00	4.00	4.00	4.00	4.00	4.00	4.00	4.00	4.00	4.00	4.00	4.00	4.00
44.4	42.4	43.4	44.4	44.0	43.4	44.9	2.3	2.3	2.3	2.4	2.6	2.2	2.4	2.4
38.1	38.4	38.6	37.5	38.6	36.9	36.4	43.4	43.1	43.8	43.9	43.7	43.8	43.4	42.6
17.5	19.1	18.0	18.1	17.4	19.7	18.7	54.3	54.7	53.9	53.7	53.7	54.1	54.2	55.0

Table S2.2a. Pyroxene analyses in wt.% and atoms per formula unit for Elsie Mountain Formation metabasalts *(cont.)*.

FSTJ301	**FSTJ301**	**FSTJ301**	**FSTJ301**	**FSTJ301**	**FSTJ301**	**FSTJ301**	**FSTJ301**	**FSTJ301**	**FSTJ301**	**FSTJ301**	**FSTJ301**	**FSTJ301**	**FSTJ301**	**FSTJ301**
FSTJ301_site_1_opx_9	FSTJ301_site_1_opx_10	FSTJ301_site_1_opx_11	FSTJ301_site_1_opx_12	FSTJ301_site_2_opx_13	FSTJ301_site_2_opx_14	FSTJ301_site_2_opx_15	FSTJ301_site_2_opx_16	FSTJ301_site_2_opx_17	FSTJ301_site_2_opx_18	FSTJ301_site_2_opx_19	FSTJ301_site_2_opx_20	FSTJ301_site_2_opx_21	FSTJ301_site_2_opx_22	FSTJ301_site_2_opx_23
BH Opx	BH Opx	BH Opx	BH Opx	BH Opx	BH Opx	BH Opx	BH Opx	BH Opx	BH Opx	BH Opx	BH Opx	BH Opx	BH Opx	BH Opx
50.14	50.05	50.17	49.94	50.47	50.56	50.27	50.03	49.89	50.13	50.32	50.07	50.12	50.05	50.07
0.16	0.18	0.18	0.16	0.18	0.15	0.16	0.17	0.16	0.16	0.19	0.15	0.18	0.16	0.19
0.60	0.50	0.58	0.51	0.53	0.56	0.56	0.57	0.58	0.58	0.52	0.45	0.49	0.54	0.55
L.O.D.	L.O.D.	L.O.D.	L.O.D.	L.O.D.	L.O.D.	L.O.D.	L.O.D.	L.O.D.	L.O.D.	L.O.D.	L.O.D.	L.O.D.	L.O.D.	L.O.D.
32.21	32.61	32.60	32.43	32.83	32.66	32.49	32.66	33.03	33.10	32.83	33.13	32.66	32.94	33.04
0.64	0.67	0.65	0.68	0.68	0.68	0.65	0.71	0.69	0.72	0.66	0.70	0.65	0.65	0.69
14.81	14.72	14.52	14.63	14.67	14.65	14.63	14.66	14.09	14.37	14.40	14.57	14.52	14.27	14.43
1.25	1.14	1.20	1.20	1.23	1.21	1.27	1.16	1.21	1.06	1.29	1.06	1.23	1.25	1.21
L.O.D.	L.O.D.	L.O.D.	L.O.D.	L.O.D.	L.O.D.	L.O.D.	L.O.D.	L.O.D.	L.O.D.	L.O.D.	L.O.D.	L.O.D.	L.O.D.	L.O.D.
0.06	L.O.D.	L.O.D.	L.O.D.	L.O.D.	L.O.D.	L.O.D.	L.O.D.	L.O.D.	L.O.D.	L.O.D.	L.O.D.	L.O.D.	L.O.D.	L.O.D.
99.88	99.86	99.89	99.55	100.60	100.46	100.04	99.95	99.65	100.11	100.19	100.12	99.84	99.87	100.17
1.97	1.97	1.97	1.97	1.97	1.98	1.97	1.96	1.97	1.97	1.97	1.97	1.97	1.97	1.97
0.03	0.02	0.03	0.02	0.02	0.02	0.03	0.03	0.03	0.03	0.02	0.02	0.02	0.02	0.03
0.01	0.01	0.00	0.01	0.01	0.00	0.00	0.01	0.00	0.00	0.00	0.01	0.01	0.00	0.01
2.00	2.00	2.00	2.00	2.00	2.00	2.00	2.00	2.00	2.00	2.00	2.00	2.00	2.00	2.00
0.00	0.01	0.01	0.00	0.01	0.00	0.00	0.00	0.00	0.00	0.01	0.00	0.01	0.00	0.01
0.00	0.00	0.00	0.00	0.00	0.00	0.00	0.00	0.00	0.00	0.00	0.00	0.00	0.00	0.00
0.03	0.02	0.02	0.02	0.02	0.01	0.02	0.02	0.02	0.02	0.01	0.02	0.02	0.02	0.02
0.87	0.86	0.85	0.86	0.85	0.85	0.86	0.86	0.83	0.84	0.84	0.85	0.85	0.84	0.84
1.03	1.04	1.05	1.04	1.05	1.05	1.05	1.04	1.07	1.06	1.06	1.05	1.05	1.06	1.05
0.02	0.02	0.02	0.02	0.02	0.02	0.02	0.02	0.02	0.02	0.02	0.02	0.02	0.02	0.02
0.05	0.05	0.05	0.05	0.05	0.05	0.05	0.05	0.05	0.04	0.05	0.04	0.05	0.05	0.05
0.00														
2.00	2.00	2.00	2.00	2.00	2.00	2.00	2.00	2.00	2.00	2.00	2.00	2.00	2.00	2.00
4.00	4.00	4.00	4.00	4.00	4.00	4.00	4.00	4.00	4.00	4.00	4.00	4.00	4.00	4.00
2.7	2.4	2.6	2.6	2.6	2.6	2.7	2.5	2.6	2.3	2.7	2.3	2.6	2.7	2.6
43.9	43.7	43.1	43.6	43.3	43.3	43.4	43.5	42.1	42.7	42.7	43.3	43.2	42.5	42.8
53.4	53.8	54.3	53.8	54.1	54.1	53.9	54.0	55.3	55.0	54.5	54.5	54.2	54.8	54.6

Table S2.2a. Pyroxene analyses in wt.% and atoms per formula unit for Elsie Mountain Formation metabasalts *(cont.)*.

FSTJ301	**FSTJ301**	**FSTJ301**	**FSTJ301**	**FSTJ301**	**FSTJ301**	**FSTJ301**	**FSTJ301**	**FSTJ301**	**FSTJ301**	**FSTJ301**	**FSTJ301**	**FSTJ299**	**FSTJ299**	**FSTJ299**
FSTJ301_site_2_opx_24	FSTJ301_site_1_cpx_1	FSTJ301_site_1_cpx_2	FSTJ301_site_1_cpx_3	FSTJ301_site_1_cpx_4	FSTJ301_site_1_cpx_5	FSTJ301_site_1_cpx_6	FSTJ301_site_2_cpx_7	FSTJ301_site_2_cpx_8	FSTJ301_site_2_cpx_9	FSTJ301_site_2_cpx_10	FSTJ301_site_2_cpx_11	FSTJ299_site_1_opx_1	FSTJ299_site_1_opx_2	FSTJ299_site_1_opx_3
BH	BH	BH	BH	BH	BH	BH	BH	BH	BH	BH	BH	BH	BH	BH
Opx	Cpx	Cpx	Cpx	Cpx	Cpx	Cpx	Cpx	Cpx	Cpx	Cpx	Cpx	Opx	Opx	Opx
49.70	51.25	51.61	51.18	51.57	51.39	51.65	51.48	51.06	51.05	51.50	51.37	49.75	49.69	49.70
0.18	0.25	0.23	0.25	0.21	0.28	0.26	0.23	0.27	0.28	0.21	0.27	0.14	0.17	0.16
0.52	1.01	1.10	1.11	1.01	1.12	1.05	1.05	1.08	1.06	0.97	1.13	0.50	0.51	0.37
L.O.D.	L.O.D.	L.O.D.	L.O.D.	L.O.D.	L.O.D.	0.03	0.03	L.O.D.	L.O.D.	L.O.D.	L.O.D.	L.O.D.	L.O.D.	L.O.D.
32.83	14.62	14.92	15.03	14.68	14.95	14.45	15.16	15.26	15.21	14.55	15.42	36.30	35.91	36.09
0.66	0.34	0.35	0.34	0.33	0.36	0.34	0.36	0.36	0.37	0.31	0.39	0.92	0.93	0.94
14.40	11.61	11.54	11.51	11.43	11.61	11.51	11.48	11.39	11.51	11.26	11.60	11.52	12.23	11.85
1.26	20.44	20.41	19.99	20.46	20.15	20.78	19.95	19.87	19.98	20.69	19.89	1.23	1.32	1.29
L.O.D.	0.17	0.17	0.20	0.16	0.19	0.16	0.17	0.18	0.16	0.18	0.18	L.O.D.	L.O.D.	L.O.D.
L.O.D.	L.O.D.	L.O.D.	L.O.D.	L.O.D.	L.O.D.	L.O.D.	L.O.D.	L.O.D.	L.O.D.	L.O.D.	L.O.D.	L.O.D.	L.O.D.	L.O.D.
99.54	99.69	100.33	99.61	99.84	100.05	100.24	99.91	99.47	99.62	99.67	100.25	100.38	100.75	100.40
1.96	1.96	1.96	1.96	1.97	1.96	1.96	1.97	1.96	1.96	1.97	1.95	1.99	1.97	1.98
0.02	0.04	0.04	0.04	0.03	0.04	0.04	0.03	0.04	0.04	0.03	0.05	0.01	0.02	0.02
0.01	0.00	0.00	0.00	0.00	0.00	0.00	0.00	0.00	0.00	0.00	0.00	0.00	0.01	0.00
2.00	2.00	2.00	2.00	2.00	2.00	2.00	2.00	2.00	2.00	2.00	2.00	2.00	2.00	2.00
0.01	0.01	0.01	0.01	0.01	0.01	0.01	0.01	0.01	0.01	0.01	0.01	0.00	0.00	0.00
0.00	0.00	0.01	0.01	0.01	0.01	0.01	0.01	0.01	0.00	0.01	0.01	0.01	0.00	0.00
						0.00	0.00							
0.03	0.04	0.03	0.03	0.02	0.03	0.02	0.02	0.03	0.04	0.02	0.04	0.00	0.02	0.01
0.85	0.66	0.65	0.66	0.65	0.66	0.65	0.65	0.65	0.66	0.64	0.66	0.69	0.72	0.70
1.04	0.43	0.45	0.45	0.45	0.44	0.44	0.47	0.46	0.45	0.45	0.45	1.21	1.17	1.20
0.02	0.01	0.01	0.01	0.01	0.01	0.01	0.01	0.01	0.01	0.01	0.01	0.03	0.03	0.03
0.05	0.84	0.83	0.82	0.84	0.82	0.85	0.82	0.82	0.82	0.85	0.81	0.05	0.06	0.06
	0.01	0.01	0.02	0.01	0.01	0.01	0.01	0.01	0.01	0.01	0.01			
2.00	2.00	2.00	2.00	2.00	2.00	2.00	2.00	2.00	2.00	2.00	2.00	2.00	2.00	2.00
4.00	4.00	4.00	4.00	4.00	4.00	4.00	4.00	4.00	4.00	4.00	4.00	4.00	4.00	4.00
2.7	42.6	42.4	41.9	42.8	42.0	43.2	41.8	41.7	41.7	43.4	41.4	2.7	2.8	2.8
43.0	33.6	33.4	33.5	33.3	33.7	33.3	33.4	33.3	33.5	32.8	33.6	35.2	36.8	35.9
54.3	23.8	24.2	24.6	24.0	24.3	23.5	24.8	25.0	24.8	23.8	25.0	62.1	60.3	61.3

Table S2.2a. Pyroxene analyses in wt.% and atoms per formula unit for Elsie Mountain Formation metabasalts *(cont.)*.

FSTJ299	**FSTJ299**	**FSTJ299**	**FSTJ299**	**FSTJ299**	**FSTJ299**	**FSTJ299**	**FSTJ299**	**FSTJ299**	**FSTJ299**	**FSTJ299**	**FSTJ299**	**FSTJ299**	**FSTJ299**	**FSTJ299**
FSTJ299_site_1_opx_4	FSTJ299_site_1_opx_5	FSTJ299_site_2_opx_4	FSTJ299_site_2_opx_5	FSTJ299_site_2_opx_6	FSTJ299_site_2_opx_7	FSTJ299_site_2_opx_8	FSTJ299_site_2_opx_9	FSTJ299_site_2_opx_10	FSTJ299_site_2_opx_11	FSTJ299_site_2_opx_12	FSTJ299_site_2_opx_13	FSTJ299_site_2_opx_14	FSTJ299_site_1_cpx_1	FSTJ299_site_1_cpx_2
BH Opx	BH Opx	BH Opx	BH Opx	BH Opx	BH Opx	BH Opx	BH Opx	BH Opx	BH Opx	BH Opx	BH Opx	BH Opx	BH Cpx	BH Cpx
49.77	49.72	49.61	49.51	49.40	49.43	49.62	49.69	49.51	49.52	49.23	49.65	49.68	50.93	50.57
0.18	0.16	0.17	0.11	0.16	0.17	0.16	0.15	0.22	0.16	0.15	0.25	0.16	0.21	0.22
0.49	0.44	0.50	0.45	0.48	0.49	0.48	0.47	0.48	0.42	0.49	0.49	0.47	0.97	1.05
L.O.D.	L.O.D.	L.O.D.	L.O.D.	L.O.D.	L.O.D.	L.O.D.	L.O.D.	L.O.D.	L.O.D.	L.O.D.	L.O.D.	L.O.D.	L.O.D.	L.O.D.
35.98	36.13	36.44	36.24	36.64	36.69	36.42	36.59	36.50	36.11	36.55	36.56	36.87	18.94	19.33
0.93	0.94	1.01	0.95	1.09	1.05	0.92	0.97	0.98	0.92	0.92	0.95	1.01	0.53	0.53
11.99	12.09	11.66	11.82	11.57	11.32	11.78	11.73	11.36	11.47	11.55	11.37	11.18	9.56	9.56
1.34	1.23	1.44	1.48	1.37	1.48	1.34	1.10	1.33	1.46	1.26	1.47	1.33	18.81	18.72
L.O.D.	L.O.D.	L.O.D.	L.O.D.	L.O.D.	L.O.D.	L.O.D.	L.O.D.	L.O.D.	L.O.D.	L.O.D.	L.O.D.	L.O.D.	0.16	0.13
L.O.D.	L.O.D.	L.O.D.	L.O.D.	L.O.D.	L.O.D.	L.O.D.	L.O.D.	L.O.D.	L.O.D.	L.O.D.	L.O.D.	L.O.D.	L.O.D.	L.O.D.
100.68	100.70	100.83	100.55	100.72	100.62	100.73	100.70	100.37	100.04	100.15	100.74	100.70	100.09	100.10
1.98	1.97	1.97	1.97	1.97	1.97	1.97	1.98	1.98	1.99	1.97	1.98	1.98	1.97	1.96
0.02	0.02	0.02	0.02	0.02	0.02	0.02	0.02	0.02	0.01	0.02	0.02	0.02	0.03	0.04
0.00	0.00	0.00	0.01	0.01	0.00	0.00	0.00	0.00	0.00	0.00	0.00	0.00	0.00	0.00
2.00	2.00	2.00	2.00	2.00	2.00	2.00	2.00	2.00	2.00	2.00	2.00	2.00	2.00	2.00
0.01	0.00	0.00	0.00	0.00	0.01	0.00	0.00	0.01	0.00	0.00	0.01	0.00	0.01	0.01
0.00	0.00	0.00	0.00	0.00	0.00	0.00	0.00	0.00	0.01	0.00	0.00	0.01	0.02	0.01
0.01	0.02	0.02	0.02	0.02	0.02	0.02	0.01	0.00	0.00	0.02	0.00	0.00	0.01	0.03
0.71	0.72	0.69	0.70	0.69	0.67	0.70	0.70	0.68	0.69	0.69	0.68	0.67	0.55	0.55
1.18	1.18	1.19	1.18	1.19	1.21	1.19	1.21	1.22	1.21	1.20	1.22	1.23	0.61	0.60
0.03	0.03	0.03	0.03	0.04	0.04	0.03	0.03	0.03	0.03	0.03	0.03	0.03	0.02	0.02
0.06	0.05	0.06	0.06	0.06	0.06	0.06	0.05	0.06	0.06	0.05	0.06	0.06	0.78	0.78
													0.01	0.01
2.00	2.00	2.00	2.00	2.00	2.00	2.00	2.00	2.00	2.00	2.00	2.00	2.00	2.00	2.00
4.00	4.00	4.00	4.00	4.00	4.00	4.00	4.00	4.00	4.00	4.00	4.00	4.00	4.00	4.00
2.9	2.7	3.1	3.2	3.0	3.2	2.9	2.4	2.9	3.2	2.8	3.2	2.9	40.1	39.7
36.2	36.5	35.3	35.7	35.1	34.4	35.6	35.5	34.7	35.0	35.1	34.5	34.1	28.4	28.2
60.9	60.9	61.6	61.1	61.9	62.4	61.5	62.1	62.4	61.8	62.1	62.3	63.0	31.5	32.0

Table S2.2a. Pyroxene analyses in wt.% and atoms per formula unit for Elsie Mountain Formation metabasalts *(cont.)*.

FSTJ299	**FSTJ299**	**FSTJ299**	**FSTJ299**	**FSTJ299**	**FSTJ299**	**FSTJ299**	**FSTJ299**	**FSTJ299**	**FSTJ299**	**FSTJ298**	**FSTJ298**	**FSTJ298**	**FSTJ298**	**FSTJ298**
FSTJ299_site_1_cpx_3	FSTJ299_site_1_cpx_4	FSTJ299_site_1_cpx_5	FSTJ299_site_2_cpx_6	FSTJ299_site_2_cpx_7	FSTJ299_site_2_cpx_8	FSTJ299_site_2_cpx_9	FSTJ299_site_2_cpx_10	FSTJ299_site_2_cpx_11	FSTJ299_site_2_cpx_12	FSTJ298_site_1_opx_1	FSTJ298_site_1_opx_2	FSTJ298_site_1_opx_3	FSTJ298_site_1_opx_4	FSTJ298_site_1_opx_5
BH Cpx	BH Cpx	BH Cpx	BH Cpx	BH Cpx	BH Cpx	BH Cpx	BH Cpx	BH Cpx	BH Cpx	BH Opx	BH Opx	BH Opx	BH Opx	BH Opx
50.75	50.94	50.97	50.67	50.60	50.91	50.53	50.74	50.59	50.71	49.57	49.72	49.82	49.46	49.94
0.23	0.20	0.24	0.23	0.21	0.21	0.21	0.20	0.24	0.21	0.17	0.15	0.15	0.14	0.10
0.97	1.02	0.97	1.08	1.05	1.01	1.08	1.01	1.06	1.03	0.42	0.45	0.40	0.45	0.46
L.O.D.	L.O.D.	L.O.D.	L.O.D.	L.O.D.	L.O.D.	L.O.D.	L.O.D.	L.O.D.	L.O.D.	L.O.D.	L.O.D.	L.O.D.	L.O.D.	L.O.D.
18.94	18.31	17.88	17.27	18.79	18.90	19.38	18.42	19.11	19.07	36.25	35.67	36.25	36.18	36.12
0.50	0.52	0.50	0.45	0.50	0.52	0.52	0.55	0.54	0.51	0.91	0.90	0.93	0.88	0.88
9.78	9.69	9.59	9.42	9.43	9.72	9.47	9.46	9.51	9.64	11.69	11.84	11.61	11.76	11.71
18.87	19.46	19.86	20.41	19.11	19.18	18.65	19.57	18.86	18.86	1.28	1.55	1.17	1.14	1.38
0.17	0.14	0.17	0.18	0.16	0.15	0.14	0.15	0.16	0.14	L.O.D.	L.O.D.	L.O.D.	L.O.D.	L.O.D.
L.O.D.	L.O.D.	L.O.D.	L.O.D.	L.O.D.	L.O.D.	L.O.D.	L.O.D.	L.O.D.	L.O.D.	L.O.D.	L.O.D.	L.O.D.	L.O.D.	L.O.D.
100.20	100.27	100.17	99.71	99.85	100.59	99.99	100.11	100.06	100.18	100.28	100.28	100.33	100.00	100.59
1.96	1.97	1.97	1.96	1.97	1.96	1.96	1.96	1.96	1.96	1.98	1.98	1.99	1.98	1.99
0.04	0.03	0.03	0.04	0.03	0.04	0.04	0.04	0.04	0.04	0.02	0.02	0.01	0.02	0.01
0.00	0.00	0.00	0.00	0.00	0.00	0.00	0.00	0.00	0.00	0.00	0.00	0.00	0.00	0.00
2.00	2.00	2.00	2.00	2.00	2.00	2.00	2.00	2.00	2.00	2.00	2.00	2.00	2.00	2.00
0.01	0.01	0.01	0.01	0.01	0.01	0.01	0.01	0.01	0.01	0.01	0.00	0.00	0.00	0.00
0.01	0.01	0.01	0.01	0.01	0.01	0.01	0.01	0.01	0.01	0.00	0.00	0.01	0.00	0.01
0.03	0.02	0.02	0.02	0.02	0.03	0.02	0.03	0.03	0.02	0.01	0.00	0.00	0.01	0.00
0.56	0.56	0.55	0.54	0.55	0.56	0.55	0.55	0.55	0.56	0.70	0.70	0.69	0.70	0.70
0.58	0.57	0.56	0.54	0.59	0.58	0.61	0.57	0.59	0.59	1.20	1.19	1.21	1.20	1.20
0.02	0.02	0.02	0.01	0.02	0.02	0.02	0.02	0.02	0.02	0.03	0.03	0.03	0.03	0.03
0.78	0.80	0.82	0.85	0.80	0.79	0.78	0.81	0.78	0.78	0.05	0.07	0.05	0.05	0.06
0.01	0.01	0.01	0.01	0.01	0.01	0.01	0.01	0.01	0.01					
2.00	2.00	2.00	2.00	2.00	2.00	2.00	2.00	2.00	2.00	2.00	2.00	2.00	2.00	2.00
4.00	4.00	4.00	4.00	4.00	4.00	4.00	4.00	4.00	4.00	4.00	4.00	4.00	4.00	4.00
39.9	41.2	42.1	43.4	40.7	40.4	39.7	41.5	40.1	40.0	2.8	3.4	2.6	2.5	3.0
28.8	28.5	28.3	27.9	28.0	28.5	28.1	27.9	28.1	28.4	35.5	35.9	35.4	35.8	35.5
31.3	30.3	29.6	28.7	31.3	31.1	32.2	30.5	31.7	31.6	61.7	60.7	62.0	61.7	61.5

Table S2.2a. Pyroxene analyses in wt.% and atoms per formula unit for Elsie Mountain Formation metabasalts *(cont.)*.

FSTJ298	**FSTJ298**	**FSTJ298**	**FSTJ298**	**FSTJ298**	**FSTJ298**	**FSTJ298**	**FSTJ298**	**FSTJ298**	**FSTJ298**	**FSTJ298**	**FSTJ298**	**FSTJ298**	**FSTJ298**	**FSTJ294**
FSTJ298_site_1_opx_6	FSTJ298_site_1_opx_7	FSTJ298_site_1_opx_8	FSTJ298_site_1_opx_9	FSTJ298_site_1_opx_10	FSTJ298_site_1_cpx_1	FSTJ298_site_1_cpx_2	FSTJ298_site_1_cpx_3	FSTJ298_site_1_cpx_4	FSTJ298_site_1_cpx_5	FSTJ298_site_1_cpx_6	FSTJ298_site_1_cpx_7	FSTJ298_site_1_cpx_8	FSTJ298_site_1_cpx_9	FSTJ294_site_1_opx_1
BH	BH	BH	BH	BH	BH	BH	BH	BH	BH	BH	BH	BH	BH	BH
Opx	Opx	Opx	Opx	Opx	Cpx	Cpx	Cpx	Cpx	Cpx	Cpx	Cpx	Cpx	Cpx	Opx
49.86	49.50	49.68	49.55	49.73	50.52	50.72	50.65	50.88	50.88	50.76	50.87	50.98	50.93	48.97
0.12	0.18	0.16	0.16	0.14	0.23	0.19	0.21	0.20	0.24	0.19	0.20	0.22	0.19	0.14
0.41	0.40	0.41	0.48	0.42	0.87	0.84	0.94	0.87	0.85	0.83	0.90	0.86	0.94	0.45
L.O.D.	L.O.D.	L.O.D.	L.O.D.	L.O.D.	L.O.D.	L.O.D.	L.O.D.	L.O.D.	L.O.D.	L.O.D.	L.O.D.	L.O.D.	L.O.D.	L.O.D.
35.95	36.92	36.34	36.43	36.27	18.91	18.06	19.00	18.66	18.36	18.65	18.42	18.63	19.46	37.91
0.90	0.86	0.89	0.91	0.90	0.48	0.48	0.52	0.51	0.50	0.47	0.46	0.46	0.52	1.17
11.89	11.39	11.76	11.70	11.78	9.64	9.68	9.54	9.66	9.55	9.59	9.43	9.54	9.64	10.08
1.50	1.34	1.26	1.19	1.17	19.27	19.65	18.90	19.25	19.31	19.25	19.72	19.49	18.73	1.09
L.O.D.	L.O.D.	L.O.D.	L.O.D.	L.O.D.	0.16	0.15	0.15	0.17	0.17	0.15	0.15	0.15	0.15	L.O.D.
L.O.D.	L.O.D.	L.O.D.	L.O.D.	L.O.D.	L.O.D.	L.O.D.	L.O.D.	L.O.D.	L.O.D.	L.O.D.	L.O.D.	L.O.D.	L.O.D.	L.O.D.
100.62	100.58	100.48	100.42	100.39	100.08	99.75	99.91	100.20	99.86	99.90	100.15	100.32	100.57	99.80
1.98	1.98	1.98	1.98	1.98	1.96	1.97	1.97	1.97	1.97	1.97	1.97	1.97	1.97	1.99
0.02	0.02	0.02	0.02	0.02	0.04	0.03	0.03	0.03	0.03	0.03	0.03	0.03	0.03	0.01
0.00	0.00	0.00	0.00	0.00	0.00	0.00	0.00	0.00	0.00	0.00	0.00	0.00	0.00	0.00
2.00	2.00	2.00	2.00	2.00	2.00	2.00	2.00	2.00	2.00	2.00	2.00	2.00	2.00	2.00
0.00	0.01	0.00	0.00	0.00	0.01	0.01	0.01	0.01	0.01	0.01	0.01	0.01	0.01	0.00
0.00	0.00	0.00	0.00	0.00	0.00	0.01	0.01	0.01	0.01	0.01	0.01	0.01	0.01	0.01
0.01	0.01	0.01	0.01	0.00	0.04	0.03	0.02	0.03	0.01	0.02	0.02	0.02	0.03	0.00
0.70	0.68	0.70	0.70	0.70	0.56	0.56	0.55	0.56	0.55	0.55	0.54	0.55	0.55	0.61
1.19	1.22	1.20	1.21	1.21	0.57	0.56	0.59	0.58	0.58	0.58	0.58	0.58	0.60	1.29
0.03	0.03	0.03	0.03	0.03	0.02	0.02	0.02	0.02	0.02	0.02	0.02	0.01	0.02	0.04
0.06	0.06	0.05	0.05	0.05	0.80	0.82	0.79	0.80	0.80	0.80	0.82	0.81	0.77	0.05
					0.01	0.01	0.01	0.01	0.01	0.01	0.01	0.01	0.01	
2.00	2.00	2.00	2.00	2.00	2.00	2.00	2.00	2.00	2.00	2.00	2.00	2.00	2.00	2.00
4.00	4.00	4.00	4.00	4.00	4.00	4.00	4.00	4.00	4.00	4.00	4.00	4.00	4.00	4.00
3.2	2.9	2.7	2.6	2.5	40.7	41.6	40.2	40.7	41.1	40.8	41.8	41.2	39.6	2.4
35.9	34.5	35.6	35.5	35.7	28.3	28.5	28.2	28.4	28.3	28.3	27.8	28.0	28.3	31.4
60.9	62.6	61.7	62.0	61.7	31.0	29.9	31.6	30.8	30.5	30.9	30.5	30.7	32.1	66.2

Table S2.2a. Pyroxene analyses in wt.% and atoms per formula unit for Elsie Mountain Formation metabasalts *(cont.)*.

FSTJ294	**FSTJ294**	**FSTJ294**	**FSTJ294**	**FSTJ294**	**FSTJ294**	**FSTJ294**	**FSTJ294**	**FSTJ294**	**FSTJ294**	**FSTJ294**	**FSTJ294**	**FSTJ294**	**FSTJ294**	**FSTJ294**
FSTJ294_site_1_opx_2	FSTJ294_site_1_opx_3	FSTJ294_site_1_opx_4	FSTJ294_site_1_opx_5	FSTJ294_site_1_opx_6	FSTJ294_site_1_opx_7	FSTJ294_site_1_opx_8	FSTJ294_site_1_opx_9	FSTJ294_site_1_opx_10	FSTJ294_site_1_opx_11	FSTJ294_site_1_opx_12	FSTJ294_site_1_opx_13	FSTJ294_site_1_opx_14	FSTJ294_site_1_opx_15	FSTJ294_site_1_opx_16
BH Opx	BH Opx	BH Opx	BH Opx	BH Opx	BH Opx	BH Opx	BH Opx	BH Opx	BH Opx	BH Opx	BH Opx	BH Opx	BH Opx	BH Opx
49.14	49.06	49.35	49.80	49.77	49.46	49.95	49.86	49.53	49.62	49.91	49.75	49.60	49.11	49.15
0.18	0.15	0.12	0.16	0.14	0.13	0.14	0.17	0.16	0.15	0.12	0.15	0.15	0.16	0.18
0.43	0.38	0.33	0.44	0.42	0.41	0.41	0.41	0.42	0.34	0.33	0.42	0.37	0.42	0.40
L.O.D.	L.O.D.	L.O.D.	L.O.D.	L.O.D.	L.O.D.	L.O.D.	L.O.D.	L.O.D.	L.O.D.	L.O.D.	L.O.D.	L.O.D.	L.O.D.	L.O.D.
38.30	38.32	38.50	36.40	36.35	36.28	36.39	36.31	36.32	36.58	36.45	37.02	36.31	39.25	38.16
1.31	1.29	1.32	0.89	0.86	0.85	0.85	0.90	0.92	0.94	0.88	0.95	0.91	1.16	1.14
9.84	9.93	9.87	11.32	11.55	11.56	11.76	11.66	11.55	11.30	11.41	11.08	11.67	9.23	10.03
1.09	1.08	0.94	1.08	1.25	1.17	1.15	1.27	1.08	1.23	1.50	1.35	1.35	1.17	1.25
L.O.D.	L.O.D.	L.O.D.	L.O.D.	L.O.D.	L.O.D.	L.O.D.	L.O.D.	L.O.D.	L.O.D.	L.O.D.	L.O.D.	L.O.D.	L.O.D.	L.O.D.
L.O.D.	L.O.D.	L.O.D.	L.O.D.	L.O.D.	L.O.D.	L.O.D.	L.O.D.	L.O.D.	L.O.D.	L.O.D.	L.O.D.	L.O.D.	L.O.D.	L.O.D.
100.27	100.20	100.42	100.09	100.34	99.87	100.65	100.58	99.97	100.17	100.60	100.71	100.36	100.49	100.32
1.99	1.99	2.00	2.00	1.99	1.99	1.99	1.99	1.99	1.99	1.99	1.99	1.98	1.99	1.99
0.01	0.01	0.00	0.00	0.01	0.01	0.01	0.01	0.01	0.01	0.01	0.01	0.02	0.01	0.01
0.00	0.00	0.00	0.00	0.00	0.00	0.00	0.00	0.00	0.00	0.00	0.00	0.00	0.00	0.00
2.00	2.00	2.00	2.00	2.00	2.00	2.00	2.00	2.00	2.00	2.00	2.00	2.00	2.00	2.00
0.01	0.00	0.00	0.00	0.00	0.00	0.00	0.01	0.00	0.00	0.00	0.00	0.00	0.00	0.01
0.01	0.01	0.01	0.02	0.01	0.01	0.01	0.01	0.01	0.01	0.01	0.01	0.00	0.01	0.01
0.00	0.00	0.00	0.00	0.00	0.00	0.00	0.00	0.00	0.00	0.00	0.00	0.01	0.00	0.00
0.59	0.60	0.60	0.68	0.69	0.69	0.70	0.69	0.69	0.68	0.68	0.66	0.69	0.56	0.60
1.30	1.30	1.30	1.22	1.22	1.22	1.21	1.21	1.22	1.23	1.22	1.24	1.20	1.33	1.29
0.04	0.04	0.05	0.03	0.03	0.03	0.03	0.03	0.03	0.03	0.03	0.03	0.03	0.04	0.04
0.05	0.05	0.04	0.05	0.05	0.05	0.05	0.05	0.05	0.05	0.06	0.06	0.06	0.05	0.05
2.00	2.00	2.00	2.00	2.00	2.00	2.00	2.00	2.00	2.00	2.00	2.00	2.00	2.00	2.00
4.00	4.00	4.00	4.00	4.00	4.00	4.00	4.00	4.00	4.00	4.00	4.00	4.00	4.00	4.00
2.4	2.4	2.1	2.4	2.7	2.6	2.5	2.8	2.4	2.7	3.3	3.0	2.9	2.6	2.8
30.6	30.8	30.7	34.8	35.2	35.3	35.6	35.4	35.3	34.6	34.6	33.8	35.4	28.8	31.0
66.9	66.8	67.2	62.8	62.1	62.1	61.9	61.8	62.3	62.7	62.1	63.3	61.7	68.6	66.2

Table S2.2a. Pyroxene analyses in wt.% and atoms per formula unit for Elsie Mountain Formation metabasalts *(cont.)*.

FSTJ294	**FSTJ294**	**FSTJ294**	**FSTJ294**	**FSTJ294**	**FSTJ294**	**FSTJ294**	**FSTJ294**	**FSTJ294**	**FSTJ294**	**FSTJ294**	**FSTJ294**	**FSTJ294**	**FSTJ294**	**FSTJ294**
FSTJ294_site_1_opx_17	FSTJ294_site_1_opx_18	FSTJ294_site_1_opx_19	FSTJ294_site_1_opx_20	FSTJ294_site_1_opx_21	FSTJ294_site_1_opx_22	FSTJ294_site_1_opx_23	FSTJ294_site_1_opx_24	FSTJ294_site_1_opx_25	FSTJ294_site_1_opx_26	FSTJ294_site_1_opx_27	FSTJ294_site_1_opx_28	FSTJ294_site_1_opx_29	FSTJ294_site_1_opx_30	FSTJ294_site_1_opx_31
BH	BH	BH	BH	BH	BH	BH	BH	BH	BH	BH	BH	BH	BH	BH
Opx	Opx	Opx	Opx	Opx	Opx	Opx	Opx	Opx	Opx	Opx	Opx	Opx	Opx	Opx
49.25	49.40	49.44	50.13	49.91	49.72	49.64	49.71	49.79	49.74	49.73	49.53	49.76	49.64	49.51
0.17	0.22	0.19	0.17	0.16	0.21	0.15	0.12	0.21	0.15	0.12	0.17	0.17	0.15	0.13
0.43	0.47	0.41	0.46	0.42	0.46	0.41	0.36	0.40	0.42	0.39	0.42	0.45	0.45	0.43
L.O.D.	L.O.D.	L.O.D.	L.O.D.	L.O.D.	L.O.D.	L.O.D.	L.O.D.	L.O.D.	L.O.D.	L.O.D.	L.O.D.	L.O.D.	L.O.D.	L.O.D.
37.32	37.85	36.89	36.31	36.29	35.91	36.40	36.06	36.43	36.57	36.49	36.78	36.94	36.94	36.53
0.95	1.07	1.03	0.83	0.81	0.81	0.83	0.83	0.82	0.86	0.84	0.89	0.90	0.88	0.85
10.69	10.61	11.05	11.70	11.56	11.69	11.58	11.73	11.52	11.50	11.48	11.25	11.05	11.25	11.45
1.26	1.07	1.19	1.29	1.33	1.23	1.41	1.49	1.39	1.16	1.41	1.14	1.20	1.23	1.24
L.O.D.	L.O.D.	L.O.D.	L.O.D.	L.O.D.	L.O.D.	L.O.D.	L.O.D.	L.O.D.	L.O.D.	L.O.D.	L.O.D.	L.O.D.	L.O.D.	L.O.D.
L.O.D.	L.O.D.	L.O.D.	L.O.D.	L.O.D.	L.O.D.	L.O.D.	L.O.D.	L.O.D.	L.O.D.	L.O.D.	L.O.D.	L.O.D.	L.O.D.	L.O.D.
100.06	100.70	100.19	100.89	100.48	100.01	100.41	100.31	100.55	100.39	100.45	100.18	100.48	100.53	100.13
1.99	1.98	1.99	1.99	1.99	1.99	1.98	1.98	1.99	1.99	1.99	1.99	1.99	1.99	1.98
0.01	0.02	0.01	0.01	0.01	0.01	0.02	0.02	0.01	0.01	0.01	0.01	0.01	0.01	0.02
0.00	0.00	0.00	0.00	0.00	0.00	0.00	0.00	0.00	0.00	0.00	0.00	0.00	0.00	0.00
2.00	2.00	2.00	2.00	2.00	2.00	2.00	2.00	2.00	2.00	2.00	2.00	2.00	2.00	2.00
0.01	0.01	0.01	0.01	0.00	0.01	0.00	0.00	0.01	0.00	0.00	0.00	0.01	0.00	0.00
0.01	0.01	0.01	0.01	0.01	0.01	0.00	0.00	0.01	0.01	0.01	0.01	0.01	0.01	0.00
0.00	0.00	0.00	0.00	0.00	0.00	0.01	0.01	0.00	0.00	0.00	0.00	0.00	0.00	0.00
0.64	0.63	0.66	0.69	0.69	0.70	0.69	0.70	0.69	0.69	0.68	0.67	0.66	0.67	0.68
1.26	1.27	1.24	1.21	1.21	1.20	1.21	1.20	1.22	1.22	1.22	1.23	1.24	1.24	1.22
0.03	0.04	0.04	0.03	0.03	0.03	0.03	0.03	0.03	0.03	0.03	0.03	0.03	0.03	0.03
0.05	0.05	0.05	0.06	0.06	0.05	0.06	0.06	0.06	0.05	0.06	0.05	0.05	0.05	0.05
2.00	2.00	2.00	2.00	2.00	2.00	2.00	2.00	2.00	2.00	2.00	2.00	2.00	2.00	2.00
4.00	4.00	4.00	4.00	4.00	4.00	4.00	4.00	4.00	4.00	4.00	4.00	4.00	4.00	4.00
2.8	2.4	2.6	2.8	2.9	2.7	3.1	3.2	3.0	2.5	3.1	2.5	2.6	2.7	2.7
32.9	32.5	33.9	35.4	35.2	35.7	35.1	35.5	35.0	35.0	34.8	34.4	33.9	34.2	34.9
64.4	65.1	63.5	61.7	61.9	61.6	61.9	61.2	62.0	62.5	62.1	63.1	63.5	63.1	62.4

Table S2.2a. Pyroxene analyses in wt.% and atoms per formula unit for Elsie Mountain Formation metabasalts *(cont.)*.

FSTJ294	**FSTJ294**	**FSTJ294**	**FSTJ294**	**FSTJ294**	**FSTJ294**	**FSTJ294**	**FSTJ294**	**FSTJ294**	**FSTJ294**	**FSTJ294**	**FSTJ294**	**FSTJ294**	**FSTJ294**	**FSTJ118**
FSTJ294_site_1_opx_32	FSTJ294_site_1_opx_33	FSTJ294_site_1_opx_34	FSTJ294_site_1_cpx_1	FSTJ294_site_1_cpx_2	FSTJ294_site_1_cpx_3	FSTJ294_site_1_cpx_4	FSTJ294_site_1_cpx_5	FSTJ294_site_1_cpx_6	FSTJ294_site_1_cpx_7	FSTJ294_site_1_cpx_8	FSTJ294_site_1_cpx_9	FSTJ294_site_1_cpx_10	FSTJ294_site_1_cpx_11	EMP118Q2S1
BH	BH	BH	BH	BH	BH	BH	BH	BH	BH	BH	BH	BH	BH	BH
Opx	Opx	Opx	Cpx	Cpx	Cpx	Cpx	Cpx	Cpx	Cpx	Cpx	Cpx	Cpx	Cpx	Opx
49.62	49.24	49.07	51.39	51.01	50.59	50.94	51.43	51.59	51.39	51.26	50.80	50.90	51.23	49.96
0.16	0.15	0.15	0.22	0.19	0.19	0.20	0.19	0.17	0.24	0.24	0.21	0.20	0.20	0.14
0.44	0.36	0.43	0.89	0.87	0.96	0.87	0.86	0.82	0.84	0.87	0.91	0.86	0.88	0.49
L.O.D.	L.O.D.	L.O.D.	0.03	L.O.D.	L.O.D.	L.O.D.	L.O.D.	L.O.D.	L.O.D.	L.O.D.	L.O.D.	L.O.D.	L.O.D.	L.O.D.
36.73	38.19	38.50	18.67	17.65	18.89	18.57	17.27	16.76	16.97	17.01	18.58	18.61	18.07	34.08
0.90	1.00	1.03	0.44	0.44	0.46	0.44	0.43	0.41	0.45	0.45	0.47	0.49	0.46	0.89
11.14	10.71	10.59	9.59	9.54	9.66	9.69	9.52	9.56	9.61	9.52	9.76	9.52	9.53	13.57
1.35	1.21	1.07	18.71	19.67	18.60	18.87	20.44	20.69	20.41	20.46	18.90	19.01	19.71	1.03
L.O.D.	L.O.D.	L.O.D.	0.16	0.18	0.14	0.16	0.17	0.16	0.19	0.19	0.16	0.15	0.19	L.O.D.
L.O.D.	L.O.D.	L.O.D.	L.O.D.	L.O.D.	L.O.D.	L.O.D.	L.O.D.	L.O.D.	L.O.D.	L.O.D.	L.O.D.	L.O.D.	L.O.D.	L.O.D.
100.33	100.86	100.83	100.09	99.53	99.49	99.74	100.32	100.16	100.10	100.00	99.79	99.74	100.27	100.16
1.99	1.97	1.97	1.99	1.98	1.97	1.98	1.98	1.99	1.98	1.98	1.97	1.98	1.98	1.97
0.01	0.02	0.02	0.01	0.02	0.03	0.02	0.02	0.01	0.02	0.02	0.03	0.02	0.02	0.02
0.00	0.01	0.01	0.00	0.00	0.00	0.00	0.00	0.00	0.00	0.00	0.00	0.00	0.00	0.00
2.00	2.00	2.00	2.00	2.00	2.00	2.00	2.00	2.00	2.00	2.00	2.00	2.00	2.00	2.00
0.00	0.00	0.00	0.01	0.01	0.01	0.01	0.01	0.01	0.01	0.01	0.01	0.01	0.01	0.00
0.01	0.00	0.00	0.03	0.02	0.02	0.02	0.02	0.03	0.02	0.02	0.01	0.02	0.02	0.00
			0.00											
0.00	0.02	0.02	0.00	0.00	0.01	0.00	0.00	0.00	0.00	0.00	0.02	0.00	0.01	0.02
0.67	0.64	0.63	0.55	0.55	0.56	0.56	0.55	0.55	0.55	0.55	0.56	0.55	0.55	0.80
1.23	1.25	1.26	0.60	0.57	0.60	0.60	0.56	0.54	0.55	0.55	0.59	0.60	0.58	1.10
0.03	0.03	0.03	0.01	0.01	0.02	0.01	0.01	0.01	0.01	0.01	0.02	0.02	0.02	0.03
0.06	0.05	0.05	0.78	0.82	0.78	0.79	0.84	0.85	0.84	0.85	0.79	0.79	0.82	0.04
			0.01	0.01	0.01	0.01	0.01	0.01	0.01	0.01	0.01	0.01	0.01	
2.00	2.00	2.00	2.00	2.00	2.00	2.00	2.00	2.00	2.00	2.00	2.00	2.00	2.00	2.00
4.00	4.00	4.00	4.00	4.00	4.00	4.00	4.00	4.00	4.00	4.00	4.00	4.00	4.00	4.00
3.0	2.6	2.3	40.1	42.1	39.8	40.3	43.3	43.9	43.4	43.6	40.2	40.6	41.9	2.2
34.0	32.6	32.3	28.6	28.4	28.7	28.8	28.1	28.3	28.4	28.2	28.9	28.3	28.2	40.7
63.0	64.8	65.3	31.3	29.5	31.5	30.9	28.6	27.8	28.2	28.3	30.9	31.1	30.0	57.1

Table S2.2a. Pyroxene analyses in wt.% and atoms per formula unit for Elsie Mountain Formation metabasalts *(cont.)*.

FSTJ118	**FSTJ118**	**FSTJ118**	**FSTJ118**	**FSTJ118**	**FSTJ118**	**FSTJ118**	**FSTJ118**	**FSTJ118**	**FSTJ118**	**FSTJ118**	**FSTJ118**	**FSTJ118**	**FSTJ118**
EMP118Q3	EMP118Q4	EMP118Q4_2	EMP118Q5O	EMP118Q5	EMP118Q	EMP118Q	EMP118Q3	EMP118Q4	EMP118Q4_2	EMP118Q5C	EMP118Q5C	EMP118Q5CP	EMP118Q5C
S1	_2S1	S2	PXS5	OPXS6	7OPX7	2S2	S11	_2S3	S5	PXS7	PXS8	XS9	PXS10
BH	BH	BH	BH	BH	BH	BH	BH	BH	BH	BH	BH	BH	BH
Opx	Opx	Opx	Opx	Opx	Opx	Cpx	Cpx	Cpx	Cpx	Cpx	Cpx	Cpx	Cpx
49.91	49.86	49.75	49.98	50.10	49.73	51.19	51.27	51.34	51.49	50.77	50.84	51.53	50.55
0.15	0.15	0.16	0.14	0.16	0.14	0.23	0.23	0.18	0.24	0.23	0.23	0.12	0.24
0.44	0.47	0.47	0.44	0.47	0.48	1.06	1.01	1.38	1.03	0.97	1.04	0.74	1.07
L.O.D.	L.O.D.	L.O.D.	L.O.D.	L.O.D.	L.O.D.	L.O.D.	L.O.D.	L.O.D.	L.O.D.	L.O.D.	L.O.D.	L.O.D.	L.O.D.
34.26	33.76	33.83	33.93	33.85	34.20	15.24	15.18	16.11	15.10	18.88	15.34	15.84	15.90
0.92	0.81	0.77	0.92	0.88	0.95	0.41	0.38	0.36	0.38	0.46	0.39	0.40	0.38
13.59	13.67	13.75	13.90	13.91	13.57	10.93	11.18	10.83	11.05	11.46	11.14	11.10	11.11
1.14	1.23	1.16	1.17	1.15	1.12	20.74	20.81	20.13	20.84	16.69	20.38	20.09	19.68
L.O.D.	L.O.D.	L.O.D.	L.O.D.	L.O.D.	L.O.D.	0.19	0.21	0.16	0.20	0.12	0.19	0.15	0.20
L.O.D.	L.O.D.	L.O.D.	L.O.D.	L.O.D.	L.O.D.	L.O.D.	L.O.D.	0.03	L.O.D.	L.O.D.	L.O.D.	L.O.D.	L.O.D.
100.39	99.95	99.89	100.48	100.53	100.19	99.99	100.27	100.53	100.33	99.57	99.56	99.97	99.13
1.97	1.97	1.97	1.96	1.97	1.96	1.96	1.95	1.96	1.96	1.96	1.95	1.97	1.95
0.02	0.02	0.02	0.02	0.02	0.02	0.04	0.05	0.04	0.04	0.04	0.05	0.03	0.05
0.01	0.01	0.01	0.01	0.01	0.01	0.00	0.00	0.00	0.00	0.00	0.00	0.00	0.00
2.00	2.00	2.00	2.00	2.00	2.00	2.00	2.00	2.00	2.00	2.00	2.00	2.00	2.00
0.00	0.00	0.00	0.00	0.00	0.00	0.01	0.01	0.01	0.01	0.01	0.01	0.00	0.01
0.00	0.00	0.00	0.00	0.00	0.00	0.00	0.00	0.02	0.01	0.01	0.00	0.01	0.00
0.02	0.02	0.02	0.03	0.02	0.03	0.04	0.05	0.03	0.03	0.03	0.05	0.02	0.05
0.80	0.81	0.81	0.81	0.81	0.80	0.62	0.63	0.62	0.63	0.66	0.64	0.63	0.64
1.09	1.09	1.09	1.07	1.08	1.09	0.45	0.43	0.49	0.45	0.58	0.44	0.48	0.46
0.03	0.03	0.03	0.03	0.03	0.03	0.01	0.01	0.01	0.01	0.01	0.01	0.01	0.01
0.05	0.05	0.05	0.05	0.05	0.05	0.85	0.85	0.82	0.85	0.69	0.84	0.82	0.81
						0.01	0.02	0.01	0.01	0.01	0.01	0.01	0.01
								0.00					
2.00	2.00	2.00	2.00	2.00	2.00	2.00	2.00	2.00	2.00	2.00	2.00	2.00	2.00
4.00	4.00	4.00	4.00	4.00	4.00	4.00	4.00	4.00	4.00	4.00	4.00	4.00	4.00
2.5	2.7	2.5	2.5	2.5	2.4	43.4	43.2	42.1	43.4	35.2	42.6	42.0	41.4
40.6	40.9	41.2	41.5	41.5	40.7	31.8	32.3	31.5	32.0	33.7	32.4	32.2	32.5
56.9	56.4	56.3	56.0	56.1	56.9	24.9	24.5	26.3	24.6	31.1	25.0	25.8	26.1

Table S2.2a. Pyroxene analyses in wt.% and atoms per formula unit for Elsie Mountain Formation metabasalts *(cont.)*.

FSTJ118	**FSTJ292**	**FSTJ292**	**FSTJ292**	**FSTJ292**	**FSTJ292**	**FSTJ292**	**FSTJ292**	**FSTJ292**	**FSTJ292**	**FSTJ292**	**FSTJ292**	**FSTJ292**	**FSTJ292**	**FSTJ292**	**FSTJ292**
EMP118Q7	FSTJ292_si	FSTJ292_si	FSTJ292_si	FSTJ292_si	FSTJ292_si	FSTJ292_si	FSTJ292_si	FSTJ292_si	FSTJ292_si	FSTJ292_si	FSTJ292_si	FSTJ292_si	FSTJ292_si	FSTJ292_si	FSTJ292_si
CPX8	te_1_opx_1	te_1_opx_2	te_1_opx_3	te_1_opx_4	te_1_opx_5	te_1_opx_6	te_1_opx_7	te_1_opx_8	te_1_opx_9	te_1_cpx_1	te_1_cpx_2	te_1_cpx_3	te_1_cpx_4	te_1_cpx_5	
BH	BH	BH	BH	BH	BH	BH	BH	BH	BH	BH	BH	BH	BH	BH	
Cpx	Opx	Opx	Opx	Opx	Opx	Opx	Opx	Opx	Opx	Cpx	Cpx	Cpx	Cpx	Cpx	
51.04	50.34	49.98	50.21	50.72	50.60	49.88	50.33	50.30	50.39	51.63	51.76	51.79	51.96	52.00	
0.27	0.12	0.09	0.12	0.12	0.11	0.10	0.13	0.11	0.12	0.12	0.16	0.17	0.17	0.16	
1.04	0.32	0.31	0.34	0.35	0.39	0.30	0.33	0.36	0.31	0.67	0.65	0.70	0.62	0.65	
L.O.D.	L.O.D.	L.O.D.	L.O.D.	L.O.D.	L.O.D.	L.O.D.	L.O.D.	L.O.D.	L.O.D.	L.O.D.	L.O.D.	L.O.D.	L.O.D.	L.O.D.	
15.63	35.40	35.57	35.17	34.70	34.76	35.22	34.96	35.53	34.84	17.58	18.13	17.53	16.61	16.34	
0.39	1.07	1.09	1.11	1.01	1.03	1.02	1.00	1.01	1.00	0.55	0.58	0.55	0.53	0.53	
11.01	12.29	12.27	12.35	12.71	12.57	12.29	12.44	12.14	12.53	10.20	10.30	10.15	10.13	10.12	
20.62	1.40	1.13	1.30	1.42	1.39	1.40	1.22	1.33	1.40	19.19	19.10	19.75	20.34	20.89	
0.18	L.O.D.	L.O.D.	L.O.D.	L.O.D.	L.O.D.	L.O.D.	L.O.D.	L.O.D.	L.O.D.	0.20	0.20	0.20	0.23	0.23	
L.O.D.	L.O.D.	L.O.D.	L.O.D.	L.O.D.	L.O.D.	L.O.D.	L.O.D.	L.O.D.	L.O.D.	L.O.D.	L.O.D.	L.O.D.	L.O.D.	L.O.D.	
100.20	100.93	100.44	100.60	101.02	100.85	100.21	100.42	100.78	100.59	100.15	100.86	100.84	100.57	100.91	
1.95	1.99	1.99	1.99	2.00	2.00	1.99	2.00	1.99	2.00	1.99	1.98	1.98	1.99	1.98	
0.05	0.01	0.01	0.01	0.00	0.00	0.01	0.00	0.01	0.00	0.01	0.02	0.02	0.01	0.02	
0.00	0.00	0.00	0.00	0.00	0.00	0.00	0.00	0.00	0.00	0.00	0.00	0.00	0.00	0.00	
2.00	2.00	2.00	2.00	2.00	2.00	2.00	2.00	2.00	2.00	2.00	2.00	2.00	2.00	2.00	
0.01	0.00	0.00	0.00	0.00	0.00	0.00	0.00	0.00	0.00	0.00	0.00	0.00	0.00	0.00	
0.00	0.01	0.00	0.01	0.01	0.02	0.00	0.01	0.01	0.01	0.02	0.01	0.01	0.02	0.01	
0.05	0.00	0.00	0.00	0.00	0.00	0.01	0.00	0.00	0.00	0.00	0.01	0.01	0.00	0.01	
0.63	0.72	0.73	0.73	0.75	0.74	0.73	0.74	0.72	0.74	0.59	0.59	0.58	0.58	0.58	
0.45	1.17	1.18	1.17	1.14	1.15	1.17	1.16	1.18	1.15	0.57	0.57	0.55	0.53	0.51	
0.01	0.04	0.04	0.04	0.03	0.03	0.03	0.03	0.03	0.03	0.02	0.02	0.02	0.02	0.02	
0.84	0.06	0.05	0.06	0.06	0.06	0.06	0.05	0.06	0.06	0.79	0.78	0.81	0.83	0.85	
0.01										0.02	0.01	0.01	0.02	0.02	
2.00	2.00	2.00	2.00	2.00	2.00	2.00	2.00	2.00	2.00	2.00	2.00	2.00	2.00	2.00	
4.00	4.00	4.00	4.00	4.00	4.00	4.00	4.00	4.00	4.00	4.00	4.00	4.00	4.00	4.00	
42.9	3.0	2.5	2.8	3.1	3.0	3.0	2.7	2.9	3.0	40.7	40.1	41.5	42.9	43.8	
31.9	37.1	37.1	37.4	38.3	38.0	37.2	37.8	36.8	37.9	30.1	30.1	29.7	29.7	29.5	
25.2	59.9	60.4	59.8	58.6	59.0	59.8	59.6	60.3	59.1	29.1	29.7	28.8	27.4	26.7	

Table S2.2a. Pyroxene analyses in wt.% and atoms per formula unit for Elsie Mountain Formation metabasalts *(cont.)*.

FSTJ292	**FSTJ292**	**FSTJ292**	**FSTJ292**	**FSTJ292**	**FSTJ292**	**FSTJ069**	**FSTJ069**	**FSTJ069**	**FSTJ069**	**FSTJ069**	**FSTJ069**	**FSTJ069**	**FSTJ069**	**FSTJ069**	**FSTJ308**
FSTJ292_site_1_cpx_6	FSTJ292_site_1_cpx_7	FSTJ292_site_1_cpx_8	FSTJ292_site_1_cpx_9	FSTJ292_site_1_cpx_10	FSTJ292_site_1_cpx_11	EMP069Q1_4S1	EMP069Q1_4S7	EMP069Q1_6S11	EMP069Q1_10S3	EMP069Q1_10S7	EMP069Q1_10S8	EMP069Q1_10S2	EMP069Q1_6S1	EMP069Q1_9S7	FSTJ308_site_1_opx_1
BH Cpx	BH Cpx	BH Cpx	BH Cpx	BH Cpx	BH Cpx	BG Opx	BG Opx	BG Opx	BG Opx	BG Opx	BG Opx	BG Opx	BG Cpx	BG Cpx	BH Opx
51.54	51.62	51.55	51.68	51.36	51.48	49.93	50.31	50.09	50.13	50.01	49.87	50.22	51.30	51.44	49.79
0.15	0.13	0.14	0.17	0.14	0.15	0.11	0.07	0.06	0.06	0.12	0.13	0.07	0.14	0.12	0.10
0.75	0.75	0.68	0.77	0.65	0.71	0.44	0.38	0.50	0.43	0.45	0.52	0.45	0.78	0.72	0.38
L.O.D.	L.O.D.	L.O.D.	L.O.D.	L.O.D.	L.O.D.	L.O.D.	L.O.D.	L.O.D.	L.O.D.	L.O.D.	L.O.D.	L.O.D.	L.O.D.	L.O.D.	L.O.D.
17.52	16.90	16.68	16.92	17.67	17.63	33.38	33.33	34.35	34.06	34.37	34.74	33.97	15.60	15.09	36.66
0.54	0.52	0.54	0.56	0.55	0.56	0.67	0.73	0.77	0.69	0.81	0.84	0.69	0.36	0.35	0.90
10.08	10.27	9.92	9.99	10.08	10.06	14.02	13.98	13.48	14.03	13.41	13.29	14.08	10.78	10.56	11.23
19.30	20.07	20.07	19.51	19.06	19.15	1.24	1.26	1.30	1.19	1.25	1.06	1.18	20.89	21.46	1.45
0.25	0.26	0.26	0.28	0.24	0.22	L.O.D.	L.O.D.	L.O.D.	L.O.D.	L.O.D.	L.O.D.	L.O.D.	0.06	0.07	L.O.D.
L.O.D.	L.O.D.	L.O.D.	L.O.D.	L.O.D.	L.O.D.	L.O.D.	L.O.D.	L.O.D.	L.O.D.	L.O.D.	L.O.D.	L.O.D.	L.O.D.	L.O.D.	L.O.D.
100.12	100.53	99.85	99.88	99.75	99.97	99.80	100.07	100.55	100.60	100.42	100.45	100.65	99.88	99.80	100.51
1.99	1.98	1.99	1.99	1.99	1.99	1.97	1.98	1.97	1.97	1.97	1.97	1.97	1.97	1.98	1.99
0.01	0.02	0.01	0.01	0.01	0.01	0.02	0.02	0.02	0.02	0.02	0.02	0.02	0.03	0.02	0.01
0.00	0.00	0.00	0.00	0.00	0.00	0.01	0.00	0.00	0.01	0.01	0.01	0.01	0.00	0.00	0.00
2.00	2.00	2.00	2.00	2.00	2.00	2.00	2.00	2.00	2.00	2.00	2.00	2.00	2.00	2.00	2.00
0.00	0.00	0.00	0.00	0.00	0.00	0.00	0.00	0.00	0.00	0.00	0.00	0.00	0.00	0.00	0.00
0.02	0.01	0.02	0.03	0.02	0.02	0.00	0.00	0.00	0.00	0.00	0.00	0.00	0.00	0.01	0.01
0.01	0.03	0.00	0.00	0.01	0.00	0.02	0.01	0.02	0.03	0.02	0.02	0.03	0.02	0.01	0.00
0.58	0.59	0.57	0.57	0.58	0.58	0.83	0.82	0.79	0.82	0.79	0.78	0.82	0.62	0.60	0.67
0.56	0.51	0.54	0.55	0.56	0.57	1.07	1.09	1.10	1.08	1.11	1.12	1.08	0.48	0.47	1.23
0.02	0.02	0.02	0.02	0.02	0.02	0.02	0.02	0.03	0.02	0.03	0.03	0.02	0.01	0.01	0.03
0.80	0.82	0.83	0.81	0.79	0.79	0.05	0.05	0.05	0.05	0.05	0.04	0.05	0.86	0.88	0.06
0.02	0.02	0.02	0.02	0.02	0.02								0.00	0.00	
2.00	2.00	2.00	2.00	2.00	2.00	2.00	2.00	2.00	2.00	2.00	2.00	2.00	2.00	2.00	2.00
4.00	4.00	4.00	4.00	4.00	4.00	4.00	4.00	4.00	4.00	4.00	4.00	4.00	4.00	4.00	4.00
41.1	42.2	42.8	41.9	40.7	40.8	2.7	2.7	2.8	2.5	2.7	2.3	2.5	43.5	44.8	3.2
29.8	30.1	29.4	29.8	29.9	29.8	41.8	41.6	40.1	41.5	40.0	39.8	41.6	31.2	30.7	34.2
29.1	27.7	27.8	28.3	29.4	29.3	55.5	55.7	57.1	55.9	57.3	58.0	55.8	25.3	24.6	62.6

Table S2.2a. Pyroxene analyses in wt.% and atoms per formula unit for Elsie Mountain Formation metabasalts *(cont.)*.

FSTJ308	**FSTJ308**	**FSTJ308**	**FSTJ308**	**FSTJ308**	**FSTJ308**	**FSTJ308**	**FSTJ307**	**FSTJ307**	**FSTJ307**	**FSTJ307**	**FSTJ307**	**FSTJ307**	**FSTJ307**	**FSTJ307**
FSTJ308_site_1_opx_2	FSTJ308_site_1_opx_3	FSTJ308_site_1_cpx_1	FSTJ308_site_1_cpx_2	FSTJ308_site_1_cpx_3	FSTJ308_site_1_cpx_4	FSTJ308_site_1_cpx_5	FSTJ307_site_1_opx_1	FSTJ307_site_1_opx_2	FSTJ307_site_1_opx_3	FSTJ307_site_1_opx_4	FSTJ307_site_1_opx_5	FSTJ307_site_1_opx_6	FSTJ307_site_1_opx_7	FSTJ307_site_2_opx_10
BH Opx	BH Opx	BH Cpx	BH Cpx	BH Cpx	BH Cpx	BH Cpx	BH Opx	BH Opx	BH Opx	BH Opx	BH Opx	BH Opx	BH Opx	BH Opx
49.57	49.62	50.67	50.66	50.86	50.83	51.07	49.51	49.23	49.69	49.65	49.45	49.07	49.61	49.34
0.12	0.11	0.21	0.18	0.21	0.20	0.18	0.08	0.15	0.10	0.11	0.13	0.11	0.15	0.12
0.40	0.41	0.89	0.86	0.95	0.98	0.86	0.31	0.36	0.36	0.40	0.44	0.39	0.41	0.40
L.O.D.	L.O.D.	L.O.D.	L.O.D.	L.O.D.	L.O.D.	L.O.D.	L.O.D.	L.O.D.	L.O.D.	L.O.D.	L.O.D.	L.O.D.	L.O.D.	L.O.D.
36.59	36.59	18.00	17.92	19.85	18.60	17.80	37.72	38.13	37.03	36.85	37.37	38.04	37.32	37.55
0.94	0.88	0.47	0.45	0.50	0.48	0.44	1.00	1.08	0.87	0.85	0.96	1.05	0.96	0.98
11.25	11.26	9.05	9.07	9.34	9.12	9.15	10.28	10.18	11.12	10.98	10.59	10.07	10.56	10.51
1.34	1.49	19.97	19.76	18.43	19.41	20.49	1.37	1.26	1.38	1.39	1.41	1.31	1.36	1.31
L.O.D.	L.O.D.	0.15	0.15	0.14	0.15	0.15	L.O.D.	L.O.D.	L.O.D.	L.O.D.	L.O.D.	L.O.D.	L.O.D.	L.O.D.
L.O.D.	L.O.D.	L.O.D.	L.O.D.	L.O.D.	L.O.D.	L.O.D.	L.O.D.	L.O.D.	L.O.D.	L.O.D.	L.O.D.	L.O.D.	L.O.D.	L.O.D.
100.19	100.36	99.41	99.05	100.27	99.76	100.13	100.27	100.38	100.56	100.22	100.35	100.03	100.36	100.21
1.99	1.99	1.98	1.98	1.97	1.98	1.98	2.00	1.99	1.99	1.99	1.99	1.99	2.00	1.99
0.01	0.01	0.02	0.02	0.03	0.02	0.02	0.00	0.01	0.01	0.01	0.01	0.01	0.00	0.01
0.00	0.00	0.00	0.00	0.00	0.00	0.00	0.00	0.00	0.00	0.00	0.00	0.00	0.00	0.00
2.00	2.00	2.00	2.00	2.00	2.00	2.00	2.00	2.00	2.00	2.00	2.00	2.00	2.00	2.00
0.00	0.00	0.01	0.01	0.01	0.01	0.01	0.00	0.00	0.00	0.00	0.00	0.00	0.00	0.00
0.01	0.01	0.02	0.02	0.02	0.02	0.02	0.01	0.00	0.01	0.01	0.01	0.01	0.01	0.01
0.00	0.00	0.00	0.00	0.01	0.00	0.01	0.00	0.00	0.00	0.00	0.00	0.00	0.00	0.00
0.67	0.67	0.53	0.53	0.54	0.53	0.53	0.62	0.61	0.66	0.66	0.63	0.61	0.63	0.63
1.23	1.22	0.58	0.59	0.64	0.61	0.57	1.27	1.29	1.24	1.24	1.26	1.29	1.26	1.27
0.03	0.03	0.02	0.02	0.02	0.02	0.01	0.03	0.04	0.03	0.03	0.03	0.04	0.03	0.03
0.06	0.06	0.83	0.83	0.77	0.81	0.85	0.06	0.05	0.06	0.06	0.06	0.06	0.06	0.06
		0.01	0.01	0.01	0.01	0.01								
2.00	2.00	2.00	2.00	2.00	2.00	2.00	2.00	2.00	2.00	2.00	2.00	2.00	2.00	2.00
4.00	4.00	4.00	4.00	4.00	4.00	4.00	4.00	4.00	4.00	4.00	4.00	4.00	4.00	4.00
2.9	3.3	42.8	42.6	39.3	41.6	43.5	3.0	2.8	3.0	3.0	3.1	2.9	3.0	2.9
34.4	34.3	27.0	27.2	27.7	27.2	27.0	31.7	31.3	33.8	33.6	32.5	31.1	32.5	32.3
62.7	62.5	30.1	30.2	33.0	31.1	29.5	65.3	65.9	63.2	63.3	64.4	66.0	64.5	64.8

Table S2.2a. Pyroxene analyses for Elsie Mountain Formation metabasalts *(cont.)*.

FSTJ307	**FSTJ307**	**FSTJ307**	**FSTJ307**	**FSTJ307**	**FSTJ307**	**FSTJ307**
FSTJ307_site_2_opx_11	FSTJ307_site_1_cpx_1	FSTJ307_site_1_cpx_2	FSTJ307_site_1_cpx_3	FSTJ307_site_2_cpx_4	FSTJ307_site_2_cpx_5	FSTJ307_site_2_cpx_6
BH	BH	BH	BH	BH	BH	BH
Opx	Cpx	Cpx	Cpx	Cpx	Cpx	Cpx
49.57	51.19	50.22	51.17	51.29	51.20	51.25
0.09	0.18	0.19	0.17	0.15	0.19	0.13
0.35	0.84	0.90	0.88	0.81	0.86	0.66
L.O.D.	L.O.D.	L.O.D.	L.O.D.	L.O.D.	L.O.D.	L.O.D.
37.67	16.93	17.97	20.98	20.82	18.36	18.46
1.00	0.44	0.45	0.49	0.52	0.45	0.46
10.25	9.08	9.06	9.31	9.39	9.17	9.10
1.34	21.14	19.70	17.37	17.82	20.02	19.82
L.O.D.	0.17	0.18	0.13	0.12	0.15	0.15
L.O.D.	L.O.D.	L.O.D.	L.O.D.	L.O.D.	L.O.D.	L.O.D.
100.26	99.97	98.67	100.49	100.93	100.40	100.03
2.00	1.98	1.97	1.99	1.98	1.98	1.99
0.00	0.02	0.03	0.01	0.02	0.02	0.01
0.00	0.00	0.00	0.00	0.00	0.00	0.00
2.00	2.00	2.00	2.00	2.00	2.00	2.00
0.00	0.01	0.01	0.00	0.00	0.01	0.00
0.02	0.02	0.01	0.03	0.02	0.02	0.02
0.00	0.00	0.01	0.00	0.00	0.00	0.00
0.62	0.52	0.53	0.54	0.54	0.53	0.53
1.27	0.55	0.58	0.68	0.67	0.59	0.60
0.03	0.01	0.01	0.02	0.02	0.01	0.02
0.06	0.88	0.83	0.72	0.74	0.83	0.82
	0.01	0.01	0.01	0.01	0.01	0.01
2.00	2.00	2.00	2.00	2.00	2.00	2.00
4.00	4.00	4.00	4.00	4.00	4.00	4.00
3.0	45.0	42.5	37.2	37.8	42.5	42.3
31.7	26.9	27.2	27.7	27.7	27.1	27.0
65.3	28.1	30.3	35.1	34.5	30.4	30.7

Table S2.2b. Amphibole analyses in wt.% and atoms per formula unit for Elsie Mountain Formation metabasalts.

Sample #		**FSTJ098**	**FSTJ098**	**FSTJ299**	**FSTJ299**	**FSTJ299**	**FSTJ299**	**FSTJ299**
Analysis		Q1_1S6	Q1_1S6-1	site_2_amph_1	site_2_amph_2	site_2_amph_3	site_2_amph_4	site_2_amph_5
Rock Type		BH	BH	BH	BH	BH	BH	BH
Amphibole Species	L.O.D.*	Act	Act	Fe2-Fe3-Hbl	Fe2-Fe3-Hbl	Fe2-Fe3-Hbl	Fe2-Fe3-Hbl	Fe2-Fe3-Hbl
SiO_2	0.036	52.123	52.147	46.039	45.963	45.862	44.839	45.592
TiO_2	0.031	0.464	0.473	0.918	0.963	1.074	1.401	1.368
Al_2O_3	0.029	3.739	4.231	7.353	7.309	7.473	7.683	7.437
Cr_2O_3	0.029	L.O.D.	L.O.D.	L.O.D.	L.O.D.	L.O.D.	L.O.D.	L.O.D.
FeO_{total}	0.026	12.134	12.411	23.322	22.969	23.371	23.628	23.418
MnO	0.022	0.171	0.173	0.310	0.341	0.334	0.343	0.348
MgO	0.031	16.290	16.251	8.287	8.536	8.241	7.965	8.291
CaO	0.024	11.596	11.442	10.598	10.513	10.518	10.528	10.407
Na_2O	0.024	0.352	0.386	1.055	1.121	1.097	1.168	1.222
K_2O	0.017	0.205	0.258	0.508	0.529	0.506	0.556	0.469
F	0.112	L.O.D.	L.O.D.	L.O.D.	L.O.D.	L.O.D.	L.O.D.	0.160
Cl	0.014	L.O.D.	L.O.D.	L.O.D.	L.O.D.	L.O.D.	0.018	L.O.D.
O=F,Cl (calc)		0.000	0.000	0.000	0.000	0.000	0.000	-0.070
INITIAL TOTAL		97.1	97.8	98.4	98.2	98.5	98.1	98.6
Final wt% values								
FeO		10.28	10.56	18.84	17.02	18.88	18.78	18.73
Fe_2O_3		2.06	2.06	4.98	6.61	4.99	5.38	5.21
H_2O+		2.10	2.09	1.98	1.99	1.98	1.97	1.90
TOTAL		99.4	100.1	100.9	100.9	101.0	100.6	101.1
T (ideally 8 a.p.f.u.)								
Si		7.499	7.457	6.914	6.878	6.885	6.781	6.844
Al		0.501	0.543	1.086	1.122	1.115	1.219	1.156
Ti		0.000	0.000	0.000	0.000	0.000	0.000	0.000
Fe^{3+}		0.000	0.000	0.000	0.000	0.000	0.000	0.000
T subtotal		8.0	8.0	8.0	8.0	8.0	8.0	8.0
C (ideally 5 a.p.f.u.)								
Ti		0.050	0.051	0.104	0.108	0.121	0.159	0.154
Al		0.133	0.170	0.215	0.167	0.208	0.151	0.159
Cr								
Fe^{3+}		0.224	0.221	0.563	0.745	0.564	0.612	0.588
Mn^{2+}								
Fe^{2+}		1.093	1.091	2.263	2.075	2.263	2.283	2.243
Mg		3.494	3.464	1.855	1.904	1.844	1.796	1.855
C subtotal		5.0	5.0	5.0	5.0	5.0	5.0	5.0
B (ideally 2 a.p.f.u.)								
Mn^{2+}		0.021	0.021	0.039	0.043	0.042	0.044	0.044
Fe^{2+}		0.143	0.173	0.103	0.055	0.108	0.094	0.109
Mg								
Ca		1.788	1.753	1.705	1.686	1.692	1.706	1.674
Na		0.049	0.053	0.152	0.217	0.158	0.156	0.173
B subtotal		2.0	2.0	2.0	2.0	2.0	2.0	2.0
A (from 0 to 1 a.p.f.u.)								
Ca		0.000	0.000	0.000	0.000	0.000	0.000	0.000
Na		0.049	0.054	0.155	0.109	0.161	0.186	0.183
K		0.038	0.047	0.097	0.101	0.097	0.107	0.090
A subtotal		0.1	0.1	0.3	0.2	0.3	0.3	0.3
O (non-W)		22.0	22.0	22.0	22.0	22.0	22.0	22.0
W (ideally 2 a.p.f.u.)								
OH		2.0	2.0	2.0	2.0	2.0	2.0	1.9
F								0.1
Cl							0.0	
O								
W subtotal		2.0	2.0	2.0	2.0	2.0	2.0	2.0
SUM T,C,B,A		15.1	15.1	15.3	15.2	15.3	15.3	15.3
^{C}(Al+Fe^{3+}+2Ti) (a.p.f.u.)		0.46	0.49	0.99	1.13	1.01	1.08	1.06
^{A}(Na+K+2Ca) (a.p.f.u.)		0.09	0.10	0.25	0.21	0.26	0.29	0.27
^{A}Si		7.50	7.46	6.91	6.88	6.89	6.78	6.84
^{C}Mg/(Mg+Fe^{2+})		0.76	0.76	0.45	0.48	0.45	0.44	0.45

Amphibole analyses recalculated and classified following the scheme of Hawthorne *et al.* (2012).

Act (actinolite); Hbl (hornblende); Gru (grunerite); Fe2-Sad (Ferro-sadanagaite); Fe2-Fe3 (Ferro-ferri), Mg-Fe3 (Magnisio-ferri).

*L.O.D. = Limit of detection is defined as 3 x standard deviation of the total accumulated bacground counts.

Table S2.2b. Amphibole analyses in wt.% and atoms per formula unit for Elsie Mountain Formation metabasalts *(cont.)*.

FSTJ299	**FSTJ299**	**FSTJ299**	**FSTJ299**	**FSTJ299**	**FSTJ299**	**FSTJ294**	**FSTJ294**
site_2_amph_6	site_2_amph_7	site_2_vein_1	site_2_vein_2	site_2_vein_3	site_2_vein_4	site_1_amph_1	site_1_amph_2
BH	BH	BH	BH	BH	BH	BH	BH
Fe2-Fe3-Hbl	Fe2-Fe3-Hbl	Fe2-Fe3-Hbl	Fe2-Fe3-Hbl	Fe2-Fe3-Hbl	Fe2-Fe3-Hbl	Fe2-Fe3-Hbl	Fe2-Fe3-Hbl
45.643	45.659	47.213	44.630	46.788	46.099	45.304	45.193
1.338	1.321	0.186	0.160	0.127	0.182	1.342	1.364
7.474	7.445	5.671	8.267	6.157	6.693	8.096	8.073
L.O.D.	L.O.D.	L.O.D.	L.O.D.	L.O.D.	L.O.D.	L.O.D.	L.O.D.
23.286	23.372	28.032	27.533	28.539	27.847	23.060	23.290
0.353	0.372	0.376	0.318	0.424	0.341	0.296	0.289
8.481	8.205	5.682	4.663	6.319	5.591	7.925	7.835
10.521	10.443	10.169	10.955	8.985	10.138	10.686	10.586
1.237	1.246	0.627	1.066	0.741	0.832	0.992	1.103
0.483	0.474	0.144	0.275	0.170	0.201	0.680	0.638
0.155	L.O.D.	L.O.D.	L.O.D.	L.O.D.	L.O.D.	L.O.D.	L.O.D.
0.021	0.021	0.431	0.741	0.469	0.612	0.024	0.032
-0.070	0.000	-0.100	-0.170	-0.110	-0.140	-0.010	-0.010
98.9	98.6	98.4	98.4	98.6	98.4	98.4	98.4
18.47	19.03	24.81	23.68	24.46	23.56	19.23	19.38
5.36	4.83	3.58	4.28	4.54	4.77	4.25	4.35
1.90	1.97	1.83	1.74	1.83	1.79	1.97	1.96
101.4	101.0	100.6	100.6	100.9	100.7	100.8	100.8
6.829	6.860	7.243	6.892	7.152	7.077	6.822	6.813
1.171	1.140	0.757	1.108	0.848	0.923	1.178	1.187
0.000	0.000	0.000	0.000	0.000	0.000	0.000	0.000
0.000	0.000	0.000	0.000	0.000	0.000	0.000	0.000
8.0	8.0	8.0	8.0	8.0	8.0	8.0	8.0
0.151	0.149	0.021	0.019	0.015	0.021	0.152	0.155
0.147	0.179	0.268	0.397	0.261	0.288	0.259	0.247
0.605	0.547	0.415	0.499	0.522	0.550	0.481	0.493
2.207	2.288	2.994	3.011	2.762	2.860	2.329	2.344
1.892	1.838	1.299	1.074	1.440	1.280	1.779	1.761
5.0	5.0	5.0	5.0	5.0	5.0	5.0	5.0
0.045	0.047	0.049	0.042	0.055	0.044	0.038	0.037
0.103	0.102	0.187	0.046	0.364	0.165	0.095	0.099
1.687	1.681	1.672	1.813	1.472	1.668	1.724	1.710
0.166	0.169	0.093	0.100	0.109	0.123	0.143	0.154
2.0	2.0	2.0	2.0	2.0	2.0	2.0	2.0
0.000	0.000	0.000	0.000	0.000	0.000	0.000	0.000
0.193	0.194	0.094	0.219	0.111	0.125	0.146	0.168
0.092	0.091	0.028	0.054	0.033	0.039	0.131	0.123
0.3	0.3	0.1	0.3	0.1	0.2	0.3	0.3
22.0	22.0	22.0	22.0	22.0	22.0	22.0	22.0
1.9	2.0	1.9	1.8	1.9	1.8	2.0	2.0
0.1							
0.0	0.0	0.1	0.2	0.1	0.2	0.0	0.0
2.0	2.0	2.0	2.0	2.0	2.0	2.0	2.0
15.3	15.3	15.1	15.3	15.1	15.2	15.3	15.3
1.05	1.02	0.73	0.93	0.81	0.88	1.04	1.05
0.29	0.29	0.12	0.27	0.14	0.16	0.28	0.29
6.83	6.86	7.24	6.89	7.15	7.08	6.82	6.81
0.46	0.45	0.30	0.26	0.34	0.31	0.43	0.43

Table S2.2b. Amphibole analyses in wt.% and atoms per formula unit for Elsie Mountain Formation metabasalts *(cont.)*.

FSTJ294	**FSTJ294**	**FSTJ294**	**FSTJ294**	**FSTJ294**	**FSTJ294**	**FSTJ294**	**FSTJ294**
site_1_amph_3	site_1_amph_4	site_1_amph_5	site_1_amph_6	site_1_amph_7	site_1_amph_8	site_1_amph_9	site_1_amph_10
BH	BH	BH	BH	BH	BH	BH	BH
Fe2-Fe3-Hbl	Fe2-Fe3-Hbl	Fe2-Fe3-Hbl	Fe2-Fe3-Hbl	Fe2-Fe3-Hbl	Fe2-Fe3-Hbl	Fe2-Fe3-Hbl	Fe2-Fe3-Hbl
45.868	45.614	45.819	45.708	45.193	45.306	44.790	44.684
1.386	1.338	1.415	1.339	1.443	1.525	1.454	1.425
7.310	7.542	7.491	7.474	7.676	7.993	7.786	8.023
L.O.D.	L.O.D.	L.O.D.	L.O.D.	L.O.D.	L.O.D.	L.O.D.	L.O.D.
23.299	23.290	22.834	22.662	23.829	23.091	23.542	23.713
0.336	0.290	0.280	0.258	0.296	0.272	0.318	0.302
8.033	8.045	8.410	8.629	7.552	7.796	7.807	7.966
10.227	10.441	10.426	10.390	10.309	10.492	10.337	10.431
0.976	1.060	1.187	1.129	1.032	1.118	1.030	1.037
0.577	0.572	0.562	0.580	0.571	0.657	0.639	0.635
L.O.D.	L.O.D.	L.O.D.	L.O.D.	L.O.D.	L.O.D.	L.O.D.	L.O.D.
L.O.D.	0.025	0.017	0.033	0.018	0.025	0.034	L.O.D.
0.000	-0.010	0.000	-0.010	0.000	-0.010	-0.010	0.000
98.0	98.2	98.4	98.2	97.9	98.3	97.7	98.2
20.04	19.49	17.47	18.56	20.21	18.24	19.33	18.73
3.63	4.22	5.96	4.56	4.03	5.39	4.68	5.53
1.98	1.97	1.98	1.97	1.96	1.97	1.96	1.97
100.4	100.6	101.0	100.6	100.3	100.8	100.2	100.8
6.935	6.881	6.852	6.872	6.861	6.812	6.806	6.747
1.065	1.119	1.148	1.128	1.139	1.188	1.194	1.253
0.000	0.000	0.000	0.000	0.000	0.000	0.000	0.000
0.000	0.000	0.000	0.000	0.000	0.000	0.000	0.000
8.0	8.0	8.0	8.0	8.0	8.0	8.0	8.0
0.158	0.152	0.159	0.151	0.165	0.173	0.166	0.162
0.237	0.222	0.172	0.196	0.235	0.228	0.200	0.174
0.413	0.479	0.671	0.514	0.461	0.609	0.535	0.630
2.381	2.337	2.123	2.204	2.430	2.243	2.330	2.241
1.811	1.809	1.875	1.934	1.709	1.747	1.768	1.793
5.0	5.0	5.0	5.0	5.0	5.0	5.0	5.0
0.043	0.037	0.035	0.033	0.038	0.035	0.041	0.039
0.151	0.122	0.062	0.131	0.134	0.052	0.126	0.124
1.657	1.688	1.670	1.674	1.677	1.690	1.683	1.687
0.149	0.153	0.232	0.163	0.150	0.223	0.150	0.150
2.0	2.0	2.0	2.0	2.0	2.0	2.0	2.0
0.000	0.000	0.000	0.000	0.000	0.000	0.000	0.000
0.137	0.157	0.112	0.166	0.153	0.103	0.153	0.153
0.111	0.110	0.107	0.111	0.111	0.126	0.124	0.122
0.2	0.3	0.2	0.3	0.3	0.2	0.3	0.3
22.0	22.0	22.0	22.0	22.0	22.0	22.0	22.0
2.0	2.0	2.0	2.0	2.0	2.0	2.0	2.0
	0.0	0.0	0.0	0.0	0.0	0.0	
2.0	2.0	2.0	2.0	2.0	2.0	2.0	2.0
15.2	15.3	15.2	15.3	15.3	15.2	15.3	15.3
0.97	1.01	1.16	1.01	1.03	1.18	1.07	1.13
0.25	0.27	0.22	0.28	0.26	0.23	0.28	0.28
6.94	6.88	6.85	6.87	6.86	6.81	6.81	6.75
0.43	0.44	0.47	0.47	0.41	0.44	0.43	0.44

Table S2.2b. Amphibole analyses in wt.% and atoms per formula unit for Elsie Mountain Formation metabasalts *(cont.)*.

FSTJ118	**FSTJ118**	**FSTJ118**	**FSTJ118**	**FSTJ118**	**FSTJ118**	**FSTJ118**	**FSTJ118**	**FSTJ118**	**FSTJ118**
Q2S5	Q2S5-1	Q2S5-2	Q3S15	Q3S6	Q5AMPHS1	Q5AMPHS2	Q5AMPHS3	Q5AMPHS4	Q7AMPH4
BH	BH	BH	BH	BH	BH	BH	BH	BH	BH
Mg-Fe3-Hbl	Mg-Fe3-Hbl	Mg-Fe3-Hbl	Mg-Fe3-Hbl	Mg-Fe3-Hbl	Mg-Fe3-Hbl	Mg-Fe3-Hbl	Mg-Fe3-Hbl	Mg-Fe3-Hbl	Mg-Fe3-Hbl
46.037	49.379	46.000	46.280	46.620	46.276	46.674	46.562	46.383	46.945
1.013	0.693	1.226	1.088	1.215	1.405	1.273	1.316	1.215	1.158
7.820	4.605	7.705	7.203	6.977	7.423	7.111	7.092	7.266	6.939
L.O.D.	L.O.D.	L.O.D.	L.O.D.	L.O.D.	L.O.D.	L.O.D.	L.O.D.	L.O.D.	L.O.D.
20.383	19.086	20.519	20.532	20.397	20.298	19.863	20.307	20.381	20.588
0.240	0.271	0.256	0.232	0.257	0.243	0.265	0.260	0.273	0.269
10.025	11.816	9.963	10.066	10.211	10.420	10.688	10.550	10.597	10.554
10.916	10.905	10.963	10.872	10.914	10.776	10.833	10.770	10.791	10.787
0.872	0.471	0.916	0.861	0.854	1.035	1.062	0.995	1.061	0.868
0.650	0.298	0.634	0.595	0.589	0.465	0.481	0.470	0.469	0.514
L.O.D.	L.O.D.	L.O.D.	L.O.D.	L.O.D.	L.O.D.	L.O.D.	L.O.D.	L.O.D.	L.O.D.
L.O.D.	L.O.D.	L.O.D.	0.022	L.O.D.	L.O.D.	L.O.D.	L.O.D.	L.O.D.	L.O.D.
0.000	0.000	0.000	-0.010	0.000	0.000	0.000	0.000	0.000	0.000
98.0	97.5	98.2	97.7	98.0	98.3	98.3	98.3	98.4	98.6
15.84	16.20	15.94	16.14	16.30	15.45	13.96	15.51	15.00	15.98
5.05	3.20	5.09	4.88	4.56	5.39	6.56	5.33	5.98	5.13
2.00	2.03	2.00	2.00	2.00	2.01	2.01	2.01	2.01	2.01
100.5	99.9	100.7	100.2	100.5	100.9	100.9	100.9	101.1	101.1
6.854	7.314	6.841	6.912	6.939	6.850	6.881	6.892	6.853	6.933
1.146	0.686	1.159	1.088	1.061	1.150	1.119	1.108	1.147	1.067
0.000	0.000	0.000	0.000	0.000	0.000	0.000	0.000	0.000	0.000
0.000	0.000	0.000	0.000	0.000	0.000	0.000	0.000	0.000	0.000
8.0	8.0	8.0	8.0	8.0	8.0	8.0	8.0	8.0	8.0
0.113	0.077	0.137	0.122	0.136	0.156	0.141	0.147	0.135	0.129
0.226	0.118	0.192	0.179	0.163	0.145	0.116	0.130	0.119	0.141
0.566	0.357	0.570	0.549	0.511	0.602	0.728	0.593	0.666	0.570
1.868	1.839	1.892	1.908	1.923	1.798	1.666	1.802	1.746	1.837
2.225	2.609	2.209	2.241	2.266	2.299	2.349	2.328	2.334	2.324
5.0	5.0	5.0	5.0	5.0	5.0	5.0	5.0	5.0	5.0
0.030	0.034	0.032	0.029	0.032	0.030	0.033	0.033	0.034	0.034
0.104	0.168	0.090	0.107	0.105	0.113	0.055	0.118	0.107	0.136
1.741	1.731	1.747	1.740	1.741	1.709	1.711	1.708	1.708	1.707
0.125	0.067	0.131	0.124	0.122	0.147	0.201	0.141	0.150	0.123
2.0	2.0	2.0	2.0	2.0	2.0	2.0	2.0	2.0	2.0
0.000	0.000	0.000	0.000	0.000	0.000	0.000	0.000	0.000	0.000
0.127	0.068	0.133	0.126	0.124	0.150	0.103	0.144	0.154	0.125
0.123	0.056	0.120	0.113	0.112	0.088	0.090	0.089	0.088	0.097
0.3	0.1	0.3	0.2	0.2	0.2	0.2	0.2	0.2	0.2
22.0	22.0	22.0	22.0	22.0	22.0	22.0	22.0	22.0	22.0
2.0	2.0	2.0	2.0	2.0	2.0	2.0	2.0	2.0	2.0
			0.0						
2.0	2.0	2.0	2.0	2.0	2.0	2.0	2.0	2.0	2.0
15.3	15.1	15.3	15.2	15.2	15.2	15.2	15.2	15.2	15.2
1.02	0.63	1.04	0.97	0.95	1.06	1.13	1.02	1.06	0.97
0.25	0.12	0.25	0.24	0.24	0.24	0.19	0.23	0.24	0.22
6.85	7.31	6.84	6.91	6.94	6.85	6.88	6.89	6.85	6.93
0.54	0.59	0.54	0.54	0.54	0.56	0.59	0.56	0.57	0.56

Table S2.2b. Amphibole analyses in wt.% and atoms per formula unit for Elsie Mountain Formation metabasalts *(cont.)*.

FSTJ118	**FSTJ118**	**FSTJ118**	**FSTJ118**	**FSTJ118**	**FSTJ118**	**FSTJ118**	**FSTJ118**	**FSTJ118**	**FSTJ118**	**FSTJ118**
Q7AMPH5	Q7AMPH6	Q6VEINS1	Q6VEINS3	Q6VEINS4	Q6VEINS5	Q4S1	Q4_2S4	Q4_2S8	Q7VEINS1	Q7VEINS2
BH	BH	BH	BH	BH	BH	BH	BH	BH	BH	BH
Mg-Fe3-Hbl	Mg-Fe3-Hbl	Fe2-Hbl	Mg-Hbl	Mg-Fe3-Hbl	Mg-Hbl	Mg-Hbl	Fe2-Hbl	Mg-Hbl	Mg-Fe3-Hbl	Mg-Fe3-Hbl
46.864	45.981	47.753	49.525	49.664	49.603	48.868	47.598	48.830	49.560	47.783
1.134	1.280	0.248	0.186	0.182	0.175	0.188	0.245	0.233	0.151	0.176
7.175	7.256	6.794	4.987	5.080	4.786	6.046	6.932	6.011	4.458	6.250
L.O.D.	L.O.D.	L.O.D.	L.O.D.	L.O.D.	L.O.D.	L.O.D.	L.O.D.	L.O.D.	L.O.D.	L.O.D.
20.214	20.409	22.609	22.332	21.855	23.312	21.518	23.682	20.968	23.240	24.357
0.263	0.259	0.331	0.397	0.356	0.433	0.300	0.341	0.301	0.459	0.418
10.403	10.192	9.170	10.949	11.128	10.789	10.286	8.648	10.464	10.406	9.590
10.908	10.911	9.840	8.709	9.315	8.301	10.125	9.848	10.304	8.767	8.503
0.836	0.863	0.259	0.155	0.195	0.181	0.319	0.319	0.292	0.189	0.373
0.542	0.600	0.266	0.348	0.180	0.298	0.234	0.453	0.229	0.217	0.426
L.O.D.	L.O.D.	L.O.D.	L.O.D.	L.O.D.	L.O.D.	L.O.D.	L.O.D.	L.O.D.	L.O.D.	L.O.D.
L.O.D.	L.O.D.	0.207	0.285	0.184	0.256	0.229	0.355	0.228	0.224	0.470
0.000	-0.050	-0.050	-0.060	-0.040	-0.060	-0.050	-0.080	-0.050	-0.050	-0.110
98.3	97.8	97.5	97.8	98.1	98.1	98.1	98.3	97.8	97.6	98.2
16.07	15.65	20.21	20.66	19.41	21.40	18.94	21.12	18.41	21.31	21.14
4.61	5.29	2.66	1.86	2.72	2.12	2.87	2.84	2.84	2.14	3.57
2.01	1.94	1.95	1.94	1.97	1.94	1.95	1.89	1.96	1.94	1.87
100.8	100.3	99.7	99.9	100.3	100.2	100.3	100.5	100.1	99.8	100.5
6.939	6.863	7.190	7.402	7.366	7.411	7.266	7.154	7.266	7.446	7.183
1.061	1.137	0.810	0.598	0.634	0.589	0.734	0.846	0.734	0.554	0.817
0.000	0.000	0.000	0.000	0.000	0.000	0.000	0.000	0.000	0.000	0.000
0.000	0.000	0.000	0.000	0.000	0.000	0.000	0.000	0.000	0.000	0.000
8.0	8.0	8.0	8.0	8.0	8.0	8.0	8.0	8.0	8.0	8.0
0.126	0.144	0.028	0.021	0.020	0.020	0.021	0.028	0.026	0.017	0.020
0.191	0.139	0.396	0.280	0.255	0.254	0.326	0.382	0.320	0.235	0.291
0.512	0.594	0.303	0.209	0.304	0.238	0.320	0.321	0.318	0.243	0.403
1.873	1.855	2.211	2.050	1.960	2.084	2.052	2.331	2.015	2.174	2.136
2.296	2.268	2.058	2.440	2.461	2.403	2.280	1.938	2.321	2.331	2.149
5.0	5.0	5.0	5.0	5.0	5.0	5.0	5.0	5.0	5.0	5.0
0.033	0.033	0.042	0.050	0.045	0.055	0.038	0.043	0.038	0.058	0.053
0.117	0.099	0.333	0.533	0.447	0.590	0.303	0.324	0.277	0.503	0.523
1.731	1.745	1.587	1.395	1.480	1.329	1.613	1.586	1.643	1.411	1.370
0.119	0.124	0.038	0.022	0.028	0.026	0.046	0.046	0.042	0.028	0.054
2.0	2.0	2.0	2.0	2.0	2.0	2.0	2.0	2.0	2.0	2.0
0.000	0.000	0.000	0.000	0.000	0.000	0.000	0.000	0.000	0.000	0.000
0.121	0.126	0.038	0.022	0.028	0.026	0.046	0.047	0.042	0.028	0.055
0.102	0.114	0.051	0.066	0.034	0.057	0.044	0.087	0.043	0.042	0.082
0.2	0.2	0.1	0.1	0.1	0.1	0.1	0.1	0.1	0.1	0.1
22.0	22.0	22.0	22.0	22.0	22.0	22.0	22.0	22.0	22.0	22.0
2.0	2.0	1.9	1.9	2.0	1.9	1.9	1.9	1.9	1.9	1.9
		0.1	0.1	0.0	0.1	0.1	0.1	0.1	0.1	0.1
2.0	2.0	2.0	2.0	2.0	2.0	2.0	2.0	2.0	2.0	2.0
15.2	15.2	15.1	15.1	15.1	15.1	15.1	15.1	15.1	15.1	15.1
0.96	1.02	0.76	0.53	0.60	0.53	0.69	0.76	0.69	0.51	0.73
0.22	0.24	0.09	0.09	0.06	0.08	0.09	0.13	0.09	0.07	0.14
6.94	6.86	7.19	7.40	7.37	7.41	7.27	7.15	7.27	7.45	7.18
0.55	0.55	0.48	0.54	0.56	0.54	0.53	0.45	0.54	0.52	0.50

Table S2.2b. Amphibole analyses in wt.% and atoms per formula unit for Elsie Mountain Formation metabasalts *(cont.)*.

FSTJ118	**FSTJ118**	**FSTJ292**	**FSTJ292**	**FSTJ292**	**FSTJ292**	**FSTJ292**	**FSTJ292**	**FSTJ069**
Q7VEINS3	Q4_2S8-1	site_1_amph_1	site_1_amph_2	site_1_amph_3	site_1_amph_4	site_1_amph_5	site_1_amph_6	Q1_4S2
BH	BH	BH	BH	BH	BH	BH	BH	BG
Mg-Fe3-Hbl	Gru	Fe2-Fe3-Hbl	Fe2-Fe3-Hbl	Mg-Fe3-Hbl	Mg-Fe3-Hbl	Fe2-Fe3-Hbl	Fe2-Fe3-Hbl	Gru
49.299	51.918	46.501	46.216	47.405	47.333	46.096	46.671	53.043
0.126	0.071	1.289	1.491	0.961	1.187	1.570	1.410	0.032
5.003	1.287	6.497	7.020	6.063	6.398	7.527	6.822	0.051
L.O.D.	L.O.D.	L.O.D.	L.O.D.	L.O.D.	L.O.D.	L.O.D.	L.O.D.	L.O.D.
25.219	28.317	22.315	22.031	21.661	22.206	22.221	22.278	28.836
0.554	0.774	0.367	0.319	0.335	0.356	0.303	0.349	0.619
10.699	12.241	9.134	9.002	9.933	9.607	8.912	9.232	13.890
6.960	3.419	10.327	10.537	10.405	10.226	10.540	10.377	0.880
0.316	0.000	1.145	1.217	0.980	1.128	1.244	1.197	0.000
0.219	0.058	0.407	0.455	0.351	0.361	0.494	0.418	0.009
L.O.D.	L.O.D.	L.O.D.	L.O.D.	L.O.D.	L.O.D.	L.O.D.	L.O.D.	L.O.D.
0.278	0.086	L.O.D.	L.O.D.	L.O.D.	L.O.D.	0.024	0.018	L.O.D.
-0.060	-0.020	0.000	0.000	0.000	0.000	-0.010	0.000	0.000
98.6	98.2	98.0	98.3	98.1	98.8	98.9	98.8	97.4
22.47	27.30	18.25	18.20	17.59	18.28	18.22	18.16	28.84
3.06	1.13	4.51	4.26	4.53	4.37	4.45	4.58	0.00
1.92	1.97	1.99	1.99	2.00	1.99	1.98	1.98	2.00
100.8	100.2	100.4	100.7	100.5	101.2	101.3	101.2	99.4
7.353	7.807	6.984	6.922	7.070	7.029	6.863	6.949	7.999
0.647	0.193	1.016	1.078	0.930	0.971	1.137	1.051	0.001
0.000	0.000	0.000	0.000	0.000	0.000	0.000	0.000	0.000
0.000	0.000	0.000	0.000	0.000	0.000	0.000	0.000	0.000
8.0	8.0	8.0	8.0	8.0	8.0	8.0	8.0	8.0
0.014	0.008	0.146	0.168	0.108	0.133	0.176	0.158	0.004
0.232	0.035	0.133	0.161	0.136	0.149	0.184	0.146	0.008
0.343	0.128	0.510	0.481	0.508	0.488	0.497	0.514	0.000
2.030	2.082	2.166	2.180	2.039	2.104	2.164	2.134	1.866
2.379	2.744	2.045	2.010	2.209	2.127	1.978	2.049	3.123
5.0	5.0	5.0	5.0	5.0	5.0	5.0	5.0	5.0
0.070	0.099	0.047	0.040	0.042	0.045	0.038	0.044	0.079
0.772	1.351	0.127	0.098	0.155	0.166	0.105	0.126	1.771
1.112	0.551	1.662	1.691	1.663	1.627	1.681	1.655	0.142
0.046		0.165	0.170	0.140	0.162	0.175	0.174	
2.0	2.0	2.0	2.0	2.0	2.0	2.0	2.0	2.0
0.000	0.000	0.000	0.000	0.000	0.000	0.000	0.000	0.000
0.046	0.000	0.169	0.183	0.143	0.163	0.184	0.171	0.000
0.042	0.011	0.078	0.087	0.067	0.068	0.094	0.079	0.002
0.1	0.0	0.2	0.3	0.2	0.2	0.3	0.3	0.0
22.0	22.0	22.0	22.0	22.0	22.0	22.0	22.0	22.0
1.9	2.0	2.0	2.0	2.0	2.0	2.0	2.0	2.0
0.1	0.0					0.0	0.0	
2.0	2.0	2.0	2.0	2.0	2.0	2.0	2.0	2.0
15.1	15.0	15.2	15.3	15.2	15.2	15.3	15.3	15.0
0.60	0.18	0.94	0.98	0.86	0.90	1.03	0.98	0.02
0.09	0.01	0.25	0.27	0.21	0.23	0.28	0.25	0.00
7.35	7.81	6.98	6.92	7.07	7.03	6.86	6.95	8.00
0.54	0.57	0.49	0.48	0.52	0.50	0.48	0.49	0.63

Table S2.2b. Amphibole analyses in wt.% and atoms per formula unit for Elsie Mountain Formation metabasalts *(cont.)*.

FSTJ069	**FSTJ069**	**FSTJ069**	**FSTJ069**	**FSTJ069**	**FSTJ308**	**FSTJ308**	**FSTJ308**	**FSTJ308**
Q5SAmph1	Q5SAmph2	Q5SAmph3	Q5SAmph4	Q5SAmph5	site_1_amph_1	site_1_amph_2	site_1_amph_3	site_1_amph_4
BG	BG	BG	BG	BG	BH	BH	BH	BH
Mg-Fe3-Hbl	Fe2-Fe3-Hbl	Mg-Fe3-Hbl	Mg-Fe3-Hbl	Mg-Fe3-Hbl	Fe2-Fe3-Hbl	Fe2-Fe3-Hbl	Fe2-Fe3-Hbl	Fe2-Fe3-Hbl
46.723	45.653	46.660	47.131	46.812	44.432	44.532	44.621	44.998
1.086	1.230	1.150	0.995	1.013	1.678	1.708	1.625	1.484
7.050	7.765	6.981	6.831	6.827	8.286	8.227	8.266	7.980
L.O.D.	L.O.D.	L.O.D.	L.O.D.	L.O.D.	L.O.D.	L.O.D.	L.O.D.	L.O.D.
21.083	21.091	20.679	20.998	20.515	23.608	23.732	23.353	23.558
0.255	0.232	0.268	0.261	0.254	0.299	0.295	0.298	0.289
9.713	9.208	10.002	10.010	10.123	7.633	7.496	7.728	7.756
10.785	10.828	10.816	10.650	10.857	10.458	10.570	10.524	10.428
0.671	0.732	0.709	0.650	0.654	1.306	1.237	1.318	1.113
0.546	0.666	0.611	0.610	0.601	0.695	0.688	0.689	0.657
L.O.D.	L.O.D.	L.O.D.	L.O.D.	L.O.D.	L.O.D.	L.O.D.	0.132	L.O.D.
L.O.D.	0.023	0.015	L.O.D.	L.O.D.	0.019	L.O.D.	0.024	L.O.D.
0.000	-0.010	0.000	0.000	0.000	0.000	0.000	-0.060	0.000
97.9	97.4	97.9	98.1	97.7	98.4	98.5	98.5	98.3
17.52	17.42	17.00	17.66	16.84	21.01	21.26	20.90	19.51
3.96	4.08	4.09	3.71	4.08	2.89	2.74	2.73	4.50
2.00	1.99	2.00	2.00	2.00	1.96	1.96	1.89	1.97
100.3	99.8	100.3	100.5	100.1	100.7	100.7	100.7	100.7
6.982	6.875	6.967	7.022	6.998	6.749	6.763	6.769	6.799
1.018	1.125	1.033	0.978	1.002	1.251	1.237	1.231	1.201
0.000	0.000	0.000	0.000	0.000	0.000	0.000	0.000	0.000
0.000	0.000	0.000	0.000	0.000	0.000	0.000	0.000	0.000
8.0	8.0	8.0	8.0	8.0	8.0	8.0	8.0	8.0
0.122	0.139	0.129	0.112	0.114	0.192	0.195	0.185	0.169
0.224	0.253	0.196	0.221	0.200	0.233	0.235	0.246	0.221
0.445	0.462	0.461	0.415	0.458	0.330	0.315	0.312	0.512
2.046	2.077	1.988	2.027	1.971	2.517	2.558	2.509	2.351
2.164	2.067	2.226	2.223	2.256	1.728	1.697	1.748	1.747
5.0	5.0	5.0	5.0	5.0	5.0	5.0	5.0	5.0
0.032	0.030	0.034	0.033	0.032	0.038	0.038	0.038	0.037
0.144	0.117	0.134	0.174	0.135	0.152	0.142	0.142	0.113
1.727	1.747	1.730	1.700	1.739	1.702	1.720	1.710	1.688
0.097	0.106	0.102	0.093	0.094	0.107	0.100	0.109	0.161
2.0	2.0	2.0	2.0	2.0	2.0	2.0	2.0	2.0
0.000	0.000	0.000	0.000	0.000	0.000	0.000	0.000	0.000
0.098	0.108	0.103	0.094	0.095	0.277	0.264	0.278	0.165
0.104	0.128	0.116	0.116	0.115	0.135	0.133	0.133	0.127
0.2	0.2	0.2	0.2	0.2	0.4	0.4	0.4	0.3
22.0	22.0	22.0	22.0	22.0	22.0	22.0	22.0	22.0
2.0	2.0	2.0	2.0	2.0	2.0	2.0	1.9	2.0
							0.1	
	0.0	0.0			0.0		0.0	
2.0	2.0	2.0	2.0	2.0	2.0	2.0	2.0	2.0
15.2	15.2	15.2	15.2	15.2	15.4	15.4	15.4	15.3
0.91	0.99	0.92	0.86	0.89	0.95	0.94	0.93	1.07
0.20	0.24	0.22	0.21	0.21	0.41	0.40	0.41	0.29
6.98	6.88	6.97	7.02	7.00	6.75	6.76	6.77	6.80
0.51	0.50	0.53	0.52	0.53	0.41	0.40	0.41	0.43

Table S2.2b. Amphibole analyses in wt.% and atoms per formula unit for Elsie Mountain Formation metabasalts *(cont.)*.

FSTJ307	**FSTJ307**	**FSTJ307**	**FSTJ307**	**FSTJ307**	**FSTJ307**	**FSTJ307**	**FSTJ307**
site_1_amph_1	site_1_amph_2	site_1_amph_3	site_2_amph_4	site_2_amph_5	site_2_amph_6	site_1_opx_8	site_1_opx_9
BH	BH	BH	BH	BH	BH	BH	BH
Fe2-Fe3-Hbl	Fe2-Fe3-Hbl	Fe2-Fe3-Hbl	Fe2-Fe3-Hbl	Fe2-Fe3-Hbl	Fe2-Fe3-Hbl	Gru	Gru
44.578	46.027	45.368	46.673	45.074	45.226	52.687	52.320
1.513	0.824	1.101	0.894	1.609	1.604	0.032	0.073
8.268	8.201	7.917	6.913	7.830	7.867	0.156	0.252
L.O.D.	L.O.D.	L.O.D.	L.O.D.	L.O.D.	L.O.D.	L.O.D.	L.O.D.
23.636	23.227	23.457	23.422	23.706	23.188	32.928	32.979
0.253	0.278	0.266	0.294	0.285	0.262	0.886	0.850
7.447	7.627	7.784	7.646	7.611	7.797	11.137	10.825
10.668	10.745	10.664	10.675	10.561	10.464	0.513	0.841
1.152	0.971	1.050	0.848	1.177	1.151	0.000	0.000
0.781	0.552	0.615	0.482	0.692	0.672	0.002	0.000
L.O.D.	L.O.D.	L.O.D.	L.O.D.	L.O.D.	L.O.D.	L.O.D.	L.O.D.
L.O.D.	L.O.D.	L.O.D.	L.O.D.	L.O.D.	L.O.D.	L.O.D.	L.O.D.
0.000	0.000	0.000	0.000	0.000	0.000	0.000	0.000
98.3	98.5	98.2	97.8	98.5	98.2	98.3	98.1
21.27	19.86	19.42	20.66	20.08	19.57	32.93	32.98
2.63	3.74	4.48	3.07	4.03	4.02	0.00	0.00
1.96	1.98	1.97	1.98	1.97	1.97	1.96	1.96
100.5	100.8	100.6	100.1	100.9	100.6	100.3	100.1
6.783	6.918	6.849	7.068	6.810	6.831	8.018	7.994
1.217	1.082	1.151	0.932	1.190	1.169		0.006
0.000	0.000	0.000	0.000	0.000	0.000	0.000	0.000
0.000	0.000	0.000	0.000	0.000	0.000	0.000	0.000
8.0	8.0	8.0	8.0	8.0	8.0	8.0	8.0
0.173	0.093	0.125	0.102	0.183	0.182	0.004	0.008
0.265	0.370	0.257	0.302	0.204	0.231	0.028	0.039
0.299	0.422	0.511	0.350	0.459	0.457	0.000	0.000
2.573	2.405	2.355	2.520	2.440	2.374	2.442	2.487
1.689	1.709	1.752	1.726	1.714	1.756	2.527	2.466
5.0	5.0	5.0	5.0	5.0	5.0	5.0	5.0
0.033	0.035	0.034	0.038	0.036	0.034	0.114	0.110
0.136	0.092	0.095	0.097	0.096	0.098	1.749	1.727
1.739	1.730	1.725	1.732	1.710	1.693	0.084	0.138
0.093	0.143	0.146	0.133	0.158	0.175		
2.0	2.0	2.0	2.0	2.0	2.0	1.9	2.0
0.000	0.000	0.000	0.000	0.000	0.000	0.000	0.000
0.247	0.140	0.161	0.116	0.187	0.162	0.000	0.000
0.152	0.106	0.118	0.093	0.133	0.129	0.000	0.000
0.4	0.2	0.3	0.2	0.3	0.3	0.0	0.0
22.0	22.0	22.0	22.0	22.0	22.0	22.0	22.0
2.0	2.0	2.0	2.0	2.0	2.0	2.0	2.0
2.0	2.0	2.0	2.0	2.0	2.0	2.0	2.0
15.4	15.2	15.3	15.2	15.3	15.3	15.0	15.0
0.91	0.98	1.02	0.86	1.03	1.05	0.04	0.06
0.40	0.25	0.28	0.21	0.32	0.29	0.00	0.00
6.78	6.92	6.85	7.07	6.81	6.83	8.02	7.99
0.40	0.42	0.43	0.41	0.41	0.43	0.51	0.50

Table S2.2b. Amphibole analyses in wt.% and atoms per formula unit for Elsie Mountain Formation metabasalts *(cont.)*.

FSTJ326	**FSTJ326**	**FSTJ326**	**FSTJ326**	**FSTJ326**	**FSTJ326**	**FSTJ326**	**FSTJ326**
site_1_amph_1	site_1_amph_2	site_1_amph_3	site_1_amph_4	site_1_amph_5	site_1_amph_6	site_1_amph_7	site_1_amph_8
BA	BA	BA	BA	BA	BA	BA	BA
Fe2-Sad	Fe2-Sad	Fe2-Sad	Fe2-Sad	Fe2-Sad	Fe2-Sad	Fe2-Sad	Fe2-Sad
38.336	37.763	38.329	39.026	38.059	38.413	38.571	38.981
0.380	0.193	0.238	0.271	0.204	0.312	0.271	0.114
17.877	18.834	18.598	16.290	18.076	17.063	16.293	16.401
L.O.D.	L.O.D.	L.O.D.	L.O.D.	L.O.D.	L.O.D.	L.O.D.	L.O.D.
23.897	23.805	23.613	24.336	23.509	24.047	24.350	24.352
0.252	0.274	0.274	0.290	0.275	0.289	0.290	0.291
3.656	3.436	3.524	4.056	3.498	3.600	4.131	4.142
11.237	11.304	11.242	10.998	11.151	11.107	11.073	11.091
1.630	1.571	1.573	1.876	1.616	1.727	1.818	1.866
0.796	0.758	0.786	0.555	0.755	0.684	0.629	0.667
L.O.D.	L.O.D.	L.O.D.	L.O.D.	L.O.D.	L.O.D.	L.O.D.	L.O.D.
0.112	0.188	0.136	0.225	0.111	0.311	0.187	0.223
-0.030	-0.040	-0.030	-0.050	-0.030	-0.070	-0.040	-0.050
98.1	98.1	98.3	97.9	97.2	97.5	97.6	98.1
20.27	19.62	20.07	20.39	20.15	20.63	19.85	20.21
4.04	4.66	3.94	4.38	3.74	3.80	5.01	4.60
1.92	1.90	1.92	1.89	1.92	1.86	1.90	1.89
100.5	100.5	100.6	100.2	99.5	99.7	100.0	100.4
5.872	5.781	5.851	6.004	5.879	5.945	5.953	5.986
2.128	2.219	2.149	1.996	2.121	2.055	2.047	2.014
0.000	0.000	0.000	0.000	0.000	0.000	0.000	0.000
0.000	0.000	0.000	0.000	0.000	0.000	0.000	0.000
8.0	8.0	8.0	8.0	8.0	8.0	8.0	8.0
0.044	0.022	0.027	0.031	0.024	0.036	0.031	0.013
1.100	1.179	1.196	0.957	1.170	1.057	0.916	0.955
0.466	0.537	0.452	0.507	0.436	0.441	0.580	0.533
2.555	2.478	2.523	2.574	2.565	2.635	2.522	2.551
0.835	0.784	0.802	0.930	0.806	0.831	0.950	0.948
5.0	5.0	5.0	5.0	5.0	5.0	5.0	5.0
0.033	0.036	0.035	0.038	0.036	0.038	0.038	0.038
0.040	0.033	0.040	0.050	0.036	0.036	0.041	0.044
1.844	1.854	1.839	1.813	1.846	1.842	1.831	1.825
0.083	0.078	0.086	0.100	0.082	0.084	0.090	0.093
2.0	2.0	2.0	2.0	2.0	2.0	2.0	2.0
0.000	0.000	0.000	0.000	0.000	0.000	0.000	0.000
0.401	0.388	0.380	0.460	0.402	0.434	0.454	0.462
0.156	0.148	0.153	0.109	0.149	0.135	0.124	0.131
0.6	0.5	0.5	0.6	0.6	0.6	0.6	0.6
22.0	22.0	22.0	22.0	22.0	22.0	22.0	22.0
2.0	2.0	2.0	1.9	2.0	1.9	2.0	1.9
0.0	0.0	0.0	0.1	0.0	0.1	0.0	0.1
2.0	2.0	2.0	2.0	2.0	2.0	2.0	2.0
15.6	15.5	15.5	15.6	15.6	15.6	15.6	15.6
1.65	1.76	1.70	1.53	1.65	1.57	1.56	1.51
0.56	0.54	0.53	0.57	0.55	0.57	0.58	0.59
5.87	5.78	5.85	6.00	5.88	5.95	5.95	5.99
0.25	0.24	0.24	0.27	0.24	0.24	0.27	0.27

Table S2.2b. Amphibole analyses in wt.% and atoms per formula unit for EMF metabasalts *(cont.)*.

FSTJ326	**FSTJ326**	**FSTJ326**	**FSTJ326**	**FSTJ326**	**FSTJ326**
site_1_amph_9	site_1_amph_10	site_1_amph_11	site_1_amph_12	site_1_amph_13	site_1_amph_14
BA	BA	BA	BA	BA	BA
Fe2-Act	Act	Act	Act	Act	Act
51.118	51.577	52.148	53.360	52.043	51.823
0.118	0.091	0.085	0.062	0.082	0.090
3.107	2.687	2.335	1.022	1.893	2.195
L.O.D.	L.O.D.	L.O.D.	L.O.D.	L.O.D.	L.O.D.
20.628	20.755	20.284	19.374	20.127	20.392
0.331	0.366	0.361	0.326	0.364	0.339
9.869	10.738	11.183	12.042	11.215	11.157
11.293	11.338	11.356	11.485	11.326	11.230
0.469	0.378	0.352	0.119	0.266	0.287
0.054	0.051	0.018	0.019	0.033	0.026
L.O.D.	L.O.D.	L.O.D.	L.O.D.	L.O.D.	L.O.D.
0.031	0.032	0.015	L.O.D.	0.023	0.020
-0.010	-0.010	0.000	0.000	-0.010	0.000
97.0	98.0	98.1	97.8	97.4	97.6
19.70	19.30	19.09	19.05	19.16	19.11
1.03	1.62	1.33	0.37	1.07	1.43
2.01	2.01	2.02	2.03	2.02	2.01
99.1	100.2	100.3	99.9	99.5	99.7
7.678	7.660	7.712	7.886	7.761	7.715
0.322	0.340	0.288	0.114	0.239	0.285
0.000	0.000	0.000	0.000	0.000	0.000
0.000	0.000	0.000	0.000	0.000	0.000
8.0	8.0	8.0	8.0	8.0	8.0
0.013	0.010	0.009	0.007	0.009	0.010
0.228	0.130	0.119	0.064	0.094	0.100
0.117	0.180	0.149	0.040	0.121	0.160
2.432	2.303	2.257	2.236	2.283	2.254
2.210	2.377	2.466	2.653	2.493	2.476
5.0	5.0	5.0	5.0	5.0	5.0
0.042	0.046	0.045	0.041	0.046	0.043
0.042	0.096	0.103	0.119	0.106	0.125
1.817	1.804	1.799	1.819	1.810	1.791
0.098	0.054	0.052	0.021	0.038	0.041
2.0	2.0	2.0	2.0	2.0	2.0
0.000	0.000	0.000	0.000	0.000	0.000
0.038	0.055	0.049	0.013	0.039	0.042
0.010	0.010	0.003	0.004	0.006	0.005
0.0	0.1	0.1	0.0	0.0	0.0
22.0	22.0	22.0	22.0	22.0	22.0
2.0	2.0	2.0	2.0	2.0	2.0
0.0	0.0	0.0		0.0	0.0
2.0	2.0	2.0	2.0	2.0	2.0
15.0	15.1	15.1	15.0	15.0	15.0
0.37	0.33	0.29	0.12	0.23	0.28
0.05	0.07	0.05	0.02	0.05	0.05
7.68	7.66	7.71	7.89	7.76	7.72
0.48	0.51	0.52	0.54	0.52	0.52

Table S2.2c. Feldspar analyses in wt.% and atoms per formula unit for Elsie Mountain Formation metabasalts.

Sample #		FSTJ098	FSTJ098	FSTJ098	FSTJ098	FSTJ098	FSTJ098	FSTJ301	FSTJ301	FSTJ301	FSTJ301	FSTJ301
Analysis		EMP098 Q1S13	EMP098 Q1S13-1	EMP098Q 1S13-2	EMP098Q 2_1S10	EMP098Q 2_1S10-1	EMP098Q 3_1S7	FSTJ301_site_1_fel_2	FSTJ301_site_1_fel_3	FSTJ301_site_1_fel_4	FSTJ301_site_1_fel_5	FSTJ301_site_1_fel_6
Rock Type		BH	BH	BH	BH	BH	BH	BH	BH	BH	BH	BH
Feldspar species	L.O.D.*	anorthite	anorthite	bytownite	bytownite	bytownite	bytownite	labradorite	labradorite	labradorite	bytownite	labradorite
SiO_2	0.036	45.535	45.651	45.579	47.982	46.767	48.644	55.070	50.584	50.307	50.008	50.952
TiO_2	0.022	L.O.D.	0.031	L.O.D.	L.O.D.	L.O.D.	0.045	L.O.D.	L.O.D.	L.O.D.	L.O.D.	L.O.D.
Al_2O_3	0.030	34.772	34.371	34.489	32.901	34.353	32.759	28.432	31.438	31.447	31.668	30.959
MgO	0.021	L.O.D.	L.O.D.	L.O.D.	L.O.D.	L.O.D.	L.O.D.	L.O.D.	L.O.D.	L.O.D.	L.O.D.	0.021
CaO	0.025	18.339	18.274	18.238	16.258	17.846	15.840	10.752	14.277	14.383	14.630	13.792
MnO	0.019	L.O.D.	L.O.D.	L.O.D.	L.O.D.	L.O.D.	L.O.D.	L.O.D.	L.O.D.	L.O.D.	L.O.D.	L.O.D.
FeO_{total}	0.024	0.391	0.372	0.332	0.353	0.347	0.410	0.219	0.443	0.288	0.164	0.325
SrO	0.100	L.O.D.	L.O.D.	L.O.D.	L.O.D.	L.O.D.	L.O.D.	0.105	0.125	0.109	L.O.D.	L.O.D.
BaO	0.054	L.O.D.	L.O.D.	L.O.D.	0.025	L.O.D.	L.O.D.	L.O.D.	L.O.D.	L.O.D.	L.O.D.	L.O.D.
Na_2O	0.013	1.056	1.127	1.185	2.263	1.531	2.495	5.564	3.476	3.421	3.213	3.737
K_2O	0.020	L.O.D.	L.O.D.	L.O.D.	0.025	L.O.D.	0.023	0.087	0.054	0.063	0.034	0.089
TOTAL		100.1	99.8	99.8	99.8	100.8	100.2	100.2	100.4	100.0	99.7	99.9
Structural formula on the basis of 8 oxygens												
Si		2.10	2.11	2.11	2.21	2.14	2.23	2.48	2.30	2.30	2.29	2.33
Ti			0.00				0.00					
Al		1.89	1.87	1.88	1.78	1.85	1.77	1.51	1.69	1.69	1.71	1.67
Mg												0.00
Ca		0.91	0.91	0.90	0.80	0.87	0.78	0.52	0.70	0.70	0.72	0.67
Mn												
Fe		0.01	0.01	0.01	0.01	0.01	0.01	0.00	0.01	0.00	0.00	0.01
Sr								0.00	0.00	0.00		
Ba					0.00							
Na		0.09	0.10	0.11	0.20	0.14	0.22	0.49	0.31	0.30	0.28	0.33
K					0.00		0.00	0.01	0.00	0.00	0.00	0.01
SUM								5.0	5.0	5.0	5.0	5.0
End-members												
Or%		0.0	0.1	0.1	0.1	0.1	0.1	0.5	0.3	0.4	0.2	0.5
Ab%		9.4	10.0	10.5	20.1	13.4	22.1	48.1	30.5	30.0	28.4	32.7
An%		90.6	90.0	89.5	79.8	86.6	77.7	51.4	69.2	69.7	71.4	66.8

*L.O.D. = Limit of detection is defined as 3 x standard deviation of the total accumulated background counts.
BA = basaltic amphibolite; BG = basaltic granofels; BH = basaltic hornfels.

Table S2.2c. Feldspar analyses in wt.% and atoms per formula unit for Elsie Mountain Formation metabasalts *(cont.)*.

FSTJ301	**FSTJ301**	**FSTJ301**	**FSTJ301**	**FSTJ301**	**FSTJ301**	**FSTJ301**	**FSTJ301**	**FSTJ301**	**FSTJ301**	**FSTJ301**	**FSTJ301**
FSTJ301_site_1_fel_7 BH labradorite	FSTJ301_site_1_fel_8 BH bytownite	FSTJ301_site_2_fel_9 BH labradorite	FSTJ301_site_2_fel_10 BH labradorite	FSTJ301_site_2_fel_11 BH bytownite	FSTJ301_site_2_fel_12 BH bytownite	FSTJ301_site_2_fel_13 BH labradorite	FSTJ301_site_2_fel_19 BH bytownite	FSTJ301_site_2_fel_20 BH bytownite	FSTJ301_site_2_fel_21 BH bytownite	FSTJ301_site_2_fel_14 BH bytownite	FSTJ301_site_2_fel_15 BH andesine
51.176	50.236	50.409	50.194	49.968	49.886	50.410	49.842	49.538	49.938	49.761	55.256
L.O.D.	0.028	0.027	L.O.D.	L.O.D.	L.O.D.	L.O.D.	L.O.D.	L.O.D.	L.O.D.	L.O.D.	L.O.D.
31.136	31.781	31.262	31.349	31.458	31.292	31.504	31.872	31.650	31.459	31.558	27.899
L.O.D.	L.O.D.	L.O.D.	L.O.D.	L.O.D.	L.O.D.	L.O.D.	L.O.D.	L.O.D.	L.O.D.	L.O.D.	L.O.D.
14.022	14.658	14.219	14.190	14.579	14.445	14.326	14.758	14.951	14.445	14.556	10.456
L.O.D.	L.O.D.	L.O.D.	L.O.D.	L.O.D.	L.O.D.	L.O.D.	L.O.D.	L.O.D.	L.O.D.	L.O.D.	L.O.D.
0.529	0.509	0.552	0.215	0.294	0.408	0.156	0.173	0.539	0.734	0.329	0.340
L.O.D.	L.O.D.	L.O.D.	L.O.D.	L.O.D.	0.103	L.O.D.	L.O.D.	0.100	0.130	L.O.D.	0.102
L.O.D.	L.O.D.	L.O.D.	L.O.D.	L.O.D.	L.O.D.	L.O.D.	L.O.D.	L.O.D.	L.O.D.	L.O.D.	L.O.D.
3.668	3.364	3.484	3.430	3.295	3.397	3.443	3.112	3.224	3.268	3.300	5.820
0.063	0.039	0.040	0.051	0.060	0.037	0.043	0.040	0.043	0.031	0.047	0.104
100.6	100.6	100.0	99.4	99.7	99.6	99.9	99.8	100.0	100.0	99.6	100.0
2.32	2.28	2.30	2.30	2.29	2.29	2.30	2.28	2.27	2.29	2.28	2.50
	0.00	0.00									
1.67	1.70	1.68	1.69	1.70	1.69	1.69	1.72	1.71	1.70	1.71	1.49
0.68	0.71	0.70	0.70	0.72	0.71	0.70	0.72	0.73	0.71	0.72	0.51
0.01	0.01	0.01	0.00	0.01	0.01	0.00	0.00	0.01	0.01	0.01	0.01
					0.00			0.00	0.00		0.00
0.32	0.30	0.31	0.30	0.29	0.30	0.30	0.28	0.29	0.29	0.29	0.51
0.00	0.00	0.00	0.00	0.00	0.00	0.00	0.00	0.00	0.00	0.00	0.01
5.0	5.0	5.0	5.0	5.0	5.0	5.0	5.0	5.0	5.0	5.0	5.0
0.4	0.2	0.2	0.3	0.3	0.2	0.2	0.2	0.2	0.2	0.3	0.6
32.0	29.3	30.6	30.3	28.9	29.8	30.2	27.6	28.0	29.0	29.0	49.9
67.6	70.5	69.1	69.4	70.7	70.0	69.5	72.2	71.8	70.8	70.7	49.5

Table S2.2c. Feldspar analyses in wt.% and atoms per formula unit for Elsie Mountain Formation metabasalts *(cont.)*.

FSTJ301	**FSTJ301**	**FSTJ301**	**FSTJ301**	**FSTJ301**	**FSTJ299**	**FSTJ299**	**FSTJ299**	**FSTJ299**	**FSTJ299**	**FSTJ299**	**FSTJ299**
FSTJ301_site_2_fel_16 BH labradorite	FSTJ301_site_1_fel_1 BH bytownite	FSTJ301_site_2_fel_17 BH bytownite	FSTJ301_site_2_fel_18 BH bytownite	FSTJ301_site_2_fel_22 BH labradorite	FSTJ299_site_1_fel_1 BH labradorite	FSTJ299_site_1_fel_2 BH labradorite	FSTJ299_site_1_fel_3 BH labradorite	FSTJ299_site_2_fel_7 BH labradorite	FSTJ299_site_2_fel_10 BH labradorite	FSTJ299_site_2_fel_13 BH andesine	FSTJ299_site_1_fel_4 BH labradorite
54.418	49.887	49.442	49.969	53.807	53.822	53.851	53.407	54.102	54.545	56.370	54.147
L.O.D.	L.O.D.	L.O.D.	L.O.D.	L.O.D.	L.O.D.	0.022	L.O.D.	0.024	L.O.D.	L.O.D.	L.O.D.
28.335	31.461	31.576	31.758	28.557	28.923	29.151	29.594	29.213	28.851	27.259	28.998
L.O.D.	L.O.D.	L.O.D.	L.O.D.	L.O.D.	L.O.D.	L.O.D.	L.O.D.	L.O.D.	L.O.D.	L.O.D.	L.O.D.
10.866	14.530	14.604	14.557	11.094	11.555	11.585	12.305	11.644	11.136	9.634	11.328
L.O.D.	L.O.D.	L.O.D.	L.O.D.	L.O.D.	L.O.D.	L.O.D.	L.O.D.	L.O.D.	L.O.D.	L.O.D.	L.O.D.
0.219	0.503	0.240	0.167	0.208	0.287	0.214	0.422	0.350	0.863	0.166	0.214
L.O.D.	0.139	L.O.D.	L.O.D.	L.O.D.	L.O.D.	L.O.D.	L.O.D.	L.O.D.	L.O.D.	L.O.D.	L.O.D.
L.O.D.	L.O.D.	L.O.D.	L.O.D.	L.O.D.	L.O.D.	L.O.D.	L.O.D.	L.O.D.	L.O.D.	L.O.D.	L.O.D.
5.429	3.379	3.219	3.203	5.355	5.098	5.071	4.706	5.063	5.105	6.311	5.225
0.114	0.046	0.039	0.029	0.065	0.068	0.060	0.062	0.105	0.320	0.134	0.093
99.4	99.9	99.1	99.7	99.1	99.8	100.0	100.5	100.5	100.8	99.9	100.0
2.47	2.29	2.28	2.29	2.45	2.44	2.44	2.41	2.44	2.46	2.54	2.45
						0.00		0.00			
1.52	1.70	1.71	1.71	1.54	1.55	1.55	1.58	1.55	1.53	1.45	1.55
0.53	0.71	0.72	0.71	0.54	0.56	0.56	0.60	0.56	0.54	0.46	0.55
0.00	0.01	0.00	0.00	0.00	0.00	0.00	0.01	0.01	0.01	0.00	0.00
	0.00										
0.48	0.30	0.29	0.28	0.47	0.45	0.44	0.41	0.44	0.45	0.55	0.46
0.01	0.00	0.00	0.00	0.00	0.00	0.00	0.00	0.01	0.02	0.01	0.01
5.0	5.0	5.0	5.0	5.0	5.0	5.0	5.0	5.0	5.0	5.0	5.0
0.7	0.3	0.2	0.2	0.4	0.4	0.3	0.4	0.6	1.8	0.8	0.5
47.2	29.5	28.4	28.4	46.5	44.2	44.0	40.8	43.8	44.5	53.8	45.3
52.2	70.2	71.3	71.4	53.2	55.4	55.6	58.9	55.6	53.7	45.4	54.2

Table S2.2c. Feldspar analyses in wt.% and atoms per formula unit for Elsie Mountain Formation metabasalts *(cont.)*.

FSTJ299	**FSTJ299**	**FSTJ299**	**FSTJ299**	**FSTJ299**	**FSTJ299**	**FSTJ298**	**FSTJ298**	**FSTJ298**	**FSTJ298**	**FSTJ298**	**FSTJ298**	**FSTJ298**
FSTJ299_site_1_fel_5 BH	FSTJ299_site_2_fel_6 BH	FSTJ299_site_2_fel_8 BH	FSTJ299_site_2_fel_9 BH	FSTJ299_site_2_fel_11 BH	FSTJ299_site_2_fel_12 BH	FSTJ298_site_1_fel_1 BH	FSTJ298_site_1_fel_2 BH	FSTJ298_site_1_fel_3 BH	FSTJ298_site_1_fel_4 BH	FSTJ298_site_1_fel_5 BH	FSTJ298_site_1_fel_6 BH	FSTJ298_site_1_fel_7 BH
andesine	andesine	labradorite	andesine	andesine	labradorite	andesine	andesine	andesine	andesine	andesine	andesine	andesine
57.433	57.869	53.724	57.863	56.378	54.221	56.901	57.234	57.426	57.241	57.198	57.553	57.253
L.O.D.	L.O.D.	L.O.D.	L.O.D.	L.O.D.	L.O.D.	L.O.D.	L.O.D.	L.O.D.	L.O.D.	L.O.D.	L.O.D.	L.O.D.
26.883	26.882	29.315	26.672	27.546	28.912	27.199	27.250	26.944	27.301	26.948	26.985	27.045
L.O.D.	L.O.D.	L.O.D.	L.O.D.	L.O.D.	L.O.D.	L.O.D.	L.O.D.	L.O.D.	L.O.D.	L.O.D.	L.O.D.	L.O.D.
8.871	8.771	11.796	8.591	9.649	11.437	9.212	9.059	9.022	9.058	9.164	8.877	9.201
L.O.D.	L.O.D.	L.O.D.	L.O.D.	L.O.D.	L.O.D.	L.O.D.	0.019	L.O.D.	L.O.D.	L.O.D.	L.O.D.	L.O.D.
0.297	0.246	0.254	0.208	0.225	0.353	0.202	0.251	0.266	0.164	0.217	0.234	0.268
L.O.D.	L.O.D.	L.O.D.	L.O.D.	L.O.D.	L.O.D.	L.O.D.	L.O.D.	L.O.D.	L.O.D.	L.O.D.	L.O.D.	0.102
L.O.D.	L.O.D.	L.O.D.	L.O.D.	L.O.D.	L.O.D.	L.O.D.	0.058	L.O.D.	L.O.D.	L.O.D.	L.O.D.	0.062
6.765	6.769	4.986	6.860	6.212	5.210	6.441	6.489	6.551	6.561	6.481	6.628	6.564
0.123	0.143	0.073	0.143	0.170	0.106	0.073	0.153	0.089	0.067	0.101	0.078	0.080
100.4	100.7	100.1	100.3	100.2	100.2	100.0	100.5	100.3	100.4	100.1	100.4	100.6
2.57	2.58	2.43	2.59	2.53	2.45	2.55	2.56	2.57	2.56	2.57	2.57	2.56
1.42	1.41	1.56	1.41	1.46	1.54	1.44	1.44	1.42	1.44	1.42	1.42	1.43
0.43	0.42	0.57	0.41	0.46	0.55	0.44	0.43	0.43	0.43	0.44	0.43	0.44
0.01	0.00	0.00	0.00	0.00	0.01	0.00	0.00	0.00	0.00	0.00	0.00	0.00
							0.00					0.00
							0.00					0.00
0.59	0.59	0.44	0.59	0.54	0.46	0.56	0.56	0.57	0.57	0.56	0.57	0.57
0.01	0.01	0.00	0.01	0.01	0.01	0.00	0.01	0.01	0.00	0.01	0.00	0.00
5.0	5.0	5.0	5.0	5.0	5.0	5.0	5.0	5.0	5.0	5.0	5.0	5.0
0.7	0.8	0.4	0.8	1.0	0.6	0.4	0.9	0.5	0.4	0.6	0.4	0.4
57.6	57.8	43.2	58.6	53.3	44.9	55.6	56.0	56.5	56.5	55.8	57.2	56.1
41.7	41.4	56.4	40.6	45.7	54.5	44.0	43.2	43.0	43.1	43.6	42.3	43.5

Table S2.2c. Feldspar analyses in wt.% and atoms per formula unit for Elsie Mountain Formation metabasalts *(cont.)*.

FSTJ298	**FSTJ298**	**FSTJ298**	**FSTJ298**	**FSTJ298**	**FSTJ118**	**FSTJ118**	**FSTJ118**	**FSTJ118**	**FSTJ118**	**FSTJ118**	**FSTJ118**	**FSTJ294**
FSTJ298_site_1_fel_8 BH andesine	FSTJ298_site_1_fel_9 BH andesine	FSTJ298_site_1_fel_10 BH andesine	FSTJ298_site_1_fel_11 BH andesine	FSTJ298_site_1_fel_12 BH andesine	FSTJ294_site_1_fel_1 BH labradorite	FSTJ294_site_1_fel_2 BH labradorite	FSTJ294_site_1_fel_3 BH labradorite	FSTJ294_site_1_fel_5 BH labradorite	FSTJ294_site_1_fel_8 BH labradorite	FSTJ294_site_1_fel_9 BH labradorite	FSTJ294_site_1_fel_10 BH labradorite	FSTJ294_site_1_fel_14 BH andesine
57.127	57.288	57.091	56.976	56.816	53.141	52.572	52.635	52.625	51.994	54.330	52.706	56.983
L.O.D.	L.O.D.	L.O.D.	L.O.D.	L.O.D.	L.O.D.	L.O.D.	L.O.D.	L.O.D.	L.O.D.	L.O.D.	L.O.D.	L.O.D.
27.387	27.151	27.140	27.080	26.965	29.838	29.888	29.799	29.609	30.247	28.825	29.924	27.168
L.O.D.	L.O.D.	L.O.D.	L.O.D.	L.O.D.	L.O.D.	0.021	L.O.D.	0.026	L.O.D.	L.O.D.	L.O.D.	L.O.D.
9.195	9.179	9.170	9.125	8.964	12.471	12.636	12.748	12.617	13.195	11.613	12.804	8.962
L.O.D.	L.O.D.	L.O.D.	0.026	L.O.D.	L.O.D.	L.O.D.	L.O.D.	L.O.D.	L.O.D.	L.O.D.	L.O.D.	L.O.D.
0.481	0.905	0.539	0.735	0.487	0.586	0.356	0.470	0.269	0.231	0.437	0.345	0.176
L.O.D.	L.O.D.	L.O.D.	L.O.D.	L.O.D.	L.O.D.	L.O.D.	L.O.D.	L.O.D.	L.O.D.	L.O.D.	L.O.D.	L.O.D.
0.074	L.O.D.	0.057	L.O.D.	0.067	L.O.D.	L.O.D.	L.O.D.	L.O.D.	L.O.D.	L.O.D.	L.O.D.	0.087
6.564	6.447	6.437	6.621	6.588	4.404	4.252	4.424	4.473	4.143	5.027	4.434	6.539
0.057	0.107	0.272	0.067	0.087	0.174	0.165	0.177	0.113	0.112	0.148	0.099	0.117
100.9	101.1	100.7	100.6	100.0	100.6	99.9	100.3	99.7	99.9	100.4	100.3	100.0
2.55	2.56	2.56	2.55	2.56	2.40	2.39	2.39	2.40	2.37	2.45	2.39	2.56
1.44	1.43	1.43	1.43	1.43	1.59	1.60	1.59	1.59	1.62	1.53	1.60	1.44
					0.00	0.00		0.00				
0.44	0.44	0.44	0.44	0.43	0.60	0.62	0.62	0.62	0.64	0.56	0.62	0.43
			0.00									
0.01	0.02	0.01	0.01	0.01	0.01	0.01	0.01	0.00	0.00	0.01	0.01	0.00
0.00		0.00		0.00								0.00
0.57	0.56	0.56	0.58	0.58	0.39	0.37	0.39	0.39	0.37	0.44	0.39	0.57
0.00	0.01	0.02	0.00	0.00	0.01	0.01	0.01	0.01	0.01	0.01	0.01	0.01
5.0	5.0	5.0	5.0	5.0								5.0
0.3	0.6	1.5	0.4	0.5	1.0	1.0	1.0	0.6	0.6	0.8	0.6	0.7
56.2	55.6	55.1	56.6	56.8	38.6	37.5	38.2	38.8	36.0	43.6	38.3	56.5
43.5	43.8	43.4	43.1	42.7	60.4	61.6	60.8	60.5	63.4	55.6	61.1	42.8

Table S2.2c. Feldspar analyses in wt.% and atoms per formula unit for Elsie Mountain Formation metabasalts *(cont.)*.

FSTJ294	**FSTJ294**	**FSTJ294**	**FSTJ294**	**FSTJ294**	**FSTJ294**	**FSTJ294**	**FSTJ294**	**FSTJ294**	**FSTJ294**	**FSTJ294**	**FSTJ294**	**FSTJ294**
FSTJ294_site_1_fel_15 BH andesine	FSTJ294_site_1_fel_4 BH andesine	FSTJ294_site_1_fel_14 BH K-spar	FSTJ294_site_1_fel_15 BH andesine	FSTJ294_site_1_fel_11 BH andesine	FSTJ294_site_1_fel_12 BH andesine	FSTJ294_site_1_fel_13 BH andesine	FSTJ294_site_1_fel_6 BH andesine	FSTJ294_site_1_fel_7 BH andesine	EMP118 Q3S5-1 BH andesine	EMP118 Q3S5 BH andesine	EMP118 Q5PLS11 BH andesine	EMP118 Q5PLS12 BH andesine
56.851	57.043	64.710	57.479	59.531	59.061	57.047	56.906	56.944	57.233	57.211	57.055	56.866
L.O.D.	L.O.D.	L.O.D.	L.O.D.	L.O.D.	L.O.D.	L.O.D.	L.O.D.	L.O.D.	L.O.D.	L.O.D.	0.022	L.O.D.
27.235	27.182	18.588	27.137	25.874	25.511	27.187	26.960	27.290	27.023	27.133	27.328	27.337
L.O.D.	L.O.D.	L.O.D.	L.O.D.	L.O.D.	L.O.D.	L.O.D.	L.O.D.	L.O.D.	L.O.D.	L.O.D.	L.O.D.	L.O.D.
9.145	9.037	0.278	8.769	7.425	7.210	8.938	8.843	9.254	8.865	9.054	9.109	9.216
L.O.D.	L.O.D.	L.O.D.	L.O.D.	L.O.D.	L.O.D.	L.O.D.	L.O.D.	L.O.D.	L.O.D.	L.O.D.	0.023	L.O.D.
0.209	0.191	0.165	0.318	0.093	0.101	0.095	0.116	0.179	0.509	0.705	1.006	0.142
L.O.D.	L.O.D.	L.O.D.	L.O.D.	L.O.D.	L.O.D.	L.O.D.	L.O.D.	L.O.D.	L.O.D.	L.O.D.	L.O.D.	L.O.D.
0.061	L.O.D.	0.668	L.O.D.	L.O.D.	L.O.D.	L.O.D.	L.O.D.	L.O.D.	L.O.D.	L.O.D.	L.O.D.	L.O.D.
6.365	6.594	1.193	6.679	7.510	7.542	6.594	6.635	6.391	6.704	6.596	6.526	6.445
0.184	0.073	14.575	0.075	0.105	0.157	0.086	0.067	0.100	0.093	0.102	0.098	0.087
100.1	100.1	100.2	100.5	100.5	99.6	99.9	99.5	100.2	100.4	100.8	101.2	100.1
2.55	2.56	2.99	2.57	2.64	2.65	2.56	2.56	2.55	2.56	2.56	2.55	2.55
1.44	1.44	1.01	1.43	1.35	1.35	1.44	1.43	1.44	1.43	1.43	0.00 1.44	1.44
0.44	0.43	0.01	0.42	0.35	0.35	0.43	0.43	0.44	0.43	0.43	0.44	0.44
0.00	0.00	0.00	0.01	0.00	0.00	0.00	0.00	0.00	0.01	0.01	0.00 0.02	0.00
0.00		0.01										
0.55	0.57	0.11	0.58	0.65	0.66	0.57	0.58	0.56	0.58	0.57	0.57	0.56
0.01	0.00	0.86	0.00	0.01	0.01	0.00	0.00	0.01	0.01	0.01	0.01	0.00
5.0	5.0	5.0	5.0	5.0	5.0	5.0	5.0	5.0	5.0	5.0	5.0	5.0
1.0	0.4	87.7	0.4	0.6	0.9	0.5	0.4	0.6	0.5	0.6	0.6	0.5
55.2	56.7	10.9	57.7	64.3	64.9	56.9	57.4	55.2	57.5	56.5	56.1	55.6
43.8	42.9	1.4	41.9	35.1	34.3	42.6	42.3	44.2	42.0	42.9	43.3	43.9

Table S2.2c. Feldspar analyses in wt.% and atoms per formula unit for Elsie Mountain Formation metabasalts *(cont.)*.

FSTJ294	**FSTJ294**	**FSTJ294**	**FSTJ292**	**FSTJ292**	**FSTJ292**	**FSTJ292**	**FSTJ292**	**FSTJ292**	**FSTJ308**	**FSTJ308**	**FSTJ308**	**FSTJ308**
EMP118 Q5PLS13 BH andesine	EMP118 Q5PLS14 BH K-spar	EMP118 Q4_2S6 BH K-spar	FSTJ292_site_1_fel_1 BH andesine	FSTJ292_site_1_fel_2 BH andesine	FSTJ292_site_1_fel_3 BH andesine	FSTJ292_site_1_fel_4 BH andesine	FSTJ292_site_1_fel_5 BH andesine	FSTJ292_site_1_fel_6 BH andesine	EMP069Q1_4S6 BH labradorite	EMP069Q1_9S3 BH labradorite	FSTJ308_site_1_fel_2 BH labradorite	FSTJ308_site_1_fel_4 BH labradorite
57.250	64.924	64.518	60.812	60.575	60.418	60.407	60.767	60.583	54.988	54.923	55.094	54.296
L.O.D.	0.023	L.O.D.	L.O.D.	0.028	0.026	L.O.D.	L.O.D.	L.O.D.	L.O.D.	L.O.D.	L.O.D.	L.O.D.
27.243	18.385	19.053	24.897	25.075	25.192	25.039	24.869	25.285	28.913	28.102	28.131	28.729
L.O.D.	L.O.D.	L.O.D.	L.O.D.	L.O.D.	L.O.D.	L.O.D.	L.O.D.	L.O.D.	L.O.D.	L.O.D.	L.O.D.	L.O.D.
9.032	0.453	0.800	6.428	6.651	6.616	6.584	6.390	6.624	11.308	10.858	10.826	11.562
L.O.D.	L.O.D.	L.O.D.	L.O.D.	L.O.D.	L.O.D.	L.O.D.	L.O.D.	L.O.D.	L.O.D.	L.O.D.	L.O.D.	L.O.D.
0.081	0.040	0.034	0.302	0.249	0.302	0.237	0.229	0.235	0.473	0.246	0.322	0.195
L.O.D.	L.O.D.	L.O.D.	L.O.D.	L.O.D.	L.O.D.	L.O.D.	L.O.D.	L.O.D.	L.O.D.	0.112	L.O.D.	L.O.D.
L.O.D.	0.877	0.894	L.O.D.	L.O.D.	L.O.D.	L.O.D.	0.069	L.O.D.	L.O.D.	L.O.D.	L.O.D.	L.O.D.
6.584	0.762	1.255	8.136	8.086	8.068	8.017	8.146	8.009	5.274	5.439	5.549	5.105
0.065	14.138	13.180	0.123	0.098	0.122	0.108	0.119	0.096	0.106	0.142	0.114	0.120
100.3	99.6	99.7	100.7	100.8	100.7	100.4	100.6	100.8	101.1	99.8	100.0	100.0
2.56	3.00	2.97	2.69	2.68	2.68	2.68	2.69	2.68	2.48	2.48	2.46	2.49
	0.00			0.00	0.00							
1.44	1.00	1.03	1.30	1.31	1.32	1.31	1.30	1.32	1.50	1.50	1.53	1.50
0.43	0.02	0.04	0.31	0.32	0.31	0.31	0.30	0.31	0.51	0.54	0.54	0.53
0.00	0.00	0.00	0.01	0.00	0.01	0.00	0.00	0.00	0.01	0.01	0.01	0.00
										0.00		
	0.02	0.02					0.00					
0.57	0.07	0.11	0.70	0.69	0.69	0.69	0.70	0.69	0.48	0.47	0.46	0.48
0.00	0.83	0.77	0.01	0.01	0.01	0.01	0.01	0.01	0.01	0.01	0.01	0.01
5.0	4.9	5.0	5.0	5.0	5.0	5.0	5.0	5.0	5.0	5.0	5.0	5.0
0.4	90.2	83.6	0.7	0.5	0.7	0.6	0.7	0.5	0.9	0.8	0.6	0.8
56.7	7.4	12.1	69.1	68.4	68.3	68.4	69.3	68.3	48.1	46.4	45.5	47.2
43.0	2.4	4.3	30.2	31.1	31.0	31.0	30.0	31.2	51.0	52.9	53.9	52.0

Table S2.2c. Feldspar analyses in wt.% and atoms per formula unit for Elsie Mountain Formation metabasalts *(cont.)*.

FSTJ308	**FSTJ308**	**FSTJ308**	**FSTJ308**	**FSTJ308**	**FSTJ307**	**FSTJ307**	**FSTJ307**	**FSTJ307**	**FSTJ307**	**FSTJ307**	**FSTJ307**	**FSTJ307**
FSTJ308_site_1_fel_5 BH labradorite	FSTJ308_site_1_fel_6 BH labradorite	FSTJ308_site_1_fel_7 BH andesine	FSTJ308_site_1_fel_8 BH labradorite	FSTJ308_site_1_fel_9 BH labradorite	FSTJ308_site_1_fel_1 BH labradorite	FSTJ308_site_1_fel_3 BH andesine	FSTJ307_site_1_fel_1 BH andesine	FSTJ307_site_1_fel_2 BH andesine	FSTJ307_site_1_fel_3 BH andesine	FSTJ307_site_1_fel_5 BH andesine	FSTJ307_site_2_fel_7 BH andesine	FSTJ307_site_2_fel_8 BH andesine
56.355	54.776	55.418	58.224	58.127	55.187	56.037	55.456	56.321	55.734	56.740	56.229	55.817
L.O.D.	0.029	L.O.D.	L.O.D.	L.O.D.	L.O.D.	L.O.D.	L.O.D.	0.023	L.O.D.	L.O.D.	L.O.D.	L.O.D.
27.543	28.205	28.001	26.696	26.736	27.968	27.943	27.896	27.707	27.903	27.033	27.434	27.708
L.O.D.	L.O.D.	L.O.D.	L.O.D.	L.O.D.	L.O.D.	L.O.D.	L.O.D.	L.O.D.	L.O.D.	L.O.D.	L.O.D.	L.O.D.
9.968	11.031	10.555	8.681	8.632	10.424	10.265	10.394	9.953	10.150	9.277	9.805	10.105
L.O.D.	L.O.D.	L.O.D.	L.O.D.	L.O.D.	L.O.D.	L.O.D.	L.O.D.	L.O.D.	L.O.D.	L.O.D.	L.O.D.	L.O.D.
0.252	0.637	0.310	0.093	0.093	0.168	0.196	0.340	0.437	0.165	0.109	0.150	0.135
L.O.D.	L.O.D.	L.O.D.	L.O.D.	L.O.D.	0.117	L.O.D.	L.O.D.	L.O.D.	L.O.D.	L.O.D.	L.O.D.	L.O.D.
L.O.D.	0.060	L.O.D.	L.O.D.	L.O.D.	L.O.D.	L.O.D.	L.O.D.	0.056	L.O.D.	L.O.D.	L.O.D.	L.O.D.
5.969	5.366	5.690	6.861	6.875	5.696	5.910	5.899	6.113	5.863	6.342	6.091	5.950
0.153	0.112	0.141	0.054	0.036	0.060	0.039	0.059	0.150	0.066	0.037	0.058	0.045
100.2	100.2	100.1	100.6	100.5	99.6	100.4	100.0	100.8	99.9	99.5	99.8	99.8
2.49	2.46	2.53	2.48	2.50	2.50	2.51	2.50	2.52	2.51	2.56	2.53	2.52
	0.00							0.00				
1.50	1.53	1.46	1.50	1.49	1.49	1.48	1.48	1.46	1.48	1.44	1.46	1.47
0.52	0.56	0.48	0.53	0.51	0.51	0.49	0.50	0.48	0.49	0.45	0.47	0.49
0.01	0.00	0.00	0.01	0.01	0.00	0.00	0.01	0.01	0.00	0.00	0.00	0.00
					0.00							
	0.00											
0.49	0.45	0.52	0.47	0.50	0.50	0.51	0.52	0.53	0.51	0.55	0.53	0.52
0.01	0.01	0.01	0.01	0.01	0.00	0.00	0.00	0.01	0.00	0.00	0.00	0.00
5.0	5.0	5.0	5.0	5.0	5.0	5.0	5.0	5.0	5.0	5.0	5.0	5.0
0.6	0.7	0.9	0.6	0.8	0.3	0.2	0.3	0.8	0.4	0.2	0.3	0.3
47.8	44.1	51.6	46.5	49.0	49.5	50.9	50.5	52.2	50.9	55.2	52.7	51.5
51.5	55.2	47.6	52.8	50.2	50.1	48.9	49.2	47.0	48.7	44.6	46.9	48.3

Table S2.2c. Feldspar analyses in wt.% and atoms per formula unit for Elsie Mountain Formation metabasalts *(cont.)*.

FSTJ307	**FSTJ307**	**FSTJ307**	**FSTJ069**	**FSTJ069**	**FSTJ326**	**FSTJ326**	**FSTJ326**	**FSTJ326**	**FSTJ326**	**FSTJ326**	**FSTJ326**	**FSTJ326**
FSTJ307_site_1_fel_4	FSTJ307_site_2_fel_6	FSTJ307_site_2_fel_9	FSTJ307_site_2_fel_10	FSTJ307_site_2_fel_11	FSTJ326_site_1_fel_1	FSTJ326_site_1_fel_2	FSTJ326_site_1_fel_3	FSTJ326_site_1_fel_4	FSTJ326_site_1_fel_5	FSTJ326_site_1_fel_6	FSTJ326_site_1_fel_7	FSTJ326_site_1_fel_8
BH andesine	BH andesine	BH andesine	BG anorthite	BG anorthite	BA andesine	BA labradorite	BA labradorite	BA labradorite	BA labradorite	BA labradorite	BA oligoclase	BA andesine
56.862	55.162	54.804	44.715	44.535	55.301	54.211	54.872	54.766	54.890	55.167	61.237	60.499
L.O.D.	L.O.D.	L.O.D.	L.O.D.	L.O.D.	L.O.D.	L.O.D.	L.O.D.	L.O.D.	L.O.D.	L.O.D.	0.025	L.O.D.
27.146	28.350	28.173	35.083	35.499	27.965	28.939	28.427	28.667	28.603	28.282	24.235	25.137
L.O.D.	L.O.D.	L.O.D.	L.O.D.	L.O.D.	L.O.D.	L.O.D.	L.O.D.	L.O.D.	L.O.D.	L.O.D.	0.042	L.O.D.
9.120	10.608	11.068	18.748	19.090	10.164	11.214	10.712	10.869	10.814	10.611	5.504	6.634
L.O.D.	L.O.D.	L.O.D.	L.O.D.	L.O.D.	L.O.D.	L.O.D.	L.O.D.	L.O.D.	L.O.D.	L.O.D.	L.O.D.	0.020
0.090	0.781	0.412	0.341	0.160	0.161	0.100	0.143	0.204	0.456	0.178	0.263	0.217
L.O.D.	0.171	0.120	0.101	L.O.D.	L.O.D.	L.O.D.	L.O.D.	L.O.D.	L.O.D.	0.107	L.O.D.	L.O.D.
L.O.D.	L.O.D.	L.O.D.	L.O.D.	L.O.D.	L.O.D.	0.052	L.O.D.	L.O.D.	L.O.D.	L.O.D.	0.108	0.070
6.378	5.531	5.360	0.822	0.604	5.810	5.225	5.685	5.579	5.589	5.693	8.407	8.006
0.049	0.149	0.132	L.O.D.	L.O.D.	L.O.D.	L.O.D.	0.034	0.026	0.024	0.022	0.241	0.119
99.6	100.8	100.1	99.8	99.9	99.4	99.7	99.9	100.1	100.4	100.1	100.1	100.7
2.56	2.59	2.59	2.07	2.06	2.50	2.45	2.48	2.47	2.47	2.49	2.72	2.68
											0.00	
1.44	1.40	1.40	1.92	1.94	1.49	1.54	1.51	1.52	1.52	1.50	1.27	1.31
											0.00	
0.44	0.41	0.41	0.93	0.95	0.49	0.54	0.52	0.53	0.52	0.51	0.26	0.31
												0.00
0.00	0.00	0.00	0.01	0.00	0.00	0.00	0.00	0.00	0.01	0.00	0.00	0.00
	0.00	0.00	0.00							0.00		0.00
						0.00					0.00	
0.56	0.59	0.59	0.07	0.05	0.51	0.46	0.50	0.49	0.49	0.50	0.73	0.69
0.00	0.00	0.00					0.00	0.00	0.00	0.00	0.01	0.01
5.0	5.0	5.0			5.0	5.0	5.0	5.0	5.0	5.0	5.0	5.0
0.3	0.3	0.2	0.0	0.1	0.0	0.0	0.2	0.1	0.1	0.1	1.4	0.7
55.7	58.7	58.9	7.4	5.4	50.8	45.7	48.9	48.1	48.3	49.2	72.4	68.1
44.0	41.0	40.9	92.6	94.5	49.2	54.3	50.9	51.8	51.6	50.7	26.2	31.2

Table S2.2c. *(cont.)* .

FSTJ326	**FSTJ326**	**FSTJ326**
FSTJ326_site_1_fel_9 BA oligoclase	FSTJ326_site_1_fel_10 BA oligoclase	FSTJ326_site_1_fel_11 BA albite
60.881	63.653	65.925
L.O.D.	0.027	L.O.D.
24.642	22.699	20.904
L.O.D.	L.O.D.	L.O.D.
6.434	3.868	1.969
L.O.D.	L.O.D.	0.022
0.194	0.219	0.499
L.O.D.	L.O.D.	L.O.D.
0.066	0.081	L.O.D.
8.766	9.898	10.899
0.028	L.O.D.	L.O.D.
101.0	100.4	100.2
2.69	2.81	2.90
	0.00	
1.28	1.18	1.08
0.30	0.18	0.09
0.00	0.00	0.01
0.00	0.00	
0.75	0.85	0.93
0.00		
5.0	5.0	5.0
0.1	0.0	0.0
71.0	82.2	90.9
28.8	17.8	9.1

Table S2.3. Whole-rock major element (wt.%) for Elsie Mountain Formation metavolcanics.

	BHVO-2	R.V. GeoRem	JB-1a	R.V. UWO	FSTJ001	FSTJ10E	FSTJ021B	FSTJ37A	FSTJ037B	FSTJ324C	FSTJ370
Notes*					1	1	1	1	1	1	1
Rock type					BA	BA	BA	BA	BA	BA	BA
XRF	GEOLABS		UWO		GEOLABS	GEOLABS	GEOLABS	GEOLABS	GEOLABS	UWO	UWO
Easting					500790	500751	500781	500805	500805	500492	501537
Northing					5154660	5154645	5154794	5154666	5154666	5154590	5155177
SiO2	49.8	49.9 ± 0.6	52.13	52.16	51.00	52.82	45.23	52.35	46.47	45.91	47.79
TiO2	2.75	2.73 ± 0.04	1.31	1.30	1.35	1.65	2.31	1.41	1.82	1.967	1.556
Al2O3	13.2	13.5 ± 0.2	14.29	14.51	13.54	11.20	13.91	13.25	14.20	17.09	14.17
Fe2O3	12.6	12.3 ± 0.2	8.95	9.10	16.13	17.22	21.01	15.67	17.08	17.87	15.61
MnO	0.17	0.17 ± 0.005	0.14	0.15	0.22	0.24	0.28	0.22	0.23	0.246	0.195
MgO	7.14	7.23 ± 0.12	7.83	7.75	5.13	4.43	5.67	4.78	6.67	3.44	6.19
CaO	11.6	11.4 ± 0.2	8.92	9.23	9.23	9.16	9.85	9.50	10.64	8.84	10.78
Na2O	2.22	2.22 ± 0.08	1.41	1.42	2.26	1.39	1.08	2.05	2.18	1.31	2.17
K2O	0.53	0.52 ± 0.01	2.68	2.74	0.75	0.80	0.48	0.68	0.87	0.83	0.58
P2O5	0.28	0.27 ± 0.02	0.26	0.26	0.13	0.21	0.26	0.16	0.30	0.27	0.17
LOI					0.51	0.71	0.37	0.26	0.35	0.34	0.42
TOTAL					100.25	99.83	100.45	100.33	100.81	98.11	99.63

Total iron expressed as Fe_2O_3; R.V. = reference value; UWO = XRF conducted at University of Ottawa; GEOLABS = XRF conducted at Ontario Geoscience Laboratories. BA = basaltic amphibolite; BG = basaltic granofels; BH = basaltic hornfels. *Notes: 1 = compositions used in calculation for the average basaltic amphibolite; 2 = compositions used in calculation for the average proximal basaltic hornfels; 3 = high Fe# basaltic amphibolites; 4 = samples with mineral chemistry data.

Table S2.3. Whole-rock major element (wt.%) for Elsie Mountain Formation metavolcanics *(cont.)* .

FSTJ084B	**FSTJ085**	**FSTJ086C**	**FSTJ087A**	**FSTJ088**	**FSTJ089**	**FSTJ091**	**FSTJ092C**	**FSTJ108A**	**FSTJ121B**	**08LEFS44**	**FSTJ098**
2	2	2	2	2	2	2	2	2	2	2	2, 4
BH	BH	BH	BH	BH	BH	BH	BH	BH	BH	BH	BH
GEOLABS	GEOLABS	GEOLABS	GEOLABS	GEOLABS	GEOLABS	GEOLABS	GEOLABS	GEOLABS	GEOLABS	GEOLABS	UWO
500313	500271	500856	500848	500863	500878	500879	500905	500217	500595	501355	500260
5155202	5155135	5155198	5155228	5155251	5155255	5155331	5155411	5154975	5155249	5155712	5155206
48.07	48.07	48.63	48.32	44.76	46.91	44.22	44.20	45.26	48.43	45.71	47.48
1.66	1.22	1.29	1.39	1.55	1.80	1.57	2.38	1.71	1.52	1.47	1.440
13.60	15.40	13.75	13.51	11.93	13.29	13.95	12.86	12.27	13.49	13.40	15.13
18.72	15.67	15.60	16.63	20.59	18.80	19.63	21.39	21.52	16.66	18.89	15.63
0.27	0.22	0.24	0.25	0.27	0.26	0.28	0.28	0.29	0.26	0.26	0.256
6.89	7.70	6.71	7.05	6.50	5.74	6.52	5.91	6.43	7.37	6.77	8.59
10.44	10.43	11.83	11.21	12.07	11.98	12.42	13.24	12.13	11.88	12.44	9.49
1.41	1.74	1.99	1.81	1.68	1.75	0.96	1.05	1.23	1.29	1.29	0.88
0.09	0.22	0.20	0.17	0.27	0.14	0.10	0.10	0.12	0.08	0.29	0.13
0.20	0.12	0.13	0.15	0.18	0.25	0.20	0.20	0.20	0.11	0.14	0.32
-0.66	-0.12	-0.02	0.20	0.27	-0.57	-0.02	-0.78	-0.54	-0.63	-0.11	0.01
100.69	100.67	100.35	100.69	100.07	100.35	99.83	100.83	100.62	100.46	100.55	99.36

Table S2.3. Whole-rock major element (wt.%) for Elsie Mountain Formation metavolcanics *(cont.)* .

FSTJ298	**FSTJ299**	**FSTJ301**	**FSTJ373**	**FSTJ010F**	**FSTJ013E**	**FSTJ322**	**FSTJ326**	**FSTJ335**	**FSTJ069**	**FSTJ118**	**FSTJ292**	**FSTJ294**
2, 4	2, 4	2, 4	2	3	3	3	3, 4	3	4	4	4	4
BH	BH	BH	BH	BA	BA	BA	BA	BA	BG	BH	BH	BH
UWO	UWO	UWO	UWO	GEOLABS	GEOLABS	UWO	UWO	UWO	GEOLABS	GEOLABS	UWO	UWO
500191	500183	500192	501444	500751	500801	500397	500475	501301	500713	500458	500238	500237
5154931	5154972	5155067	5155760	5154645	5154729	5154554	5154499	5154949	5154981	5155015	5154829	5154886
46.19	44.69	45.98	45.36	47.41	53.41	48.32	46.20	53.67	47.17	47.35	46.10	46.78
2.179	2.157	1.471	1.563	1.66	1.63	2.480	2.500	1.958	2.20	1.65	2.370	2.327
12.38	12.95	13.84	14.23	12.69	12.68	12.38	12.23	12.29	12.60	13.18	12.12	13.27
21.98	21.65	18.67	18.38	19.79	15.84	21.47	21.98	17.26	21.28	19.31	23.42	22.06
0.270	0.277	0.242	0.228	0.29	0.23	0.249	0.249	0.195	0.31	0.27	0.263	0.248
4.47	4.46	6.41	7.16	3.99	3.15	3.51	4.31	3.04	6.02	5.72	3.86	3.90
8.79	10.68	11.34	11.21	11.58	11.42	7.63	9.80	7.34	10.36	11.38	7.69	7.25
2.62	2.02	1.30	1.21	1.10	0.58	1.32	1.93	2.27	0.40	1.81	3.56	2.84
0.18	0.21	0.18	0.30	0.68	0.36	1.61	0.36	1.45	0.58	0.20	0.31	0.45
0.31	0.29	0.11	0.15	0.34	0.21	0.38	0.30	0.27	0.24	0.21	0.33	0.30
-0.54	-0.47	-0.32	-0.19	0.78	0.57	0.07	-0.01	0.24	-0.39	-0.45	-0.60	-0.62
98.83	98.91	99.22	99.60	100.31	100.08	99.42	99.85	99.98	100.77	100.63	99.42	98.81

Table S2.3. *(cont.)* .

FSTJ307	FSTJ308
4	4
BH	BH
UWO	UWO
500287	500269
5154684	5154725
47.24	44.00
2.247	2.516
12.56	11.73
22.01	23.62
0.268	0.274
4.25	4.38
8.03	10.66
2.32	1.93
0.49	0.21
0.31	0.32
-0.32	-0.80
99.41	98.84

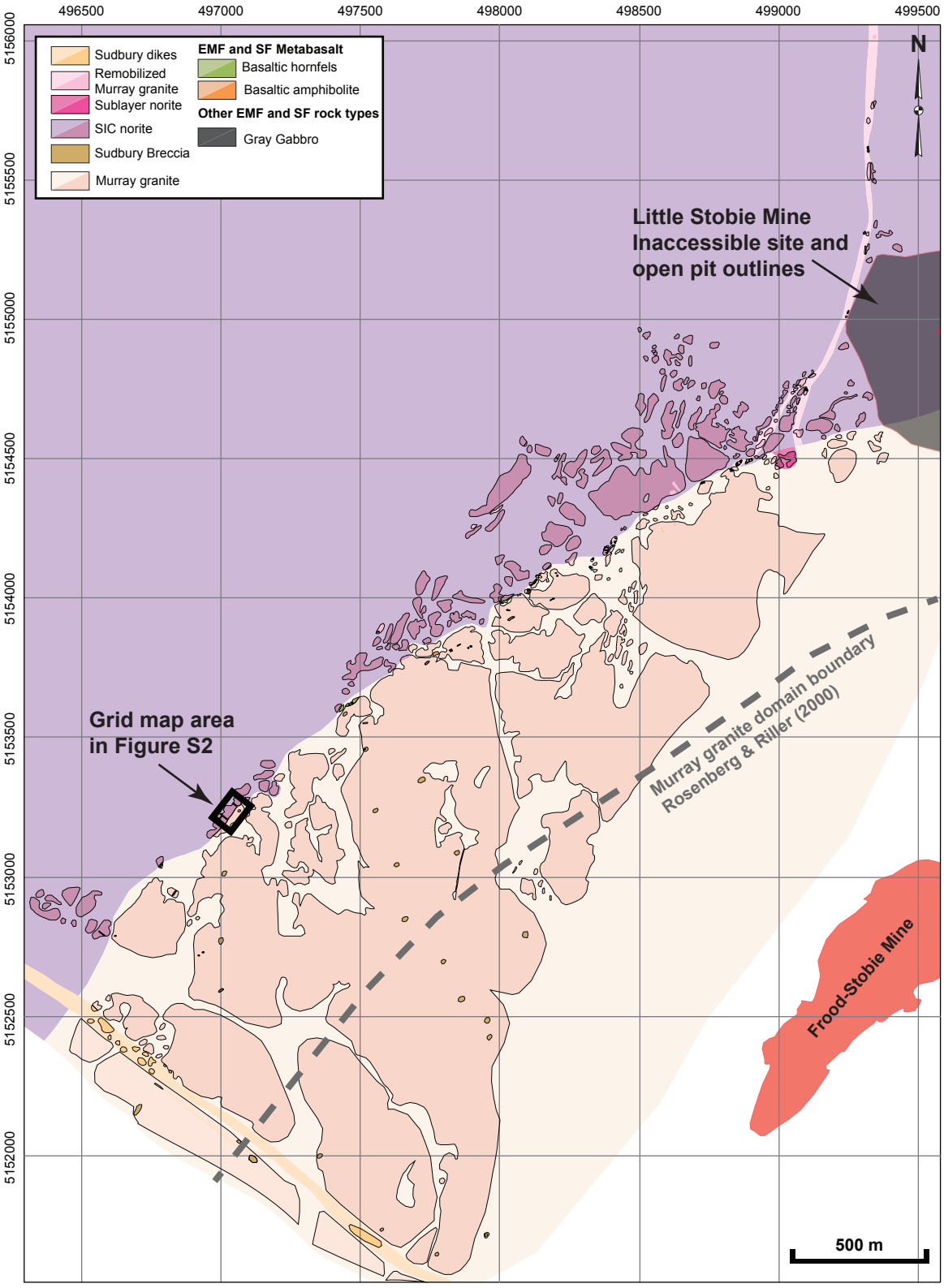

Fig. S2.1. Map showing the contact relationship between the Murray granite and the SIC norite, and the Murray granite domain boundary of Rosenberg & Riller (2000). The grid map area presented in Figure S2.2 is indicated by a black box outline.

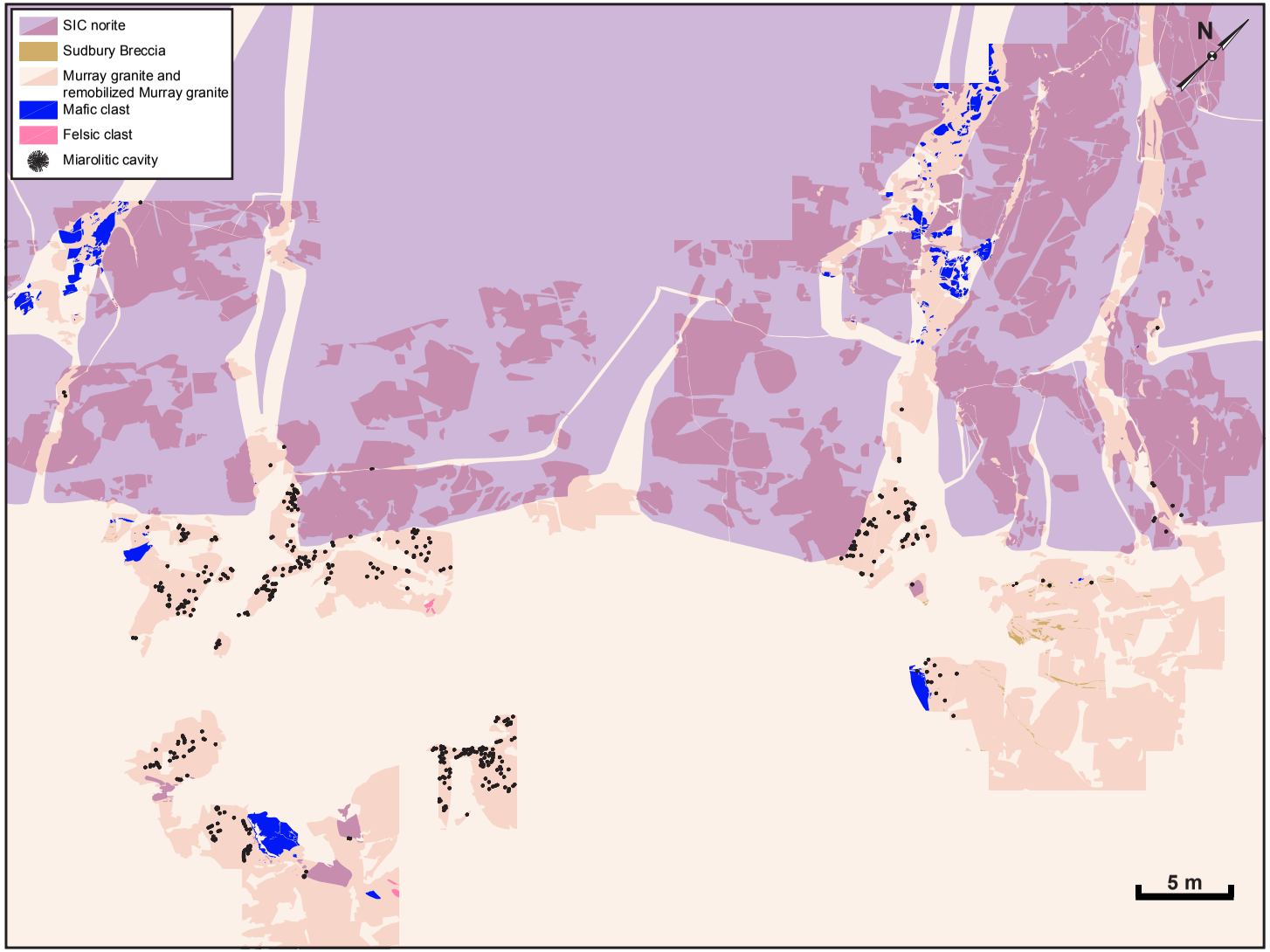

Fig. S2.2. Grid map showing the contact relationship between the Murray granite, the SIC norite, and the nature of remelted Murray granite dikes back-injecting the SIC.

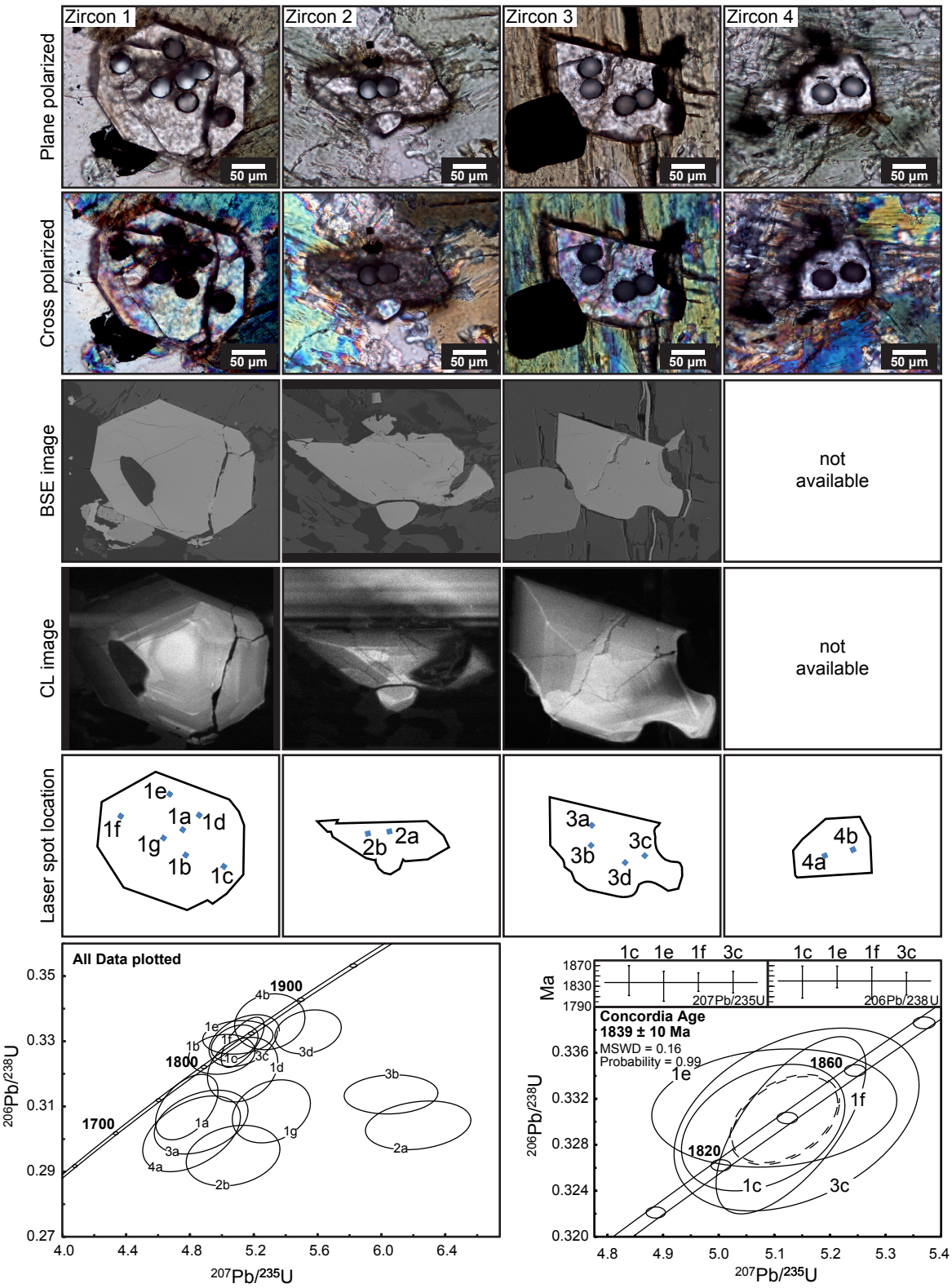

Fig. S2.3. Plane- and cross polarized light photomicrographs, back-scatter electron and cathodo-luminescence image, and laser spot location maps of zircons from leucocratic melt patches in the Elsie Mountain Formation metabasalts located in the pyroxene hornfels zone. The images document euhedral to subhedral zircon grains with oscillatory zoning consistent with having

Fig. S2.3. *(cont.)* grown from a melt. All grains have fine irregular fractures that locally appear to contain other material. Minor incipient alteration is observed in the BSE image of Zircon-2. The concordia diagrams are showing zircon ages for all data and a concordia age calculated for a tight cluster of concordant ages yielding an age of 1839 ± 10 Ma. Zircon-1 and Zircon-3 that contributes the analyses for this age estimate are also the grains least compromised by fractures and alteration according to the available images. Thus, the age provided by this cluster of analyses are interpreted to represent the formation of these zircon and falls within error of the crystallization of the Sudbury igneous complex and therefore the formation of the metamorphic aureole surrounding it. Two analyses (1b and 4b) are clearly concordant and although they fall slightly outside the aforementioned cluster it could be argued that they should be included in the calculation of the combined concordia age. However, a similar age of 1839 ± 8 Ma (MSWD = 1.11; probability = 0.35) is obtained with the addition of analyses 1b and 4b. See Table S1 for U-Pb data.

CHAPTER 3: HIGH FIELD-STRENGTH ELEMENT MOBILITY AND FORMATION OF METAMORPHIC CHEMOSTRATIGRAPHY: AN EXAMPLE FROM IMPACT MELT SHEET INDUCED CONTACT METAMORPHISM AND ANATEXIS OF BASALTS, SUDBURY, CANADA

T.R.C. JØRGENSEN[1*], D.K. TINKHAM[1], and C.M. LESHER[1]

[1]*Harquail School of Earth Sciences, Mineral Exploration Research Centre, Laurentian University, 935 Ramsey Lake Rd., Sudbury, ON, P3E 2C6, Canada*

(trc.joergensen@gmail.com; dtinkham@laurentian.ca; mlesher@laurentian.ca)

**corresponding author*

ABSTRACT

Systematic changes in the compositions of ca. 2.45 Ga Elsie Mountain Formation (EMF) metabasalts along the southern margin of the 1.85 Ga Sudbury Igneous Complex (SIC) provide evidence for extensive mobilization of highly-incompatible lithophile elements (HILE) relative to moderately-incompatible lithophile elements accompanying impact-melt induced contact metamorphism and anatexis. EMF metabasalts up to 3.5 km from the SIC contact (maximum exposed extent) have systematically lower LOI-Na than stratigraphically-equivalent Thessalon metabasalts, suggesting that all EMF metabasalts experienced some degree of contact and/or regional metamorphic dehydration and despilitization. Basaltic amphibolites and two-pyroxene granofels rocks greater than 500 m from the SIC contact are enriched in Cs-Rb-K-Ba-Sr-U-Th-LREE relative to Zr-Hf-MREE-Y-HREE with pronounced negative Nb-Ta-(Ti) anomalies. The enrichments are comparable to the Thessalon metabasalts, whose signatures have been interpreted to represent subduction-related enrichment of their mantle source and/or crustal contamination of an unenriched mantle source. Up to 500 m of the SIC contact basaltic two-pyroxene hornfels rocks experienced partial melting and melt segregation, and the geochemical variability allows for subdivision of the rocks into: 1) a Hornfels B unit from ~250-500 m characterized by generally higher Cs-Rb-K-Ba, higher W-Th-U-Nb-Ta-LREE-Zr-Hf and higher Zr-Hf anomalies (Zr/Zr* 0.87-1.37) than: 2) a Hornfels A unit within ~250 m from the SIC contact, which have lower Cs-Rb-K-Ba, lower W-Th-U-Nb-Ta-LREE-Zr-Hf and Zr-Hf anomalies (Zr/Zr* 0.25-0.67). The contact metamorphism has, in effect, defertilized the rocks by reversing the original HILE enrichment signature and produced rocks with transitional N-MORB to E-MORB

signatures. A comparison with experimental results and REE modelling indicate that metabasalts in the proximal aureole locally experienced upwards of 20% melting. This study confirms the ability of high-grade metamorphism to mobilize high-field-strength elements (Th-U-Nb-Ta-Zr-Hf) during not only high-P, high-T subduction-related metamorphism and high-P, high-T regional metamorphism, but also low-P, high-T contact metamorphism.

INTRODUCTION

Previous studies have documented a low-pressure contact metamorphic aureole in the gneissic footwall rocks along the northern margin of the 1.85 Ga Sudbury Igneous Complex (SIC; Krogh et al., 1984) comprising an outer 1000m-wide zone of albite-epidote hornfels, a 900m-wide zone of hornblende hornfels, a 200m-wide zone of pyroxene hornfels, and an inner 25m-thick zone of partial melting (e.g., Dressler, 1984a, b; Boast and Spray, 2006). Most workers have assumed that the contact metamorphic aureole in Huronian metabasalts on the South Range has been obscured by superimposed Penokean metamorphism and deformation (e.g., Coats and Snadjr, 1984; Dressler, 1984a, b; Boast and Spray, 2006), but Jørgensen et al. (Chapter 2) have shown not only that it is present, but that the higher-temperature parts are much thicker, comprising an inner pyroxene hornfels zone with local partial melting extending up to 500 m from the SIC contact, an intermediate pyroxene granofels zone extending up to 750 m from the SIC contact, and an outer hornblende hornfels zone extending to at least 1000 m from the SIC contact (Jørgensen et al., Chapter 2). The differences in the thicknesses of the higher-temperature parts of the contact metamorphic aureoles implies that the South Range was

closer to the central parts of the impact crater and that the North Range was closer to the peripheral parts of the impact crater, as proposed by Golightly (1994), and have important implications for cooling and crystallization models of the SIC (e.g., Ivanov and Deutsch, 1999; Prevec and Cawthorn, 2002), for thermomechanical erosion and contamination processes related to the formation of Sublayer (e.g., Lightfoot et al., 1997a; Prevec, 2000; Prevec et al., 2000), and for the localization of Ni-Co-Ru-Ir-(Cu)-rich contact mineralization and Cu-Pt-Pd-(Ni)-rich footwall mineralization (e.g., Naldrett 2004; Farrow and Lightfoot, 2002; Ames and Farrow, 2007).

Because of the high variance mineral assemblages typical of mafic rocks metamorphosed at high-temperature and low-pressure conditions (e.g., Tracy and Frost, 1991), it is difficult to make further metamorphic zone subdivisions in the pyroxene hornfels rocks based purely on mineral assemblages. However, geochemical variations in the metabasalts provide a method of increasing the resolution of the contact metamorphic zones and identifying the hottest parts that were most conducive to thermomechanical erosion, localization of contact ores, and emplacement of footwall vein systems.

This study shows that basaltic amphibolites and pyroxene granofels rocks greater than 500 m from the SIC contact are enriched in highly-incompatible lithophile elements (HILE: Cs-Rb-K-Ba-Sr-U-Th-LREE) relative to moderately incompatible lithophile elements (MILE: Zr-Hf-MREE-Y-HREE) with pronounced negative Nb-Ta and Ti anomalies. The enrichments in HILE are similar to stratigraphically-equivalent metabasalts in the Thessalon area 200 km to the west and consistent with subduction-related enrichment of their mantle source and/or crustal contamination (e.g., Jolly, 1987a, b, 1992; Hocking, 2003; Ketchum et al., 2013). However, two-pyroxene hornfels rocks

250-500 m from the SIC contact have significantly lower Cs-Rb-K-Ba-Th-U-Nb-Ta-LREE-Zr-Hf-W contents and two-pyroxene hornfels rocks within 250 of the SIC contact have experienced local partial melting and melt segregation, and have much lower Cs-Rb-K-Ba-Th-U-Nb-Ta-LREE-Zr-Hf-W contents with pronounced negative Zr-Hf anomalies (Zr/Zr* 0.25-0.67). Comparison with experimental data and modelling of REE abundances indicate that metabasalts in the proximal zone experienced up to 20% melt loss. In effect, the contact metamorphism has produced rocks that have geochemical signatures more like MORB than arc basalts, essentially erasing the subduction signature. The elements lost from the proximal zone were likely incorporated into the SIC Sublayer and/or discrete zones, e.g., footwall breccias. Although previous studies have shown that LILE-Th-U-Nb-Ta-LREE-Zr-Hf can be mobile during high grade subduction-related and/or regional metamorphism (e.g., Weaver and Tarney, 1981; Kamber and Collerson, 2000; Kessel et al., 2005; Babechuk and Kamber, 2011), the low-P/high-T contact metamorphism reported here was also able to mobilize these elements on a scale of hundreds of meters.

GEOLOGICAL BACKGROUND

THE SUDBURY IMPACT STRUCTURE

The 1.85 Ga Sudbury Structure (Krogh et al., 1984) is recognized as one of the world's oldest, largest (estimated original diameter of 150-250 km), and best exposed impact craters and the only site of its size with a well-preserved and exposed differentiated impact melt sheet (Fig. 3.1; e.g., Dietz, 1964; Dence, 1972; Grieve et al., 1977; Faggart et

al., 1985; Grieve et al., 1991; Golightly, 1994; Grieve and Therriault, 2000; Therriault et al., 2002; Spray et al., 2004). The original circular multi-ring crater was subsequently deformed by Proterozoic tectonometamorphic events, and eventually eroded to form an elliptical circumferential plan-view shape (e.g., Grieve et al., 1991; Shanks and Schwerdtner, 1992; Riller, 2005). It comprises 1) the SIC that formed from the superheated impact melt sheet and includes a 2-3 km-thick differentiated Main Mass, laterally-discontinuous inclusion-rich norites (Sublayer), and associated radial and concentric offset dikes; 2) overlying fall-back, suevitic, and phreatic breccias (Onaping Formation) and crater-fill sediments (Onwatin and Chelmsford Formations); and 3) underlying pseudotachylitic and cataclastic breccias (Sudbury Breccia; SUBX) and anatectic breccias (Footwall Breccia) (e.g., Pattison, 1979; Ames et al., 2002; Lightfoot and Farrow, 2002; Rousell et al., 2003, 2009; Keays and Lightfoot, 2004; Naldrett, 2004; Ames and Farrow, 2007).

The SIC straddles the boundary between the Archean Superior Province to the west, north, and northeast (North Range) and Paleoproterozoic Huronian Supergroup of the Southern Province to the east and south (East and South Ranges; Fig. 3.1). North Range footwall lithologies are dominated by Archean felsic-mafic gneisses, whereas South Range footwall lithologies include metamorphosed and polydeformed Huronian granitoid, metavolcanic, metasedimentary, and mafic intrusive rocks (e.g., Dressler, 1984a, b). Deep drilling and geophysical data indicate that the basal contact of the SIC dips 40° southward in the North Range and 60° northward to steeply southward in the South Range (e.g., Milkereit et al., 1994; Wu et al., 1995; Olaniyan et al., 2014).

The Ni-Cu-(PGE) ores associated with the SIC have been divided into three styles based on their environment: 1) disseminated and semi-massive contact ores in Sublayer norite and underlying Footwall Breccia, 2) Cu-rich veins and stockworks in footwall rocks, particularly in zones of Sudbury Breccia within 200-300m of the SIC basal contact, and 3) disseminations and semi-massive to massive sulfides in quartz diorite offset dikes (e.g., Coleman, 1913; Naldrett, 2004).

The Main Mass varies in thickness between ~300-5000 m with the thickest parts likely overlaying the heavily mineralized Creighton embayment in the South Range (Keays and Lightfoot, 2004). However, true stratigraphic thickness is difficult to measure in the South Range because of extensive faulting along the South Range Shear Zone (e.g., Shanks and Schwertner, 1992; Mukwakwami et al., 2012). The difference in thickness of South and North Range SIC Main Mass is potentially explained by the South Range representing a deeper and thicker part of the complex (Naldrett and Hewins, 1984; Golightly, 1994).

THE SIC SOUTH RANGE FOOTWALL

Significant parts of the South Range of the SIC is bordered by the Elliot Lake Group of the Huronian Supergroup (Fig. 3.1), a southward-younging sequence of metavolcanic and lesser metasedimentary rocks. The South Range footwall also contains 2490-2470 Ma East Bull Lake (EBL) gabbro-anorthosite intrusives (Krogh et al., 1984; Prevec, 1993), a proposed intrusive counterpart to the EMF metabasalts, the 2477 ±9 Ma Murray granite (Krogh et al., 1996), the 2415 ± 5 Ma Creighton granite (Smith et al., 2002), 2210-2217 Ma Nipissing gabbroic intrusives (Corfu and Andrews, 1986; Noble and Lightfoot, 1993;

Buchan et al., 1989) , and several Proterozoic dike swarms including 2473 +16/-9 Ma and 2446 ± 3 Ma Matachewan dikes (Heaman, 1997), 1238 ± 4 Ma Sudbury dikes (Krogh et al., 1987), and 590 +2/-1 Ma Grenville dikes (Kamo et al., 1995).

From north (oldest) to south (youngest) the Elliot Lake Group sequence includes the Elsie Mountain Formation (mainly pillowed and massive basalt), Stobie Formation (mainly mafic-intermediate volcanics and wacke), Copper Cliff Formation (mainly rhyolitic flows, domes, and associated autoclastic breccias; dated at 2452.5 ± 6.2 Ma by Ketchum et al., 2013), Matinenda Formation (crossbedded arkose, wacke, and conglomerates), and the McKim Formation (laminated thin- to thick-bedded wacke and siltstone). The Elsie Mountain Formation is the major immediate footwall rock to the SIC along much of the South Range and within the study area (Fig. 3.1). The criteria used to differentiate between the Elsie Mountain Formation and the Stobie Formation is the percentage of intercalated metasedimentary rocks: EMF contains <15% and Stobie Formation contains >15% (Card, 1978a).

THE ELLIOT LAKE GROUP VOLCANICS

The Elliot Lake Group volcanic sequence in the Sudbury area represents the eastern segment of a ca. 200 km volcanic belt that extends west to Sault Saint Marie (Fig. 3.2a) and has been the focus of several geological, geochemical, and tectonic studies (e.g., Innes, 1977; Card 1978a; Jolly, 1987a, b; Jolly et al., 1992; Bennett et al., 1991; Hocking, 2003; Ketchum et al., 2013). The mafic-intermediate lavas in the Thessalon region are stratigraphic equivalents of the EMF and share the same fundamental geochemical characteristics, including enrichments in HILE relative to Nb-Ta-(Ti) and MILE (Jolly,

1992; Hocking, 2003; Ketchum et al., 2013). Models for the formation of these rocks invoke, implicitly or explicitly, derivation from an enriched mantle source (typically subduction modified) with or without contamination by upper continental crust (Jolly, 1992; Hocking, 2003; Ketchum et al., 2013), interpretations similar to those of Vogel et al. (1998) and James et al. (2002) for genetically-related EBL intrusives. The lavas in the Thessalon region have been subdivided into 6 units based on mapping, petrography, and geochemistry (Ketchum et al., 2013). For this study, Thessalon Unit 1, 3, and 6 samples with a complete dataset are presented for comparison in appropriate figures, whereas Unit 2, 4 and 5 are ignored because they are significantly more primitive (Ni > 300 ppm; Unit 2) or dominantly andesitic to rhyolitic lavas (Units 4 and 5). Samples from Hocking (2003; see Fig. 3.1 for location) are also plotted for comparison in several figures but samples MH-03A (SiO_2 ~65 wt. %) and MH-11 (xenolith in granitic intrusion) are excluded.

METAMORPHISM

REGIONAL METAMORPHISM

The Southern Province near Sudbury underwent multiple orogenic deformational events both prior to and after emplacement of the SIC (e.g., Card, 1978a,b; Bennett et al., 1991; Rousell et al., 1997; Bailey et al., 2004; Spray et al., 2004; Riller, 2005; Mukwakwami et al., 2012; Raharimahefa et al., 2014). Figure 3.2b shows regional metamorphic grades in and around the Sudbury area. Metamorphic pressures and temperatures during the ca. 1744-1704 Ma Yavapai orogenic event in the Chief Lake area (~20-25 km SW of the

study area) were 2.8-4 kbar and 540-565 °C during staurolite growth, and increased to 4.5-7.6 kbar and 580-615 °C during kyanite growth (Raharimahefa et al., 2014). U-Pb titanite ages indicate that the main regional metamorphic event near the Garson Mine (~10 km ENE of the study area) occurred during the 1870-1820 Ma Penokean orogeny, and that peak metamorphism reached amphibolite facies temperatures of 550-590 °C (Mukwakwami et al., 2014).

SIC CONTACT AUREOLE IN THE EMF METABASALTS

Thomson (1935) proposed a contact metamorphic origin for pyroxene hornfels metabasalts of the EMF occurring in the vicinity of the SIC, but recent workers (e.g., Dressler, 1984a, b; Prevec and Cawthorn, 2002; Boast and Spray, 2006) have suggested that the contact metamorphic aureole in the South Range has been more-or-less obliterated. Jørgensen et al. (Chapter 2) have shown that it is not only present, but much thicker in the South Range (Jørgensen et al. Chapter 2; Fig. 3.3). They recognized three zones within the map area of this study: 1) an inner pyroxene hornfels zone (PHZ) extending up to 500 m from the base of the SIC and characterized by a plagioclase-orthopyroxene-clinopyroxene-ilmenite-magnetite ± melt assemblage 2) an intermediate pyroxene granofels zone (PGZ) extending up to 750 m from the SIC contact and characterized by a plagioclase-clinopyroxene-orthopyroxene-ilmenite-magnetite ± high-Ti hornblende ± quartz ± biotite assemblage, and 3) an outer hornblende-hornfels zone (HHZ) that extends at least 1000 m from the SIC contact and characterized by a high-Ti hornblende-plagioclase-quartz-ilmenite ± biotite ± magnetite assemblage. Thus, the outer limit of the HHZ represents the high-Ti hornblende-in isograd and the pyroxene-in

isograd correlates with the HHZ-PGZ contact. The nature of the PGZ-PHZ contact is gradational and defined by an overall grain size decrease and a significant decrease in high-Ti hornblende. Phase equilibria modelling indicates peak metamorphism in the PHZ reached conditions of ≥925 °C and 1-3 kbar near the SIC contact, and that anatexis resulted in at least 10-20% melt generation in the inner 500 m of the aureole (Jørgensen et al., Chapter 2).

SAMPLING AND ANALYTICAL METHODS

This study focused on an approximately 2 km x 1.5 km area near the Frood-Stobie and Little Stobie mines (Fig. 3.3), where the EMF is well exposed on surface and consists dominantly of homogeneous metabasalts (dominantly massive and locally pillowed and amygdaloidal rocks) and lesser intercalated metasediments of variable metamorphic grade. Samples of metabasalt totaling 56 were collected, including 28 PHZ samples, 18 PGZ samples, and 10 HHZ zone samples, including a SUBX sample (FSTJ037B). Pyroxenes were absent from two amphibolite samples within the PGZ (FSTJ013E and FSTJ021B) because of retrogression. UTM coordinates of collected samples are listed in Table S3.1 under Supporting Information. Weathered surfaces were removed in the field when possible and any remaining weathering was removed by a rock saw with a water-cooled diamond-embedded saw blade. Visible saw marks were removed by grinding on a diamond-embedded steel lapping disc. Samples for geochemical analysis were rinsed in tap water, air dried, crushed in a case-hardened low-Cr steel jaw crusher, and pulverized in an agate ball mill. The crusher was opened and the plates were cleaned with a wire brush, ethanol, and compressed air between samples. The agate mill was emptied and

cleaned with Killarney quartzite between samples. All samples were studied in polished thin section using a compound polarizing microscope and representative samples were studied using a scanning electron microscope to derive mineralogical and textural information relevant to the interpretation of their geochemistry and petrogenesis.

All samples were analyzed for minor and 36 analyzed for major elements at the Ontario Geoscience Laboratories (Geo Labs) in Sudbury, Ontario, and 20 samples were analyzed for major elements in the Department of Earth Sciences (Dr. C. Wu, analyst) at the University of Western Ontario. Loss-on-ignition (LOI) was determined by heating at 1000 °C under oxygen atmosphere until a constant weight percent was determined. 1.0 g aliquots of the residues were fused with a 49.75:49.75:0.5 dilithium tetraborate:lithium metaborate:lithium iodide flux (Geo Labs) and 49.75:49.75:0.5 lithium tetraborate:lithium metaborate:lithium bromine (UWO) to produce glass discs that were analyzed for major elements by wavelength-dispersive X-ray fluorescence spectrometry (XRFS). Replicate samples analyzed at both laboratories indicate that analytical precision (relative standard deviation) is better than 1% for high-moderate abundance elements and up to 3% for low-abundance elements. Interlaboratory precision (relative percent difference) is 0.5% for Si, 1.4% for Ti, 2.0% for Al, 2.2% for Fe, 14.6% for Mn, 2.3% for Mg, 7.1% for Ca, 3.4% Na, 3.0% for K, 0.0% for P and 4% for LOI. Rock standard BHVO-2 (Hawaiian Volcano Observatory basalt) was analyzed with the samples at Geo Labs, and the measured results are within uncertainty of recommended values for all oxides except Ca (+0.2% relative), Fe (+0.6%), and Al (+0.8%) (Table S3.1). Rock standard JB-1a (Kitamatsuura basalt) was analyzed with the samples at UWO and the results are within 4.4% (relative) of the recommended values (no uncertainties; Table

S3.1). Titanium concentrations determined by XRFS and ICP-MS (see below) are comparable (r2 = 0.9935 and r2 = 0.9825 for Geo Labs and UWO, respectively).

Trace elements were analyzed on 1.0 g aliquots of the same sample powders by inductively-coupled plasma mass spectrometry (ICP-MS) at Geo Labs. Dissolution employed a 7-day closed-vessel multi-acid digest at 110 °C (stage 1: hydrofluoric-hydrochloric-perchloric; stage 2: hydrochloric-perchloric; for further details see Burnham et al., 2002) and no insoluble residues were reported. Precision was monitored by analyzing five duplicate samples with each batch and the relative standard deviations for all elements in both batches are below 10%. Rock standard BHVO-2 was analyzed thrice and the results are within 15% (relative) of the recommended values with the exception of Cd (115% and 62%) and Mo from the second batch (24%) (See Supporting Information Table S3.1). Because of variable hydration and dehydration (see below), all major element data have been recalculated to 100% volatile-free in Table 3.1 and for plotting purposes.

RESULTS

The complete data set (major, minor, and trace elements) for the samples analyzed in this study are presented in Supporting Information Table S3.1. Analyzed EMF metabasalts have been subdivided into 3 groups, PHZ, PGZ, and HHZ, based on the map units of Jørgensen et al. (Chapter 2). PHZ samples have been further subdivided into two subzones: more-proximal PHZ A samples with $Zr/Zr^* < 0.67$ and less-proximal samples PHZ B with $Zr/Zr^* > 0.67$, where Zr is the analyzed abundance and Zr* is the abundance interpolated between mantle-normalized Nd and Sm. Ranges, averages, medians and

standard deviations for individual oxides, elements, and significant element ratios for each unit are given in Table 3.1.

MAJOR AND MINOR ELEMENTS, AND LOI

The majority of the samples analyzed in this study are quartz normative, generally plagioclase-orthopyroxene-clinopyroxene-magnetite-ilmenite ± quartz ± olivine. All analyzed EMF samples plot within the field of high-Fe tholeiite basalts (HFT) on an Al–Fe+Ti–Mg classification diagram (Fig. 3.4), similar to the majority of analyzed Thessalon and Sudbury Elsie Mountain mafic volcanic rocks (Hocking, 2003; Ketchum et al., 2013).

Selected bivariate plots, using MgO (or Mg#: atomic $Mg^{2+}/(Mg^{2+}+Fe^{2+})$ with total Fe allocated as 0.82 Fe^{2+} and 0.18 Fe^{3+}; see Jørgensen et al., Chapter 2) as a fractionation indicator, are presented in Figure 3.5. HHZ, PGZ and PHZ B samples largely overlap in MgO, ranging from ~3 to 6.5 wt. % and with an average of ~5 wt. %, whereas the PHZ A samples partially overlap but tends toward higher MgO (~4.5-8.5 wt. %; avg. = 6.5 wt. %; Figure 3.5; Table 3.1). Some elements scatter over fairly wide ranges in MgO, but trends and systematic differences are evident in the samples:

1. LOI ranges from +0.8 (i.e., small weight loss) to –1.3 (i.e., moderate weight gain). LOIs in PGZ and PHZ samples are mostly lower than in the HHZ and EMF samples, which are in turn lower than in Thessalon samples (Fig. 3.5a). Most HHZ samples (9 of 10) have positive LOI, whereas most PGZ (13 of 18) and PHZ (25 of 28) samples have negative LOI. The LOI in HHZ, PGZ, PHZ and EMF samples show a broad

negative correlation with Fe, which is not the case for the Thessalon samples, e.g., the two HHZ samples with the lowest LOI also have the highest Fe content (Table S3.1).

2. HHZ, PGZ, and PHZ samples show broad negative trends for Ti-Fe-P, broad positive trends for Al-Ca and relatively strong positive trends for Ni-Cr. Si-Na-K shows no meaningful correlation with Mg, but PHZ samples are in general significantly lower in K (Fig. 3.5b-g, Table 3.1, and Table S3.1).
3. The Hocking (2003) EMF samples generally show a broad overlap with the samples of this study. However, EMF samples generally plot on the lower side of trends formed by Ti-Fe-P vs. Mg, where it partially overlaps with mainly HHZ samples (e.g., Fig. 3.5b).
4. The Thessalon samples are similar in range for MgO from ~2.5 to 7.25 wt. % compared to the other samples. Generally, the Thessalon units are lower in Ti-Fe-Mn-Ca, similar to higher in K-Cr, and higher in Si-Al-Na-Ni at a given Mg content (e.g., Fig. 3.5b-f).

RARE EARTH ELEMENTS

Primitive mantle normalized extended trace element diagrams and chondrite-normalized rare earth element (REE) plots for all units are presented in Figure 3.6 with Thessalon and EMF samples plotted in the extended diagrams for comparison. Ranges for the REEs and selected ratios for each unit are summarized in Table 3.1 and some are presented in Fig. 3.5 and 3.7. Key features include:

1. The REE patterns for the HHZ and PGZ units are consistent and essentially identical with small positive to negative Eu anomalies. Relative to chondritic abundances they

both show enrichment in the LREE compared to the MREE-HREE with [La/Sm]cn from ~2-4 and [La/Yb] from ~3-6. The PHZ-B unit also shows smooth and consistent trends but the LREE enrichment is less significant with [La/Sm]cn from ~1.5-2 and [La/Yb] from ~2-3. In contrast, the PHZ-A unit is much less consistent in the LREE pattern including nearly flat REE profiles and [La/Sm]cn from ~1-2 and [La/Yb] from ~1-3 (Table 3.1; Figure 3.5i and 3.6).

2. The MREE-HREE patterns are consistent for all HHZ, PGZ, and PHZ samples with [Gd/Lu]cn from ~1-1.4 (Fig. 3.7g).
3. The Hocking (2003) EMF samples are not particularly smooth in the REE profile and the irregularities, particularly among neighboring HREE, might question the data quality. Nonetheless, the patterns partially overlap and share the same LREE-MREE characteristics as the HHZ, PGZ, and PHZ B units but overlaps more significantly with the PHZ A unit in absolute concentrations. In the MREE-HREE part of the profile some EMF samples plot even closer to chondritic values than the PHZ-A unit but with similar slopes.
4. The Thessalon units are similar to the HHZ, PGZ, and PHZ B and EMF units in their LREE profiles with [La/Sm]cn from ~1.6-4. Relative to chondritic values the enrichment of LREE compared to MREE is greater in Unit 1 than Unit 3 that is similar or greater than Unit 6. The MREE-HREE profiles Unit 3 are clearly distinct from the HHZ, PGZ, and PHZ units displaying a steep negative slope and an average [Gd/Lu]cn of ~3. Unit 1 samples are fairly consistent in their MREE-HREE patterns and on average only slightly more negatively sloping than the HHZ, PGZ, and PHZ

units. MREE-HREE profiles for Unit 1 partially overlaps with the HHZ, PGZ, and PHZ units but are inconsistent with a range in [Gd/Lu]cn from ~1-2.4.

LARGE-ION LITHOPHILE ELEMENTS (LILE) AND HIGH FIELD-STRENGTH ELEMENTS (HFSE)

LILE and HFSE element abundances and selected ratios are summarized in Table 3.1 and plotted in Figures 3.5j, 3.6, and 3.7 together with Thessalon and EMF samples (note that W data is unavailable for the Thessalon samples and limited to a few samples for the Hocking (2003) EMF samples). Significant features include:

1. The PHZ A unit is consistently low in LILEs Cs-Rb-Ba (and K) compared to Thessalon, EMF, HHZ, PGZ, and PHZ B samples that all exhibit wider ranges and higher average values (Fig. 3.6). The Sr content is generally higher in Thessalon units 1 and 3, whereas all remaining units largely overlap.
2. Except for overlapping with the EMF in Nb-Ta and the Thessalon Unit 6 in Nb-Ta and Zr-Hf the PHZ A unit is consistently low in HFSEs W-Th-U-Nb-Ta-Zr-Hf compared the other units that all exhibit wider ranges and higher average values (Figure 3.6 and Table 3.1).
3. The PHZ B unit is generally lower or slightly overlapping in W-Th-U-Nb-Ta-Zr-Hf compared to the HHZ and PGZ units except for W that shows considerable overlap with the PGZ unit.
4. The HHZ, PGZ, EMF, and Thessalon units all show negative Nb-Ta anomalies relative to Th and La on primitive mantle normalized extended trace element diagrams (Fig. 3.6). In contrast, the negative Nb-Ta anomalies relative to Th are

partially lacking from the PHZ B and is essentially only present in 1 PHZ A sample ([Nb/Th]mn ~0.7; Fig. 3.5j). Nonetheless, it is still possible to discern a negative Nb-Ta anomaly in the PHZ samples relative to La except for 1 PHZ A sample that shows a small positive anomaly.

5. Nb/Th range from 1.4 to 6.1 in the HHZ and PGZ units and from 6.0 to 29.2 in the PHZ A with no HHZ and only a single PGZ sample falling at higher values than one PHZ A sample. PHZ B samples forms a transition by Nb/Th ranging from 3.5 to 25.3 (e.g., Fig. 3.5j and Table 3.1). Except for 2 Thessalon Unit 3 samples with Nb/Th ~6.05 all other Thessalon and EMF samples fall below Nb/Th = 6.
6. Zr/Nb is on average much lower in the PHZ A unit (average ~10) than in the HHZ, PGZ, PHZ B, and EMF samples (averages ~19-20) and the Thessalon units (averages ~15-22) (Fig. 3.7a-b).
7. Zr/Zr* is systematically lower in the PHZ A samples than in HHZ, PGZ, PHZ B, EMF and Thessalon Unit 6 samples. Some Thessalon Unit 3 samples and a single from Unit 1 overlap with the highest values in the PHZ A unit (Fig. 3.7a).
8. Zr/Hf is superchondritic and more consistent in the HHZ, PGZ, and PHZ B samples (~39-43) and subchondritic (~30-39) with a much wider range in the PHZ A samples (Fig. 3.7b). The EMF and Thessalon Unit 1 both average ~38 and show a little more overlap with the PHZ A samples. Thessalon Unit 3 and 6 both show remarkably wide ranges (~35-51 and ~32-66, respectively) and averages of ~42-43 that were not discussed by Ketchum et al. (2013).
9. Nb/Ta in the HHZ unit forms the tightest range from ~13 to 18 with the maximum values increasing in the PGZ unit (~20), and further in the PHZ units (~23) (Fig.

3.7e). The EMF and Thessalon Unit 3 samples are similar in range and average to the HHZ although 1 EMF sample has a value of ~20. Thessalon Unit 1 and 6 dominantly falls at significantly lower Nb/Ta with averages of ~10 and ~11, respectively (excluding 1 Unit 6 extreme outlier).

10. W/Th is generally < ~0.2 for the HHZ, PGZ and PHZ B units, but > 0.2 for PHZ A samples (Fig. 3.7f).
11. Ta/W is generally lower in the HHZ and PHZ A (~1.5-4) than in the PHZ B (< ~2.5-8), which in turn is lower than the PGZ (~2-17) (e.g., Fig. 3.7f).
12. Th/U in the PHZ samples defines a relatively narrow range at low values from ~1.4-3.8. At slightly higher values the HHZ samples range from ~3.3-5.5. The PGZ samples show the widest range from ~3.3 to 10.2 (Fig. 3.7i-j). The EMF samples are similar to the HHZ and all values < 5. The Thessalon Unit 1 samples define a tight cluster at Th/U ~3, whereas Unit 6 samples are higher and similar to the HHZ and EMF units, except for a few outlies > 6. With an average of Th/U at ~5.7 the Thessalon Unit 3 more closely resembles the PGZ unit.

DISCUSSION

Several processes may have contributed to the geochemical variability observed in the EMF metabasalts in the SIC South Range contact aureole, including variations in mantle source composition, degree of partial melting, mantle source variations, crustal contamination, fractional crystallization/accumulation, post-emplacement seafloor alteration, and/or contact metamorphism.

ALTERATION AND REGIONAL METAMORPHISM

EMF metabasalts are locally pillowed, so it may be assumed that they all experienced some degree of pre-SIC seafloor hydrothermal alteration. They have also experienced pre-SIC and post-SIC greenschist-amphibolite facies regional metamorphism, so unraveling the mobility of the most mobile elements during each of these processes is difficult if not impossible. Some interpretations can be made based on expected mobility during post-SIC metamorphism and the likelihood of preserving signatures of pre-SIC mobility through contact metamorphism, but the focus of this section is on establishing which elements have been least mobile during pre-seafloor metamorphism and post-SIC regional metamorphism and can therefore be used to evaluate mobility during contact metamorphism.

Element mobility during seafloor alteration and metamorphism depends on the stabilities of the phases that house them in the rock, their solubilities in the hydrothermal/metamorphic fluids, and the effective water:rock ratio (e.g., Mottl, 1983). In general, alkalis (Cs-Rb-K-Na) and calc-alkalis (Ba-Sr±Ca) are most mobile because they are hosted in more easily-altered glass and feldspars, and because they have low charges and large ionic radii, which makes them more soluble in hydrothermal-metamorphic fluids. The high field-strength elements (U-Th-Nb-Ta- Zr-Hf) and MREE-HREE-P are generally least mobile because they are hosted in more resistant accessory minerals and have high charges and small ionic radii, which make them less soluble in hydrothermal-metamorphic fluids. Most fourth period transition metals (FPTMs) have variable oxidation states and therefore variable coordinations and ionic radii, which affects which minerals host them and their solubilities in hydrothermal/metamorphic

fluids, but Group 3-6 FPTMs (Sc-Ti-V-Cr), which are hosted in silicates/oxides, are normally less mobile than Group 7-10 FPTMs (Mn-Fe-Co-Ni), which are hosted in silicates/oxides and sulfides, and much less mobile than Group 11-12 FPTMs (Cu-Zn), which are hosted mainly in sulfides.

LOI is often used when exploring the extent of hydrothermal alteration, but the majority of EMF samples yield negative LOI values (Table 3.1), which is attributed to oxidation of Fe2+ during the heat treatment in combination with the rocks originally being more anhydrous and/or having higher Fe contents. Negative LOI values indicate that the material started out nearly volatile free. For example, a sample containing 13.3 wt. % FeO (~average FeO in a HHZ rock) would gain ~1.5 wt. % during complete oxidation to Fe2O3, which technically could offset dehydration of ~15 wt. % stoichiometric clinochlore-chamosite solid solution or ~70 wt. % stoichiometric actinolite or some combination of the two. The typical mineralogy of a EMF sample from Hocking (2003) is described as containing approximately 80% calcic amphibole and ~5% combined chlorite and epidote, which on the basis of empirical formulae equates to ~2 wt. % H2O. Unit 6 of the Thessalon assemblages is described as containing the highest abundance of hydrous mafic minerals with ≥ 80% combined actinolite-chlorite-epidote-biotite-stilpnomelane. Because of a lower metamorphic grade (lower greenschist) it is reasonable to assume a higher chlorite content in Unit 6 compared to the EMF samples, e.g., a Unit 6 metabasalt with approximately 40% actinolite, 30% chlorite, 7.5% epidote, and 2.5% biotite would technically result in ~4.1 wt. % H2O. The average FeO is lower in both the EMF unit (~11.1 wt. %) and Thessalon Unit 6 (~10 wt. %) than the HHZ unit and technically could offset LOI by ~1.2 and 1.1 wt. %. respectively. The estimations from

these examples would yield 3 wt. % H2O for the Thessalon Unit 3 sample and 0.85 wt. % H2O for the EMF sample, which is in good agreement with the average LOI of 3 wt. % and 0.57 wt. %, respectively. Thus, the higher LOIs of Ketchum et al.'s (2013) Thessalon samples reflects their lower metamorphic grade (greenschist facies) and higher chlorite contents combined with a slightly lower average in FeO content compared to Hocking's (2003) EMF samples. The lower LOIs of Hocking's (2003) EMF samples (and also Card's (1978b) samples) reflects their higher metamorphic grade (amphibolite facies) and lower chlorite contents, part of which may reflect regional metamorphism and part of which may reflect contact metamorphism, and higher FeO contents. Most HHZ samples have LOIs similar to EMF samples but the HHZ unit is slightly lower on average. The hydrous phases responsible in the HHZ samples are a combination of low pressure/high temperature high-Ti hornblende that formed on the prograde and/or retrograde path during SIC contact metamorphism (Jørgensen et al. Chapter 2) and higher pressure/lower temperature sadanagaite overgrowing the contact metamorphic assemblage during post-SIC Penokean regional metamorphism, and minor chlorite, biotite, and epidote (Mukwakwami et al., 2012; Jørgensen et al. Chapter 2). The slightly lower average LOI in the HHZ sample compared to the EMF samples is then best explained by the slightly higher average FeO content in the HHZ unit. The negative LOIs in most PGZ, PHZ samples reflect dehydration during high temperature contact metamorphism and higher FeO content, and consequently LOI is inadequate as an indicator of hydrothermal/metamorphic alteration in these rocks.

The dispersion of Cs-Tl-Rb-K in Thessalon (no Tl data), EMF, HHZ, and PGZ samples and partial and consistent depletion in PHZ B and PHZ A samples, respectively, likely

reflects a combination of mobility during pre-SIC seafloor alteration and metamorphism, systematic expulsion (with normally less mobile elements: see below) from PHZ A and mobilization into the melt sheet, Sublayer, and/or more distal footwall during contact metamorphism, and subsequent redistribution during syn- to post-SIC regional metamorphism.

Na is systematically lower in the EMF, HHZ, PGZ, and PHZ units than in the Thessalon samples, suggesting that the former have lost Na during regional metamorphism or contact metamorphism. Conversely, Ca is generally higher in the EMF, HHZ, PGZ, PHZ samples than in the Thessalon samples.

The scatter of Rb-K-Na and to a lesser degree Sr -Ba in Thessalon and EMF, HHZ, PGZ and to a lesser extent the PHZ B samples on bivariate and primitive mantle normalized plots (Fig. 3.5 and 3.6) indicate that they were mobile during seafloor hydrothermal alteration and/or Penokean regional metamorphism. However, the uniformly low K-Cs-Tl-Rb-Ba within the PHZ A samples located in the proximal SIC contact metamorphic aureole suggests that they were originally more abundant. In contrast, the Mg versus Ti-Ni-Cr trends on bivariate plots and the coherence of most other elements (HFSE and REE) on primitive mantle normalized plots of the Thessalon, EMF, HHZ, and PHZ samples indicate that these elements were much less mobile. As discussed below, the depletion of the HFSEs and LREEs in most PHZ A samples and in some PHZ B samples can be attributed to them being lost to partial melting and fluid phases during contact metamorphism. The coherent behavior of these elements during the progression from HHZ through PGZ and PHZ B to PHZ A indicates that these elements were relatively immobile during seafloor alteration and both pre- and post-SIC regional metamorphism.

IGNEOUS VARIATIONS

Jolly et al., (1987a, b, 1992) showed that Thessalon basalts exhibited geochemical and Nd isotopic evidence for up to 50% contamination by continental crust during ascent and magma processing, but suggested that low La/Sr ratios were evidence for subduction-related metasomatic enrichment of the subcontinental lithospheric mantle source. Ketchum et al. (2013) argued that Thessalon basalts exhibited only minor degree of fractional crystallization and limited crustal contamination, and suggested that most of the compositional variations were generated by variable degrees of partial melting of metasomatically-enriched subcontinental lithospheric mantle. Hocking (2003) noted that EMF basalts have extraordinarily low Nb/U ratios, much lower than average continental crust but characteristic of the Huronian Supergroup, and suggested that they were derived by contamination of an Ontong-Java-like basaltic magma with up to 19% Huronian-like upper continental crust. Below we look more closely at some of the potential igneous variations in EMF basalts.

Plagioclase accumulation

Plagioclase glomeroporphyritic and phenocrystic basaltic flows are described in EMF metabasalts outside of the SIC contact aureole (Innes, 1977). However, within the study area the metabasalts are devoid of primary phenocrysts. Combined with the mostly negative or absent Sr-Eu anomalies plagioclase accumulation did not have any major effect on the compositional variations in the sample suite.

Fractional crystallization (FC) ± assimilation (AFC)

Cr, Ni, Sc, Al, and Ti exhibit relatively consistent trends on MgO (and Mg#, not shown) variation diagrams (Fig. 3.5). The trends of decreasing Ni, Cr, and Sc (diffuse) with decreasing MgO, scattered trends of decreasing Al and Ca with decreasing Mg combined with minor negative Sr-Eu anomalies, and the trend of increasing Ti with decreasing are consistent with ± olivine/orthopyroxene ± clinopyroxene ± plagioclase crystallization from a primary melt (Fig. 3.5). Hocking's (2003) EMF samples falls on top of some trends but in general plots at lower Ti, Fe and Co for a given Mg value. Although the ranges of most elements in HHZ, PGZ, PHZ B samples overlap, most PHZ A samples have higher Mg-Ni-Cr-Al-Ca contents. Residual concentration during removal of a partial melt (see below) would increase the abundances of all conserved elements, so the lower Ti and HREE contents (which should have been conserved at least until high degrees of melting; Fig. 3.5b) of some of the PHZ A samples might be partially explained by their crystallization from a less evolved magma. Because the PHZ A samples occur in the lowest part of the stratigraphic sequence it is plausible that there might be some upwards evolution of the system over time. Together, the HHZ and PGZ samples display a crude inverse correlation between MgO and some incompatible element concentrations (e.g., Th, LREE) and slightly with [La/Yb]cn. These relations are also present within Hocking's (2003) EMF samples and suggest that fractionation may have played a role in the overall trace element budget and may have started to affect the gradient of the REE patterns for these units. Conversely, a ratio composed of equally incompatible HFSEs like Nb/Th is largely unaffected (Fig. 3.5j), as predicted by their low partition coefficients for olivine, pyroxene, and plagioclase. In contrast, there are no correlations in the PHZ

samples, which have uniformly lower Th (and other HFSE), La/Sm, and La/Yb compared to the HHZ and PGZ samples and regardless of Mg. Nb/Th scatters widely up to extreme values (Nb/Th > 16). These features, which are most pronounced in PHZ A, cannot be produced by fractional crystallization of basaltic magmas. The differences in the absolute abundances of least-mobile incompatible elements and HFSE ratios between the samples in this study largely reflect depletion and fractionation during segregation of partial melts (see below).

The role of fractional crystallization ± crustal assimilation on the abundances of trace elements has been further evaluated using the AFC modeler of Ersoy and Helvacı (2010), an average of least-contaminated PHZ A samples as an approximate starting composition, Gowganda Formation argillites (Young, 2001) as the contaminant, fractionating phases and modes (5% Ol, 44% Cpx, 50% Plag, 0.5% Ilm, and 0.5% Mag) similar to Ketchum et al. (2013), appropriate distribution coefficients (Fujimaki et al., 1984; McKenzie and O'Nions, 1991; Rollinson, 1993; Foley et al., 1996; Zack and Brumm, 1998; Zanetti et al., 2004), and an A:FC ratio "r" value of 0.3 (the ratio of the rate of assimilation to the rate of fractional crystallization). The results are plotted in a Th/Yb vs. Nb/Yb plot in Fig. 3.8. Although the trajectory of EMF basalts is similar to that observed for AFC of a mantle-derived melt, the trend is reversed, i.e., PHZ samples plot closer to the mantle array and Thessalon-EMF-HHZ-PGZ samples plot closer to crustal contaminants. The degree of AFC that is required to explain the observed variation is much too great to preserve basaltic compositions. Although some degree of AFC must have been involved in generating the metabasalts from this study, this cannot account for most of the variations in the sample suite.

Partial melting of mantle source

Ketchum et al. (2013) ascribed variations in the Gd/Lu of the Thessalon basalts to different degrees of partial melting of an enriched mantle source that contained garnet and rutile in the restite. Variations in the degree of partial melting, particularly at low degrees of melting, are capable of systematically fractionate element ratios, e.g. Zr/Nb, that usually would remain constant during igneous processes (e.g., Niu and Batiza, 1997). Thus, the anomalously low Zr/Nb values observed in the PHZ A unit compared to the other units in this study could lead to the suggestion of variations in the degree of partial melting of the source (Table 3.1; Fig. 3.7g). However, the narrow range in Gd/Lu observed in all HHZ, PGZ, and PHZ samples ([Gd/Lu]cn ~1-1.4; avg. ~1.25) would suggest a comagmatic origin and insignificant variations in the degree of partial melting of the source. Furthermore, the PHZ A samples in Figure 3.7g could be described as defining no to a mildly positive correlation that is more compatible with fractionation of the Zr/Nb produced by partial melting and segregation during SIC contact metamorphism.

Mantle source composition

Ketchum et al. (2013) suggested that at least three mantle source compositions are required to explain the Th-Nb-Yb variations in Thessalon samples. However, all of the EMF samples fall more-or-less along a single trend in that plot (Fig. 3.8), so this cannot account of the variations in the sample suite. Almost all of the Thessalon samples have higher Ni and Si but lower Mn, Ca and Sc (Fig. 3.5g). The higher Ni could be attributed to the samples of this study having fractionated sulfides, but the similar Cu contents and

the other observations suggest that the source for the Thessalon may have contained more pyroxene, rather than olivine, in the source (Sobolev et al., 2007). Although the Thessalon units each share some characteristics with the samples in this study the differences eliminate all of the Thessalon units as simply a lower metamorphic grade equivalent.

EFFECTS OF SIC CONTACT METAMORPHISM

After making the above allowances for element mobility during seafloor alteration and regional metamorphism (affecting mainly alkalis), and variations resulting from fractional crystallization/accumulation (minor), degree of partial melting (minor if any), and variations in mantle source composition (minor if any), and, the remaining variations, especially in the abundances and ratios of least-mobile HFSEs (particularly Th, Nb-Ta, and Zr-Hf) are attributed to mobilization during SIC contact metamorphism. Kessel et al. (2005) have shown that trace elements Cs-Rb-Ba-Sr-Pb-Th-U-Nb-Ta-La-Ce-Pr-Nd can be mobilized in aqueous fluids (~700-900 °C) with addition of Zr-Hf-Sm-Eu in hydrous melts (~1000 °C) during subduction-related dehydration and partial melting of eclogite, whereas the HREE-Y-Sc remains relatively immobile. The contact metamorphism associated with the SIC occurring at significantly lower pressures also caused mobilization of Cs-Tl-Rb-Ba-W-Th-U-Nb-Ta-LREE-Zr-Hf-(MREE) as well as fractionating pairs of element with high chemical affinity with one another, e.g., Nb-Ta and Zr-Hf, whereas the HREE appear to have behaved relatively immobile.

Element mobility and HFSE fractionation

Changes in chemical components during alteration of rocks are commonly assessed through mass-balance calculations (e.g., Gresens, 1967; MacLean, 1990). A fundamental ingredient to successfully constraining the alteration is fresh (or close to) precursor rock samples to anchor the chemical modifications. Having several such 'least altered' samples is particularly important in multi precursor systems where a correction for primary igneous variability is required and the reconstruction of precursor compositions hinges on establishment of well-defined fractionation lines (e.g., Barrett and MacLean, 1994). Unfortunately, relatively fresh samples to adequately constrain fractionation lines are not available for the metabasalts in this study and the samples of lower metamorphic grade in Hocking (2003) and Ketchum (2013) show chemical differences that are inconsistent with a common parental source and/or liquid line of descent. In an attempt to circumvent the requirement for well-constrained fractionation lines and revert to a single precursor system a sample from each unit was selected with similar Mg#. Provided that a HHZ sample is the protolith (A) to a metamorphosed PHZ A sample (B) their compositions and volume are related by the following mass balance equation (after Gresens, 1967):

$$100\left[f_v\left(\frac{\rho^B}{\rho^A}\right)x_i^B - x_i^A\right] - \Delta x_i = 0 \quad (1)$$

where, f_v is the ratio of the volume of rock A to that of rock B; ρ^A and ρ^B are rock densities, x_i^A and x_i^B are weight fractions of element i, and Δx_i is the absolute mass flux of i between rocks B and A. At constant volume ($f_v = 1$) equation (1) reduces to:

$$\Delta x_i = \left[x_i^B \left(\frac{\rho^B}{\rho^A}\right)\right] - x_i^A \quad (2)$$

and for constant mass ($\Delta x_i = 0$):

$$f_v = (x_i^A \rho^A / x_i^B \rho^B). \quad (3)$$

Graphical analysis of the composition-volume relationships by solving Eqn. (1) at hypothetical values for f_v and Δx_i and using the known compositions and similar densities (small increases in S.G. of the altered samples does not change the results significantly) of the rocks (Table S3.1) indicates that the heavier MREE and Y-HREE have behaved immobile: linear solutions to Eqn. (1) intersect the Δx_i = 0 axis in clusters corresponding to negligible mass changes within a limited range of volume factors. Hence, the composition-volume relationships can be plotted on enrichment-depletion diagrams where the variation is represented by f_v for Δx_i = 0 (Fig. 3.9a). If the relatively constant interelement ratios (thus, similar f_v values) of the HREE in the samples can be interpreted to indicate that those elements have remained relatively immobile (Gresens, 1967; Lesher et al., 1986), the indicated volume factors range from ~1 for PGZ to ~1.2-1.4 for PHZ B and A. These values correspond to a volume increase in the PHZ B and A samples, which is in contrast to the expected for rocks that have undergone partial melting and melt segregation. This suggest: 1) picking samples of similar Mg# does not successfully remove the primary igneous effects, or 2) HREE were indeed mobilized but not fractionated because of their high chemical affinity with one another. The similar enrichment-depletion diagram when using averages of the individual units (Fig. 3.9b) combined with the similarity of HREE ratios (Fig. 3.7g) of all units suggests that primary igneous processes probably exert a control on the mass-balance calculations with respect

to the HREE, which result in the ostensible volume increase of the PHZ samples. Because of the uncertainties regarding primary controls, the mass changes are less well constrained. Nevertheless, the enrichment-depletion diagram (Fig. 3.9b) indicates significant mobility and relative depletion of Cs-Rb-K-Ba-LREE-HFSE in the PHZ units even if allowing for some control by primary igneous processes. To further establish the mobile behavior displayed by the HFSEs in particularly the PHZ A, a discussion of certain HFSE ratios, i.e., Nb/Th, Ta/W, Nb/Ta, Zr/Hf, and U/Th is meaningful.

The trend on the Th/Yb vs. Nb/Yb plot formed by the samples in this study (Fig. 3.8) cannot be explained by AFC processes (see Section 6.2.2) but also draws similarity to the Isua greenstones (Pearce, 2008; Fig. 3.8). The favored explanation for the trend defined by the Isua samples is metamorphism based on the displacement magnitude and the steepness of the trend. The displacement direction for the Isua samples is thought to be controlled by Th (and LILE) enrichment caused by metasomatic fluids rich in these elements, whereas, the displacement direction in the EMF assemblage in this study is considered the opposite. Evidence for subsolidus Th enrichment in volcanic rocks is most likely to occur where these are interlayered with sediments in volcano-sedimentary sequences (Pearce, 2008). The absence of significant sedimentary sequences within the EMF in the study area and the distribution of the relative Th depleted PHZ rocks (proximal/distal relative to the SIC rather than metasedimentary rocks) is inconsistent with enrichment of the HHZ and PGZ units during subsolidus metamorphism. Conversely, the trend on the Th/Yb vs. Nb/Yb plot is consistent with Th-loss in the PHZ rocks during SIC contact metamorphism.

Ta/W is another proxy commonly used to investigate crustal contamination because of the relative mobility of W during subduction zone processes. Therefore, a greater degree of interaction with arc-modified mantle (relative to N-MORB-like ratios) should result in lower Ta/W ratios (König et al., 2008; Babechuk and Kamber, 2011). The Ta/W ratio for subduction zone magmas presented by König et al., (2008) range from 0.3 to 2.9 (average of 1.0 ± 0.5), those from the Flin Flon arc assemblage are ca. 0.5 (Babechuk and Kamber, 2011), whereas MORB values range from 5-10 (Münker et al., 2007; Babechuk et al., 2010). Consequently, the enriched nature of the HHZ and PGZ units reflected in the low Nb/Th values (Table 3.1) should similarly be expressed in low Ta/W values but this is only true for the HHZ samples that form a relatively tight cluster close to the origin in a Ta/W vs. Nb/Th plot (Fig. 3.7h). In contrast, the PGZ samples define a trend toward higher Ta/W values and the PHZ A samples another trend toward higher Nb/Th. Thus, the Nb/Th and Ta/W values of the HHZ samples are similar to Hocking's (2003) EMF samples and subduction related volcanics such as the Flin Flon arc assemblage (Babechuk and Kamber, 2011). The two trends defined by the PGZ and PGZ A units (with the PHZ B samples forming sort of its own trend between the other two) is then a result of the difference in mobility between W, Th, Ta, and Nb. Because W is a relatively fluid-mobile element relative to Th (König et al., 2008), the discrepancy between the HHZ and PGZ units is consistent with a higher metamorphic grade and stronger dehydration of the pyroxene bearing PGZ unit. The PHZ B unit marks the transition to melt segregation where Th becomes mobile and Ta also has started to behave mobile, resulting in a trend intermediate between the PGZ and PHZ A trends. The PHZ A samples represent the highest metamorphic grade and similar mobility of W and Ta result

in high Nb/Th but low Ta/W rations similar to the HHZ. Ultimately, Nb also behaved mobile, consistent with some of the PHZ samples plotting close to the HHZ samples. The combination of low Nb/Th and low Ta/W observed in the HHZ unit is highly diagnostic of crustal-like contamination, and therefore probably represent the primary signature of these rocks, supported by similar values from samples more distal to the SIC (Hocking, 2003; Ta/W < 1.5, Nb/Th < 4). The Nb/Th and Ta/W then offers an insight into the relative mobility of some of the HFSE during SIC contact metamorphism.

Nb/Ta histograms for the HHZ, PGZ, and PHZ units (Fig. 3.7e) closely approximate normal distributions with the mean located close to the chondritic value of ca. 17. However, noticeable deviations toward higher values are present in mainly the PHZ samples (up to Nb/Ta = 23.2), whereas the HHZ samples all fall below Nb/Ta values of 18. The Nb/Ta ratios of some PHZ samples are higher than what is commonly expected in most basaltic rocks. Higher Nb/Ta ratios have been reported in the Solomon arc assemblage (up to 25.6) and attributed to inheritance from subduction components in equilibrium with rutile (König et al., 2008). Also, high-pressure metamorphic rocks, i.e., refractory eclogites are generally characterized by superchondritic Nb/Ta values (Kamber and Collerson, 2000). Thus, Ta was fractionated from Nb in the PGZ (slightly) and PHZ units consistent with Ta > Nb mobility for at least part of the prograde evolution of the contact aureole.

The HHZ, PGZ, and PHZ B samples have superchondritic Zr/Hf that range tightly around 40.9 ± 1.1 (1σ), whereas the PHZ A samples are systematically lower with a much greater variation at 34.8 ± 2.8 (1σ) ranging down to 29.7 (Fig. 3.7b). There is no obvious correlation between Zr/Hf ratios and MgO, suggesting that clinopyroxene fractionation

was unlikely to have had a controlling effect on the Zr/Hf. Also, there is no clear co-variation of Nb/Ta and Zr/Hf variation as would be expected from trends produced by mantle partial melting at very low degrees of melting (e.g., Niu and Batiza, 1997; David et al., 2000). Furthermore, Gd/Yb that is also sensitive to the degree of mantle melting shows good overlap among all the units in this study. Another remarkable characteristic of the PHZ A samples are their low Zr/Zr* ratios (<0.67; 0.47 average) that works as the primary discriminator between the PHZ A and the HHZ, PGZ, PHZ B units (Fig. 3.7a). A subset of the Thessalon volcanics (Unit 3; Ketchum et al., 2013) also show consistent negative Zr and Hf anomalies (avg. Zr/Zr* = 0.66) but are accompanied by an average Zr/Hf ratio of 41.6 (with extreme values upwards of 50) and Zr concentrations ≥ 150 ppm. More importantly, the Thessalon Unit 3 samples show no correlation between Zr/Zr* and the fairly narrow range in Zr/Nb (avg. = 15) observed in, whereas the PHZ A samples show a fair positive correlation where the more extreme Zr/Zr* values generally correspond to more extreme (lower) Zr/Nb (Fig. 3.7a). While the origin of the negative Zr anomaly in the Thessalon Unit 3 samples is not specifically discussed by Ketchum et al. (2013), the unit is thought to have originated from the lowest amount of partial melting of a garnet bearing source because it has the steepest HREE profiles ([Gd/Lu]cn ~ 3). Because garnet is considered a potential Zr-repository mineral then offers an explanation for the fairly consistent negative Zr anomaly in the Thessalon Unit 3 (e.g., Fraser et al., 1997). Conversely, the more extreme negative Zr anomalies in the PHZ A unit combined with the fractionation of Zr from Hf and Nb is consistent with Zr > Hf > Nb mobility during SIC contact metamorphism.

Uranium generally behaves similarly to Th in magmatic processes, but is prone to behave relatively mobile during surface weathering, seafloor alteration and metamorphism (Babechuk and Kamber, 2011). Th/U ratios in the PGZ unit diverge toward extreme superchondritic values (Th/U up to 10.24; Fig. 3.7i, j) that would require a mantle source component higher than upper continental crust (UCC Th/U = 6, Taylor and McLennan, 1985) to produce such extreme Th/U ratios. The trend formed by the HHZ and PGZ samples in Figure 3.7i compared to the scatter observed in Figure 3.7j indicates that U is the controlling factor of the Th/U ratio. Therefore, the suprachondritic values are easily explained by post-depositional U > Th mobility, particularly in the PGZ unit, rather than the involvement of an exotic mantle component. This is consistent with U mobility during early stages of dehydration reactions in the SIC contact aureole, lowering the U content of the HHZ unit (insignificantly to slightly) and PGZ unit (insignificantly to significantly), and consequently driving Th/U toward anomalously high values. In the higher temperature part of the SIC contact aureole Th also starts to behave mobile as melting and melt segregation becomes the governing process leading to the lower U, Th, and Th/U observed in the PHZ units. Anatexis might even drive the Th/U ratio in the opposite direction and explain the generally low Th/U values of the PHZ samples.

Element signatures of aqueous fluids versus partial melting

Dehydration and partial melting of an average MORB in a subduction environment show distinct changes in the partitioning of trace elements with increasing temperature for an aqueous fluid and when moving from a fluid to a hydrous melts (e.g., Kessel et al., 2005). Obviously, the fluid-solid and melt-solid bulk partition coefficients ($D^{fluid/solid}$ and $D^{melt/solid}$) suitable for subduction zone conditions are not directly applicable to the low-P

conditions under which SIC contact metamorphism took place. Nonetheless, certain aspects might shed some light on what mobile phases were responsible for transporting certain elements from the metabasalts in this study. For example, in a subduction zone environment: 1) Zr-Hf only becomes mobile in hydrous melts ($D^{\text{melt/solid}} > 1$; ~1000 °C), 2) Nb-Ta and the LREE becomes mobile in hydrous melts or aqueous fluids only at high temperatures (900 °C), 3) MREE and HREE remains immobile in aqueous fluids at any temperature and only the lightest of the MREE (Sm-Eu) starts behaving mobile in hydrous melts, 4) aqueous fluids are characterized by $D_{\text{U}}^{\text{fluid/solid}} \geq D_{\text{Th}}^{\text{fluid/solid}}$, whereas a hydrous melt has $D_{\text{U}}^{\text{melt/solid}} < D_{\text{Th}}^{\text{melt/solid}}$ (Kessel et al., 2005). Because most bulk fluid-solid partition coefficients increase with pressure the requirement for a melt as the mobile phase in order to significantly mobilize Th-LREE-Zr-Hf in the PHZ appears evident. However, the Zr-Hf (and Nb-Ta) fractionation trend in the PHZ A samples is opposite to that expected in a garnet-clinopyroxene +/- rutile residue (Kessel et al., 2005). The Zr/Hf ratio in metamorphic minerals averages ~20 for most silicates (incl. ortho- and clinopyroxene) and ~40 for garnet (Bea et al., 2006). Thus, the contrasting residual mineralogy of the PHZ samples (e.g., no garnet) in combination with zircon dissolution during anatexis can explain the low Zr/Hf ratios in the PHZ A unit. Other studies have shown that $D^{\text{mineral/fluid}}$ is commonly greater for Nb than for Ta and that Nb/Ta fractionation can occur during dehydration of metabasalts resulting in higher Nb/Ta values in the restite as observed in some of the PGZ and PHZ samples.

Conditions of partial melting and Th-REE modelling of the melting process

The geochemical variability discussed above is consistent with partial melting and melt segregation during SIC contact metamorphism. To initiate melt extraction, the threshold for a stable melt fraction at around 7%, must be surpassed (Nicolas, 1986; Rosenberg and Handy, 2005). Non-modal dynamic melting models involve retention of a stable fraction of melt in the restite, and can be considered an intermediate between the two end-member models of batch and fractional melting (e.g., Zou, 1998). Figure 3.10 shows the effect of a non-modal dynamic melting model with a critical value of separation of 7% when applied to the EMF metabasalts of this study. From the experiments by Beard and Lofgren (1991) the model can be separated into two stages defined by the two melting reactions encountered in the experiments at 3 kbar.

The stage 1 melt-forming reaction is:

9 Qtz + 33 Amph + 5 Pl = 2 Mt + 6 Opx + 20 Cpx + 19 Melt

The stage 2 melt-forming reaction is:

13 Pl + 1 Cpx + 1 Opx + 1 Ilm + 2 Mt = 18 Melt

The stage 1 reaction occurs from 850-900°C and is terminal for both amphibole and quartz. At higher temperatures from 900-1000°C the stage 2 reaction produces melt dominantly from the breakdown of plagioclase (Beard and Lofgren, 1991). In an attempt to reflect these stages the source and melt modes from stage 1 melting is used in combination with a HHZ sample as starting composition (Fig. 3.10a), and stage 2 melting is combined with a starting composition of average PHZ B (Fig. 3.10b). Mineral-melt

partition coefficients for rhyolitic compositions are identical to those used by Gillis and Coogan (2002) with the addition of *D*'s for Th and all elements concerning the distribution between amphibole and melt (Mahood and Hildreth, 1983 (only $D_{\mathrm{Th}}^{\mathrm{ilm/melt}}$); Bacon and Druitt, 1988). The non-modal dynamic melting models presented here predict Th and LREE depletion trends that are comparable to those observed in the PHZ units. However, these models are resting upon numerous assumptions and uncertainties (e.g., validity of equilibrium conditions between melt and restite, and the role of accessory phases) and some caution must be exerted when interpreting the similarities. Nevertheless, the models indicate that several PHZ samples experienced up to ~20% melting and some PHZ A samples in excess of 35%. The effect of partial melt extraction on the major element composition is illustrated in Figure 3.5 by the restite compositions from the Beard and Lofgren (1991) experiments. Even at 20-25% melting several major elements remains fairly consistent (e.g., wt. % MgO, TiO_2, Al_2O_3 and Na_2O) but likely contributed to some of the scatter in the bivariate plots. The mostly higher CaO and consistently lower K_2O of the PHZ A unit is comparable to the more significant increase in CaO and rapid depletion in K_2O observed in the experimental restites as the abundance of melt increase.

A comparison to SIC thermal modelling

In their mathematical model analyzing the cooling of the SIC and its effect on mafic and granitic footwall rocks, Prevec and Cawthorn (2002) estimate the cooling period of the melt sheet to reach its solidus by 2 models: 1) a combined conductive-convective heat loss model yielding 56 kyr, and 2) a conductive heat loss model yielding 97 kyr. Both

models assume an initial melt-sheet and country-rock temperature of 1800 °C and 200 °C, respectively. In the conductive model, the footwall at the SIC contact would stay at 1000 °C for nearly 20 kyr and produce partial melting that extends 300 m (only 20 m in excess of 60% partial melting) into the footwall rocks, and a T_{max} = 820 °C at 500 m below the SIC melt sheet. The convective model predicts a similar T_{max} at 500 m below the SIC melt sheet, ca. 750 °C at 750 m below, and 620 °C at depths of a 1000 m, including >120 m total melting, 230 m of 60% partial melting, and steadily decreasing amounts of partial melting down to 500 m below the melt sheet. This is in good agreement with the PHZ and its width of up to 500 m, and also supports an inner up to 250 m zone represented by the PHZ A unit where melt and melt segregation was significant. Furthermore, the less significant geochemical changes observed in the PGZ unit correlates well with a zone extending from ca. 500 m to 750 m from the SIC contact that experienced significant dehydration and potentially incipient melting below the stable melt threshold. Thus, the geochemical signatures seems to support the estimated width of the SIC contact aureole as predicted by the convective model of Prevec and Cawthorn (2002). However, their model was used to argue for extensive thermomechanical erosion (800 m) of the SIC North Range footwall in order to match the observed width of the North Range contact aureole (e.g., Boast and Spray, 2006). In contrast, the geochemical systematics of the EMF metabasalts appears to support that the high-T metamorphic aureole on average is wider in the South Range mafic footwall than in the North Range footwall dominated by felsic gneisses (Jørgensen et al., Chapter 2).

Where did the melt go?

Finding a complementary geochemical unit to a restite like the PHZ A unit is complicated by the evolution of melt segregations that would inevitably have experienced variable degrees of partial crystallization, crystal accumulation, mixing (potentially with melts generated from sources other than metabasalts), and localized entrapment. However, it would be expected that melt segregation of these magnitudes would be evident in the field. Indeed, field observations of minor felsic leucocratic patches that locally coalesce and melt microtextures are documented in the PHZ unit metabasalts and compatible with melt segregations (Jørgensen et al., Chapter 2). However, the extent to which the macroscopic features occur in the field seems insufficient to account for the amount of melt extraction as constrained by the experiments and melting models. Back-injections of aplitic dikes in the SIC have long been recognized as deriving from the partial melting of the Murray and Creighton plutons and locally mapped from the margin of the granites and up into the SIC (e.g., Peredery and Morrison, 1984; Ames et al., 2005; Jørgensen et al., Chapter 2). However, direct observations of dikes back-injecting from the EMF metabasalts and into the SIC have not been documented. Thus, melt extractions from the metabasalts probably did not contribute to the formation of the back-injected aplitic dikes in any major way. Instead, if partial melting of the metabasalts was constrained to earlier in the cooling history of the impact melt sheet (i.e., prior to near solidification at which point the formation of back-injections likely would have occurred) this would support the model in which melt segregations from the EMF metabasalts participated directly in the formation of the SIC contact sublayer (e.g., Lightfoot et al., 1997b; Prevec, 2000; Prevec et al., 2000; Prevec and Cawthorn, 2002).

Alternatively, mobile phases from metabasalts in the proximal contact aureole were driven further away from the SIC contact. While a couple of aspects in the chemistry of the HHZ and PGZ units might suggest that they accommodated the mobile phases escaping the PHZ units, e.g., the relatively high Th-LREE concentrations and some anomalously high positive Zr anomalous, this seems unlikely for several reasons: 1) there exist no field or petrographical evidence to support this scenario, 2) the higher element concentrations are comparable to some of the Thessalon volcanics and not conspicuously elevated, 3) multi-element diagrams for the HHZ and PGZ units show smooth patterns in comparison to the PHZ A samples, 4) Zr/Hf and Nb/Ta ratios are remarkably consistent, and 5) the PGZ unit appear to have lost elements like U and W during dehydration, whereas Ta/W and Nb/Th of the HHZ unit represents a primary signature with a crustal input. It is possible that certain LILEs have moved around during retrogression and potentially contributed to the scatter observed in the samples of this study, but there is no evidence for partial melts and/or high temperature fluids from the PHZ units having percolated through the PGZ and HHZ to significantly alter their HFSE-REE budgets. However, this does not rule out the option that the mobile phases ended up in discrete zone, e.g., exploited preexisting zones of weakness like Sudbury breccia zones or quartz diorite dikes, but such observations are yet to be documented.

Implications for exploration

This study has two important implications for mineral exploration in Sudbury: 1) identifying areas where Main Mass norite might be thicker, which correlates with ore tenor (Farrow and Lightfoot, 2002; Keays and Lightfoot, 2004), and 2) identifying areas where the thermal aureole may be thicker, which correlates with the ability of Fe-Ni-Cu

sulfide melts and Au-Pd-Pt-As-Sb-Bi-Te-bearing magmatic-hydrothermal fluids to penetrate into footwall rocks.

Keays and Lightfoot (2004) showed that there is an empirical correlation between the quality (tenor and abundance of mineralization) and the thickness of overlying main mass norite. The field area in this study is located where SIC norite (Keays and Lightfoot, 2004), PHZ, and PHZ A all thin towards the NE. This is consistent with the SIC contact aureole being wider beneath thicker parts of the SIC and suggests that the mineral assemblages and geochemical signatures identified in this study (or analogous assemblages/signatures in other lithologies) could be used to establish the relative thickness of main mass norite in places where this is uncertain because of structural deformation (e.g., in several areas along the South and East Ranges).

Studies have shown that Cu-Ni-Pd-Pt-rich footwall vein mineralization is restricted to within 200-300m (true thickness) of the SIC contact and that Pt-Pd-Au-As-Sb-Bi-Te-rich footwall disseminated mineralization is restricted to within ~300-400m of the SIC contact (e.g., Morrison et al., 1984; McLean et al. 2005; Farrow et al., 2005). Gregory (2005), Stout (2009), and Nelles and Lesher (in press) have argued that this defines the limit to which Fe-Cu-Ni sulfide melts, which solidify at ~800°C, and exsolved magmatic-hydrothermal fluids, which precipitate metals at much lower temperatures, can penetrate into the footwall rocks. Experiments by Cafagna (2015) have shown that Pd-Pt-Au can also be fractionated from the other highly siderophile elements and transported away from a sulfide assemblage through a relatively low-porosity, low-permeability medium in the absence of hydrothermal fluids. In all cases, the main driver for the mobilization of economically important elements into the footwall appears to be temperature, which

means that understanding the width of the SIC contact aureole is critical to understand when exploring for footwall mineralization.

CONCLUSIONS

We have shown the presence of a metamorphic chemostratigraphy in the EMF mafic volcanic suite that developed during SIC contact metamorphism. The geochemical zonation consists of: 1) an inner zone (PHZ A unit), extending up to approximately 250 m from the SIC contact, characterized by strong mobilization of K, LILEs Cs-Rb-Ba, LREE, and HFSEs W-Th-U. This zone also shows moderate to strong mobility of otherwise immobile HFSEs Ta-Nb-Zr-Hf including fractionation of Zr/Hf and to a lesser extent Nb/Ta; 2) a transitional zone (PHZ B unit) extending from the PHZ A unit and up to 500 m from the base of the SIC, characterized by moderate-strong mobility of K and LILEs Cs-Rb-Ba, moderate LREE and HFSEs W-Th-U mobility, and weak-moderate HFSEs Ta > Nb mobility; 3) an outer zone (PGZ unit) extending to at least ca. 750 m from the SIC contact, that shows only minor element control by contact metamorphic processes other than U > Th mobility, and an increasing mobility of W as the transition zone is approached. The study clearly demonstrates that significant mobilization of elements otherwise considered highly immobile is possible during low-P/high-T contact metamorphic processes.

The strong mobilization of K, Th, LREE, and Zr-Hf in the PHZ A unit is interpreted to reflect melt extraction. Constrains from melting experiments and geochemical modeling suggests that the PHZ A unit locally could have experienced upwards of 35% melt extraction. This further demonstrates that the thickness of the zone that records high

modes of melting and melt segregation in the SIC South Range mafic footwall is significantly thicker than the anatectic zone reported in felsic gneisses of the North Range footwall (ca. 25 m). Additionally, the thickness of the anatectic zone are reasonable close to proposed thermal models indicating significant melting within 230 m of the SIC contact and a steady decrease in partial melting down to 500 m into the footwall (Prevec and Cawthorn, 2002). Thus, the continuous obliteration of the contact aureole by the process of thermomechanical erosion required to explain the narrow anatectic zone in the North Range aureole evidently played a lesser role in mafic rocks of the South Range aureole.

An important observation with implications for exploration is that the width of the contact aureole in the EMF metabasalts appear to correlate with the thickness of the SIC which in turn is thought to be a controlling factor for the location of contact deposits (Keays and Lightfoot, 2004; Jørgensen et al., Chapter 2). This correlation also appears to be true for the geochemical zonation that indicates a wider high-T zone in the direction where the SIC is correspondingly thicker. Furthermore, the width of the high-T contact aureole might be the deciding factor for the extent to which low-S Cu-PGE rich mineralization can penetrate into the footwall.

ACKNOWLEDGEMENTS

Financial support was provided by grants from the Centre for Excellence in Mining Innovation (project sponsors Vale Ltd. and Glencore Ltd.) and the Natural Sciences and Engineering Council of Canada (CRD to DKT and CML, Discovery Grant to DKT, and Discovery Grants #203171-2007 and #203171-2012 to CML). Field and logistical

support was provided by Vale Ltd. and we are particularly grateful to Peter Lightfoot and Lisa Gibson for their assistance.

REFERENCES

Ames, D.E., Buckle, J., Davidson, A., and Card, K., 2005. Sudbury bedrock compilation; Geology: Geological Survey of Canada, Open File 4570, scale 1:50000.

Ames D.E. and Farrow, C.E.G., 2007. Metallogeny of the Sudbury mining camp, Ontario, GAC-MDD Spec. Publ. 5: p. 329–350.

Ames, D.E., Golightly, J.P., Lightfoot, P.C., and Gibson, H.L., 2002. Vitric compositions in the Onaping Formation and their relationship to the Sudbury Igneous Complex, Sudbury structure: Economic Geology, v. 97, p. 1541-1562.

Babechuk, M.G. and Kamber, B.S., 2011. An estimate of 1.9 Ga mantle depletion using the high-field-strength elements and Nd–Pb isotopes of ocean floor basalts, Flin Flon Belt, Canada. Precambrian Research 189, p. 114-139.

Babechuk, M.G., Kamber, B.S., Greig, A., Canil, D., Kodolányi, J., 2010. The behaviour of tungsten during mantle melting revisited with implications for planetary differentiation time scales. Geochim. Cosmochim. Acta 74, p. 1448–1470.

Bacon, C.R., and Druitt, T.H., 1988. Compositional evolution of the zoned calcalkaline magma chamber of Mount Mazama, Crater Lake, Oregon. Contrib. Mineral. Pet., 98, p. 224-256.

Bailey, J., Lafrance, B., McDonald, A.M., Fedorowich, J.S., Kamo, S. and Archibald, D.A., 2004. Mazatzal–Labradorian-age (1.7-1.6 Ga) ductile deformation of the South Range Sudbury impact structure at the Thayer Lindsley Mine, Ontario; Canadian Journal of Earth Sciences, v.41, p. 1491-1505.

Barrett T.J. and MacLean, W.H., 1994. Chemostratigraphy and hydrothermal alteration in exploration for VHMS deposits in greenstones and younger volcanic rocks, in Lentz, D.R., ed., Alteration and Alteration Processes associated with Ore-forming Systems: Geological Association of Canada, Short Course Notes, v. 11, p. 433-467.

Bea F., Montero P., and Ortega M., 2006. A LA-ICP-MS evaluation of Zr reservoirs in common crustal rocks: implications for Zr and Hf geochemistry and zircon-forming processes. Can. Mineral, v. 44, p. 693–714.

Beard, J.S., and Lofgren, G.E., 1991. Dehydration melting and watersaturated melting of basaltic and andesitic greenstones and amphibolites. Journal of Petrology 32, p. 365-401.

Bennett, G., Dressler, B.O., Robertson, J.A., 1991. The Huronian Supergroup. In: Geology of Ontario, OGS, Special Volume 4, Part 1, p. 549-591.

Boast, M. and Spray, J.G. 2006. Superimposition of a thrust-transfer fault system on a large impact structure: Implications for Ni-Cu-PGE exploration at Sudbury; Economic Geology, v. 101, p. 1583-1594.

Buchan, K.L., Card, K.D. and Chandler, F.W. 1989. Multiple ages of Nipissing Diabase intrusion: paleomagnetic evidence from the Englehart area, Ontario; Canadian Journal of Earth Sciences, v. 26, p. 427-445.

Burnham, O.M., Hechler, J.H., Semenyna L., and Schweyer, J., 2002. Mineralogical controls on the determination of trace elements following mixed acid dissolution; in Summary of Field Work and Other Activities 2002, Ontario Geological Survey, Open File Report 6100, p.36-1 to 36-12].

Cafagna, F., 2015. The geochemical behavior of metalloids and their effect on the highly siderophile elements during the crystallization of a magmatic sulfide liquid in relation to the formation of Ni-Cu-PGE magmatic sulfide deposits. Unpublished PhD thesis, Laurentian University, Sudbury, Ontario, 206p.

Card, K.D., 1978a. Geology of the Sudbury-Manitoulin area, districts of Sudbury and Manitoulin. Ontario Geological Survey, Report 166, pp 1-238. Accompanied by Map 2360, scale 1 inch to 2 miles (1:126,720), and 4 charts.

Card, K.D., 1978b. Metamorphism of the middle Precambrian (Aphebian) rocks of the eastern Southern Province; in Metamorphism in the Canadian Shield, Geological Survey of Canada, Paper 78-10, p. 269-282.

Coleman, A. P., 1913. The nickel industry, with special reference to the Sudbury Region, Ontario; Canada Department of Mines, Mines Branch, no. 170, 206p.

Corfu, F. and Andrews, A. 1986. A U-Pb age for mineralized Nipissing diabase, Gowganda, Ontario; Canadian Journal of Earth Sciences, v.23. p.107-112.

David, K., Schiano, P., Allègre, C.J., 2000. Assessment of the Zr/Hf fractionation in oceanic basalts and continental materials during petrogenetic processes. Earth Planet. Sci. Lett. 178, p. 285–301.

Dence, M.R. 1972. Meteorite impact craters and the origin of the Sudbury Basin; in New Developments in Sudbury Geology, Geological Association of Canada, Special Paper Number 10, p. 7-18.

DeWolfe, Y.M., Gibson, H.L., Piercey, S.J., 2009. Petrogenesis of the 1.9 Ga mafic hanging wall sequence to the Flin Flon, Callinan, and Triple 7 massive sulphide deposits, Flin Flon, Manitoba, Canada. Can. J. Earth Sci. 46, p. 509–527.

Dietz, R.S., 1964. Sudbury structure as an astrobleme. J. Geol. 72, p. 412–434.

Dressler, B.O., 1984a, General geology of the Sudbury area. In: Pye, E.G., Naldrett, A.J., Giblin, P.E. (Eds.), The geology and ore deposits of the Sudbury structure: Ontario Geological Survey Special Volume 1, p. 57–82.

Dressler, B.O., 1984b. The effects of the Sudbury event and the intrusion of the Sudbury Igneous Complex on the Footwall Rocks of the Sudbury structure. In: Pye, E.G., Naldrett, A.J., Giblin, P.E. (Eds.), The geology and ore deposits of the Sudbury structure: Ontario Geological Survey Special Volume 1, p. 97–136.

Ersoy, Y. and Helvacı, C., 2010. FC–AFC–FCA and mixing modeler: A Microsofts® Excel© and spreadsheet program for modeling geochemical differentiation of magma by crystal fractionation, crustal assimilation and mixing. Computer and Geosciences 36, p. 383-390.

Faggart, B.E. Jr., Basu, A.R., and Tatsumoto, M., 1985. Origin of the Sudbury complex by meteoritic impact: Neodymium isotopic evidence. Science 230, p. 436-439.

Farrow, C.E.G. Everest, J.O., King, D.M., Jolette, C., 2005. Sudbury Cu-(Ni)-PGE systems: Refining the classification using McCreedy West mine and Podolsky project case studies, in Mungall, J.E., ed., Exploration for Deposits of Platinum-Group Elements: Mineralogical Association of Canada, Short Course Series v. 35, p. 163-180.

Farrow, C.E.G., and Lightfoot, P.C., 2002. Sudbury PGE revisited: Toward an Integrated model, in Cabri, L.J., ed., The Geology, Geochemistry, Mineralogy and Mineral Beneficiation of Platinum Group Element: Canadian Institute of Mining, Metallurgy and Petroleum, Special Volume 54, p. 13-130.

Foley, S.F., Jackson, S.E., Fryer, B.J., Greenough, J.D. and Jenner, G.A., 1996. Trace element partition coefficients for clinopyroxene and phlogopite in an alkaline lamprophyre from Newfoundland by LAM-ICP-MS. Geochimica et Cosmochimica Acta, v. 60(4), p. 629-638.

Fraser, G., Ellis, D., and Eggins, S., 1997. Zirconium abundance in granulite-facies minerals, with implications for zircon geochronology in high-grade rocks. Geology, 25, p. 607-610.

Fujimaki, H., Tatsumoto, M. and Aoki, K.-i., 1984. Partition coefficients of Hf, Zr, and REE between phenocrysts and groundmasses. Journal of Geophysical Research v. 89, p. 662-672.

Gillis, K.M., and Coogan, L.A., 2002. Anatectic migmatites from the roof of an ocean ridge magma chamber. Journal of Petrology, 43, p. 2075-2095.

Golightly, J.P., 1994. The Sudbury Igneous Complex as an Impact Melt: Evolution and Ore Genesis. In: Lightfoot, P.C., Naldrett, A.J. (Eds.), Proceedings of the Sudbury-Noril'sk Symposium. OGS Special Volume 5, 105-118.

Gregory, S.K., 2005. Geology, Mineralogy, and Geochemistry of Transitional Contact/Footwall Mineralization in the McCreedy East Ni-Cu-PGE Deposit, Sudbury Igneous Complex. Unpublished MSc Thesis, Sudbury, Ontario, Laurentian University, 138 p.

Gresens, R.L., 1967. Composition-volume relationships of metasomatism. Chem. Geol. v. 2, p. 47-65.

Grieve, R.A.F., Dence, M.R. and Robertson, P.B., 1977. Cratering processes: As interpreted from the occurrence of impact melts, in Impact and Explosion Cratering, edited by D. J. Roddy, R. O. Pepin, and R. B. Merrill, p. 791–814, Pergamon, New York.

Grieve, R.A.F., Stöffler, D., and Deutsch, A., 1991, The Sudbury structure-controversial or misunderstood: Journal of Geophysical Research, v. 96, p. 22753–22764.

Grieve, R.A.E, Therriault, A.M. 2000. Vredefort, Sudbury, Chicxulub: Three of a kind? Annual Review of Earth and Planetary Sciences, v. 28, p. 305-338.

Heaman, L.M., 1997. Global mafic magmatism at 2.45 Ga: Remnants of an ancient large igneous province? Geology 25, p. 299-302.

Hocking, M.W.A., 2003. The geology and geochemistry of the Elsie Mountain Formation: implications for Paleoproterozoic magmatism in the Southern Province. Unpublished BSc thesis, Laurentian University, Sudbury, Ontario, 79p.

Innes, D.G., 1977. Proterozoic volcanism in the Southern Province of the Canadian Shield. M.Sc. Thesis, Laurentian University.

Ivanov, B.A., and Deutsch, A., 1999. Sudbury impact event: Cratering mechanics and thermal history, in Dressler, B.O., and Sharpton, V.L., eds., Large meteorite impacts and planetary evolution II: GSA Special Paper #339. Boulder: Geological Society of America, p. 389–398.

James, R.S., Easton, R.M., Peck, D.C., and Hrominchuk, J.L., 2002. The East Bull Lake Intrusive Suite: Remnants of a ~2.48 Ga Large Igneous and Metallogenic Province in the Sudbury Area of the Canadian Shield. Economic Geology 97, p. 1577-1606.

Jensen, L.S., 1976. A new plot for classifying subalkalic volcanic rocks; Ontario Division of Mines, Miscellaneous Paper 66, p. 1-22.

Jolly, W.T., 1987a. Geology and geochemistry of Huronian rhyolites and low-Ti continental tholeiites from the Thessalon region, central Ontario. Canadian Journal of Earth Sciences 24, p. 1360-1385.

Jolly, W.T., 1987b. Lithophile elements in Huronian low-Ti continental tholeiites from Canada, and evolution of the Precambrian mantle. Earth and Planetary Science Letters 85, p. 401-415.

Jolly, W.T., Dickin, A.P., Wu, T., 1992. Geochemical stratigraphy of the Huronian continental volcanics at Thessalon, Ontario: contributions of two-stage crustal fusion. Contributions to Mineralogy and Petrology 110, p. 411-428.

Kamber, B.S., Collerson, K.D., 2000. Role of 'hidden' deeply subducted slabs in mantle depletion. Chem. Geol. 166, p. 241–254.

Kamo, S.L., Krogh, T.E., Kumarapeli, P.S., 1995. Age of the Grenville dyke swarm, Ontario-Quebec: Implications for the timing of Iapetan rifting. Canadian Journal of Earth Sciences 32, 273–280.

Keays, R.R., Lightfoot P.C., 2004. Formation of Ni–Cu–PGE sulfide mineralization in the Sudbury Impact Melt, Min. Pet. 82: p. 217–258.

Kessel R., Schmidt M.W., Ulmer P., and Pettke T., 2005. Trace element signature of subduction-zone fluids, melts and supercritical liquids at 120–180 km depth. Nature, v. 437(29), p. 724–727.

Ketchum, K.Y., Heaman, L.M., Bennett, G., Hughes, D.J., 2013. Age, Petrogenesis and Tectonic Setting of the Thessalon Volcanic Rocks, Huronian Supergroup, Canada. Precambrian Research, v. 233, p. 144-172.

König, S., Münker, C., Schuth, S., Garbe-Schönberg, D., 2008. Mobility of tungsten in subduction zones. Earth Planet. Sci. Lett. 274, p. 82–92.

Krogh, T.E., Corfu, F., Davis, D.W., Dunning, G.R., Heaman, L.M., Kamo, S.L., Machado, N., Greenhough, J.D., and Nakamura, E., 1987. Precise U-Pb isotopic ages of

diabase dykes and mafic to ultramafic rocks using trace amounts of baddeleyite and zircon, in Halls, H.C. and Fahrig, W.F., eds., Mafic dyke swarms: Geological Association of Canada Special Paper 34, p. 147–152.

Krogh, T.E., Davis, D.W., Corfu, F., 1984. Precise U-Pb zircon and baddeleyite ages for the Sudbury area. In: The Geology and Ore Deposits of the Sudbury Structure, Ontario Geological Survey, Special Volume 1, p. 431-446.

Krogh, T.E., Kamo, S.L., and Bohor, B.F. 1996. Shock metamorphosed zircons with correlated U-Pb discordance and melt rocks with concordant protolith ages indicate an impact origin for the Sudbury structure. American Geophysical Union Geophysical Monograph 95: p. 343-353.

Lesher C.M., Gibson H.L., and Campbell I.H., 1986. Composition-volume changes during hydrothermal alteration of andesite at Buttercup Hill, Noranda District, Québec. Geochimica et Cosmochimica Acta 50, p. 2693-2705.

Lightfoot, P.C., Keays, R.R., Morrison, G.G., Bite, A., and Farrell, K.P., 1997a. Geologic and geochemical relationships between the contact sublayer, inclusions, and the main mass of the Sudbury Igneous Complex: a case study of the Whistle mine embayment. Economic Geology, v. 92, p. 647-673.

Lightfoot, P.C., Doherty, W., Farrell, K., Keays, R.R., Moore, M., and Pekeski, D., 1997b. Geochemistry of the Main Mass, Sublayer, Offsets, and Inclusions from the Sudbury Igneous Complex, Ontario: Ontario Geological Survey, Open File Report 5959, 231 p.

MacLean, W.H., 1990. Mass changes in altered rock series. Miner. Deposita, v. 25, p. 44-49.

Mahood, G.A., and Hildreth, E.W., 1983. Large partition coefficients for trace elements in high-silica rhyolites. Geochimica et Cosmochimica Acta, 47, p. 11-30.

McDonough, W.F., Sun, S.S., 1995. The composition of the Earth. Chemical Geology, v. 120, p. 223–253.

McKenzie, D. and O'Nions, R.K., 1991. Partial melt distributions from inversion of rare Earth element concentrations. Journal of Petrology, v. 32, p. 1021-1091.

McLean, S.A., Straub, K.H., and Stevens, K.M., 2005. The discovery and characterization of the Nickel Rim South deposit, Sudbury, Ontario, in Mungall, J.E., ed., Exploration for Deposits of Platinum-Group Elements: Mineralogical Association of Canada, Short Course Series,

v. 35, p. 358-368.

Milkereit, B., and the Sudbury Working Group, 1992. Deep geometry of the Sudbury Structure from seismic reflection profiling: Geology, v. 20, p. 807-811.

Morrison, G.G., Jago, B.C., and White, T.L., 1994. Footwall mineralization of the Sudbury Igneous Complex, in Lightfoot, P.C., and Naldrett, A.J., eds., Proceedings of the Sudbury-Noril'sk Symposium: Ontario Geological Survey, Special Volume 5, p. 119-132.

Mottl, M.J., 1983. Metabasalts, axial hot springs, and the structure of hydrothermal systems at mid-ocean ridges. Geol. Soc. Amer. Bull. v. 94, p. 161-180.

Mukwakwami, J., Lafrance, B., Lesher, M. C., 2012. Back-thrusting and overturning of the southern margin of the 1.85 Ga Sudbury Igneous Complex ar the Garson mine, Sudbury, Ontario. Precambrian Research 196-197, p. 81-105.

Mukwakwami J., Lafrance, B., Lesher, C.M., Tinkham, D., Rayner, N., Ames, D.E., 2014. Fabrics and textures of deformed and metamorphosed Ni-Cu-PGE sulfide ores at Garson Mine and their implications for sulfide mobilization processes, Mineralium Deposita 49(2): p. 175-198.

Münker, C., Paulick, H., König, S., 2007. The geochemical behaviour of W, Nb-Ta, and Zr-Hf during mid ocean ridge melting. Geochim. Cosmochim. Acta 71, A696.

Naldrett, A.J., 2004. Magmatic Sulfide Deposits: Geology, Geochemistry, and Exploration; Springer, 727p.

Naldrett, A. J., and R. H. Hewins, 1984. The main mass of the Sudbury Igneous Complex in Pye, E.G., Naldrett, A.J., and Giblin, P.E., eds., The Geology and Ore Deposits of the Sudbury Structure: Ontario Geological Survey, Special Volume 1, p. 235-251.

Nelles E. and Lesher, C.M., (accepted). Genesis of Cu-PGE-rich footwall-type mineralization in the Morrison deposit, Sudbury. Economic Geology.

Nicolas, A., 1986. A melt extraction model based on structural studies in mantle peridotites. Journal of Petrology, v. 27, p. 999-1022.

Niu, Y.L. and Batiza, R., 1997. Trace element evidence from seamounts for recycled oceanic crust in the eastern Pacific mantle. Earth and Planetary Science Letters 148, p. 471-483.

Noble, S.R. and Lightfoot, P.C. 1992. U-Pb baddeleyite ages for the Kerns and Triangle Mountain intrusions, Nipissing diabase, Ontario; Canadian Journal of Earth Sciences, v.29, p.1124-1129.

Olaniyan, O., Smith, R.S., Lafrance, B., 2014. A constrained potential field data interpretation of the deep geometry of the Sudbury structure. Canadian Journal of Earth Sciences, v. 51(7), p. 715-729.

Pattison, E.F., 1979. The Sudbury sublayer. Canadian Mineralogist, v. 17, p. 257-274.

Pearce, J.A., 2008. Geochemical fingerprinting of oceanic basalts with applications to ophiolite classification and the search for Archean oceanic crust. Lithos 100, p. 14–48.

Pearce, J.A., Peate,D.W., 1995. Tectonic implications of the composition of volcanic arc magmas. Annual Reviews of Earth and Planetary Sciences v. 23, p. 251–285.

Peredery, W.V., and Morrison, G.G., 1984. Discussion of the origin of the Sudbury structure, in Pye, E.G., Naldrett, A.J., and Giblin, P.E., eds.,The Geology and Ore Deposits of the Sudbury Structure: Ontario Geological Survey, Special Volume 1, p. 491-511.

Prevec, S.A., 1993. An isotopic, geochemical and petrographic investigation of the genesis of early Proterozoic mafic intrusions and associated volcanism near Sudbury, Ontario; unpublished PhD thesis, University of Alberta, Edmonton, Alberta, 223p.

Prevec, S. A., 2000. An examination of modal variation mechanisms in the contact sublayer of the Sudbury Igneous Complex, Canada, Mineral. Petrol., v. 68, p. 141– 157.

Prevec, S.A. and Cawthorn, R.G. 2002. Thermal evolution and interaction between impact melt sheet and footwall: A genetic model for the contact sublayer of the Sudbury Igneous Complex, Canada; Journal of Geophysical Research, v. 107(B8), p. 2176.

Prevec, S. A., Lightfoot, P.C., and Keays R.R., 2000. Evolution of the sublayer of the Sudbury Igneous Complex: Geochemical, Sm-Nd isotopic and petrologic evidence, Lithos, v. 51, p. 271– 292.

Raharimahefa T., Lafrance, B., Tinkham, D.K., 2014. Structural, metamorphic, and U-Pb Geochronological evolution of the Southern Province, Sudbury, Canada. Precambrian Research, v. 51, p. 750-774.

Riller, U., 2005. Structural characteristics of the Sudbury impact structure, Canada: impact-induced versus orogenic deformation-a review: Meteoritics and Planetary Science, v. 40, p. 1723–1740.

Rollinson, H. R., 2003. Using Geochemical Data: Evaluation, Presentation, Interpretation. London (Longman Scientific and Technical).

Rosenberg, C.L., and Handy, M.R., 2005. Experimental deformation of partially melted granite revisited: Implications for the continental crust. Journal of Metamorphic Geology, 23, p. 19-28.

Rousell, D.H., and Card, K.D., 2009. Sudbury Area Geology and Mineral Deposits; in A Field Guide to the Geology of Sudbury, Ontario; Ontario Geological Survey, Open File Report 6243, p. 14-30.

Rousell, D.H., Fedorowich, J.S., Dressler, B.O., 2003. Sudbury breccia (Canada): a product of the 1850 Ma Sudbury event and host to footwall Cu–Ni–PGE deposits. Earth Science Reviews, v. 60, p. 147-174.

Rousell, D.H., Gibson, H.L. and Jonasson, I.R., 1997. The tectonic, magmatic and mineralization history of the Sudbury Structure; Exploration and Mining Geology, v.6, p. 1-22.

Rudnick, R.L., Fountain, D.M., 1995. Nature and composition of the continental crust: a lower crustal perspective. Rev. Geophys. 33, 267–309.

Shanks, W.S., and Schwerdtner, W.M., 1991. Structural analysis of the central and southwestern Sudbury Structure, Southern Province, Canadian Shield, Canadian Journal of Earth Sciences, v. 28, p. 411-430.

Smith, M.D., 2002. The timing and petrogenesis of the Creighton pluton, Ontario: An example of felsic magmatism associated with Matachewan igneous events. M.Sc. thesis, University of Alberta, Canada.

Sobolev, A.V., Hofmann, A.W, Kuzmin, D.V., et al., 2007. The amount of recycled crust in sources of mantle-derived melts. Science, 316, p. 412-417.

Spray, J.G., Butler, H.R., Thompson, L.M., 2004. Tectonic influence on the morphometry of the Sudbury impact structure: Implications for terrestrial cratering and modeling. Meteoritics and Planetary Science 39 (2), p. 287-301.

Stout, A.E., 2009. Geology, Mineralogy, and Geochemistry of the McCreedy East 153 Cu-Ni-PGE Deposit, Sudbury, Ontario. Unpublished MSc Thesis, Utrecht, Netherlands, Utrecht University, 39 p.

Sun, S.S., McDonough, W.F., 1989. Chemical and isotopic systematics of oceanic basalts: implications for mantle composition and processes. In: Saunders, A.D., Norry, M.J. (Eds.), Magmatism in the Ocean Basins. Geological Society of London, London, p. 313–345.

Taylor, S.R., McLennan, S.M., 1985. The Continental Crust: its composition and Evolution. Blackwell Scientific Publications, p. 1-312.

Therriault, A.M., Fowler, A.D., and Grieve, R.A.F., 2002. The Sudbury Igneous Complex: A differentiated impact melt sheet. Economic Geology, v. 97, p. 1521–1540.

Thomson, R., 1935. Sudburite, a metamorphic rock near Sudbury, Ontario. Journal of Geology, v. 43, p. 427-435.

Tracy, R. J., and Frost, B. R. 1991. Phase equilibria and thermobarometry of calcareous, ultramafic and mafic rocks, and iron formations. In Kerrick, D. (ed.), Contact

Metamorphism. Review in Mineralogy 26, 43-104, Mineralogical Society of America, Washington, DC.

Vogel, D.C., James, R.S. and Keays, R.R., 1998. The early tectono-magmatic evolution of the Southern Province: implications from the Agnew intrusion, central Ontario, Canada; Canadian Journal of Earth Sciences, v.35, p. 854-8790.

Weaver, B.L. and Tarney, J., 1981. Lewisian Gneiss Geochemistry and Archean Crustal Development Models. Earth and Planetary Science Letters, v. 55(1), p. 171-180.

Wu, J., Milkereit, B., Boerner, D, 1995. Seismic Imaging of the enigmatic Sudbury structure. Journal of Geophysical Research, v. 100, p. 4117-4130.

Young, G.M., 2001. Comparative Geochemistry of Pleistocene and Paleoproterozoic (Huronian) Glaciogenic Laminated Deposits: Relevance to Crustal and Atmospheric Composition in the Last 2.3 Ga. The Journal of Geology, v. 109, p. 463-477.

Zack, T. and Brumm, R., 1998. Ilmenite/liquid partition coefficients of 26 trace elements determined through ilmenite/clinopyroxene partitioning in garnet pyroxene. In: 7th International Kimberlite Conference. Gurney, J.J., Gurney, J.L., Pascoe, M.D. and Richardson, S.H. (Editors), Red Roof Design, Cape Town, p. 986-988.

Zanetti, A., Tiepolo, M., Oberti, R. and Vannucci, R., 2004. Trace-element partitioning in olivine: modelling of a complete data set from a synthetic hydrous basanite melt. Lithos, v. 75, p. 39-54.

Zou, H.B., 1998. Trace element fractionation during modal and non-modal dynamic melting and open-system melting: A mathematical treatment. Geochimica et Cosmochimica Acta, v. 62, p. 1937-1945.

FIGURES AND TABLES

Table 3.1. Major (volatile free) and minor element ranges, averages, medians and standard deviations for samples belonging to each of the 4 metamorphic zones in the EMF.

	HHZ (n = 10)					PGZ (n = 18)					PHZ B (n = 12)					PHZ A (n = 16)				
Oxides (wt.%)	**min.**	**max.**	**average**	**median**	**S.D.**	**min.**	**max.**	**average**	**median**	**S.D.**	**min.**	**max.**	**average**	**median**	**S.D.**	**min.**	**max.**	**average**	**median**	**S.D.**
SiO2	46.26	53.81	49.45	48.40	2.77	43.00	53.67	47.85	47.71	2.83	43.96	48.46	46.36	46.72	1.32	43.50	48.45	46.23	46.34	1.49
TiO2	1.35	2.50	1.84	1.74	0.38	1.45	2.42	1.99	2.11	0.28	1.63	2.53	2.11	2.14	0.27	1.21	2.34	1.64	1.56	0.32
Al2O3	11.30	17.48	13.38	13.00	1.62	10.97	15.20	13.28	13.51	0.96	11.77	14.03	12.85	12.82	0.57	11.95	15.28	13.45	13.38	0.92
Fe2O3*	15.66	22.01	18.10	17.34	2.20	15.92	22.19	19.61	20.19	1.88	18.64	23.86	21.64	21.97	1.60	15.54	22.12	18.71	18.69	2.19
MnO	0.20	0.29	0.23	0.24	0.03	0.21	0.32	0.26	0.26	0.03	0.23	0.31	0.28	0.28	0.02	0.22	0.29	0.26	0.26	0.02
MgO	3.05	6.64	4.57	4.39	1.11	3.17	6.30	5.29	5.66	0.88	3.86	6.59	4.62	4.20	0.93	4.49	8.65	6.52	6.61	1.02
CaO	7.36	11.63	9.50	9.37	1.26	7.02	11.83	9.65	9.72	1.46	7.29	12.01	9.60	9.72	1.60	8.85	13.03	11.31	11.57	1.08
Na2O	1.11	2.28	1.81	1.99	0.43	0.36	2.27	0.97	0.72	0.61	0.86	3.56	1.89	1.75	0.74	0.89	2.64	1.51	1.35	0.45
K2O	0.36	1.62	0.87	0.78	0.37	0.10	2.17	0.85	0.63	0.63	0.19	0.65	0.36	0.29	0.16	0.08	0.30	0.17	0.17	0.07
P2O5	0.13	0.38	0.25	0.27	0.08	0.18	0.32	0.25	0.24	0.04	0.19	0.34	0.29	0.32	0.05	0.11	0.32	0.19	0.19	0.07
LOI	-0.10	0.78	0.37	0.35	0.24	-1.28	0.57	-0.28	-0.26	0.48	-0.80	-0.28	-0.52	-0.53	0.18	-0.78	0.27	-0.28	-0.26	0.32
Minor elements (ppm)																				
Ba (0.8)	107	506	310	322	131	92	1306	407	269	322	114	381	230	219	81	54	243	105	93	49
Be (0.04)	1.0	2.5	1.7	1.6	0.4	1.0	2.2	1.5	1.5	0.3	0.8	1.5	1.2	1.2	0.2	0.4	1.2	0.8	0.7	0.2
Bi (0.15)	<0.15	1.0	-	-	-	<0.15	1.0	-	-	-	<0.15	0.2	-	-	-	<0.15	-	-	-	-
Cd (0.013)	0.12	0.68	0.26	0.22	0.15	0.18	0.51	0.31	0.29	0.09	0.24	0.38	0.30	0.29	0.04	0.16	0.47	0.31	0.32	0.08
Ce (0.12)	37.3	113.6	80.3	79.2	19.8	53.6	110.0	75.9	72.4	14.4	29.9	51.3	40.9	40.3	5.6	10.9	48.2	23.5	22.0	9.6
Co (0.13)	48.5	69.2	56.2	55.7	5.9	44.1	79.9	62.6	63.8	8.0	54.2	69.9	63.2	64.6	4.6	55.2	78.7	65.9	66.9	5.8
Cr (3)	8	190	50	17	64	8	103	31	26	20	6	76	28	18	22	20	428	143	111	107
Cs (0.013)	0.17	2.48	0.92	0.86	0.67	0.19	2.21	1.04	0.77	0.70	0.17	2.05	0.76	0.46	0.62	0.09	0.41	0.23	0.23	0.08
Cu (1.4)	20	364	156	132	117	7	651	163	70	182	10	293	99	98	77	5	288	112	123	91
Dy (0.009)	6.47	11.95	9.95	10.46	1.67	7.41	11.44	9.23	9.21	1.27	5.87	9.36	7.70	7.51	1.05	4.45	8.38	5.76	5.48	1.11
Er (0.007)	4.04	7.25	6.16	6.52	1.00	4.92	6.82	5.77	5.81	0.63	3.57	5.71	4.71	4.60	0.61	2.75	5.18	3.56	3.38	0.66
Eu (0.0031)	1.55	2.88	2.42	2.58	0.42	1.91	2.66	2.40	2.47	0.23	1.67	2.51	2.17	2.19	0.26	1.09	2.16	1.49	1.37	0.31
Ga (0.04)	19.4	29.0	21.7	20.8	2.8	17.3	25.6	22.2	22.8	2.0	19.4	25.2	23.0	23.2	1.8	15.9	23.9	19.3	19.3	2.1
Gd (0.009)	5.90	11.22	9.29	9.63	1.67	6.52	10.37	8.46	8.48	1.18	5.45	8.47	7.20	7.06	0.97	3.72	7.60	5.12	4.86	1.12
Hf (0.14)	3.7	8.6	7.1	7.5	1.4	5.4	9.9	8.3	8.4	1.1	3.0	6.7	5.0	5.1	0.9	1.0	3.7	1.7	1.4	0.7
Ho (0.0025)	1.36	2.46	2.08	2.21	0.35	1.60	2.35	1.94	1.93	0.25	1.21	1.96	1.60	1.56	0.22	0.95	1.76	1.21	1.15	0.23
In (0.0018)	0.09	0.17	0.13	0.13	0.02	0.10	0.17	0.13	0.14	0.02	0.12	0.15	0.13	0.13	0.01	0.09	0.14	0.11	0.11	0.01
La (0.04)	16.4	58.4	40.2	37.9	11.2	25.0	56.8	38.0	37.2	8.6	12.8	23.4	17.8	17.8	2.7	4.5	19.3	9.7	9.2	4.0
Li (0.4)	9	25	15	14	5	3	21	9	7	5	4	13	8	6	3	2	23	8	6	5
Lu (0.002)	0.57	1.05	0.89	0.93	0.14	0.71	0.97	0.87	0.89	0.07	0.52	0.80	0.69	0.68	0.08	0.40	0.71	0.51	0.48	0.09
Mo (0.08)	0.5	2.8	1.1	0.7	0.8	0.3	3.8	0.9	0.6	0.8	0.3	2.3	0.8	0.6	0.6	0.3	0.9	0.5	0.5	0.2
Nb (0.028)	8.06	20.61	14.88	14.74	3.32	11.68	27.93	18.10	17.76	3.21	7.23	12.74	9.85	9.54	1.96	2.99	8.91	5.89	5.63	1.77
Nd (0.06)	20.9	49.1	39.0	39.5	8.2	27.8	45.9	35.8	36.1	4.8	18.8	30.5	25.2	25.2	3.5	8.3	28.5	15.5	14.5	5.2
Ni (1.6)	11	112	44	36	34	19	65	42	42	12	25	67	39	32	15	33	167	86	80	36
Pb (0.6)	8	29	14	13	6	6	42	14	13	8	4	19	8	7	4	4	16	8	7	4
Pr (0.014)	4.89	12.89	9.66	9.70	2.20	6.64	12.13	8.93	8.52	1.42	4.11	6.95	5.57	5.60	0.76	1.63	6.58	3.32	3.12	1.25
Rb (0.23)	6.2	51.2	22.8	22.1	15.8	2.8	73.4	27.9	21.3	21.7	2.7	19.5	9.3	7.1	5.8	1.1	7.6	3.2	2.6	1.8
Sb (0.04)	0.3	0.8	0.5	0.5	0.2	0.0	0.8	0.3	0.2	0.2	0.1	0.6	0.2	0.1	0.1	0.0	0.5	0.2	0.1	0.1
Sc (1.1)	35	51	40	39	5	35	52	44	45	4	44	55	50	51	3	46	60	54	54	4
Sm (0.012)	5.20	10.78	8.83	9.21	1.70	6.20	9.61	8.04	8.24	1.04	4.81	7.82	6.47	6.39	0.91	2.76	7.10	4.33	4.09	1.19
Sn (0.16)	1.5	4.1	2.6	2.5	0.9	1.0	2.7	1.8	1.8	0.5	0.7	1.5	1.1	1.1	0.2	0.2	1.5	0.6	0.6	0.3
Sr (0.6)	139	200	157	151	18	110	284	178	170	46	155	365	231	223	51	146	340	188	179	45
Ta (0.023)	0.49	1.32	0.95	0.93	0.23	0.73	1.57	1.11	1.12	0.20	0.39	0.73	0.55	0.52	0.11	0.16	0.50	0.33	0.34	0.10
Tb (0.0023)	0.97	1.81	1.53	1.60	0.27	1.09	1.74	1.40	1.39	0.20	0.89	1.43	1.18	1.15	0.17	0.66	1.30	0.87	0.82	0.18
Th (0.018)	2.03	14.90	7.60	7.94	3.95	1.91	11.07	7.06	6.92	2.37	0.46	2.31	1.29	1.33	0.60	0.15	0.82	0.45	0.40	0.21
Ti (7)	7945	14900	10735	10585	2155	8022	14629	12110	12089	1837	9702	15168	12912	13399	1653	6951	14862	9923	9771	2070
Tl (0.005)	0.05	0.36	0.15	0.14	0.10	0.02	0.38	0.16	0.14	0.11	0.02	0.16	0.08	0.07	0.05	0.02	0.17	0.04	0.04	0.04
Tm (0.0019)	0.584	1.066	0.900	0.944	0.146	0.717	0.995	0.857	0.870	0.084	0.522	0.818	0.684	0.671	0.083	0.403	0.759	0.517	0.490	0.095
U (0.011)	0.56	3.84	1.76	1.67	1.00	0.57	2.18	1.25	1.23	0.47	0.21	0.73	0.45	0.42	0.17	0.06	0.26	0.15	0.15	0.06

*Total iron expressed as Fe2O3; HHZ = hornblende hornfels zone; PGZ = pyroxene granofels zone; PHZ = pyroxene hornfels zone; LOI = loss on ignition; detection limit for minor elements are provided in the brackets.

Table 3.1. Major (volatile free) and minor element ranges, averages, medians and standard deviations for samples belonging to each of the 4 metamorphic zones in the EMF *(cont.)*.

	HHZ (n = 10)					PGZ (n = 18)					PHZ B (n = 12)					PHZ A (n = 16)				
(ppm)	**min.**	**max.**	**average**	**median**	**S.D.**	**min.**	**max.**	**average**	**median**	**S.D.**	**min.**	**max.**	**average**	**median**	**S.D.**	**min.**	**max.**	**average**	**median**	**S.D.**
V (0.8)	118	>370	-	-	-	>370	>370	-	-	-	>370	>370	-	-	-	119	>370	-	-	-
W (0.05)	0.2	0.5	0.4	0.4	0.1	0.1	0.6	0.2	0.2	0.1	0.1	0.2	0.1	0.1	0.0	0.1	0.2	0.1	0.1	0.0
Y (0.05)	35.5	64.5	54.4	57.3	9.0	39.3	61.0	50.1	49.7	6.3	31.9	49.1	41.1	40.6	4.9	24.6	46.3	31.6	30.3	5.9
Yb (0.009)	3.87	7.05	5.90	6.15	0.95	4.68	6.44	5.71	5.84	0.49	3.44	5.35	4.50	4.44	0.52	2.66	4.84	3.38	3.20	0.60
Zn (7)	118	211	150	137	30	142	213	180	186	20	172	241	203	207	18	119	209	169	172	25
Zr (6)	143	353	290	305	59	226	402	344	347	44	127	278	201	202	37	33	141	62	49	30
Significant element ratios																				
Zr/Hf	38.7	42.7	40.6	40.2	1.3	39.0	43.2	41.4	41.6	1.0	38.8	42.2	40.6	40.7	1.0	29.7	38.7	34.8	35.1	2.7
Nb/Ta	13.1	18.0	15.8	15.7	1.2	12.4	20.3	16.4	16.2	1.8	14.7	22.5	18.1	17.7	2.3	14.4	23.2	17.8	16.9	2.4
Th/U	3.3	5.6	4.4	4.4	0.8	3.3	10.2	6.0	5.6	2.0	1.4	3.8	2.8	3.0	0.6	1.7	3.5	2.9	2.9	0.5
Nb/Th	1.4	5.8	2.7	1.9	1.6	1.5	6.1	2.9	2.7	1.1	3.5	25.3	9.9	8.3	5.9	6.0	29.2	15.6	14.4	7.0
Ta/W	1.6	4.2	2.5	2.4	0.7	2.0	16.9	6.6	5.2	3.6	2.6	7.8	4.8	4.3	1.5	1.6	4.1	2.7	2.7	0.8
W/Th	0.04	0.18	0.07	0.05	0.05	0.01	0.08	0.03	0.03	0.02	0.07	0.19	0.11	0.09	0.04	0.14	1.08	0.36	0.30	1.08
[La/Sm]cn	1.97	3.63	2.82	2.70	0.52	1.86	4.11	2.97	3.01	0.60	1.31	2.00	1.72	1.76	0.18	1.02	2.30	1.37	1.32	0.32
[La/Yb]cn	2.89	5.62	4.56	4.67	0.85	3.12	6.56	4.52	4.36	0.92	2.11	3.05	2.68	2.73	0.23	1.15	3.08	1.90	1.91	0.54
[Gd/Lu]cn	1.15	1.44	1.29	1.29	0.09	0.91	1.39	1.20	1.23	0.12	1.12	1.39	1.30	1.30	0.07	1.11	1.38	1.24	1.24	0.08
Zr/Nb	15.0	23.1	19.6	19.9	2.0	14.3	23.9	19.3	19.3	2.6	15.4	26.1	20.8	20.9	3.4	5.4	17.3	10.5	9.9	3.3
Zr/Zr*	0.87	1.33	1.01	0.98	0.14	0.99	1.80	1.31	1.23	0.20	0.87	1.37	1.03	0.99	0.15	0.25	0.67	0.49	0.49	0.11

*Total iron expressed as Fe2O3; HHZ = hornblende hornfels zone; PGZ = pyroxene granofels zone; PHZ = pyroxene hornfels zone; LOI = loss on ignition; detection limit for minor elements are provided in the brackets.

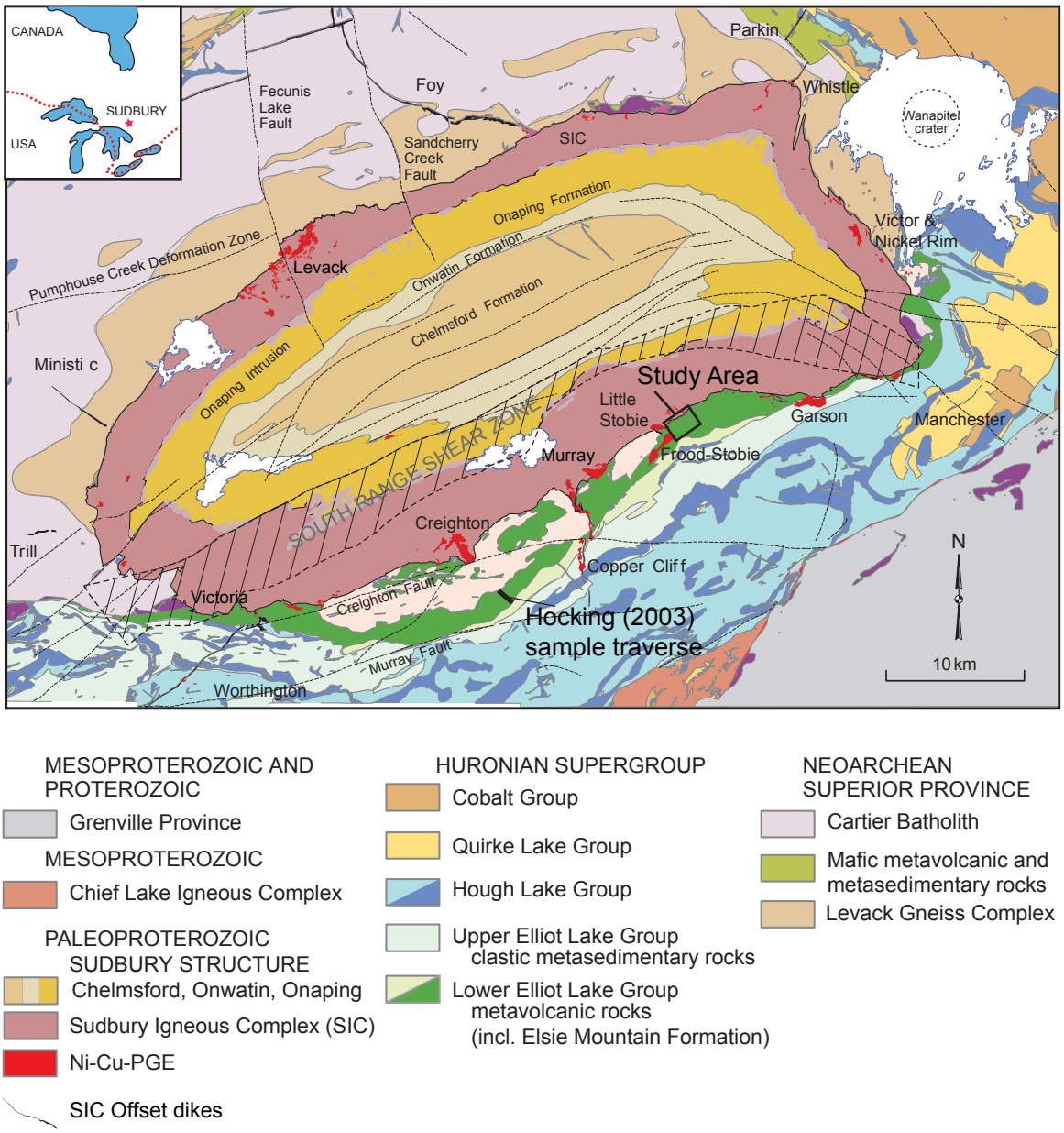

Fig. 3.1. Geology of the Sudbury area (after Ames et al., 2005).

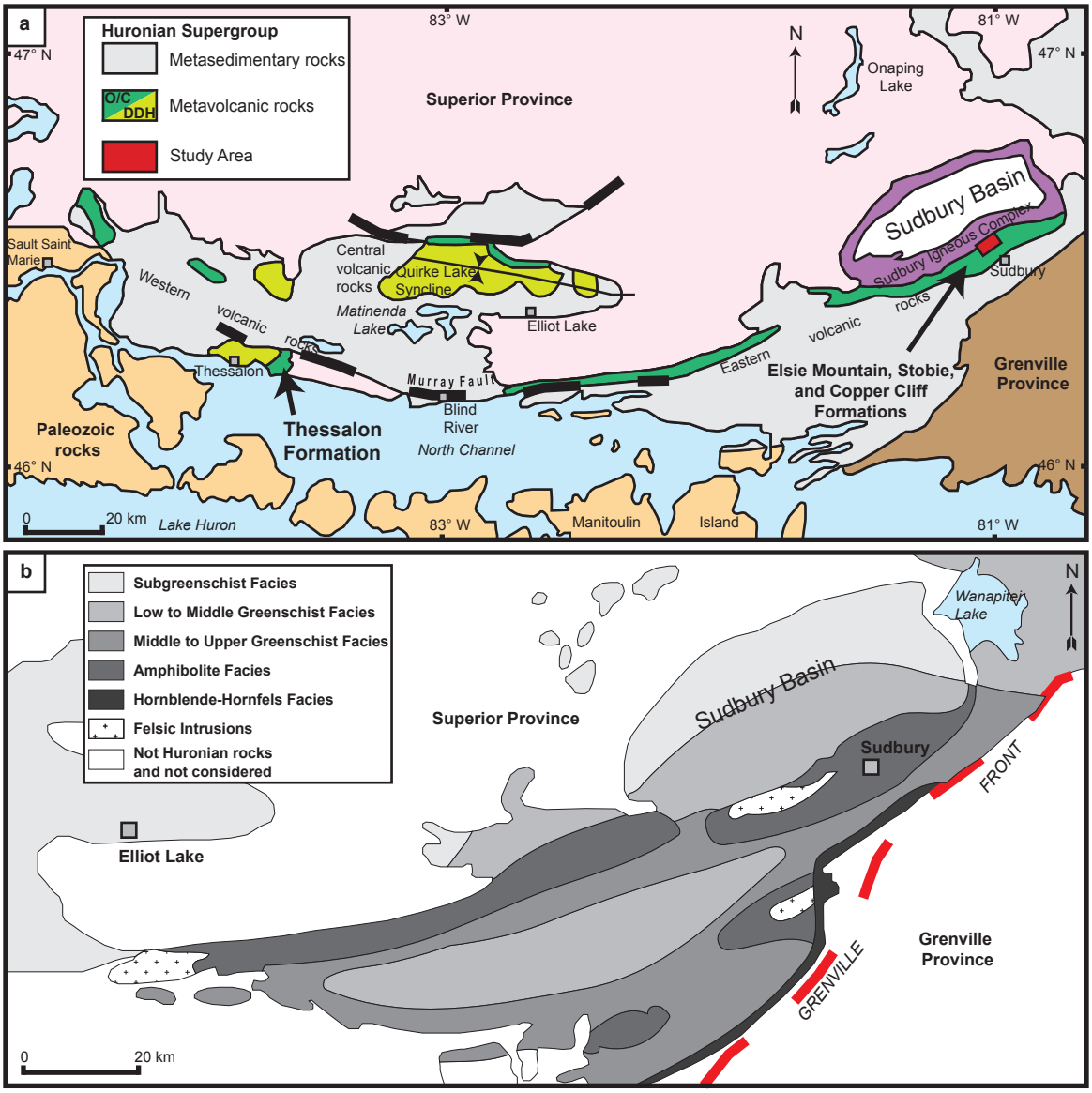

Fig. 3.2. Regional geological setting. a) Distribution of the Huronian metavolcanics from Sault Saint Marie in the west to Sudbury in the east, and the Sudbury Structure straddling the boundary between the Superior Province and the Huronian Supergroup that is part of the Southern Province (after Card, 1978b; Bennett et al., 1991; Rousell et al., 2009). b) Regional metamorphic map showing the distribution of metamorphic facies from the Grenville Front and northwest to the Sudbury Structure (after Card, 1978b).

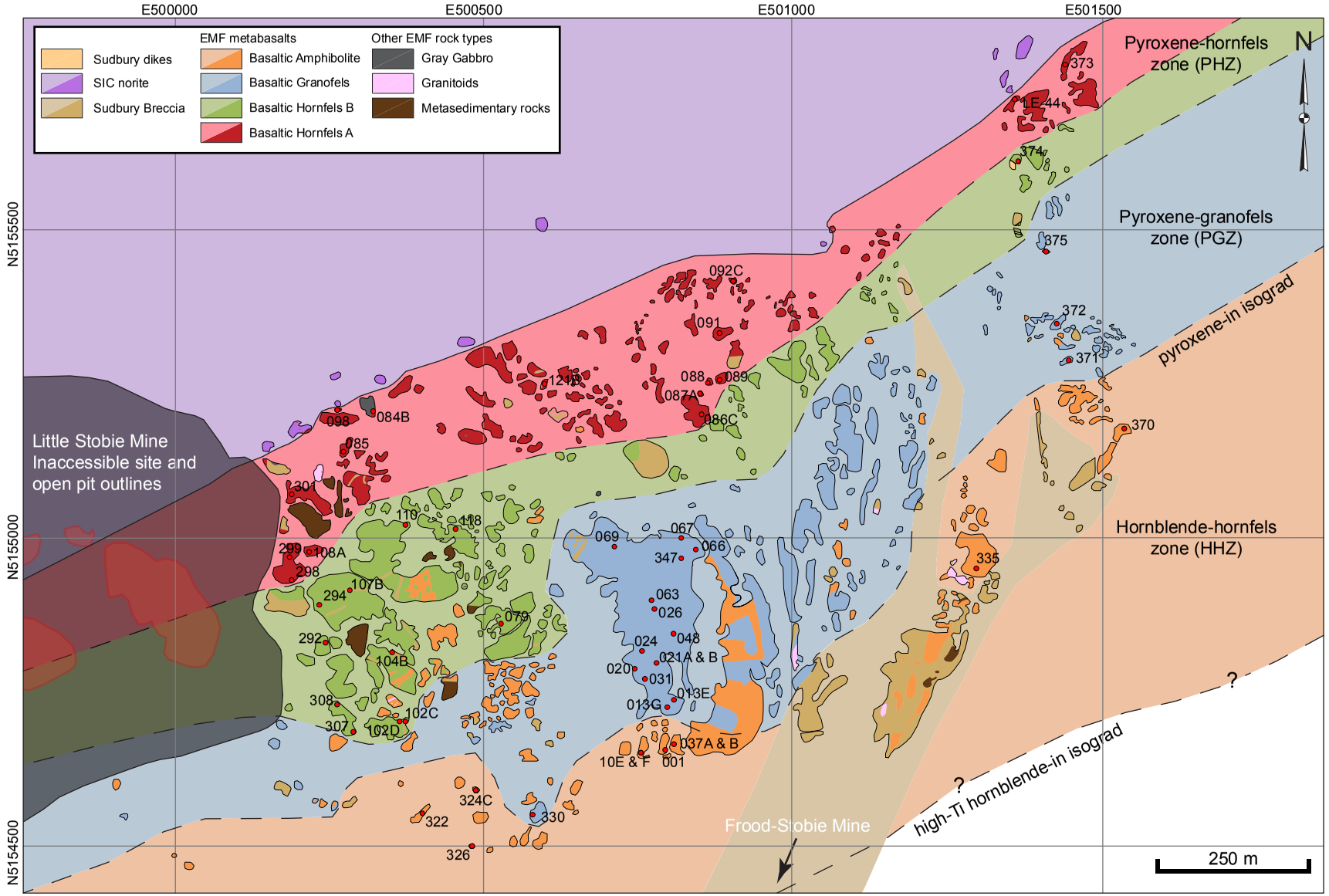
E500000
E500500
E501000
E501500
N5155500
N5155000
N5154500
EMF metabasalts
Basaltic Amphibolite
Basaltic Granofels
Basaltic Hornfels B
Basaltic Hornfels A
Other EMF rock types
Gray Gabbro
Granitoids
Metasedimentary rocks
Sudbury dikes
SIC norite
Sudbury Breccia
Little Stobie Mine
Inaccessible site and
open pit outlines
Pyroxene-hornfels
zone (PHZ)
Pyroxene-granofels
zone (PGZ)
Hornblende-hornfels
zone (HHZ)
pyroxene-in isograd
high-Ti hornblende-in isograd
Frood-Stobie Mine
N
250 m
373
1E-44
374
375
372
371
370
335
092C
091
088
089
087A
086C
084B
085
301
299
298
108A
107B
294
292
104B
308
307
102C
102D
324C
322
326
330
10E & F
001
037A & B
013G
013E
031
020
024
048
021A & B
063
026
067
066
347
069
079
118
119

Fig. 3.3. *(from previous page)* The map is showing sample locations, the metamorphic zones described in Jørgensen et al. (Chapter 2), and the metabasalt units for this study. Moving south-east from the SIC contact the metabasalt samples belong to: 1) the PHZ A unit (red) and PHZ B unit (green) within the PHZ, 2) the PGZ unit (blue) within the PGZ, and 3) the HHZ (orange) unit within the HHZ. The distinction between the PHZ units is defined by their geochemistry (e.g., see Results and Discussion sections).

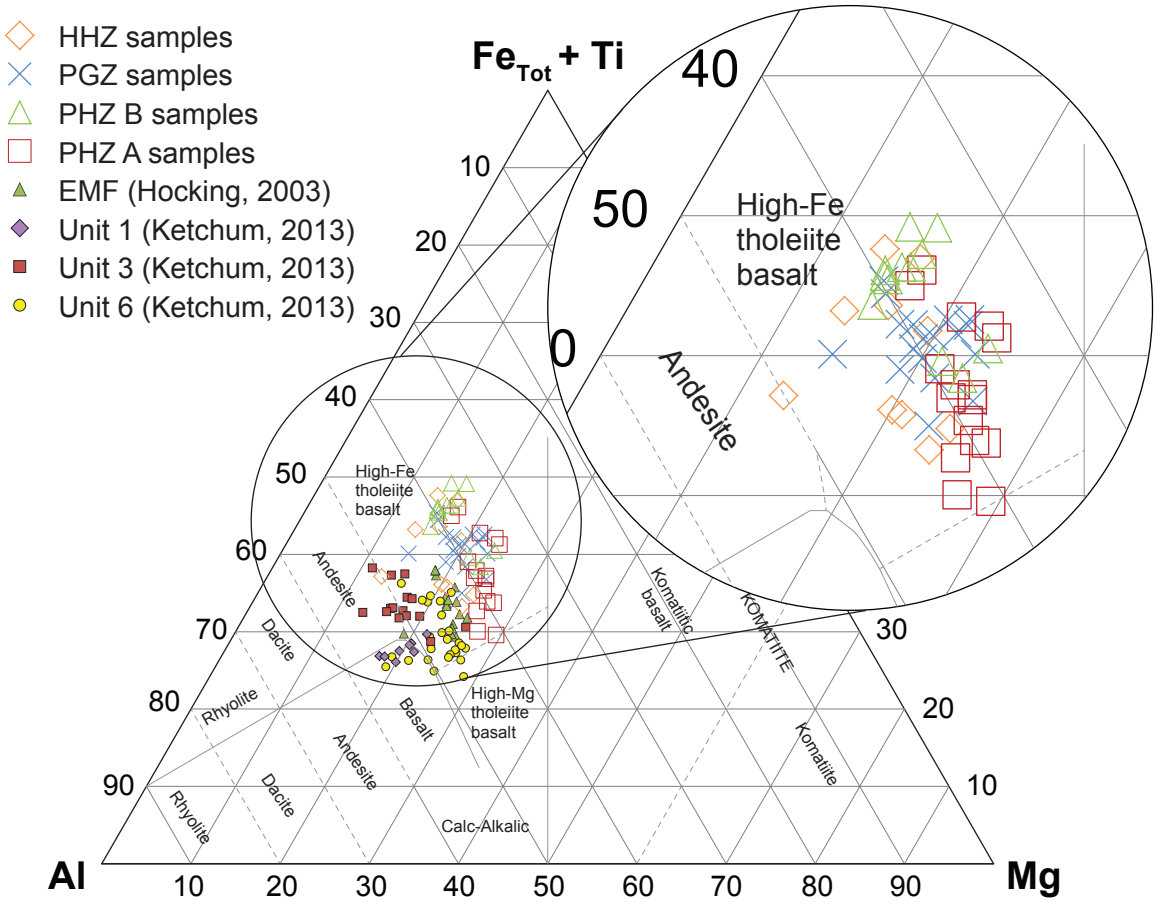

Fig. 3.4. Classification of the Elsie Mountain Formation metabasalts on a Fe_{Total} + Ti-Mg-Al plot (Jensen, 1967).

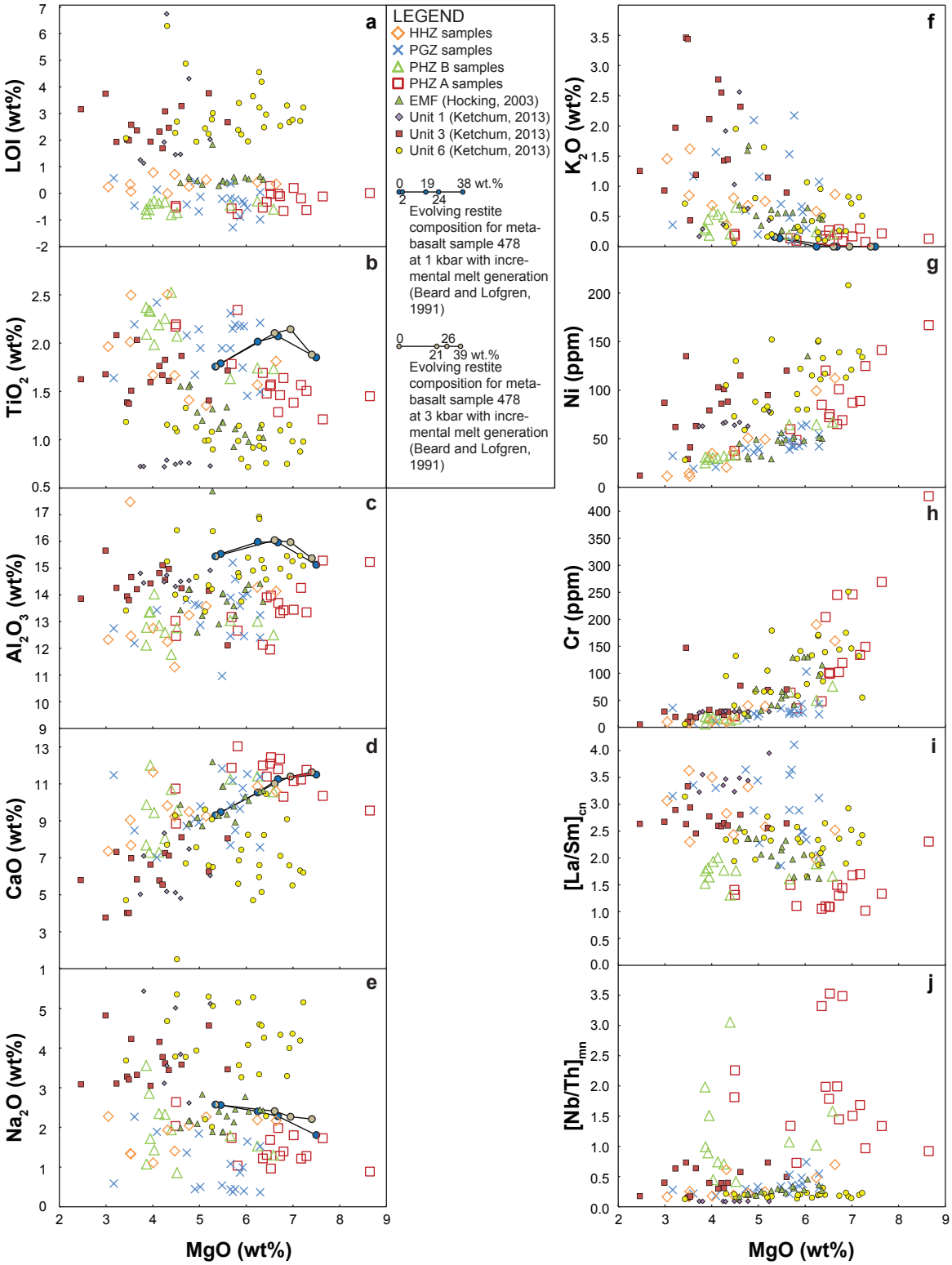

Fig. 3.5. Select MgO bivariate plots for the Elsie Mountain Formation and Thessalon metabasalts: a) LOI (wt.%) b) TiO_2 (wt.%); c) Al_2O_3 (wt.%); d) CaO (wt.%); e) Na_2O (wt.%); f) K_2O wt.%; g) Ni (ppm); h) Cr (ppm); i) $[La/Sm]_{cn}$; and j) $[Nb/Th]_{mn}$. The major element plots also show trends for restite compositions at increasing melt increments at 1and 3 kbar for dehydration melting experiments on MORB-like starting material (Beard and Lofgren, 1991).

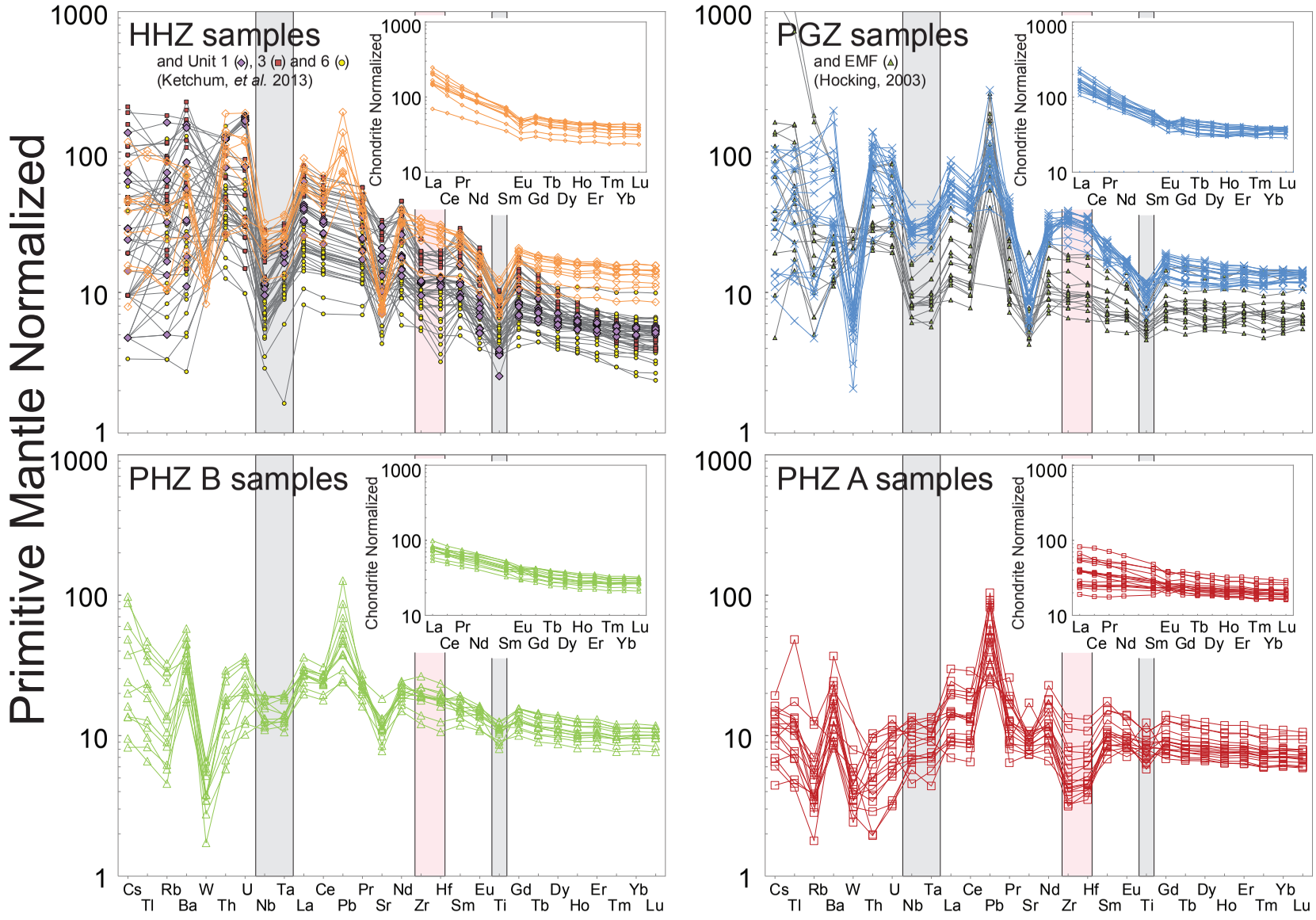
Primitive Mantle Normalized
HHZ samples
and Unit 1 (◇), 3 (□) and 6 (○)
(Ketchum, et al. 2013)
PGZ samples
and EMF (△)
(Hocking, 2003)
PHZ B samples
PHZ A samples
Chondrite Normalized
1000
100
10
1
Cs Rb W U Ta Ce Pr Nd Hf Eu Gd Dy Er Yb
Tl Ba Th Nb La Pb Sr Zr Sm Ti Tb Ho Tm Lu
La Pr Eu Tb Ho Tm Lu
Ce Nd Sm Gd Dy Er Yb

Fig. 3.6. *(from previous page)* Extended trace element plots (normalized to primitive mantle, using McDonough and Sun, 1995) for all units, with insets of chondrite normalized REE plots. The order of elements reflects their compatibility during mantle melting from the most to least incompatible starting from the left. The grey vertical bands highlights Nb-Ta-Ti anomalies characteristic of arc magmatism. The pink vertical bands highlight Zr-Hf that show strong negative anomalies in the PHZ A unit.

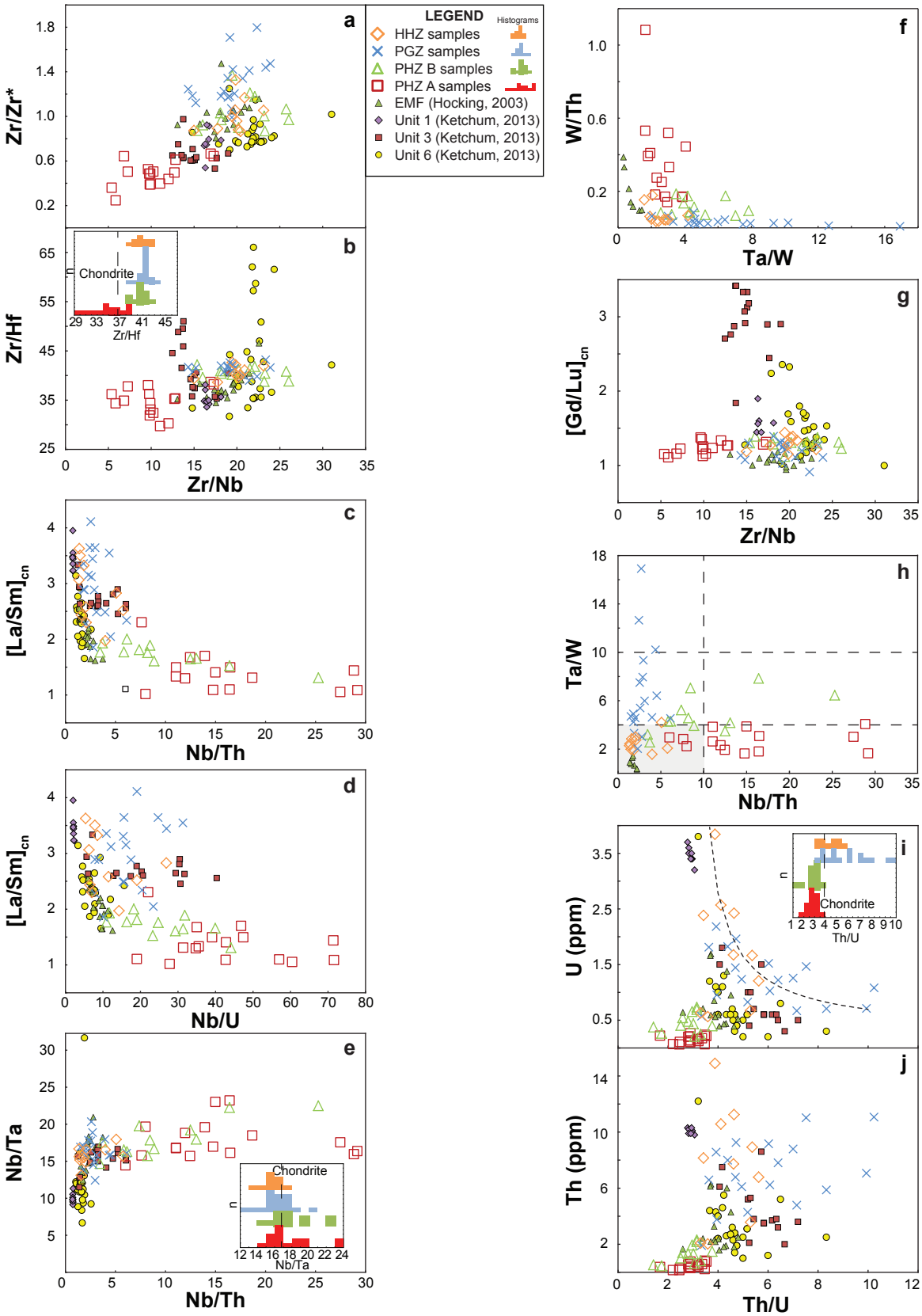

Fig. 3.7. Bivariate plots of trace element ratios. a) and b) are showing Zr/Zr* and Zr/Hf against Zr/Nb that works well to discriminate the PHZ A unit; c) and d) $[La/Sm]_{cn}$ versus Nb/Th and Nb/U

Fig. 3.7. *(cont.)* illustrating the Th and LREE mobility in the PHZ A unit and the U > Th mobility in general; e) Nb/Ta against Nb/Th showing that the PHZ units plots at the highest value for both ratios; f) W/Th versus Ta/W showing the HHZ unit plotting as a fairly tight cluster near the origin, whereas the other units show evidence for W and/or Th mobility; g) [Gd/Lu]cn versus Zr/Nb showing a broad overlap for all samples in the $[Gd/Lu]_{cn}$ ratio, whereas the PHZ A unit is mostly plotting at lower Zr/Nb values. h) Ta/W against Nb/Th that are two ratios sensitive to crustal contamination. The horizontal stippled lines indicate modern Ta/W N-MORB values from 4-10 (Babechuk and Kamber, 2011). The vertical stippled line at Nb/Th = 10 is the minimum conservative ratio used by Stern et al., (1995) and Babechuk and Kamber (2011) to separate subduction zone contaminated ocean floor basalts. The HHZ and PGZ units dominantly fall within the shaded area where both proxies suggest crustal input. In contrast, the PGZ and PHZ A units each form separate trends towards higher Ta/W and higher Nb/Th, respectively, and the PHZ B unit appears to be transitional; i) and j) U and Th versus Th/U illustrating the U control on the Th/U ratio in the HHZ and PGZ units. Primitive mantle and chondrite normalization data are from McDonough and Sun (1995). Note the histogram insets in b) Zr/Hf, e) Nb/Ta, and i) Th/U ratios highlighting the fractionation of these elements. The PHZ A unit shows the most extreme values for Zr/Hf and Nb/Ta ratios, whereas the HHZ unit only shows a narrow range. The HHZ and PGZ units show the most divers and highest Th/U ratios, whereas the PHZ units show a fairly narrow range with a tendency towards lower values.

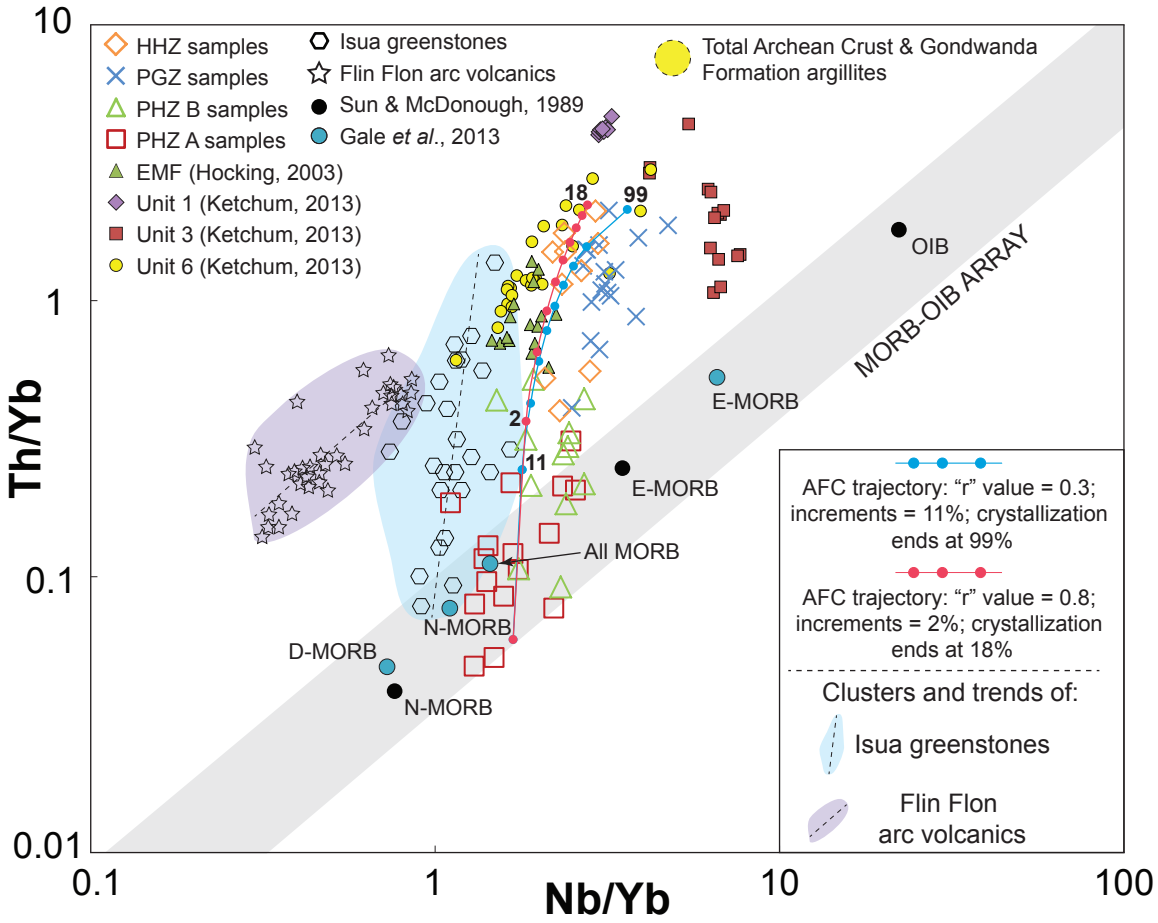

Fig. 3.8. Th/Yb versus Nb/Yb plot (Pearce and Peate, 1995; Pearce 2008) commonly employed to examining crustal contaminated or subduction zone modified volcanics with samples plotting above the MORB-OIB array as a result of Th enrichment relative to Nb. The Flin Flon arc volcanic suite of DeWolfe et al. (2009) plot in an array sub-parallel to the MORB-OIB array, whereas Isua greenstones (Pearce, 2008) experienced Th enrichment during metamorphism forms a steep trend away from the MORB-OIB array and towards Archaen crust. Assimilation-fractional crystallization processes (AFC) with a contaminant similar to, e.g., Total Archean Crust (TAC; Rudnick and Fountain, 1995) might also result in samples plotting above the MORB-OIB array. The diagram illustrates two AFC models with similar starting material (an average of the PHZ A samples with the lowest Nb/Th: FSTJ084B, FSTJ091, and FSTJ108A) and contaminant (Gowganda Formation argillites of the Huronian Supergroup as a proxy for Archean Crust; Young, 2001), but different model parameters. The "r" value represents the ratio of the rate of assimilation to the rate of fractional crystallization, and each increment reflects the percentage of crystallization that has transpired. Note that although both the Isua and AFC trends appear to fit well with the trend formed by the EMF volcanics the latter formed by Th mobility during SIC contact metamorphism.

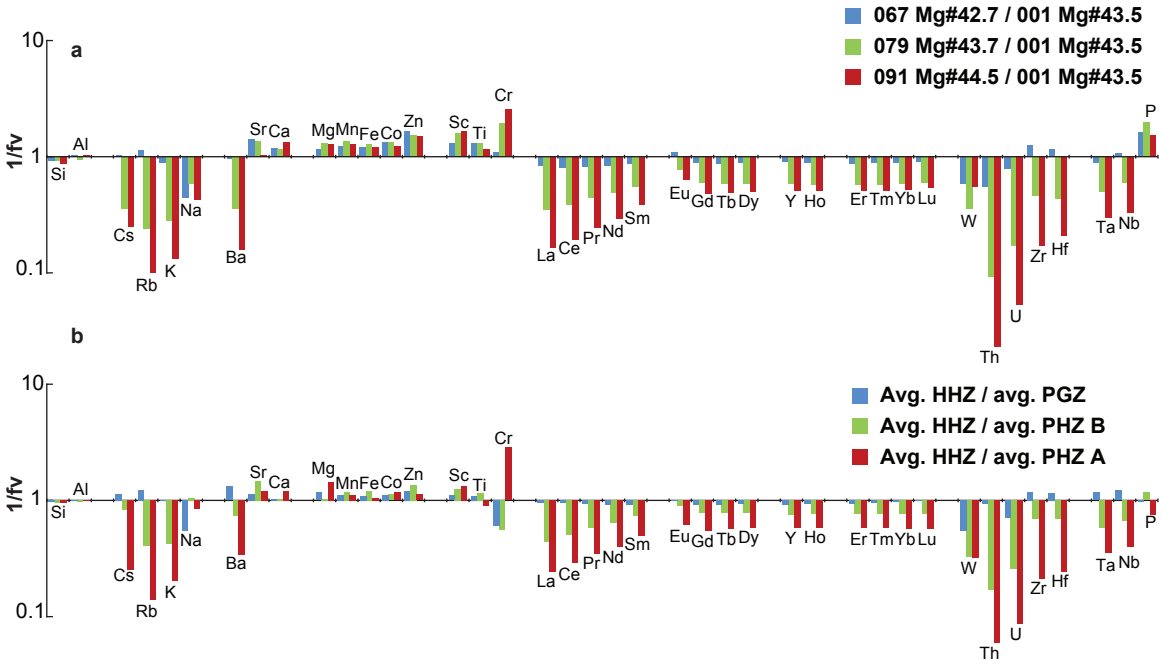

Fig. 3.9. Diagrams showing calculated enrichment/depletion of elements in a) high grade metamorphic (altered) rocks from the PGZ, PHZ B and PHZ A units relative to a lower metamorphic (least altered) from the HHZ unit all with similar Mg#, and b) the same diagram but using averages of the various units instead. The relative enrichment/depletion, 1/fv, represents the density weighted ratio of the abundances of the components in the inferred protolith and higher grade metamorphic rocks (Eqn. (3) in text). Note that the actual degree of enrichment/depletion depends on the true value of fv and that primary processes appears to have some influence on the results even when samples of similar Mg# are used.

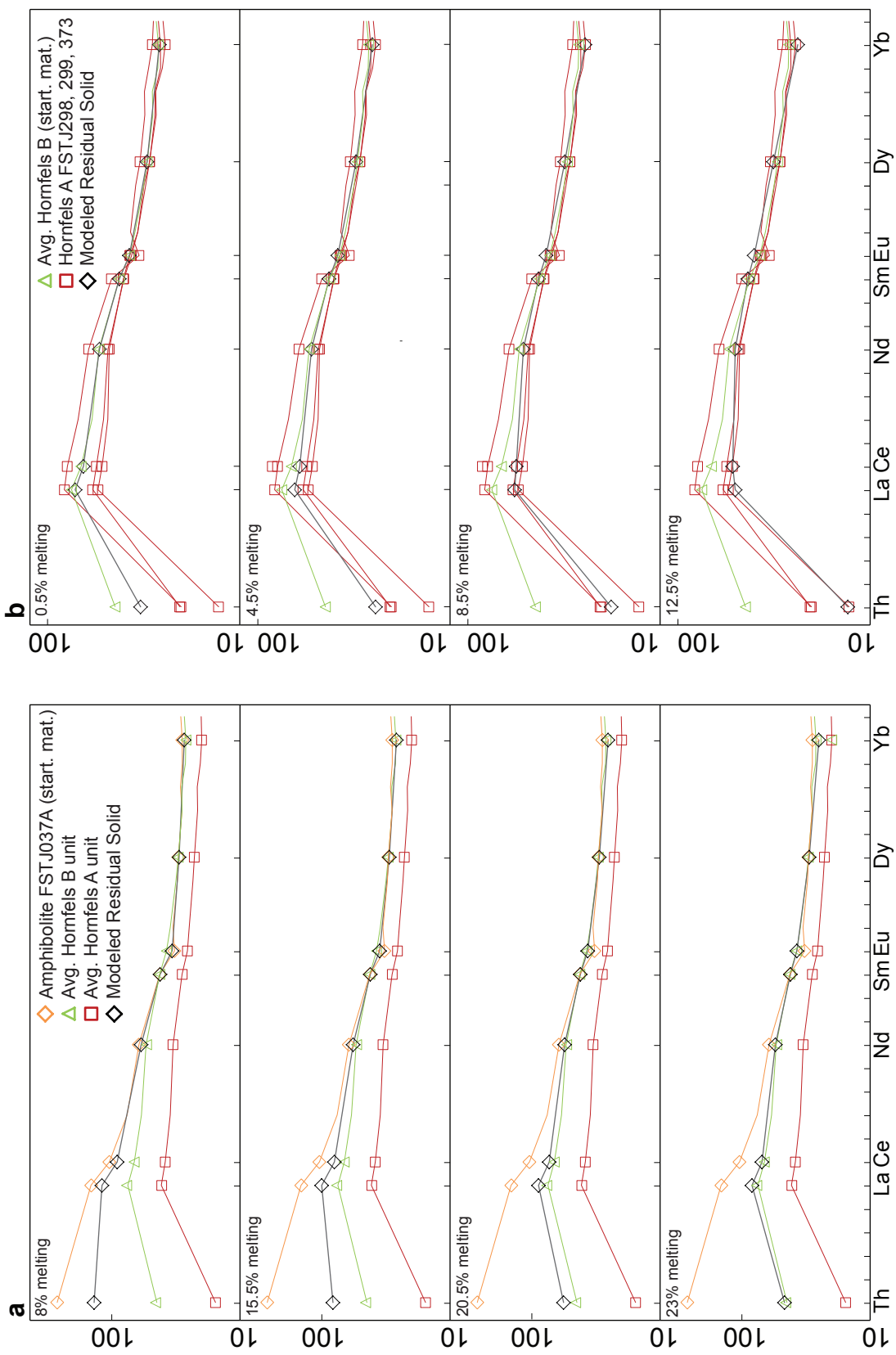
Chondrite Normalized
a
8% melting
15.5% melting
20.5% melting
23% melting
Amphibolite FST.J037A (start. mat.)
Avg. Hornfels B unit
Avg. Hornfels A unit
Modeled Residual Solid
b
0.5% melting
4.5% melting
8.5% melting
12.5% melting
Avg. Hornfels B (start. mat.)
Hornfels A FST.J298, 299, 373
Modeled Residual Solid
100
10
Th
La
Ce
Nd
Sm
Eu
Dy
Yb

Fig. 3.10. *(from previous page)* Models of two melt-forming reactions. In a) the starting material is the average HHZ unit and the melt forming reactions corresponds to the first reaction encountered in experiments by Beard and Lofgren (1991; see text). After approximately 23% melting the modelled residual solid corresponds to the pattern exhibited by the average PHZ B unit. In b), the starting material is the average PHZ B unit and it is plotted together with examples of relatively Th and LREE depleted PHZ A samples (FSTJ298, 299, and 373). Continued melting of the average PHZ B unit by the second melting reaction encountered in the Beard and Lofgren (1991; see Section 6.3.3) eventually results in a modelled Th-LREE pattern for the residual solid that is very close to the more depleted trends observed among the PHZ A unit samples after an additional ~12.5% melting. Collectively, the modelling predicts up to 35.5% melting. These predictions are fairly close to experiments by Beard and Lofgren (1991) where around 20% melt is produced at 900-925 °C and just above 35% melt is produced at 1000 °C. Chondrite normalization data is from Sun and McDonough (1989).

SUPPORTING INFORMATION

HIGH FIELD-STRENGTH ELEMENT MOBILITY AND FORMATION OF METAMORPHIC CHEMOSTRATIGRAPHY: AN EXAMPLE FROM IMPACT MELT SHEET INDUCED CONTACT METAMORPHISM AND ANATEXIS OF BASALTS, SUDBURY, CANADA

T.R.C. Jørgensen, D.K. Tinkham, and C.M. Lesher

Table S3.1. Whole-rock major element (wt%) and trace element (ppm) data for Elsie Mountain Formation metavolcanics.

ID	FSTJ001	FSTJ010E	FSTJ010F	FSTJ037A	FSTJ037B	FSTJ322	FSTJ324C	FSTJ326
Metamorphic zone	HHZ	HHZ	HHZ	HHZ	HHZ	HHZ	HHZ	HHZ
Rock type	Amphibolite	Amphibolite	Amphibolite	Amphibolite	Amphibolite	Amphibolite	Amphibolite	Amphibolite
XRF Lab (batch)	Geo Labs (1)	Geo Labs (1)	Geo Labs (1)	Geo Labs (1)	Geo Labs (1)	UWO (2)	UWO (2)	UWO (2)
ICP-MS lab (batch)	Geo Labs (1)	Geo Labs (1)	Geo Labs (1)	Geo Labs (1)	Geo Labs (1)	Geo Labs (2)	Geo Labs (2)	Geo Labs (2)
Easting	500790	500751	500751	500805	500805	500397	500492	500475
Northing	5154660	5154645	5154645	5154666	5154666	5154554	5154590	5154499
n	1	1	1	1	1	1	1	1
notes					SUBX			
SiO2	51.00	52.82	47.41	52.35	46.47	48.32	45.91	46.20
TiO2	1.35	1.65	1.66	1.41	1.82	2.48	1.97	2.50
Al2O3	13.54	11.20	12.69	13.25	14.20	12.38	17.09	12.23
Fe2O3*	16.13	17.22	19.79	15.67	17.08	21.47	17.87	21.98
MnO	0.22	0.24	0.29	0.22	0.23	0.25	0.25	0.25
MgO	5.13	4.43	3.99	4.78	6.67	3.51	3.44	4.31
CaO	9.23	9.16	11.58	9.50	10.64	7.63	8.84	9.80
Na2O	2.26	1.39	1.10	2.05	2.18	1.32	1.31	1.93
K2O	0.75	0.80	0.68	0.68	0.87	1.61	0.83	0.36
P2O5	0.13	0.21	0.34	0.16	0.30	0.38	0.27	0.30
LOI	0.51	0.71	0.78	0.26	0.35	0.07	0.34	-0.01
Ba	337.3	313.8	129.5	327.8	452.1	443.6	163.7	315.5
Be	1.45	1.61	1.65	1.54	1.21	1.95	2.54	1.85
Bi	<0.15	<0.15	0.16	<0.15	<0.15	0.40	0.98	0.18
Cd	0.146	0.225	0.123	0.222	0.201	0.320	0.235	0.680
Ce	76.97	81.38	89.03	63.85	76.79	72.81	113.55	90.02
Co	48.54	54.58	56.86	49.44	57.15	63.21	54.18	69.18
Cr	39	20	11	40	160	13	8	10
Cs	0.795	0.921	0.166	0.969	0.941	2.476	0.557	0.326
Cu	50.1	19.8	179.1	84.8	85.7	364.3	31.2	331.2
Dy	10.095	11.950	9.541	7.687	9.160	11.181	10.825	11.558
Er	6.250	7.254	6.054	4.822	5.579	6.785	6.980	6.989
Eu	2.143	2.486	2.365	1.881	2.883	2.726	2.696	2.833
Ga	20.19	19.37	21.95	19.71	19.46	23.03	29.01	22.96
Gd	9.196	10.836	8.905	6.854	8.785	10.568	10.070	11.223
Hf	6.90	8.24	7.20	6.71	6.10	8.59	7.85	8.25
Ho	2.099	2.456	2.007	1.602	1.901	2.312	2.326	2.411
In	0.115	0.144	0.138	0.106	0.166	0.137	0.132	0.144
La	36.39	39.38	47.24	34.43	34.25	35.38	58.36	48.83
Li	13.6	14.9	14.8	11.1	13.4	24.7	24.7	9.6
Lu	0.874	1.049	0.905	0.736	0.783	0.977	1.048	0.963
Mo	0.46	0.81	0.45	1.04	2.82	2.13	0.54	0.65
Nb	13.810	16.770	13.067	14.264	12.007	16.897	20.610	18.096
Nd	38.58	41.11	39.16	28.67	38.20	39.74	49.13	47.18
Ni	49.3	36.5	34.9	50.7	112.3	11.3	14.5	20.5
Pb	10.9	10.5	8.9	15.6	10.6	20.6	14.8	28.8
Pr	9.360	9.937	10.073	7.222	9.468	9.272	12.890	11.502
Rb	20.78	24.26	6.24	24.30	23.43	51.00	14.32	6.20
Sb	0.54	0.55	0.74	0.55	0.30	0.47	0.41	0.77
Sc	34.6	41.7	38.6	36.3	37.7	42.3	38.6	50.5
Sm	8.807	10.093	8.420	6.469	8.489	9.607	10.046	10.780
Sn	1.99	4.06	3.77	1.70	2.68	2.41	2.91	1.54
Sr	143.4	140.8	139.2	150.5	147.9	175.3	200.1	161.7
Ta	0.931	1.279	0.862	0.920	0.766	1.019	1.319	1.008
Tb	1.5330	1.8130	1.4460	1.1520	1.4150	1.7516	1.6596	1.8092
Th	6.785	10.574	8.924	7.730	2.081	8.149	14.899	3.566
Ti	7945	10539	10092	8446	10951	14177	10858	14900
Tl	0.138	0.156	0.047	0.137	0.170	0.318	0.096	0.051
Tm	0.9080	1.0660	0.8960	0.7190	0.8120	0.9881	1.0486	0.9981
U	1.206	2.570	1.663	1.674	0.630	2.384	3.842	0.673
V	>370	>370	>370	>370	349.4	283.7	350.2	>370
W	0.31	0.45	0.43	0.48	0.37	0.37	0.54	0.24
Y	54.81	64.50	54.36	42.36	48.59	59.80	61.78	62.14
Yb	5.913	7.011	5.955	4.793	5.219	6.352	7.049	6.417
Zn	118	138	131	131	135	211	152	204
Zr	276	332	302	283	245	353	309	352

*total iron expressed as Fe2O3

Table S3.1. Whole-rock major element (wt%) and trace element (ppm) data for Elsie Mountain Formation metavolcanics *(cont.)* .

ID	FSTJ335	FSTJ370	FSTJ013E	FSTJ021B	FSTJ013G	FSTJ020	FSTJ021A
Metamorphic zone	HHZ	HHZ	PGZ	PGZ	PGZ	PGZ	PGZ
Rock type	Amphibolite	Amphibolite	Amphibolite	Amphibolite	Pyroxene granofels	Pyroxene granofels	Pyroxene granofels
XRF Lab (batch)	UWO (2)	UWO (2)	Geo Labs (1)	Geo Labs (1)	Geo Labs (1)	Geo Labs (1)	Geo Labs (1)
ICP-MS lab (batch)	Geo Labs (2)	Geo Labs (2)	Geo Labs (1)	Geo Labs (1)	Geo Labs (1)	Geo Labs (1)	Geo Labs (1)
Easting	501301	501537	500801	500781	500793	500747	500781
Northing	5154949	5155177	5154729	5154794	5154723	5154782	5154794
n	1	1	1	1	1	1	1
notes			retrogressed	retrogressed			
SiO2	53.67	47.79	53.41	45.23	51.56	49.12	45.35
TiO2	1.96	1.56	1.63	2.31	1.96	1.66	2.20
Al2O3	12.29	14.17	12.68	13.91	11.04	13.55	13.73
Fe2O3*	17.26	15.61	15.84	21.01	16.92	18.09	22.43
MnO	0.20	0.20	0.23	0.28	0.25	0.26	0.27
MgO	3.04	6.19	3.15	5.67	5.52	4.87	5.93
CaO	7.34	10.78	11.42	9.85	11.91	9.04	9.75
Na2O	2.27	2.17	0.58	1.08	0.54	0.44	0.87
K2O	1.45	0.58	0.36	0.48	0.71	2.08	0.27
P2O5	0.27	0.17	0.21	0.26	0.27	0.21	0.26
LOI	0.24	0.42	0.57	0.37	-0.21	0.45	-0.88
Ba	505.5	107.1	160.0	193.6	199.4	579.6	189.0
Be	2.11	1.02	1.47	1.23	1.56	1.71	1.03
Bi	0.42	<0.15	<0.15	<0.15	<0.15	<0.15	<0.15
Cd	0.293	0.178	0.507	0.485	0.220	0.344	0.389
Ce	101.17	37.32	83.03	74.68	62.50	80.29	76.32
Co	52.43	56.89	44.09	79.93	54.34	54.87	65.16
Cr	10	190	36	29	35	25	27
Cs	1.713	0.298	0.263	1.481	1.293	2.209	0.293
Cu	230.5	182.9	37.5	651.3	6.6	29.6	190.1
Dy	10.991	6.466	8.707	7.929	10.994	9.595	10.241
Er	6.802	4.041	5.343	5.190	6.492	5.972	6.406
Eu	2.667	1.547	2.156	2.452	2.203	2.456	2.571
Ga	21.40	19.56	20.47	21.51	17.31	22.86	23.80
Gd	10.601	5.902	8.275	7.113	10.117	8.815	9.296
Hf	7.74	3.70	7.41	9.43	7.93	8.03	9.88
Ho	2.325	1.360	1.788	1.698	2.252	2.000	2.138
In	0.125	0.087	0.120	0.120	0.136	0.136	0.156
La	51.13	16.43	40.84	38.57	27.75	39.34	39.21
Li	16.5	8.6	13.4	20.0	8.6	20.7	3.5
Lu	0.954	0.575	0.786	0.857	0.898	0.874	0.958
Mo	1.46	0.47	0.92	0.42	0.39	1.03	0.45
Nb	15.209	8.059	20.264	20.951	18.355	17.395	17.959
Nd	47.33	20.86	37.46	32.44	36.24	38.02	36.25
Ni	11.4	99.4	32.3	48.9	53.5	35.8	42.4
Pb	15.5	7.8	41.6	15.3	10.8	23.1	8.4
Pr	11.994	4.885	9.618	8.310	8.261	9.424	8.915
Rb	51.20	6.30	6.41	19.58	21.25	67.73	6.05
Sb	0.50	0.28	0.77	0.23	0.34	0.50	0.07
Sc	36.7	44.7	34.5	48.1	44.2	38.2	45.8
Sm	10.417	5.203	8.089	6.789	9.331	8.514	8.487
Sn	3.20	1.54	1.99	1.02	1.72	2.56	1.60
Sr	152.4	160.0	184.7	284.2	109.5	185.2	268.5
Ta	0.912	0.487	1.136	1.327	1.264	1.061	1.192
Tb	1.7406	0.9746	1.3330	1.1840	1.6980	1.4590	1.5440
Th	11.245	2.026	8.795	4.783	6.586	9.257	6.236
Ti	10631	8807	10019	14629	11852	10399	13120
Tl	0.358	0.050	0.057	0.170	0.104	0.318	0.042
Tm	0.9803	0.5841	0.7900	0.7980	0.9370	0.8880	0.9510
U	2.424	0.564	1.256	0.669	1.812	1.961	1.027
V	276.1	345.4	>370	>370	>370	>370	>370
W	0.40	0.31	0.56	0.13	0.42	0.32	0.15
Y	59.82	35.51	48.05	44.91	59.07	54.05	51.74
Yb	6.405	3.865	5.206	5.459	6.036	5.814	6.314
Zn	150	132	149	177	149	167	184
Zr	307	143	308	402	333	333	385

*total iron expressed as Fe2O3

Table S3.1. Whole-rock major element (wt%) and trace element (ppm) data for Elsie Mountain Formation metavolcanics *(cont.)* .

ID	FSTJ024	FSTJ026	FSTJ031	FSTJ048	FSTJ063	FSTJ066
Metamorphic zone	PGZ	PGZ	PGZ	PGZ	PGZ	PGZ
Rock type	Pyroxene granofels	Pyroxene granofels	Pyroxene granofels	Pyroxene granofels	Pyroxene granofels	Pyroxene granofels
XRF Lab (batch)	Geo Labs (1)	Geo Labs (1)	Geo Labs (1)	Geo Labs (1)	Geo Labs (1)	Geo Labs (1)
ICP-MS lab (batch)	Geo Labs (1)	Geo Labs (1)	Geo Labs (1)	Geo Labs (1)	Geo Labs (1)	Geo Labs (1)
Easting	500760	500777	500760	500805	500771	500845
Northing	5154809	5154882	5154769	5154842	5154898	5154976
n	1	1	1	1	1	1
notes						
SiO2	50.42	44.48	45.97	49.08	43.81	47.97
TiO2	1.97	2.25	2.22	1.95	2.19	1.46
Al2O3	12.61	13.48	14.78	12.87	15.49	14.10
Fe2O3*	20.18	22.37	20.70	19.16	22.16	16.86
MnO	0.27	0.33	0.25	0.26	0.30	0.26
MgO	5.73	6.41	5.84	5.02	5.82	6.05
CaO	7.77	11.58	8.60	9.79	11.39	11.58
Na2O	0.44	0.37	0.45	0.50	0.38	1.65
K2O	1.55	0.20	2.20	1.16	0.10	0.31
P2O5	0.24	0.31	0.30	0.23	0.25	0.18
LOI	-0.18	-0.98	-0.23	-0.13	-1.28	-0.55
Ba	677.6	161.4	1078.3	454.1	92.0	207.3
Be	1.22	1.14	1.26	1.58	1.26	1.22
Bi	<0.15	<0.15	0.20	<0.15	<0.15	<0.15
Cd	0.261	0.283	0.293	0.260	0.286	0.354
Ce	66.15	63.27	110.01	70.13	69.65	53.61
Co	59.86	64.35	63.31	58.58	65.77	55.01
Cr	25	24	25	25	29	103
Cs	2.037	0.289	2.199	1.675	0.188	0.230
Cu	181.0	88.9	309.0	50.6	7.6	16.3
Dy	7.875	11.439	8.753	11.155	7.414	7.884
Er	5.023	6.821	5.639	6.778	4.981	4.916
Eu	2.204	2.546	2.587	2.489	2.498	1.905
Ga	21.02	23.18	25.58	22.73	24.53	19.66
Gd	7.196	10.370	8.379	9.917	6.518	7.201
Hf	8.22	8.73	9.59	8.20	9.77	5.40
Ho	1.653	2.352	1.853	2.304	1.604	1.643
In	0.137	0.161	0.149	0.139	0.142	0.108
La	32.35	29.90	56.77	33.44	36.18	24.96
Li	8.6	4.2	8.1	6.0	3.4	4.8
Lu	0.803	0.974	0.913	0.962	0.884	0.706
Mo	0.32	3.76	0.31	0.43	0.57	0.84
Nb	14.312	19.332	27.927	17.245	17.410	11.678
Nd	31.33	34.92	45.93	36.65	29.94	27.84
Ni	38.7	42.0	41.9	38.5	42.5	64.6
Pb	12.6	5.9	15.6	17.9	10.6	11.5
Pr	7.880	8.023	12.132	8.731	7.777	6.639
Rb	52.82	7.54	73.35	37.50	2.83	8.51
Sb	0.19	0.05	0.16	0.26	0.04	0.22
Sc	41.2	52.0	45.8	45.1	46.1	42.1
Sm	6.983	9.122	8.626	9.167	6.203	6.659
Sn	2.00	1.57	2.12	2.65	0.99	1.47
Sr	123.7	120.5	165.9	234.8	130.5	171.6
Ta	1.032	1.218	1.574	1.097	1.401	0.726
Tb	1.1930	1.7400	1.3290	1.6800	1.0920	1.1970
Th	7.996	4.278	11.023	8.567	5.875	1.909
Ti	11732	14181	13551	11816	13439	8998
Tl	0.262	0.046	0.360	0.198	0.022	0.048
Tm	0.7600	0.9870	0.8530	0.9950	0.7760	0.7170
U	1.824	0.825	1.465	2.182	0.705	0.571
V	>370	>370	>370	>370	>370	>370
W	0.21	0.19	0.21	0.24	0.15	0.16
Y	44.12	60.33	48.51	60.96	39.32	44.03
Yb	5.214	6.439	5.882	6.406	5.495	4.675
Zn	213	188	204	172	201	142
Zr	342	366	400	340	389	226

*total iron expressed as Fe2O3

Table S3.1. Whole-rock major element (wt%) and trace element (ppm) data for Elsie Mountain Formation metavolcanics *(cont.)* .

ID	FSTJ067	FSTJ069	FSTJ330	FSTJ347	FSTJ371	FSTJ372
Metamorphic zone	PGZ	PGZ	PGZ	PGZ	PGZ	PGZ
Rock type	Pyroxene granofels	Pyroxene granofels	Pyroxene granofels	Pyroxene granofels	Pyroxene granofels	Pyroxene granofels
XRF Lab (batch)	Geo Labs (1)	Geo Labs (1)	UWO (2)	UWO (2)	UWO (2)	UWO (2)
ICP-MS lab (batch)	Geo Labs (1)	Geo Labs (1)	Geo Labs (2)	Geo Labs (2)	Geo Labs (2)	Geo Labs (2)
Easting	500822	500713	500577	500822	501451	501429
Northing	5154994	5154981	5154548	5154962	5155284	5155346
n	1	1	1	1	1	1
notes						
SiO2	46.65	47.17	49.94	52.05	48.05	47.04
TiO2	1.76	2.20	2.19	1.49	2.41	2.14
Al2O3	14.06	12.60	12.16	12.37	13.37	13.59
Fe2O3*	19.33	21.28	19.52	16.99	20.75	20.61
MnO	0.27	0.31	0.21	0.21	0.22	0.26
MgO	5.97	6.02	3.60	6.28	4.07	4.98
CaO	10.86	10.36	8.46	7.55	6.99	8.90
Na2O	1.00	0.40	2.26	1.52	1.88	1.84
K2O	0.67	0.58	1.16	1.07	1.56	0.20
P2O5	0.21	0.24	0.26	0.20	0.27	0.32
LOI	-0.29	-0.39	-0.46	0.04	0.13	-0.68
Ba	322.6	317.5	537.3	435.1	1306.1	203.1
Be	1.74	1.44	1.91	1.72	1.85	1.83
Bi	<0.15	<0.15	<0.15	<0.15	<0.15	<0.15
Cd	0.418	0.376	0.294	0.221	0.255	0.175
Ce	62.21	67.89	99.06	63.65	78.97	93.43
Co	64.20	69.92	63.02	57.42	75.77	66.89
Cr	43	27	8	43	9	20
Cs	0.821	0.728	1.459	0.616	1.727	0.612
Cu	151.9	414.4	307.5	15.3	420.2	9.4
Dy	8.892	9.851	10.207	7.884	7.627	10.175
Er	5.442	5.990	6.244	5.226	4.955	6.305
Eu	2.361	2.306	2.587	1.919	2.638	2.662
Ga	23.01	22.34	22.75	19.20	23.40	23.45
Gd	8.194	8.874	9.620	6.937	7.224	9.748
Hf	8.08	8.76	7.84	6.39	8.61	8.71
Ho	1.844	2.041	2.134	1.709	1.637	2.172
In	0.137	0.170	0.126	0.102	0.113	0.135
La	30.47	32.89	51.64	32.84	38.28	50.71
Li	7.1	7.2	14.7	12.7	6.3	3.3
Lu	0.797	0.898	0.914	0.798	0.804	0.923
Mo	0.54	0.86	1.67	0.55	1.03	0.42
Nb	14.940	18.956	16.586	17.553	16.687	19.155
Nd	31.96	34.25	44.24	29.70	35.93	42.19
Ni	63.0	45.5	19.1	54.3	20.7	40.6
Pb	14.7	8.7	14.5	13.6	16.1	9.3
Pr	7.623	8.162	11.347	7.511	9.242	10.800
Rb	23.45	18.76	43.11	30.72	55.97	5.64
Sb	0.16	0.18	0.33	0.34	0.43	0.07
Sc	45.1	50.9	42.7	41.1	41.7	46.4
Sm	7.651	8.249	9.606	6.573	7.234	9.193
Sn	1.99	1.74	2.52	1.91	1.71	1.42
Sr	204.6	172.6	168.8	165.7	167.0	176.3
Ta	0.832	1.198	0.974	0.863	0.987	1.015
Tb	1.3410	1.4830	1.5884	1.1718	1.1648	1.5932
Th	3.766	6.107	9.165	6.781	11.068	7.064
Ti	10955	14194	13307	8022	14013	12326
Tl	0.133	0.104	0.270	0.182	0.376	0.078
Tm	0.7980	0.8860	0.9178	0.7807	0.7630	0.9305
U	0.953	1.235	1.521	1.444	1.081	0.711
V	>370	>370	>370	>370	>370	>370
W	0.18	0.20	0.23	0.16	0.21	0.06
Y	49.19	52.99	55.52	43.36	41.31	53.60
Yb	5.271	5.861	5.996	5.242	5.219	6.144
Zn	194	195	176	157	197	195
Zr	349	370	322	260	345	363

*total iron expressed as Fe2O3

Table S3.1. Whole-rock major element (wt%) and trace element (ppm) data for Elsie Mountain Formation metavolcanics *(cont.)* .

ID	FSTJ375	FSTJ374	FSTJ079	FSTJ102C	FSTJ102D	FSTJ104B
Metamorphic zone	PGZ	PHZ B	PHZ B	PHZ B	PHZ B	PHZ B
Rock type	Pyroxene granofels	Pyroxene hornfels	Pyroxene hornfels	Pyroxene hornfels	Pyroxene hornfels	Pyroxene hornfels
XRF Lab (batch)	UWO (2)	UWO (2)	Geo Labs (1)	Geo Labs (1)	Geo Labs (1)	Geo Labs (1)
ICP-MS lab (batch)	Geo Labs (2)	Geo Labs (2)	Geo Labs (1)	Geo Labs (1)	Geo Labs (1)	Geo Labs (1)
Easting	501414	501361	500531	500369	500362	500344
Northing	5155463	5155606	5154857	5154703	5154703	5154807
n	1	1	1	1	1	1
notes						
SiO2	47.66	46.73	46.74	49.13	48.23	44.33
TiO2	2.08	1.74	1.76	2.12	2.21	2.35
Al2O3	13.81	13.01	12.68	12.96	12.97	13.49
Fe2O3*	20.59	18.64	20.76	21.25	22.43	22.05
MnO	0.26	0.23	0.30	0.28	0.30	0.29
MgO	4.73	6.24	6.68	3.92	4.17	3.98
CaO	8.72	11.42	10.72	10.01	7.37	12.11
Na2O	1.36	1.53	1.32	1.09	2.37	1.73
K2O	0.60	0.25	0.21	0.28	0.54	0.19
P2O5	0.23	0.19	0.26	0.34	0.32	0.33
LOI	-0.42	-0.29	-0.60	-0.77	-0.37	-0.39
Ba	219.9	190.7	121.0	136.0	330.0	197.9
Be	2.22	1.49	0.84	1.38	1.13	1.35
Bi	1.04	<0.15	<0.15	<0.15	<0.15	<0.15
Cd	0.222	0.288	0.274	0.384	0.246	0.343
Ce	91.66	51.31	29.90	40.53	38.49	45.76
Co	64.52	64.95	64.23	58.61	61.67	54.18
Cr	16	50	76	20	16	18
Cs	0.524	0.286	0.284	0.420	1.269	0.505
Cu	39.3	56.4	57.8	138.7	292.9	151.8
Dy	9.528	9.357	5.871	7.463	6.717	8.376
Er	6.070	5.709	3.566	4.564	4.282	4.990
Eu	2.572	2.145	1.667	1.941	2.198	2.431
Ga	23.67	22.36	19.43	22.54	21.32	25.07
Gd	8.572	8.471	5.446	6.973	6.209	8.019
Hf	8.64	6.65	3.01	5.60	5.77	5.15
Ho	2.039	1.957	1.214	1.545	1.431	1.721
In	0.132	0.128	0.128	0.126	0.125	0.151
La	48.01	23.40	12.77	17.78	17.78	19.04
Li	7.0	5.3	4.6	5.5	8.6	6.3
Lu	0.946	0.797	0.517	0.680	0.685	0.712
Mo	0.83	1.32	0.30	0.70	0.33	2.27
Nb	19.029	12.594	8.267	10.781	11.934	12.741
Nd	39.75	30.52	18.75	24.73	21.96	28.63
Ni	40.3	64.6	67.1	30.9	29.8	31.7
Pb	9.6	13.0	3.8	4.4	7.9	6.8
Pr	10.403	6.950	4.108	5.450	5.016	6.301
Rb	21.40	5.41	5.02	8.28	16.98	6.34
Sb	0.21	0.25	<0.04	0.10	0.12	0.12
Sc	44.9	47.1	54.6	46.6	49.0	51.3
Sm	8.226	7.724	4.809	6.309	5.539	7.222
Sn	2.05	1.45	0.74	0.91	0.92	0.98
Sr	168.8	168.6	196.8	261.0	264.0	365.0
Ta	1.138	0.705	0.460	0.685	0.732	0.663
Tb	1.4315	1.4314	0.8920	1.1410	1.0100	1.2920
Th	7.804	1.490	0.632	1.314	1.941	1.020
Ti	11422	9702	11004	12860	13845	15012
Tl	0.154	0.045	0.040	0.082	0.131	0.065
Tm	0.9052	0.8180	0.5220	0.6680	0.6430	0.7190
U	1.219	0.396	0.207	0.436	0.655	0.406
V	>370	>370	>370	>370	>370	>370
W	0.09	0.10	0.11	0.15	0.17	0.19
Y	50.12	49.13	31.92	40.91	37.16	43.36
Yb	6.139	5.346	3.441	4.434	4.402	4.702
Zn	188	172	180	200	216	211
Zr	352	278	127	232	232	204

*total iron expressed as Fe2O3

Table S3.1. Whole-rock major element (wt%) and trace element (ppm) data for Elsie Mountain Formation metavolcanics *(cont.)* .

ID	FSTJ107B	FSTJ110	FSTJ118	FSTJ292	FSTJ294	FSTJ307
Metamorphic zone	PHZ B	PHZ B	PHZ B	PHZ B	PHZ B	PHZ B
Rock type	Pyroxene hornfels	Pyroxene hornfels	Pyroxene hornfels	Pyroxene hornfels	Pyroxene hornfels	Pyroxene hornfels
XRF Lab (batch)	Geo Labs (1)	Geo Labs (1)	Geo Labs (1)	UWO (2)	UWO (2)	UWO (2)
ICP-MS lab (batch)	Geo Labs (1)	Geo Labs (1)	Geo Labs (1)	Geo Labs (2)	Geo Labs (2)	Geo Labs (2)
Easting	500285	500370	500458	500238	500237	500287
Northing	5154912	5155021	5155015	5154829	5154886	5154684
n	1	1	1	1	1	1
notes						
SiO2	47.04	45.69	47.35	46.10	46.78	47.24
TiO2	2.00	2.10	1.65	2.37	2.33	2.25
Al2O3	14.13	12.94	13.18	12.12	13.27	12.56
Fe2O3*	21.34	24.18	19.31	23.42	22.06	22.01
MnO	0.29	0.31	0.27	0.26	0.25	0.27
MgO	4.06	4.58	5.72	3.86	3.90	4.25
CaO	9.51	9.70	11.38	7.69	7.25	8.03
Na2O	1.44	0.87	1.81	3.56	2.84	2.32
K2O	0.59	0.66	0.20	0.31	0.45	0.49
P2O5	0.32	0.32	0.21	0.33	0.30	0.31
LOI	-0.28	-0.73	-0.45	-0.60	-0.62	-0.32
Ba	255.5	226.9	114.4	298.7	294.3	381.2
Be	1.14	1.10	0.94	1.13	1.24	1.25
Bi	0.19	<0.15	<0.15	<0.15	<0.15	<0.15
Cd	0.262	0.367	0.243	0.311	0.283	0.331
Ce	44.83	43.49	32.73	45.33	38.77	39.99
Co	56.13	67.22	61.60	66.35	66.69	66.42
Cr	18	15	66	6	17	17
Cs	2.047	0.790	0.173	0.339	1.019	1.847
Cu	10.4	10.8	114.4	137.5	81.2	16.2
Dy	7.566	8.206	6.501	8.987	7.139	7.164
Er	4.626	5.123	3.977	5.395	4.410	4.431
Eu	2.453	2.184	1.713	2.505	2.362	2.109
Ga	23.98	25.16	20.27	23.23	24.12	23.09
Gd	7.149	7.597	6.009	8.473	6.764	6.902
Hf	5.13	5.07	3.54	5.02	4.57	4.92
Ho	1.571	1.724	1.360	1.861	1.495	1.494
In	0.149	0.144	0.115	0.152	0.118	0.120
La	20.01	18.95	14.09	19.12	17.43	17.42
Li	4.2	4.7	5.4	12.9	9.9	12.3
Lu	0.679	0.764	0.568	0.762	0.650	0.650
Mo	0.35	1.05	1.32	0.28	0.54	0.39
Nb	8.586	7.561	7.233	8.727	10.346	7.806
Nd	25.71	26.19	20.72	29.86	23.32	24.44
Ni	30.5	33.1	64.3	25.1	28.9	32.0
Pb	5.7	5.6	3.6	10.3	8.8	19.0
Pr	5.896	5.807	4.544	6.387	5.218	5.421
Rb	14.49	17.23	3.72	3.45	7.86	19.54
Sb	0.23	0.14	0.05	0.16	0.16	0.56
Sc	44.4	48.6	51.7	50.5	51.7	50.6
Sm	6.466	6.695	5.464	7.821	6.008	6.138
Sn	1.36	1.11	0.82	1.49	1.15	1.08
Sr	232.4	220.7	154.8	222.0	217.2	249.4
Ta	0.488	0.515	0.433	0.392	0.523	0.472
Tb	1.1560	1.2370	0.9940	1.4122	1.1241	1.1246
Th	2.314	2.185	0.816	0.532	1.403	1.337
Ti	12512	13273	10423	13859	13762	13525
Tl	0.119	0.147	0.029	0.034	0.076	0.164
Tm	0.6730	0.7510	0.5790	0.7760	0.6426	0.6428
U	0.734	0.693	0.247	0.375	0.543	0.477
V	>370	>370	>370	>370	>370	>370
W	0.19	0.16	0.11	0.05	0.10	0.11
Y	40.26	43.58	35.88	47.39	38.38	38.63
Yb	4.455	5.008	3.808	4.986	4.221	4.248
Zn	204	241	178	207	211	209
Zr	199	197	146	203	187	201

*total iron expressed as Fe2O3

Table S3.1. Whole-rock major element (wt%) and trace element (ppm) data for Elsie Mountain Formation metavolcanics *(cont.)* .

ID	FSTJ308	FSTJ084B	FSTJ085	FSTJ086C	FSTJ087A	FSTJ088
Metamorphic zone	PHZ B	PHZ A	PHZ A	PHZ A	PHZ A	PHZ A
Rock type	Pyroxene hornfels	Pyroxene hornfels	Pyroxene hornfels	Pyroxene hornfels	Pyroxene hornfels	Pyroxene hornfels
XRF Lab (batch)	UWO (2)	Geo Labs (1)	Geo Labs (1)	Geo Labs (1)	Geo Labs (1)	Geo Labs (1)
ICP-MS lab (batch)	Geo Labs (2)	Geo Labs (1)	Geo Labs (1)	Geo Labs (1)	Geo Labs (1)	Geo Labs (1)
Easting	500269	500313	500271	500856	500848	500863
Northing	5154725	5155202	5155135	5155198	5155228	5155251
n	1	1	1	1	1	1
notes						
SiO2	44.00	48.07	48.07	48.63	48.32	44.76
TiO2	2.52	1.66	1.22	1.29	1.39	1.55
Al2O3	11.73	13.60	15.40	13.75	13.51	11.93
Fe2O3*	23.62	18.72	15.67	15.60	16.63	20.59
MnO	0.27	0.27	0.22	0.24	0.25	0.27
MgO	4.38	6.89	7.70	6.71	7.05	6.50
CaO	10.66	10.44	10.43	11.83	11.21	12.07
Na2O	1.93	1.41	1.74	1.99	1.81	1.68
K2O	0.21	0.09	0.22	0.20	0.17	0.27
P2O5	0.32	0.20	0.12	0.13	0.15	0.18
LOI	-0.80	-0.66	-0.12	-0.02	0.20	0.27
Ba	210.8	110.4	150.1	102.6	72.6	161.0
Be	1.23	0.78	0.64	0.71	0.67	0.45
Bi	<0.15	<0.15	<0.15	<0.15	<0.15	<0.15
Cd	0.301	0.337	0.233	0.237	0.443	0.233
Ce	39.37	21.91	22.45	22.88	21.10	14.79
Co	69.88	67.42	60.62	55.16	61.95	61.02
Cr	13	119	269	245	246	101
Cs	0.200	0.179	0.225	0.311	0.341	0.405
Cu	123.7	64.4	152.1	110.1	288.1	38.4
Dy	9.017	5.717	5.567	5.393	4.564	5.247
Er	5.405	3.609	3.385	3.346	2.777	3.292
Eu	2.283	1.515	1.303	1.271	1.340	1.089
Ga	24.83	17.56	17.35	15.90	16.90	17.91
Gd	8.408	4.968	4.921	4.733	4.054	4.344
Hf	5.22	1.16	1.75	1.98	1.35	1.28
Ho	1.870	1.219	1.158	1.136	0.948	1.115
In	0.147	0.113	0.090	0.088	0.087	0.101
La	15.53	9.63	8.93	9.41	9.27	5.84
Li	11.1	4.9	6.5	6.0	8.2	22.9
Lu	0.758	0.533	0.456	0.461	0.409	0.477
Mo	0.88	0.41	0.29	0.51	0.60	0.72
Nb	11.605	7.787	4.409	5.454	7.004	4.444
Nd	27.63	14.43	15.22	14.48	12.82	11.03
Ni	33.3	69.1	141.2	65.0	87.1	72.1
Pb	7.1	5.2	7.3	5.4	15.6	12.3
Pr	5.748	3.069	3.241	3.165	2.835	2.227
Rb	2.73	1.70	3.25	3.43	3.15	7.19
Sb	0.14	<0.04	0.15	0.08	0.41	0.22
Sc	54.5	59.7	46.4	52.3	51.7	55.6
Sm	7.404	4.177	4.188	3.930	3.454	3.342
Sn	1.03	0.30	0.65	0.54	0.41	0.43
Sr	224.9	195.6	200.6	214.4	172.2	167.0
Ta	0.516	0.488	0.263	0.338	0.446	0.262
Tb	1.3930	0.8420	0.8370	0.8020	0.6740	0.7810
Th	0.459	0.270	0.399	0.331	0.562	0.301
Ti	15168	10335	7548	7702	8678	10140
Tl	0.023	0.024	0.027	0.046	0.047	0.169
Tm	0.7707	0.5310	0.4810	0.4820	0.4080	0.4810
U	0.263	0.109	0.124	0.115	0.200	0.104
V	>370	>370	>370	365.7	>370	>370
W	0.08	0.12	0.10	0.11	0.23	0.16
Y	46.45	31.72	31.27	30.23	24.96	29.44
Yb	5.005	3.516	3.090	3.125	2.736	3.144
Zn	207	171	119	125	146	195
Zr	211	42	53	70	51	44

*total iron expressed as Fe2O3

Table S3.1. Whole-rock major element (wt%) and trace element (ppm) data for Elsie Mountain Formation metavolcanics *(cont.)* .

ID	FSTJ089	FSTJ091	FSTJ092C	FSTJ108A	FSTJ121B	08LEFS44
Metamorphic zone	PHZ A	PHZ A	PHZ A	PHZ A	PHZ A	PHZ A
Rock type	Pyroxene hornfels	Pyroxene hornfels	Pyroxene hornfels	Pyroxene hornfels	Pyroxene hornfels	Pyroxene hornfels
XRF Lab (batch)	Geo Labs (1)	Geo Labs (1)	Geo Labs (1)	Geo Labs (1)	Geo Labs (1)	Geo Labs (1)
ICP-MS lab (batch)	Geo Labs (1)	Geo Labs (1)	Geo Labs (1)	Geo Labs (1)	Geo Labs (1)	Geo Labs (1)
Easting	500878	500879	500905	500217	500595	501355
Northing	5155255	5155331	5155411	5154975	5155249	5155712
n	1	1	1	1	1	1
notes						
SiO2	46.91	44.22	44.20	45.26	48.43	45.71
TiO2	1.80	1.57	2.38	1.71	1.52	1.47
Al2O3	13.29	13.95	12.86	12.27	13.49	13.40
Fe2O3*	18.80	19.63	21.39	21.52	16.66	18.89
MnO	0.26	0.28	0.28	0.29	0.26	0.26
MgO	5.74	6.52	5.91	6.43	7.37	6.77
CaO	11.98	12.42	13.24	12.13	11.88	12.44
Na2O	1.75	0.96	1.05	1.23	1.29	1.29
K2O	0.14	0.10	0.10	0.12	0.08	0.29
P2O5	0.25	0.20	0.20	0.20	0.11	0.14
LOI	-0.57	-0.02	-0.78	-0.54	-0.63	-0.11
Ba	82.4	53.7	56.4	59.3	84.0	59.1
Be	0.85	0.85	0.43	0.50	0.66	0.73
Bi	<0.15	<0.15	<0.15	<0.15	<0.15	<0.15
Cd	0.306	0.388	0.332	0.337	0.300	0.391
Ce	30.08	14.77	13.68	17.04	10.87	22.12
Co	61.99	60.31	72.19	78.66	61.31	72.12
Cr	64	99	35	48	149	102
Cs	0.145	0.198	0.093	0.137	0.127	0.295
Cu	193.3	157.1	11.0	243.8	7.9	208.7
Dy	6.434	5.032	4.666	5.729	4.452	6.026
Er	3.869	3.172	2.878	3.464	2.752	3.717
Eu	1.611	1.343	1.265	1.478	1.262	1.463
Ga	19.07	19.80	19.59	19.07	19.57	19.51
Gd	5.974	4.391	4.021	4.965	3.716	5.287
Hf	2.13	1.45	1.11	1.27	1.29	1.73
Ho	1.338	1.065	0.980	1.198	0.949	1.274
In	0.109	0.097	0.107	0.115	0.103	0.103
La	12.61	5.94	5.57	6.75	4.50	9.22
Li	6.0	7.8	2.3	7.3	3.9	6.1
Lu	0.537	0.469	0.403	0.489	0.397	0.516
Mo	0.65	0.75	0.43	0.47	0.53	0.86
Nb	8.408	4.582	2.989	4.231	6.589	4.797
Nd	19.52	11.38	10.00	13.10	8.25	15.16
Ni	59.8	75.2	48.5	84.9	124.8	100.9
Pb	4.2	12.7	4.3	6.9	9.3	8.4
Pr	4.217	2.290	2.038	2.604	1.627	3.198
Rb	2.31	2.09	2.25	2.10	1.07	7.60
Sb	0.13	0.50	<0.04	0.07	0.05	0.09
Sc	52.6	57.4	60.3	58.8	54.3	54.4
Sm	5.265	3.412	3.145	4.004	2.763	4.433
Sn	0.60	0.35	0.38	0.41	0.23	0.72
Sr	203.4	147.3	146.1	167.8	146.1	179.0
Ta	0.500	0.280	0.207	0.241	0.335	0.255
Tb	0.9780	0.7460	0.6920	0.8510	0.6580	0.8990
Th	0.760	0.157	0.498	0.154	0.823	0.401
Ti	11093	9874	14862	10798	9667	9139
Tl	0.016	0.046	0.017	0.026	0.015	0.061
Tm	0.5560	0.4660	0.4100	0.4980	0.4030	0.5350
U	0.215	0.064	0.157	0.070	0.237	0.138
V	>370	>370	>370	>370	>370	>370
W	0.13	0.17	0.07	0.08	0.15	0.11
Y	35.03	28.07	24.61	30.37	25.18	33.56
Yb	3.577	3.086	2.694	3.253	2.655	3.454
Zn	162	176	163	181	151	172
Zr	81	47	33	42	45	61

*total iron expressed as Fe2O3

Table S3.1. Whole-rock major element (wt%) and trace element (ppm) data for Elsie Mountain Formation metavolcanics *(cont.)* .

ID	FSTJ098	FSTJ298	FSTJ299	FSTJ301	FSTJ373	FSTJ118_1
Metamorphic zone	PHZ A	PHZ A	PHZ A	PHZ A	PHZ A	PHZ B
Rock type	Pyroxene hornfels	Pyroxene hornfels	Pyroxene hornfels	Pyroxene hornfels	Pyroxene hornfels	Pyroxene hornfels
XRF Lab (batch)	UWO (2)	UWO (2)	UWO (2)	UWO (2)	UWO (2)	Geo Labs (1)
ICP-MS lab (batch)	Geo Labs (2)	Geo Labs (2)	Geo Labs (2)	Geo Labs (2)	Geo Labs (2)	Geo Labs (1)
Easting	500260	500191	500183	500192	501444	500458
Northing	5155206	5154931	5154972	5155067	5155760	5155015
n	1	1	1	1	1	1
notes						duplicate
SiO2	47.48	46.19	44.69	45.98	45.36	47.12
TiO2	1.44	2.18	2.16	1.47	1.56	1.67
Al2O3	15.13	12.38	12.95	13.84	14.23	13.13
Fe2O3*	15.63	21.98	21.65	18.67	18.38	19.25
MnO	0.26	0.27	0.28	0.24	0.23	0.27
MgO	8.59	4.47	4.46	6.41	7.16	5.74
CaO	9.49	8.79	10.68	11.34	11.21	11.33
Na2O	0.88	2.62	2.02	1.30	1.21	1.83
K2O	0.13	0.18	0.21	0.18	0.30	0.20
P2O5	0.32	0.31	0.29	0.11	0.15	0.21
LOI	0.01	-0.54	-0.47	-0.32	-0.19	-0.33
Ba	118.0	243.0	120.5	64.9	139.0	114.1
Be	0.72	0.99	1.22	1.08	1.05	0.82
Bi	<0.15	<0.15	<0.15	<0.15	<0.15	<0.15
Cd	0.217	0.230	0.466	0.346	0.158	0.217
Ce	34.08	31.78	34.06	15.46	48.21	30.84
Co	71.27	66.69	67.03	68.15	68.22	60.53
Cr	428	20	21	204	134	68
Cs	0.253	0.226	0.262	0.300	0.238	0.198
Cu	158.6	134.9	11.0	4.7	6.5	104.5
Dy	5.126	7.463	7.484	4.853	8.382	6.363
Er	3.376	4.557	4.529	3.070	5.180	3.857
Eu	1.398	2.162	2.119	1.265	1.937	1.616
Ga	17.68	20.86	23.85	23.32	20.78	19.80
Gd	4.806	6.962	6.968	4.286	7.596	5.880
Hf	0.99	3.05	2.40	1.16	3.69	3.39
Ho	1.115	1.560	1.538	1.032	1.762	1.325
In	0.110	0.133	0.137	0.093	0.116	0.106
La	15.82	12.94	13.78	6.18	19.34	13.45
Li	9.5	5.4	13.1	4.2	6.2	5.9
Lu	0.536	0.672	0.636	0.435	0.714	0.558
Mo	0.50	0.35	0.40	0.42	0.38	1.51
Nb	5.803	6.967	8.905	3.760	8.150	7.043
Nd	18.31	22.27	22.64	11.57	28.50	20.02
Ni	166.9	32.9	37.5	120.2	88.8	60.1
Pb	7.5	3.6	13.8	13.2	3.5	3.8
Pr	4.296	4.609	4.851	2.348	6.582	4.356
Rb	1.86	2.20	3.88	2.92	4.21	4.09
Sb	0.04	<0.04	0.23	0.20	0.05	0.07
Sc	49.4	54.5	53.9	48.3	49.5	50.3
Sm	4.288	6.168	6.126	3.515	7.104	5.243
Sn	0.60	0.77	0.98	1.09	1.54	0.71
Sr	185.6	179.1	203.0	340.4	158.2	153.8
Ta	0.368	0.377	0.387	0.162	0.416	0.410
Tb	0.7790	1.1765	1.1524	0.7516	1.2996	0.9690
Th	0.762	0.373	0.594	0.229	0.585	0.779
Ti	6951	12649	12688	8250	8399	9982
Tl	0.043	0.024	0.035	0.038	0.039	0.033
Tm	0.5151	0.6580	0.6439	0.4495	0.7591	0.5610
U	0.263	0.222	0.208	0.066	0.174	0.253
V	368.9	>370	>370	>370	>370	>370
W	0.13	<0.05	0.10	0.09	<0.05	0.12
Y	29.43	39.66	39.89	26.37	46.26	34.63
Yb	3.489	4.397	4.145	2.884	4.837	3.669
Zn	200	188	194	209	153	141
Zr	34	118	87	37	141	137

*total iron expressed as Fe2O3

Table S3.1. Whole-rock major element (wt%) and trace element (ppm) data for Elsie Mountain Formation metavolcanics *(cont.)* .

ID	FSTJ118_2	FSTJ118_3	FSTJ118_4	FSTJ118_5	FSTJ118_6	FSTJ118_7
Metamorphic zone	PHZ B	PHZ B	PHZ B	PHZ B	PHZ B	PHZ B
Rock type	Pyroxene hornfels	Pyroxene hornfels	Pyroxene hornfels	Pyroxene hornfels	Pyroxene hornfels	Pyroxene hornfels
XRF Lab (batch)	Geo Labs (1)	Geo Labs (1)	Geo Labs (1)	Geo Labs (1)	UWO (2)	UWO (2)
ICP-MS lab (batch)	Geo Labs (1)	Geo Labs (1)	Geo Labs (1)	Geo Labs (1)	Geo Labs (2)	Geo Labs (2)
Easting	500458	500458	500458	500458	500458	500458
Northing	5155015	5155015	5155015	5155015	5155015	5155015
n	1	1	1	1	1	1
notes	duplicate	duplicate	duplicate	duplicate	duplicate	duplicate
SiO2	47.29	47.23	46.97	47.17	46.81	46.95
TiO2	1.67	1.65	1.66	1.66	1.68	1.68
Al2O3	13.13	13.10	12.99	13.11	13.41	13.37
Fe2O3*	19.38	19.31	19.36	19.13	18.77	18.96
MnO	0.27	0.27	0.27	0.26	0.24	0.23
MgO	5.79	5.76	5.69	5.67	5.81	5.91
CaO	11.40	11.39	11.37	11.32	10.55	10.57
Na2O	1.80	1.82	1.79	1.84	1.74	1.71
K2O	0.20	0.19	0.19	0.19	0.20	0.21
P2O5	0.20	0.21	0.20	0.21	0.21	0.20
LOI	-0.39	-0.44	-0.30	-0.50	-0.47	-0.34
Ba	114.0	117.6	118.6	114.3	115.2	112.2
Be	0.82	0.87	0.80	0.97	0.91	0.86
Bi	<0.15	<0.15	<0.15	<0.15	<0.15	<0.15
Cd	0.236	0.226	0.249	0.263	0.186	0.185
Ce	32.40	32.70	32.80	31.55	31.04	31.76
Co	61.21	61.70	56.53	60.20	63.83	65.19
Cr	67	65	61	66	69	67
Cs	0.201	0.205	0.186	0.185	0.195	0.193
Cu	109.7	122.5	105.3	106.9	106.9	109.2
Dy	6.590	6.552	6.732	6.340	6.300	6.389
Er	3.988	3.941	4.101	3.867	3.878	3.885
Eu	1.672	1.660	1.706	1.646	1.645	1.669
Ga	20.24	20.05	19.20	20.35	21.24	20.88
Gd	6.086	6.053	6.188	5.831	5.906	5.952
Hf	3.44	3.43	3.52	3.47	3.08	3.04
Ho	1.355	1.356	1.392	1.316	1.341	1.335
In	0.113	0.109	0.110	0.111	0.104	0.108
La	13.95	14.04	14.06	13.65	13.45	13.59
Li	5.8	5.6	4.8	5.5	5.6	5.6
Lu	0.575	0.567	0.594	0.554	0.548	0.567
Mo	1.32	1.25	1.18	1.23	1.42	1.27
Nb	7.001	7.384	6.692	7.210	6.505	6.586
Nd	20.78	20.76	20.75	19.88	20.10	20.14
Ni	61.6	63.0	57.2	61.9	62.1	64.8
Pb	4.0	3.8	3.9	3.5	3.7	3.8
Pr	4.560	4.533	4.522	4.319	4.328	4.404
Rb	3.84	4.06	3.59	3.88	3.58	3.17
Sb	0.07	0.06	0.05	0.05	0.07	0.07
Sc	51.5	51.1	47.4	50.3	53.0	52.9
Sm	5.448	5.373	5.465	5.219	5.222	5.360
Sn	0.77	0.74	0.71	0.73	0.82	0.97
Sr	155.3	156.8	150.9	155.2	151.7	147.9
Ta	0.408	0.436	0.438	0.420	0.350	0.372
Tb	1.0060	0.9860	1.0110	0.9700	0.9874	0.9861
Th	0.805	0.801	0.874	0.791	0.767	0.759
Ti	10148	10422	9738	10214	9468	9404
Tl	0.031	0.032	0.032	0.030	0.029	0.029
Tm	0.5830	0.5810	0.6000	0.5610	0.5681	0.5764
U	0.244	0.254	0.270	0.242	0.220	0.219
V	>370	>370	>370	>370	>370	>370
W	0.11	0.11	0.12	0.11	0.06	0.06
Y	35.86	35.71	34.35	34.69	34.91	35.12
Yb	3.794	3.763	3.948	3.666	3.701	3.747
Zn	151	164	158	176	162	162
Zr	139	140	134	144	125	118

*total iron expressed as Fe2O3

Table S3.1. Whole-rock major element (wt%) and trace element (ppm) data for Elsie Mountain Formation metavolcanics *(cont.)* .

ID	FSTJ118_8	FSTJ118_9	FSTJ118_10	BHVO-2	BHVO-2	BHVO-2	JB-1a
Metamorphic zone	PHZ B	PHZ B	PHZ B	n/a	n/a	n/a	
Rock type	Pyroxene hornfels	Pyroxene hornfels	Pyroxene hornfels				
XRF Lab (batch)	UWO (2)	UWO (2)	UWO (2)	Geo Labs (1)	n/a	n/a	UWO (2)
ICP-MS lab (batch)	Geo Labs (2)	Geo Labs (2)	Geo Labs (2)	Geo Labs (1)	Geo Labs (2)	Geo Labs (2)	n/a
Easting	500458	500458	500458				
Northing	5155015	5155015	5155015				
n	1	1	1				
notes	duplicate	duplicate	duplicate	standard	standard	standard	standard
SiO2	47.21	46.50	47.06	49.79			52.13
TiO2	1.70	1.68	1.70	2.75			1.31
Al2O3	13.20	13.49	13.30	13.19			14.29
Fe2O3*	18.92	18.82	18.84	12.57			8.95
MnO	0.23	0.23	0.23	0.17			0.14
MgO	5.89	5.81	5.89	7.14			7.83
CaO	10.63	10.54	10.64	11.62			8.92
Na2O	1.77	1.78	1.78	2.22			1.41
K2O	0.20	0.19	0.20	0.53			2.68
P2O5	0.21	0.20	0.21	0.28			0.26
LOI	-0.39	-0.31	-0.38	-0.62			
Ba	121.2	113.6	112.4	137.8	137.7	136.3	
Be	1.05	0.95	0.92	1.01	1.11	1.07	
Bi	<0.15	<0.15	<0.15	0.02	0.05	0.02	
Cd	0.215	0.189	0.199	0.121	0.149	0.103	
Ce	33.68	30.92	31.16	40.51	40.53	40.13	
Co	68.46	63.02	63.00	47.79	46.86	48.51	
Cr	69	66	68	317	309	315	
Cs	0.209	0.193	0.188	0.114	0.113	0.108	
Cu	128.6	104.8	103.9	135.7	135.8	133.3	
Dy	6.964	6.452	6.524	5.729	5.516	5.518	
Er	4.255	3.976	4.002	2.683	2.638	2.675	
Eu	1.770	1.694	1.679	2.193	2.182	2.186	
Ga	21.98	20.95	20.68	20.81	20.51	20.84	
Gd	6.470	5.982	6.078	6.636	6.471	6.453	
Hf	3.55	3.16	3.05	4.58	4.51	4.36	
Ho	1.454	1.370	1.350	1.028	1.010	1.023	
In	0.113	0.105	0.102	0.087	0.089	0.085	
La	14.22	13.21	13.11	16.62	16.42	16.19	
Li	6.5	5.9	5.9	4.6	4.3	4.6	
Lu	0.610	0.569	0.575	0.290	0.281	0.285	
Mo	1.32	1.17	1.18	4.27	3.66	5.15	
Nb	7.309	6.561	6.667	18.160	18.133	17.303	
Nd	21.96	19.95	19.89	26.36	25.83	25.66	
Ni	68.7	61.1	62.8	126.7	125.2	130.4	
Pb	3.8	3.5	3.6	1.7	1.6	1.6	
Pr	4.739	4.382	4.294	5.710	5.613	5.634	
Rb	3.70	3.38	3.44	10.28	10.02	9.26	
Sb	0.06	0.07	0.06	0.11	0.12	0.13	
Sc	55.8	51.8	52.0	35.0	34.1	34.6	
Sm	5.722	5.250	5.406	6.604	6.456	6.466	
Sn	0.97	0.81	0.93	2.06	2.02	2.11	
Sr	159.3	152.0	150.4	411.5	406.6	397.0	
Ta	0.400	0.368	0.370	1.178	1.182	1.009	
Tb	1.0683	1.0030	0.9878	0.9840	0.9500	0.9814	
Th	0.781	0.782	0.772	1.246	1.295	1.196	
Ti	10061	9323	9535	17548	17591	16444	
Tl	0.031	0.031	0.029	0.023	0.021	0.019	
Tm	0.6131	0.5811	0.5811	0.3510	0.3410	0.3515	
U	0.235	0.219	0.227	0.473	0.452	0.432	
V	>370	>370	>370	347.7	340.8	320.6	
W	0.07	0.06	0.07	0.27	0.26	0.22	
Y	36.23	34.53	34.91	26.83	26.46	26.25	
Yb	4.084	3.795	3.738	2.091	2.040	2.051	
Zn	169	157	158	92	109	100	
Zr	138	124	120	182	181	173	

*total iron expressed as Fe2O3

CHAPTER 4: FORMATION OF POIKILITIC ZIRCON AND Zr-Hf MOBILIZATION DURING PARTIAL MELTING OF METABASALTS IN AN IMPACT MELT SHEET INDUCED CONTACT AUREOLE, SUDBURY, CANADA

T.R.C. JØRGENSEN[1*], D.K. TINKHAM[1], and C.M. LESHER[1]

[1]*Harquail School of Earth Sciences, Mineral Exploration Research Centre, Laurentian University, 935 Ramsey Lake Rd., Sudbury, ON, P3E 2C6, Canada*

(trc.joergensen@gmail.com; dtinkham@laurentian.ca; mlesher@laurentian.ca)

**corresponding author*

ABSTRACT

Zircon occurs as poikilitic, branching, and interstitial networks in two-pyroxene hornfels metabasalts in the proximal contact aureole of the impact-generated 1850 Ma Sudbury Igneous Complex (SIC). Zircon morphologies with these characteristics are previously described only in lunar meteorites, and the restriction of such textures to the peak contact metamorphic mineral assemblage of the SIC is consistent with zircon crystallizing from trapped melt films during retrograde cooling. This interpretation is supported by petrographic evidence of the zircons in contact with pseudomorphed melt films, an 1850 ± 24 Ma U-Pb concordia age, relatively low temperature estimates by Ti-in-zircon geothermometry (ca. 660-710 °C; Ti contents averaging 5.2 ± 0.8 ppm), and high Yb contents ranging from 30-330 ppm. Furthermore, poikilitic zircon textures occur only in pyroxene-hornfels facies metabasalts exhibiting strong negative whole-rock Zr and Hf anomalies ($Zr/Zr^* < 0.67$) and Zr/Hf trending toward sub-chondritic values (low of 29.73), indicating that Zr and Hf were mobile during contact metamorphism. The zircons relationship with trapped melt films and the presence of leucocratic quartz-plagioclase melt patches in other parts of the aureole indicate that silicate melt was the mobilizing phase, and that significant melt segregation occurred within at least 250 m of the contact of the SIC.

INTRODUCTION

Zircon is known to exhibit a wealth of different morphologies dependent on the environment under which it forms (see review by Corfu et al., 2003). Distinct poikilitic morphologies displayed by zircons from lunar meteorite Sayh al Uhaymar (SaU) 169,

which exhibit a poikilitic morphology interpreted to have formed during equilibrium crystallization of a shock melt immediately following impact melt and are unlike any zircon reported thus far in terrestrial rocks (e.g., Gnos et al., 2004; Nemchin et al, 2008; Lie et al., 2012).

Zirconium and Hf are interpreted to be largely immobile during metamorphism until the presence of a partial melt phase. For example, zircon saturated hydrous granitic melts formed during crustal fusion in subduction zones contains on the order of 100 to 200 ppm at temperatures from 800 °C to 900 °C (e.g., Watson, 1983; Rubatto and Hermann, 2003). Zirconium redistribution during high-grade metamorphism has been reported in studies on the textures and chemistry of zircon and other Zr-repository silicate minerals (e.g., garnet, amphibole, pyroxene, and ilmenite; e.g., Roberts and Finger, 1997; Bingen et al., 2001; and Hokada and Harley, 2004), but such studies have not reported significant effects on whole-rock compositions.

In this paper we report the first documented examples of terrestrial occurring poikilitic zircons, and evidence for significant whole-rock redistribution and fractionation of Zr and Hf contents. We show that: 1) poikilitic zircons are restricted to two-pyroxene metabasalts within the proximal parts of the contact metamorphic aureole of the 1850 ± 1 Ma Sudbury Igneous Complex (SIC; Krogh et al., 1984), 2) the poikilitic zircon overgrow the peak contact metamorphic mineral assemblage, 3) the presence of poikilitic zircons correlates with metabasalts showing significant depletion in Zr and Hf relative to lower-grade and unmetamorphosed equivalents, and 4) these rocks exhibit trends toward sub-chondritic Zr/Hf values (as low as ca. 30), indicating preferential mobility of Zr relative to Hf. We argue that the formation of poikilitic zircon and whole-rock Zr-Hf

systematics resulted from partial melting and melt segregation during SIC contact metamorphism, and that zircon textures reflect crystallization from trapped partial melts during retrograde isobaric cooling. Thus, poikilic zircon is not unique to cooling of impact shock melts, and highlights that zircon crystallization not only can postdate the pressure peak during high-grade metamorphism, but also peak temperatures (Roberts and Finger, 1997).

GEOLOGICAL SETTING

The two-pyroxene hornfels metabasalts reported in this study are part of the Elsie Mountain Formation (EMF), which has a minimum age of 2452.5 ± 6.2 Ma (Ketchum et al., 2013) and which occurs in the lowermost part of the Paleoproterozoic Huronian Supergroup in the Sudbury area (Fig. 4.1). The EMF is the easternmost part of a *ca.* 200 km long volcanic belt interpreted to represent continental flood basalts associated with continental rifting (Jolly, 1992). The EMF in the Sudbury area is composed of pillowed and massive basalt flows, and forms a significant amount of the footwall rock along much of the southern margin of the SIC (e.g., Innes, 1977; Jolly, 1992). EMF basalts away from the SIC and equivalent rocks in other parts of the volcanic belt are enriched in Th and LREE relative to MREE-HREE (e.g., Innes, 1977; Jolly, 1992; Hocking, 2003; Ketchum et al., 2013). However, EMF metabasalts in the innermost contact aureole of the SIC have been metamorphosed to two-pyroxene hornfels rocks that are depleted in Cs, Rb, K, and Ba relative to Na, Sr, and Ca, depleted in LREE relative to MREE-HREE, and depleted in Th, U, Zr, Hf, Ta, and Nb relative to MREE-HREE (Jørgensen et al., Chapter 3). The dominant mineral assemblage in the hornfels rocks is plagioclase-clinopyroxene-

orthopyroxene-magnetite-ilmenite with textural evidence for partial melting provided pseudomorphed melt films now defined by anhedral cuspate quartz and relatively Ca-poor plagioclase networks along grain boundaries of relatively Ca-rich plagioclase and pyroxene (Jørgensen et al., Chapter 2).

The metamorphic history of the EMF includes pre- and post-SIC regional events (Card, 1978; Riller, 2005). Post-impact Penokean orogenic temperatures at the Garson Mine, Sudbury peaked at 550-590 °C and had declined to ~400 °C by 1,849 ± 6 Ma (U-Pb titanite age: Mukwakwami, 2014). Consequently, the contact aureole and shock metamorphic features in the proximal footwall along the southern margin of the SIC are locally metamorphic downgraded, but not completely destroyed (Jørgensen et al., Chapter 2). Peak contact metamorphic temperatures are difficult to estimate because the initial temperature of the impact melt, the temperature of the footwall rocks immediately after impact, and the amount of footwall rocks that were thermo-mechanically eroded are not known. However, estimates from two-feldspar geothermometry applied on SIC-hosted xenoliths indicate Or_{60} growth at the highest grades of contact metamorphism and peak metamorphic temperatures of about 900 °C (Prevec et al., 2008). Because of their high variance, the two-pyroxene-bearing mineral assemblages of the metabasalts and the presence of melt only provide minimum temperatures of 875 °C, defined by the melt-in reaction on phase diagram sections (Jørgensen et al., Chapter 2). However, temperatures of ≥925 °C are reasonable from phase equilibria calculations investigating the evolution of bulk rock compositions of metabasalts undergoing melt segregation and plagioclase compositions, and trace element modelling considerations (Jørgensen et al., Chapter 2 and 3).

A common observation from zircon U-Pb studies is that SIC country rocks give 1850 Ma ages (e.g., Krogh et al., 1984). This is presumably a direct response to the shock metamorphic resetting of the geochronometer as indicated by planar fractures (PF) in zircons, subsequent annealing, or new growth of zircon during contact metamorphism, typically resulting in euhedral and equant "soccerball" morphologies (Krogh et al. 1984). The ages constraining the Penokean orogeny are provided by metamorphic titanite grains in Hurronian gabbro (associated with EMF metabasalts) and norite at the base of the SIC (Bailey et al., 2004; Mukwakwami, 2014).

ZIRCON PETROGRAPHY

Multiple thin sections were prepared from two samples (FSTJ301 and FSTJ098A) collected from the EMF in the immediate southern footwall within 70 m and 10 m, respectively, of the basal contact with the SIC. The samples contain < 40 ppm Zr, and zircons are present in trace amounts and randomly distributed in the rocks as: 1) subrounded, subhedral, equant-stubby grains, and 2) irregular poikilitic anhedral to subhedral grains, sometimes forming branching, interstitial networks with apophyses of thin (1-2 μm) films forming cuspate outlines at grain contacts between other silicate phases (Fig. 4.2a). The grains are dominantly between 10-25 μm and rarely up to 30-50 μm in size, and only 1 observed grain approached 100 μm in the longest dimension. The zircons occur in association with all the phases considered part of the contact metamorphic peak assemblage (orthopyroxene, clinopyroxene, magnetite, ilmenite, and plagioclase) and generally share contacts with more than one of these minerals. Only plagioclase occurs locally as the lone contact phase, although occasionally two

plagioclases of different composition are present: interstitial relatively Na-rich plagioclase (An55 in sample FSTJ301) and polygonal granoblastic Ca-rich plagioclase (An70 in sample FSTJ301; Fig. 4.2b). The nature of the contacts between zircons and associated phases varies, but zircon tends to be subrounded against pyroxenes and straight to subrounded against oxides and plagioclase. Rounded to subrounded inclusions of relatively Ca-rich plagioclase and lesser clinopyroxene in zircons are common.

Cathodoluminescence and back-scattered electron imaging of zircon show the local presence of sector zoning and otherwise fairly simple internal morphologies with no evidence for shock metamorphic features or any significant signs of metamictization (Fig. 4.2c). Thorite, coffinite, xenotime, thortveitite, and other phases that are commonly described in hydrothermally re-equilibrated zircons were not seen as inclusions, and qualitative element maps show no signs of non-essential elements (e.g., Ca and Al: Geisler et al., 2007). Qualitative element maps collected on the scanning electron microscope also indicate a homogeneous distribution of trace elements (e.g., Th, Hf, Pb, and HREE; Fig. 4.2d).

ZIRCON TRACE ELEMENT AND U-Pb RESULTS

Three zircon grains from two different thin sections of sample FSTJ301 were selected for U-Pb dating to establish the age of their growth. U-Pb and trace element data for 13 analyses are presented in Table 4.1 and shown on a concordia diagram and a chondrite-normalized REE diagram in Figures 4.3a-b. The data were acquired at the Laurentian University Geochemical Fingerprinting Laboratory, Canada by in-situ laser ablation (Resonetic RESOlution M-50 193 nm ArF excimer laser) inductively coupled plasma

mass spectrometry (Thermo X-Series II; LA-ICP-MS). Due to the poikilitic texture and small grain size, single spot analyses involved a risk of contaminating the signal by neighboring phases. Of the 13 data points presented in this study, 1 represents a single spot-analysis, whereas the remaining 12 constitute carefully selected parts from 2 zircon element maps. Data were processed with Iolite (e.g., Paton et al., 2010, 2011) and VizualAge (Petrus and Kamber, 2012), and concordia ages were calculated using Isoplot (e.g., Ludwig, 2003).

Results of individual grains are presented in Figure 4.3a and are within error of the 1850 Ma SIC emplacement age (Krogh et al. 1984; Davis 2008). Concordia ages were calculated for each of the 3 grains, and yield 1847 ± 36 Ma (R-S33-1; n=6), 1823 ± 92 Ma (grain R-S37; n=1), and 1857 ± 33 Ma (grain (6)-S2; n=6). When all 13 analyses are considered together they yield a concordia age of 1850 ± 24 Ma (2σ; MSWD $_{(Concord. + Equiv.)}$ = 0.68; probability $_{(Concord. + Equiv.)}$ = 0.88; decay-constant errors included).

Chondrite-normalized HREE compositions of zircons from sample FSTJ301 (Fig. 4.3b) show a smooth decreasing trend from Lu to Gd. All analyses conform to and are bracketed by zircon trends observed in low pressure metamorphic and magmatic zircons (Rubatto and Hermann, 2007). Titanium contents measured for use in Ti-in-zircon thermometry range from 3.9-7.0 ppm with an average of 5.2 ± 0.8 ppm.

DISCUSSION

The new U-Pb zircon ages reported here (Fig. 4.3a) overlap the Sudbury impact event, the interval over which contact metamorphism would have occurred, and the timing of

the concurrent Penokean orogeny. Thus, petrographic evidence is essential to any interpretation relating the zircons to the SIC contact metamorphism. An age reflecting the impact could be achieved by resetting of the U-Pb system during shock metamorphism or from zircon growth in an impact shock melt. However, the lack of planar fractures (e.g., Erickson et al. 2013) or other microstructural evidence suggests that a shock metamorphic origin is improbable. The poikilitic textures described are similar to those documented in zircon from lunar impact melt breccias (e.g., Gnos et al., 2004; Grange et al. 2013), but the lunar examples also contain zircons with pronounced acicular habit indicative of undercooling. The absence of such textures in the samples of this study further questions an impact origin.

Important in the samples studied here is the growth of zircon around and along grain boundaries of pyroxene, ilmenite, and relatively Ca-rich plagioclase, which indicate a post-impact metamorphic origin (Fig. 4.2a and b). The peak regional amphibolite facies Penokean metamorphic temperatures (550-590 °C) were not high enough to form the two-pyroxene hornfels assemblage. Thus, these textures also preclude a Penokean metamorphic origin. Another problem with an interpretation relating the zircons to Penokean metamorphism is the absence of blue-green ferro-tschermakitic amphibole and garnet that is characteristic of the mineral assemblage elsewhere in the EMF metabasalts, and ascribed to Penokean peak metamorphism (Mukwakwami, 2014). Finally, the presence of garnet in the Penokean mineral assemblage might have been expected to exert a greater control on the HREE than observed in Figure 4.3b, where the HREE trends of zircons from this study are in agreement with a low-pressure metamorphic or magmatic environment.

The assumption that metamorphic zircon grow during peak metamorphic P-T conditions have previously been shown to be erroneous (Roberts and Finger, 1997). As such, detailed textural investigations combined with geochemical signatures are critical to interpret the exact timing, and determine the physiochemical processes responsible for the zircon growth. For example, the equant multi-faceted zircon habits with sector zoning that are one of the common habits in the two-pyroxene hornfels rocks have been attributed to both high-T subsolidus growth (Schaltegger et al., 1999) and prograde or post-peak high-T anatexis (Vavra et al., 1999; Harley et al., 2007). Bingen et al. (2001) interpreted unusual zircon overgrowths on ilmenite in mafic granulites and amphibolites to result from ilmenite exsolving baddeleyite that subsequently reacted with silica to form zircon. Also, by progressive cooling, residual partial melts will eventually reach zircon saturation and crystallize new zircon often documented as overgrowths on pre-existing zircons (e.g., Harley 2004; Harley et al., 2007). The zircon habits described here share more characteristics with zircon grown in impact shock melts, but this is not a reasonable intepretation based on petrograhic observations. Microtextural evidence for trapped partial melts in the two-pyroxene hornfels rocks is provided by highly cuspate relatively Ca-poor plagioclase micron-scale films at three-grain junctions of Ca-rich plagioclase, which are interpreted to have formed during contact metamorphism and not during impact melting (Jørgensen et al., Chapter 2). Figure 4.2b shows the critical relationship between pseudomorphed melt film defined by relatively Ca-poor plagioclase, and zircon that grows around the Ca-rich plagioclase, and shares a straight contact with the melt film. Thus, the nature of the zircons in this study, including the poikilitic textures, irregular morphologies, lack of internal complexity, overprinting relationship with the

peak contact metamorphic assemblage, and intimate relationship with textures relating to anatexis (Fig. 4.2) are most compatible with formation during post-peak contact metamorphic cooling of trapped intergranular partial melts in the two-pyroxene hornfels rocks.

Another line of evidence that supports post-peak metamorphic zircon formation are the apparent Ti-in-zircon temperatures calculated using the Ti-in-zircon thermometer (Watson et al., 2006). The Ti content of the 13 analyses range 3.9-5.2 ppm yielding temperatures ranging from 660-710 °C. These estimates cannot be taken as accurate because they rely on rutile to be part of the equilibrium assemblage as an indication of a_{TiO2} at unity. However, underestimates by more than 70 °C are unlikely (Hayden and Watson, 2007; Ferry and Watson, 2007). Thus, with peak metamorphic temperatures above 900 °C the Ti-in-zircon thermometer still indicate post-peak metamorphic temperatures, even if the apparent temperatures are grossly underestimated.

Negative Zr-Hf and Nb-Ta anomalies relative to neighboring elements of similar compatibility during mid-ocean ridge basalt (MORB) mantle melting are commonly observed in volcanic rocks with a subduction and/or crustal source component (Pearce, 2008). In this case, the high field strength twin pairs reflect the mantle component because of their conservative behavior, whereas the relative enrichment in otherwise equally compatible elements reflects their relative mobility during subduction processes (Pearce and Stern, 2006). Rubatto and Hermann (2003) demonstrated that negative Zr-Hf anomalies in primitive arc lavas might result from residual zircon in subducted oceanic crust, and that significant Zr-Hf mobilization is likely to occur only if the liquid phase is silicate melt. Because silicate melts are able to dissolve zircon, anatexis may lead to Zr-

Hf redistribution (Roberts and Finger, 1997; Hokada and Harley, 2004). Igneous processes involving silicate melts rarely fractionate Zr-Hf, consistent with the uniform near-chondritic Zr/Hf ratios (36.6 ± 2.9: Jochum et al., 1986) of MORB and continental magmatic rocks other than granites (Bau, 1996). However, substantial Zr-Hf fractionation can occur during fractional crystallization of clinopyroxene, and the generally lower Zr/Hf ratios of MORB relative to ocean island basalts are interpreted to reflect the difference in the degree of partial melting of the mantle source (David et al. 2000). Figure 4.3c is a Zr/Zr* versus Zr/Hf plot of EMF metabasalts within the contact aureole around the SIC (data from Jørgensen et al., Chapter 3), where Zr is the measured Zr abundance and Zr* is the Zr abundance interpolated between chondrite-normalized Nd and Sm abundances (Zr/Zr* values less than unity indicate a negative Zr anomaly). Two distinct populations are evident with EMF metabasalts further from the SIC contact (black symbols) plotting at higher Zr/Zr* and Zr/Hf ratios, and two-pyroxene hornfels metabasalts (red squares) plotting at lower Zr/Zr* and Zr/Hf ratios. The population showing lower Zr/Zr* and Zr/Hf anomalies defines a proximal contact metamorphic zone within 250 m of the SIC contact (Jørgensen et al., Chapter 3). These data combined with the interpretation of zircon textures above strongly suggest that Zr-Hf were mobilized during partial melting of the metabasalts. The greater depletion of Zr relative to Hf indicates that Zr was slightly more incompatible than Hf during the partial melting process, likely reflecting greater retention of Hf than Zr in clinopyroxene.

CONCLUSIONS

Zircons in two-pyroxene hornfels facies metabasalts in the inner (< 250 m) contact metamorphic aureole of SIC form poikilitic, branching, interstitial network textures that are previously reported only in extraterrestrial impact shock melts (Lie et al., 2012). However, textural and geochemical evidence indicate that the zircons crystallized from small amounts of silicate melts trapped after partial melting and melt segregation from metabasalts during contact metamorphism. Thus, it cannot automatically be assumed that grains exhibiting this morphology represent an extraterrestrial origin. The presence of zircon in the EMF metabasalts illustrates that even rocks with exceedingly low concentrations of Zr (< 40 ppm) could contain negligible amounts of zircon in high grade metamorphic terrains where partial melting have ensued. Ignoring such zircon could prevent retrieval of critical information about the conditions and age of metamorphism. Furthermore, the timing of zircon formation represents a prime example of post-peak temperature crystallization during the retrograde path in high grade rocks. The correlation between the complex zircon textures and strong negative whole-rock Zr and Hf anomalies and relatively low Zr/Hf compared to more distal metabasalts, indicate that Zr and Hf were mobilized and fractionated during high grade metamorphism. The intimate relationship between zircon and pseudomorphed melt films, and the presence of melt patches elsewhere in the proximal aureole suggests that mobilization of Zr and Hf required a silicate melt. Metabasalts further from the SIC contact that only experienced subsolidus dehydration does not show signs of Zr and Hf mobilization, suggesting that subsolidus dehydration by itself was insignificant to mobilize Zr and Hf.

ACKNOWLEDGMENTS

Financial support was provided by grants from the Centre for Excellence in Mining Innovation, Vale Ltd., Glencore Ltd., and the Natural Sciences and Engineering Research Council of Canada (CRD to DTK and CML, Discovery Grant to DTK, and Discovery Grants #203171-2007 and #203171-2012 to CML). TRCJ acknowledges Richard Stern and Joe Petrus for discussions on how to successfully analyse the studied zircons. Field and logistical support was provided by Vale Ltd. and we are particularly grateful to Peter Lightfoot and Lisa Gibson for their assistance.

REFERENCES

Bailey, J., McDonald, A.M., Lafrance, B., and Fedorowich, J.S., 2006. Variations in Ni content in sheared magmatic sulfide ore at the Thayer Lindsley mine, Sudbury, Ontario. The Canadian Mineralogist 44, p. 1063–1077.

Bau, M., 1996. Controls on the fractionation of isovalent trace elements in magmatic and aqueous systems — evidence from Y/Ho, Zr/Hf, and lanthanide tetrad effect. Contrib. Mineral. Petrol. 123, p. 323–333.

Bingen, B., Austrheim, H., and Whitehouse, M., 2001. Ilmenite as a source for zirconium during high-grade metamorphism? Textural evidence from the Caledonides of Western Norway and Implications for zircon geochronology. Journal of Petrology, 42, p. 355-375.

Card, K.D., 1978. Geology of the Sudbury-Manitoulin area, districts of Sudbury and Manitoulin. Ontario Geological Survey, Report 166, pp 1-238. Accompanied by Map 2360, scale 1 inch to 2 miles (1:126,720), and 4 charts.

Corfu, F., Hanchar, J.M., Hoskin, P.W.O., and Kinny, P., 2003. Atlas of zircon textures. In: Hanchar, J.M., and Hoskin, P.W.O. (eds.) Zircon. Mineralogical Society of America and Geochemical Society, Reviews in Mineralogy and Geochemistry 53: p. 469-500.

David, K., Schiano, P., Allègre, C.J., 2000. Assessment of the Zr/Hf fractionation in oceanic basalts and continental materials during petrogenetic processes. Earth Planet. Sci. Lett. 178, p. 285–301.

Erickson, T.M., Cavosie, A.J., Moser, D.E., Barker, I.R., and Radovan, H.A., 2013. Correlating planar microstructures in shocked zircon from the Vredefort Dome at multiple scales: Crystallographic modeling, external and internal imaging, and EBSD structural analysis. Am. Min. 98, p. 53-65.

Ferry, J.M., and Watson, E.B., 2007. New thermodynamic models and revised calibrations for the Ti-in-zircon and Zr-in-rutile thermometers. Contrib. Mineral. Petrol. 154, p. 429–437.

Geisler, T., Schaltegger, U., and Tomaschek F., 2007. Re-equilibration of zircon in aqueous fluids and melts. Elements 3, p. 43–50.

Gnos, E., Hofmann, B. A., Al-Katgiri, A., Lorenzetti, S., Eugster, O., Whitehouse, M. J., Villa, I. M., Jull, A. J. T., Eikenberg, J., Spettel, B., Krähenbühl, U., Franchi, I. A., and

Greenwood R. C., 2004. Pinpointing the source of a lunar meteorite: implications for the evolution of the Moon. Science 305, 657–659.

Grange, M.L., Pidgeon, R.T., Nemchin, A.A., Timms, N.E., and Meyer, C., 2013. Interpreting U-Pb data from primary and secondary features in lunar zircon. Geochim. Cos. Acta., 101, p. 112-132.

Harley, S.L., 2004. Extending our understanding of Ultrahigh temperature crustal metamorphism. Journal of Mineralogical and Petrological Sciences, 99, p. 140-158.

Harley, S.L., Kelly, N.M., and Möller, A., 2007. Zircon behaviour and the thermal histories of mountain chains. Elements, 3, p. 25-30.

Hayden, L.A., and Watson, E.B., 2007. Rutile saturation in hydrous siliceous melts and its bearing on Ti-thermometry of quartz and zircon. Earth Planet Sci. Lett., 258, p. 561–568.

Hocking, M.W.A., 2003. The geology and geochemistry of the Elsie Mountain Formation: implications for Paleoproterozoic magmatism in the Southern Province; unpublished BSc thesis, Laurentian University, Sudbury, Ontario, 79p.

Hokada T., and Harley S.L., (2004). Zircon growth in UHT leucosome: constraints from zircon garnet rare earth element (REE) relations in Napier Complex, East Antarctica. Journal of Mineralogical and Petrological Sciences, 99, p.180-190.

Innes, D.G., 1977. Proterozoic volcanism in the Southern Province of the Canadian Shield. M.Sc. Thesis, Laurentian University.

Jochum, K.P., Seufert, H.M., Spettel, B., Palme, H., 1986. The solar system abundances of Nb, Ta and Y and the relative abundances of refractory elements in differentiated planetary bodies, Geochim. Cosmochim. Acta 50, p. 1173-1183.

Jolly, W.T., Dickin, A.P., Wu, T., 1992. Geochemical stratigraphy of the Huronian continental volcanics at Thessalon, Ontario: contributions of two-stage crustal fusion. Contributions to Mineralogy and Petrology 110, p. 411-428.

Ketchum, K.Y., Heaman, L.M., Bennett, G., Hughes, D.J., 2013. Age, Petrogenesis and Tectonic Setting of the Thessalon Volcanic Rocks, Huronian Supergroup, Canada. Precambrian Research.

Krogh, T.E., Davis, D.W., Corfu, F., 1984. Precise U-Pb zircon and baddeleyite ages for the Sudbury area. In: The Geology and Ore Deposits of the Sudbury Structure, Ontario Geological Survey, Special Volume 1, p. 431-446.

Liu, D., Jolliff, B., Zeigler, R.A., Korotev, R.L., Wan, Y., Xie, H., Zhang, Y., Dong, C., and Wang, W., 2012. Comparative zircon U–Pb geochronology of impact melt breccias from Apollo 12 and lunar meteorite SaU 169, and implications for the age of the Imbrium impact. Earth and Planetary Science Letters, 319-320, p. 277-286.

Ludwig, K.R., 2003. Isoplot/Ex Version 3.00: a Geochronological Toolkit for Microsoft Excel. Berkeley Geochronology Center, Berkeley, CA.

Mukwakwami J, Lafrance B, Lesher CM, Tinkham D, Rayner N, Ames DE, 2014. Fabrics and textures of deformed and metamorphosed Ni-Cu-PGE sulfide ores at Garson

Mine and their implications for sulfide mobilization processes, Mineralium Deposita 49(2): 175-198.

Nemchin, A.A., Pidgeon, R.T., Whitehouse, M.J., Vaughan, J.P., Meyer, C., 2008. SIMS U–Pb study of zircon from Apollo 14 and 17 breccias: implications for the evolution of lunar KREEP. Geochim. Cosmochim. Acta. 72, 668–689.

Paton, C., Hellstrom, J., Paul, B.,Woodhead, J. and Hergt, J. 2011. Iolite: Freeware for the visualisation and processing of mass spectrometric data. Journal of Analytical Atomic Spectrometry, 26, 2508-2518.

Paton C., Woodhead J.D., Hellstrom J.C., Hergt J.M., Greig A., and Maas R., 2010. Improved laser ablation U-Pb zircon geochronology through robust downhole fractionation correction. Geochemistry Geophysics Geosystems, 11, p. 1–36.

Pearce, J.A., 2008. Geochemical fingerprinting of oceanic basalts with applications to ophiolite classification and the search for Archean oceanic crust. Lithos 100, p. 14–48.

Pearce, J.A., and Stern, R.J., 2006. Origin of Back-Arc Basin Magmas: Trace Element and Isotope Perspectives. American Geophysical Union, Geophysical Monograph Series, 166, p. 63-86.

Petrus, J.A., and Kamber, B.S., 2012. VizualAge: A Novel Approach to Laser Ablation ICP-MS U-Pb Geochronology Data Reduction. Geostandards and Geoanalytical Research, 36, 247-270.

Prevec, S.A., and Cawthorn, R.G., 2002. Thermal evolution and interaction between impact melt sheet and footwall: A genetic model for the contact sublayer of the Sudbury Igneous Complex, Canada; Journal of Geophysical Research 107(B8), 2176.

Prevec, S.A, Kuhn, B., and Büttner, S.H., 2008. Tectosilicate oikocrysts in impact melt-hosted mafic xenoliths, contact sublayer of the Sudbury Igneous Complex, Canada. Large Meteorite Impacts and Planetary Evolution IV, Abstract Volume, 182-183.

Riller, U., 2005. Structural characteristics of the Sudbury impact structure, Canada: impact-induced versus orogenic deformation-a review: Meteoritics and Planetary Science, v. 40, p. 1723–1740.

Roberts, M.P., and Finger, F., 1997. Do U-Pb zircon ages from granulites reflect peak metamorphic conditions? Geology 25, p. 319-322.

Rubatto, D., and Hermann, J., 2003. Zircon formation during fluid circulation in eclogites (Monviso, Western Alps): implications for Zr and Hf budget in subduction zones. Geochimica et Cosmochimica Acta 67, p. 2173-2187.

Rubatto, D. and Hermann, J., 2007. Zircon behaviour in deeply subducted rocks. Elements, 3, p. 31-35.

Schaltegger U., Fanning C.M., Günther D., Maurin J.C., Schulmann K., and Gebauer D., 1999. Growth, annealing and recrystallization of zircon and preservation of monazite in high-grade metamorphism: conventional and in-situ U-Pb isotope, cathodoluminescence and microchemical evidence. Contributions to Mineralogy and Petrology 134, p. 186-201.

Vavra, G., Schmid, R., and Gebauer, D., 1999. Internal morphology, habit and U-Th-Pb microanalysis of amphibolite-to-granulite facies zircons: geochronology of the Ivrea Zone (Southern Alps). Contributions to Mineralogy and Petrology 134, p. 380-404.

Watson, E.B. and Harrison, T.M., 1983. Zircon saturation revisited temperature and composition effects in a variety of crustal magma types, Earth and Planetary Science Letters, 64, p. 295-304.

Watson E.B., Wark D.A., and Thomas J.B., 2006. Crystallization thermometers for zircon and rutile. Contributions to Mineralogy and Petrology 151, p. 413-433.

FIGURES AND TABLES

Table 4.1. U-Pb and trace element data for zircon in Elsie Mountain Formation metabasalts.

	Samples	301 Remake SOI 33						301 Remake SOI 37	301(6) SOI2					
	Spot	1	2	3	4	5	7	1	1	2	4	5	6	7
Isotopic ratios	$^{207}Pb/^{235}U$	5.19	5.58	5.7	5.61	5.6	5.3	4.91	5.7	6.1	5.3	5.36	5.2	5.14
	2σ	0.46	0.79	1.5	0.75	1.2	0.78	0.57	1.1	1.5	1.2	0.64	0.59	0.76
	$^{206}Pb/^{238}U$	0.327	0.333	0.324	0.324	0.321	0.325	0.339	0.329	0.347	0.372	0.328	0.329	0.333
	2σ	0.017	0.023	0.026	0.021	0.033	0.028	0.026	0.017	0.046	0.04	0.018	0.016	0.02
	ρ	0.21	-0.06	0.23	0.26	0.46	-0.13	0.50	-0.07	0.15	0.02	0.19	-0.05	0.00
	$^{207}Pb/^{206}Pb$	0.12	0.127	0.124	0.131	0.124	0.115	0.114	0.129	0.148	0.109	0.119	0.12	0.121
	2σ	0.011	0.019	0.032	0.02	0.023	0.015	0.011	0.028	0.039	0.026	0.014	0.016	0.019
Age estimates [Ma]	$^{207}Pb/^{235}U$	1809	1840	1800	1910	1860	1820	1790	1910	1900	1770	1820	1825	1760
	2σ	82	130	250	140	190	130	95	160	210	200	100	85	140
	$^{206}Pb/^{238}U$	1817	1850	1810	1805	1790	1810	1880	1833	1910	2020	1821	1828	1845
	2σ	80	110	130	99	160	130	130	85	210	190	88	77	96
	$^{207}Pb/^{206}Pb$	1830	1810	1640	1970	1880	1760	1830	2020	2060	1610	1740	1880	1700
	2σ	170	330	570	290	330	250	170	330	470	540	240	210	340
% Discordance		1	-2	-10	8	5	-3	-3	9	7	-25	-5	3	-9
Compositional data	Pb [ppm]	15.3	10.8	12.1	23.9	17.5	14.8	24.4	25.3	21.8	13.1	15.3	21.2	14.1
	2σ	2	2.3	3	4.1	2.7	2.9	5.8	8.2	4.1	2.1	2.2	2.8	2.6
	U [ppm]	29.9	24.6	18	37.5	32.6	30.1	42.9	44.1	31.1	26.1	30.2	33	20.9
	2σ	3.6	1.6	2.2	6.3	2.6	4	2.5	6.1	2.1	1.6	1.9	2.9	1.2
	Th [ppm]	17.2	14.3	13.1	20.7	17.9	16.1	19.4	23.9	19.7	17	21.6	23.4	11.16
	2σ	1.9	1.1	1.2	4.9	2.2	2.3	1.1	3.5	1.8	1.1	1.5	2.6	0.91
	U/Th	1.7	1.7	1.4	2.0	2.0	2.0	2.2	2.0	1.8	1.7	1.5	1.5	1.9
	Gd [ppm]	12.8	9.6	7.7	4.4	12.1	5.3	8.7	7.3	3.6	17.7	23.3	25.3	10.3
	2σ	3.2	4.3	5.1	3.1	2.9	3.3	1.9	3.9	2.6	4	3.8	4.2	3.5
	Tb [ppm]	3.97	2.69	1.9	3.3	3.46	2.7	2.8	3.92	1.8	9.6	8.2	10.3	3.08
	2σ	0.73	0.8	1.2	1.5	0.88	1	0.65	0.96	0.7	1.6	1.2	1.4	0.69
	Dy [ppm]	51.5	36.6	30.7	46	42.8	18.1	33.2	49	26	90.3	109.1	114	45.4
	2σ	6.7	5.7	7.9	11	7.5	4.5	4.4	12	5.1	7.8	8.8	15	5.1
	Ho [ppm]	19.7	13.5	11.1	12.6	13.3	7	15.1	19.4	12.5	31.8	37.6	43.4	16.6
	2σ	2.2	2	3.3	1.7	2.3	1.5	1.5	4	2.3	3.4	3.1	4.5	2
	Er [ppm]	91.1	76.5	61.9	76	64	28.9	85	73.4	57.7	137	146.8	174	74.3
	2σ	9.5	6.7	9	10	12	7.5	10	8.4	8.7	12	9.4	18	9.5
	Tm [ppm]	20.9	16.7	15.1	16.8	14.9	4.3	18.8	20.3	14.9	29.6	35	38.6	18.9
	2σ	2.9	2.5	2.8	6.1	2.8	1.4	1.6	3.4	2.2	2.4	3.4	4.1	2
	Yb [ppm]	196	156	121	194	127	55.9	179	182	133	303	297	332	156
	2σ	11	18	17	16	19	8.3	19	37	19	29	23	29	14
	Lu [ppm]	34.4	28.7	25.2	30.5	23.9	10.2	33.3	41	23.2	47.7	49.6	58.1	28.9
	2σ	2.9	2.6	3.9	4.3	3.4	1.9	3	9	2.7	3.7	3	4.3	2.8
	Ti [ppm]	5.92	4.85	4.6	6.96	6.38	4.16	5.37	5.17	3.88	4.96	5.13	5.12	5.13
	2σ	0.27	0.25	0.5	0.41	0.5	0.22	0.23	0.61	0.29	0.3	0.22	0.26	0.27
Ti-in-zircon thermometry	T [°C]	697	681	677	710	703	669	689	686	664	683	685	685	685

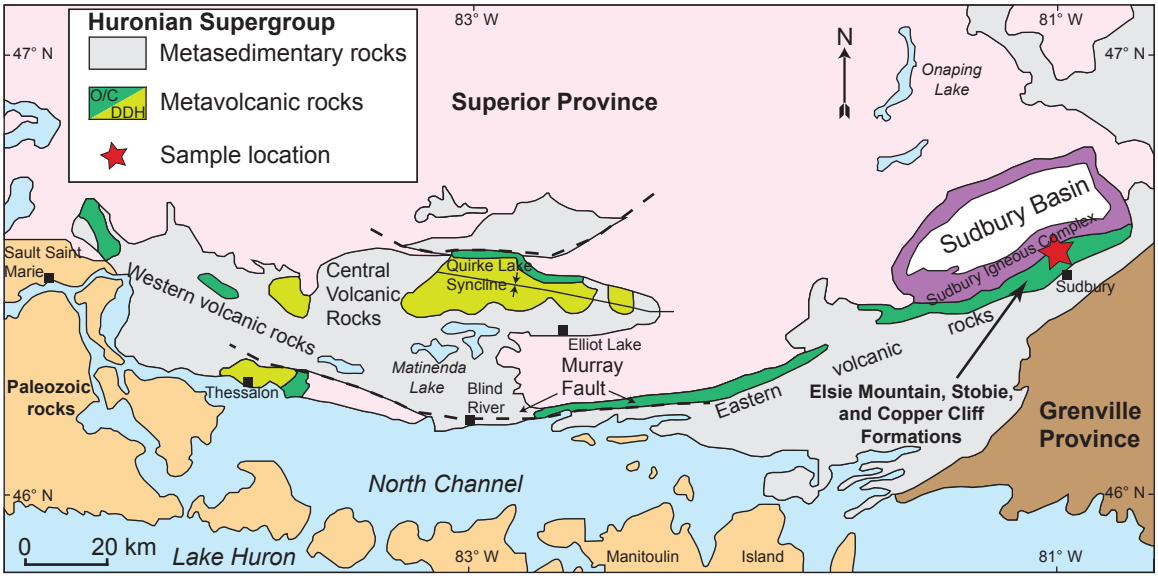

Fig. 4.1. Simplified geological map showing the distribution of the Huronian metavolcanic rocks from Sault Ste. Marie (west) to Sudbury (east), and the Sudbury Structure straddling the boundary between the Superior Province and the Huronian Supergroup. The sample location within the Elsie Mountain Formation right at the contact with the SIC is indicated by a red star (modified after Card (1978)).

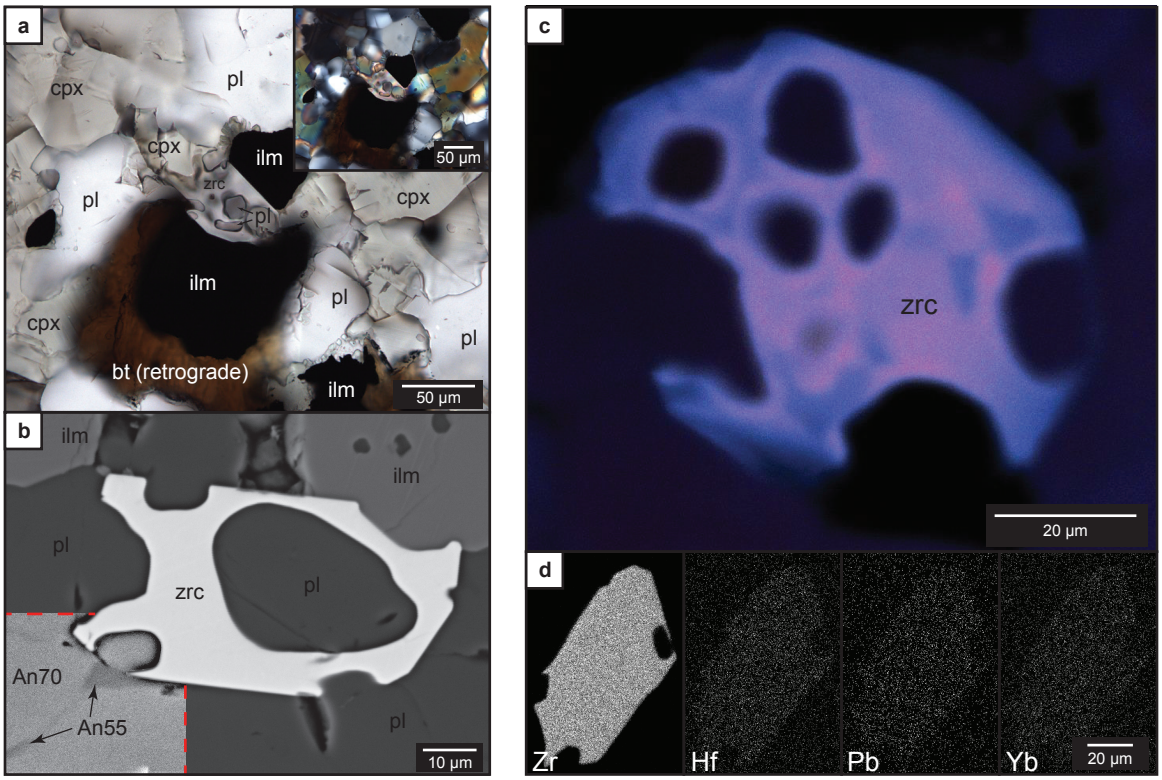

Fig. 4.2. a) Irregular and poikilitic zircon (R-S33) with inclusions of plagioclase and contacts toward clinopyroxene (Cpx), ilmenite (Ilm), and matrix plagioclase (Pl). Inset shows the same field of view in cross-polarized light, highlighting the granoblastic polygonal texture of the high temperature mineral assemblage. b) BSE image with contrast in lower left corner (indicated by red dashed lines) adjusted to better show the presence of two compositional distinct plagioclase phases (An55 and An70). The low-Na plagioclase reflects trapped partial melt in the hornfels rocks. c) CL image showing the typical complex habit of the zircon with weak sector zoning and no indication of multiple generations, alteration or metamictization. d) Qualitative SEM element maps showing homogenous distribution of Zr, Hf, Pb, and Yb in zircon grain ((6)-S2).

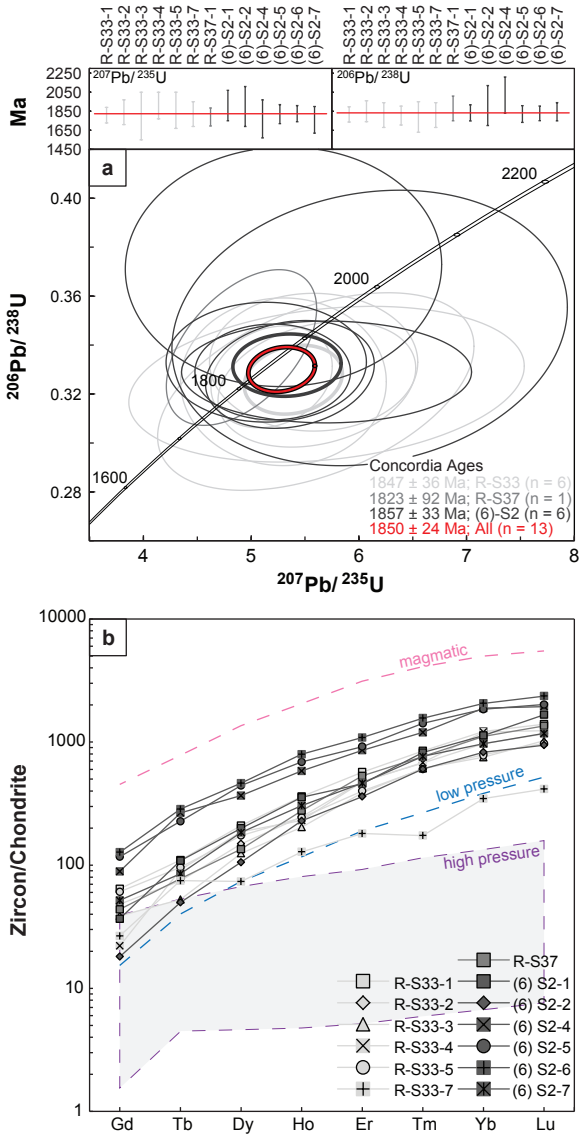

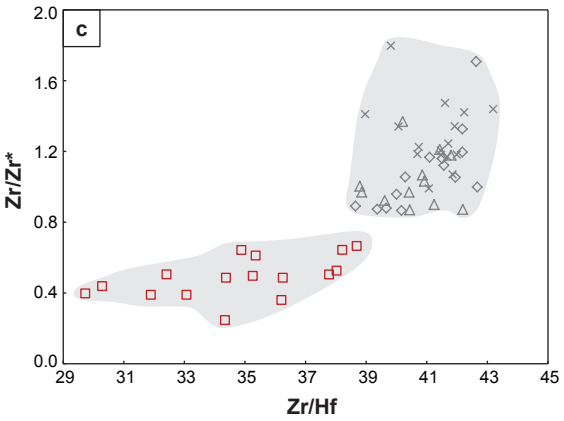

Fig. 4.3. a) Concordia diagram showing zircon ages from the EMF metabasalts. Individual analyses are presented as thin error ellipses, whereas thicker ellipses are concordia ages for all analyses within each grain (note grain R-S37 consist of only a single spot analyses). The thick red error ellipse represents the concordia age calculated for all 13 analyses together and yields an age of 1850 ± 24 Ma. Inset at the top are a weighted-average plot of each individual analyses for both 207Pb/235U and 206Pb/238U ages. b) HREE chondrite-normalized diagram showing results for the same 13 analyses as above. The trends are smooth and fall within the range of low-P magmatic zircons of Rubatto and Hermann (2007). c) Whole-rock Zr/Zr* vs. Zr/Hf plot showing two distinct groups within the Elsie Mountain Formation metabasalts: distal protoliths (black symbols) have higher Zr/Zr* and Zr/Hf ratios, whereas 2-pyroxene hornfels metabasalts have lower Zr/Zr* and Zr/Hf ratios. Together with the petrographical observations this indicates mobility of Zr and Hf and greater mobility of Zr relative to Hf. Whole-rock Zr and Hf data from Jørgensen et al. (Chapter 3).

CHAPTER 5: CONCLUDING STATEMENTS

CONCLUSIONS

The metamorphic aureole produced by the 1850 Ma Sudbury Igneous Complex (SIC; Krogh *et al.*, 1984) is partially preserved along its southern margin in Elsie Mountain Formation (EMF) metabasalts belonging to the Huronian Supergroup. The EMF metabasalts form a significant portion of the southern footwall and locally exhibit several features indicative of SIC contact metamorphism: 1) preserved peak contact metamorphic mineral assemblages including partial melting textures; 2) a metamorphic chemostratigraphy; and 3) the presence of zircon grown from trapped partial melt that yield a U/Pb age of 1850 ±24 Ma. These observations should unequivocally dispel the common assumption stated in the literature that the SIC South Range contact aureole has been all but obliterated by later tectonometamorphic events (e.g., Dressler, 1984; Boast and Spray, 2006; White, 2012). Based on field mapping and petrography the SIC contact aureole in the EMF metabasalts is divided into three zones: 1) a pyroxene hornfels zone (PHZ) extending up to 500 m from the SIC contact that is defined by a metamorphic peak assemblage consisting of plagioclase-orthopyroxene-clinopyroxene-ilmenite-magnetite; 2) a pyroxene granofels zone (PGZ) extending from the PHZ up to 750 m from the SIC contact that is characterized by a metamorphic peak assemblage composed by plagioclase-clinopyroxene-orthopyroxen-ilmenite-magnetite ± high-Ti hornblende ± quartz ± biotite ± grunerite; and 3) a hornblende hornfels zone (HHZ) extending from the limit of the PGZ to at least 1000 m from the SIC contact, and is characterized by a metamorphic peak assemblage comprised of high-Ti hornblende-plagioclase-quartz-

ilmenite ± biotite ± magnetite. Incipient partial melting is locally present in the PGZ, whereas melt segregation textures are also present locally in the PHZ. The SIC contact aureole in the EMF metabasalts is also preserved in the whole-rock major and trace element geochemistry. The geochemical zonation allows for subdividing the PHZ into: 1) an inner zone (Hornfels A unit), extending up to approximately 250 m from the SIC contact and characterized by strong mobilization of K, Cs, Rb, Ba, LREE, and W, Th, and U. This zone also shows moderate to strong mobilization of otherwise immobile Ta, Nb, Zr, and Hf, which is accompanied by significant Zr/Hf fractionation and minor fractionation of Nb/Ta; 2) a transitional zone (Hornfels B unit) extending from the Hornfels A unit and up to 500 m from the base of the SIC. This zone is characterized by moderate-strong mobility of K, Cs, Rb, Ba, moderate LREE and W, Th, U mobility, and weak-moderate Ta > Nb mobility. Outside the PHZ and to at least ca. 750 m from the SIC contact, the effects of contact metamorphism is less pronounced other than perhaps U > Th mobility, and an increasing mobility of W as the transition zone is approached. Petrological modelling constrains peak contact metamorphic temperatures in the PHZ to upwards of 925 °C and up to 680 °C in the HHZ at 1000 from the SIC contact. Constrains on partial melting from both phase equilibria modelling and trace element modelling suggest melting reached at least 10-20% in the PHZ and could have reached upwards of 35% melting within the proximal 250 m of the SIC.

The results presented in this thesis have implications for both so-called contact deposits and footwall deposits. The decreasing width of the contact aureole in a northeastern direction observed in the EMF metabasalts in Map Area 1 (north of the world-class Ni-Cu-PGE Frood-Stobie offset deposit and east of the Little Stobie contact deposit)

correlates with empirical observations of a thinner SIC in the same direction (Keays and Lightfoot, 2004). Because thicker parts of the SIC correlates with the location of significant contact ore deposits (Keays and Lightfoot, 2004) our observations would suggest that the presence of such deposits might also be associated with thicker contact aureoles as observed in the vicinity of the Little Stobie deposit. Another implication concerning the low-S Cu-PGE rich footwall mineralization is the width of the high-T contact aureole that might be a deciding factor for the distance from the SIC contact that these deposit types can form. This is suggested by experiments documenting Au, Pd, and Pt transport down to 600 °C by S-dominated volatiles (Cafagna, 2015). The evidence for melt segregation in the EMF metabasalts is overwhelming from macro- and microscopic observations, whole rock geochemistry and petrological modelling. Nevertheless, the absence of dikes back-injecting the SIC equivalent to those observed deriving from the Creighton and Murray plutons (e.g., Peredery and Morrison, 1984) supports the interpretation that partial melts from the EMF metabasalts contributed directly to the formation of the commonly mineralized SIC Sublayer (e.g., Lightfoot *et al*., 1997; Prevec, 2000; Prevec *et al*., 2000; Prevec and Cawthorn, 2002).

The research results from this thesis also have value to the broader scientific community. The intensive phase equilibria modelling of basaltic compositions at LP-HT conditions carried out as part of this work have shown through comparison with experimental results that this method is tremendously useful at constraining peak metamorphic temperatures and predicting peak metamorphic mineral assemblages. Although phase equilibria modelling continuously benefits from the improvement of *a-x* models the investigation presented here indicates that advances to the activity models for pyroxenes, amphibole,

and melt could resolve specific issues, including: underestimation of the solidus temperature in a compositional system that includes K, underestimation of temperatures for orthopyroxene stability, and clino- and orthopyroxene modal abundances. Nonetheless, it is recommended that the method of phase equilibria modelling is always utilized for rocks of basaltic composition at LP-HT metamorphic conditions when constraining peak conditions in addition to more conventional two-pyroxene geothermometry. In particular, the phase equilibria method could be useful in the investigation of contact metamorphism occurring at axial magma chambers at mid-ocean ridges. To our knowledge, this is the first study to document a large scale metamorphic chemostratigraphy in a suite of mafic volcanics. Commonly regarded immobile elements including Th and Zr were mobilized by silicate melts rather than hydrous fluids as indicated by the relative depletion of these elements in the Hornfels units compared to the Granofels unit. These observations could have implications for element mobility during subduction processes. The discovery of poikilitic zircons in EMF metabasalts from the Hornfels A unit is unique to terrestrial rocks, and provides the first examples of zircon with this texture that did not form during crystallization of an impact generated shock melt. Thus, these textures should not automatically result in the interpretation of a shock metamorphic history. In this case, several lines of evidence including textural relationships with the contact metamorphic peak mineral assemblage, U/Pb dates, zircon trace element chemistry, and Ti-in-zircon thermometry strongly supports the interpretation of formation from trapped partial melt films on the retrograde path.

FUTURE WORK

The majority of the work presented in this thesis focusses on the EMF metabasalts and their physicochemical characteristics because they best preserved the expression of SIC contact metamorphism and host the widest high-temperature contact aureole. For this reason, future work could emphasize on the Murray and Creighton plutons that constitute the other dominant footwall rocks along the SIC southern margin. Of particular interest is the seemingly large discrepancy in the preserved high-temperature aureole between the granites and the metabasalts, and the apparent continuation of partial melting of the granite bodies while the SIC was below its solidus. This should also include a closer look at triple junctions where the SIC, basaltic footwall, and granitic footwall meet. Little geochemistry exists from the granites and therefore it would also be beneficial to investigate whether the granites possess geochemical signatures that can be related to the contact metamorphism.

There are curiously few footwall deposits described in the South Range footwall compared to the North Range, and a clear explanation for this is discrepancy is missing. Geochemistry focusing on the metalloids and the elements of economic interest should be acquired from the EMF metabasalts to further address the seemingly underendowed South Range footwall. Furthermore, areas where the EMF metabasalts have experienced complete retrogression or downgrading should be sampled and analyzed for whole rock geochemistry to evaluate the if the geochemical signatures identified in this thesis to reflect contact metamorphism are retained in retrograded hornfels and granofels rocks. The ability to identify these geochemical signatures in retrograded and structurally modified rocks could be useful in pre-deformation reconstructions due the the SIC-

proximal implications of these geochemical signatures. It would also be beneficial to look at core intervals that crosscut the SIC-footwall contact that were not available for this study to get a better understanding of the proximal partial melt zone in the EMF metabasalts. More detailed work should be carried out on high-Ti hornblende to explore if chemical signatures exist that could distinguish retrograde and prograde hornblendes from one another. Higher precision U/Pb dating could be attempted on the metamorphic zircons to determine if it is possible to achieve a resolution good enough to distinguish post-impact contact metamorphic zircon growth from the SIC crystallization event. More work could also be done on accessory phases to learn more about the trace element budget and in particular the distribution and partitioning of REEs and the HFSEs.

REFERENCES

Boast, M. and Spray, J.G. 2006. Superimposition of a thrust-transfer fault system on a large impact structure: Implications for Ni-Cu-PGE exploration at Sudbury; Economic Geology, v. 101, p. 1583-1594.

Cafagna, F., 2015. The geochemical behavior of metalloids and their effect on the highly siderophile elements during the crystallization of a magmatic sulfide liquid in relation to the formation of Ni-Cu-PGE magmatic sulfide deposits. Unpublished PhD thesis, Laurentian University, Sudbury, Ontario, 206p.

Dressler, B.O., 1984b. The effects of the Sudbury event and the intrusion of the Sudbury Igneous Complex on the Footwall Rocks of the Sudbury structure. In: Pye, E.G.,

Naldrett, A.J., Giblin, P.E. (Eds.), The geology and ore deposits of the Sudbury structure: Ontario Geological Survey Special Volume 1, p. 97–136.

Keays, R.R., Lightfoot P.C., 2004. Formation of Ni–Cu–PGE sulfide mineralization in the Sudbury Impact Melt, Min Pet 82: p. 217–258.

Krogh, T.E., Davis, D.W., Corfu, F., 1984. Precise U-Pb zircon and baddeleyite ages for the Sudbury area. In: The Geology and Ore Deposits of the Sudbury Structure, Ontario Geological Survey, Special Volume 1, p. 431-446.

Lightfoot, P.C., Doherty, W., Farrell, K., Keays, R.R., Moore, M., and Pekeski, D., 1997. Geochemistry of the Main Mass, Sublayer, Offsets, and Inclusions from the Sudbury Igneous Complex, Ontario: Ontario Geological Survey, Open File Report 5959, 231 p.

Prevec, S. A., 2000. An examination of modal variation mechanisms in the contact sublayer of the Sudbury Igneous Complex, Canada, Mineral. Petrol., v. 68, p. 141– 157.

Prevec, S.A. and Cawthorn, R.G. 2002. Thermal evolution and interaction between impact melt sheet and footwall: A genetic model for the contact sublayer of the Sudbury Igneous Complex, Canada; Journal of Geophysical Research, v. 107(B8), p. 2176.

Prevec, S. A., Lightfoot, P.C., and Keays R.R., 2000. Evolution of the sublayer of the Sudbury Igneous Complex: Geochemical, Sm-Nd isotopic and petrologic evidence, Lithos, v. 51, p. 271– 292.

White, C. J., 2012. Low-Sulfide PGE-Cu-Ni Mineralization From Five Prospects Within The Footwall Of The Sudbury Igneous Complex, Ontario, Canada. Unpublished PhD thesis, University of Toronto, Ontario, 337p.